Plasma Physics Reports, Vol. 27, No. 11, 2001, p. 1000. Translated from Fizika Plazmy, Vol. 27, No. 11, 2001, p. 1056.

OBITUARY

In Memory of Vitaly Adol'fovich Schweigert (August 30, 1955–April 3, 2001)

Vitaly Adol'fovich Schweiger, an eminent theoretical physicist and expert in the fields of gas discharge physics, dusty plasmas, and solid-state physics, died of brain cancer on April 3, 2001, being just 45 years old, full of energy, and at the height of his scientific achievements.

Vitaly Schweigert was born August 30, 1955, in the town of Krasnokutsk, Kazakhstan. After graduating with honors from the Physics Department at Novosibirsk State University in 1977, he worked for more than 20 years in Novosibirsk at the Institute of Theoretical and Applied Mechanics of the Russian Academy of Sciences. In 1983, he defended his candidate's dissertation and, in 1997, his doctoral dissertation. Both dissertations were devoted to numerical simulations of gas discharges. Vitaly Schweigert was one of the first scientists to demonstrate the potentialities of numerical simulations in gas discharge physics and one of the pioneers in developing multidimensional kinetic codes based on Boltzmann equation solvers and the Monte Carlo and particle-in-cell techniques. Vitaly Schweigert applied these codes to study the fundamental effects related to the nonlocality of the electron energy distribution functions in gas discharges. His ability to efficiently simulate very complicated physical systems with disparate time and space scales was extraordinary.

The scientific productivity of Vitaly Schweigert exploded in the past decade when he applied his simulation capabilities to other areas, such as the physics of fullerenes, the formation of atomic clusters and dusty crystals, the structure of two-dimensional Wigner crystals, quantum dots, phase transitions, vortex matter in mesoscopic superconductors, and the design of semiconductor devices.

Vitaly Schweigert was a creative person who generated a lot of ideas. As a result of sharing his ideas and numerical codes with other scientists, he co-authored more than fifty articles during the last five years. In total, he published 156 papers in the leading scientific journals. His recent papers (1996–2000) on mesoscopic superconductivity and dusty plasmas were widely recognized and often quoted, each of them receiving, on average, 30–40 citations.

Vitaly Schweigert's computational ability was in high demand by many experimental and theoretical groups in Russia, USA, Germany, Belgium, and the Netherlands. Owing to those numerous collaborations, Vitaly Schweigert had more than thirty co-authors around the world. His remarkable research was supported by numerous funding agencies in Russia and abroad.

The colleagues and friends of Vitaly Schweigert knew him as a sincere and honest man who was devoted to science. His warm and generous personality, his considerable expertise, and his enthusiasm for life will be sorely missed by his family, friends, and colleagues.

N. L. Aleksandrov, É. M. Bazelyan,
I. D. Kaganovich, F. M. Peeters, Yu. P. Raizer,
A. T. Rakhimov, A. N. Starostin,
M. N. Shneider, I. V. Schweigert,
L. D. Tsendin, and others
(in total, 37 signatures)

1063-780X/01/2711-1000$21.00

Plasma Physics Reports, Vol. 27, No. 11, 2001, pp. 907–921. Translated from Fizika Plazmy, Vol. 27, No. 11, 2001, pp. 963–977.

MAGNETIC CONFINEMENT SYSTEMS

Plasma Convection near the Threshold for MHD Instability in Nonparaxial Magnetic Confinement Systems

V. P. Pastukhov and N. V. Chudin

Russian Research Centre Kurchatov Institute, pl. Kurchatova 1, Moscow, 123182 Russia

e-mail: past@nfi.kiae.ru

Received June 25, 2001

Abstract—Using a highly nonparaxial magnetic confinement system with an internal levitated ring as an example, it is shown that, in a plasma near the threshold for ideal MHD instability, the external heating and the original local dissipative processes may give rise to and maintain self-consistent nonlinear MHD convection, which leads to an essentially nonlocal, enhanced heat transport. A closed set of equations is derived that makes it possible to describe such convective processes in a weakly dissipative plasma with $\beta \sim 1$. Numerical simulations carried out with a specially devised computer code demonstrate that the quasisteady regime of nonlinear convection actually exists and that the marginally stable profile of the plasma pressure is maintained. A large amount of data on the structure of the nascent convective flows is obtained and analyzed. © *2001 MAIK "Nauka/Interperiodica".*

1. INTRODUCTION

One of the fundamental problems hindering the creation of an economically competitive and ecologically attractive magnetic confinement fusion reactor is that of achieving higher values of the parameter $\beta = 8\pi p/B^2$ (which is the ratio of the plasma pressure to the magnetic field pressure) as compared with those available in modern-day tokamaks. By increasing the β value, it is possible to raise the density of the energy released in fusion reactions at a fixed maximum magnetic-field strength and, thus, to make the reactor more compact and improve its economic benefits. Moreover, achieving the conditions under which a plasma with $\beta \sim 1$ can be confined for a sufficiently long time opens promising new ways to create a low-radioactivity fusion reactor based on the neutronless D–^{3}He reaction. Unfortunately, despite the advantages of tokamaks, progress toward achieving high β values in these devices is hampered by the conditions for tokamak plasmas to be equilibrium and MHD stable. Thus, in present-day experiments, the tokamaks operate at $\beta < 0.1$; moreover, even the most optimistic theoretical estimates show that, in tokamaks, the parameter β cannot be higher than 0.2–0.3. On the other hand, the possibility of creating magnetic systems capable of confining plasmas with $\beta \sim 1$ does not contradict basic principles. A number of such systems have already been proposed and investigated experimentally. For example, in experiments with a levitated magnetic octopole, β values amounted to about 44% [1]. In this context, it is expedient not only to investigate possible ways of increasing β values in tokamaks but also to carry out a more systematic analysis of the potential of alternative magnetic systems for confinement of a plasma with $\beta \sim 1$.

The first step in the analysis of alternative systems is to examine the equilibrium and MHD stability of the plasma. There is a fairly wide class of magnetic confinement systems capable of ensuring the equilibrium of a plasma with $\beta \sim 1$. However, the condition for the plasma to be MHD stable substantially reduces this class. Regardless of the value of β, magnetic systems in which MHD instabilities of a confined plasma are suppressed most efficiently are those in which the magnetic field strength B has an absolute minimum, i.e., in which the vacuum magnetic field in the plasma confinement region increases toward the plasma periphery in all directions. However, it is well known that the only systems where the plasma can be confined entirely inside the minimum-B region are open magnetic devices. In systems in which the confinement region is bounded by a closed magnetic surface, a softer averaged minimum-B condition can only be provided. In such systems, the main MHD instabilities are suppressed if the parameter β is lower than a certain critical value (which is, as a rule, substantially smaller than unity); an increase in β above this critical value is prevented by the onset of unstable ballooning modes.

At the same time, there is an alternative approach to the problem of MHD stability in confinement systems that possess neither an absolute nor average minimum B. The essence of this alternative approach consists in the following: convective MHD modes can be stable not only in minimum-B systems, but also in systems without absolute or average minimum B if the plasma pressure decreases sufficiently gradually toward the periphery of the confinement region. In the ideal isotropic one-fluid MHD model, the plasma pressure profile at the stability margin of convective modes satisfies the

1063-780X/01/2711-0907$21.00 © 2001 MAIK "Nauka/Interperiodica"

condition $S \equiv pU^\gamma = \text{const}$, where $U = \oint dl/B$ is the specific flux tube volume, γ is the adiabatic index, and S is a single-valued function of the entropy density of a magnetized plasma. It is important to note that, because of the condition for the entropy density to be constant, convective modes are marginally stable for any β value consistent with plasma equilibrium. Of course, in such systems, MHD modes that are not convective in origin (e.g., kink modes in toroidal configurations) may be unstable, so that the stability of these modes is to be proved when analyzing any particular magnetic confinement system. For some systems, the restrictions imposed on β values by these modes are not too stringent, $\beta \sim 1$.

The existence of marginally stable pressure profiles (MSPPs) was discussed as early as the late 1950s [2–4]. More recently, papers were published that dealt with marginally stable equilibria of plasmas with $\beta \sim 1$ in field-reversed configurations (FRC) [5] and with the so-called divertor stabilization of plasmas in an axisymmetric mirror system [6, 7]. Also, the concept of a dipole reactor was developed [8] and a conceptually similar idea of a mirror system with a levitated ring, which forms an FRC, was originated [9, 10]. In these papers, a study was made of MHD stable plasma states in systems without minimum *B*. Marginally stable plasma states have also been discussed in connection with research on the Earth's magnetosphere [11–13].

The above alternative method for stabilizing magnetically confined plasmas is of practical interest when an MSPP admits a substantial (orders-of-magnitude) decrease in the plasma pressure at the periphery. It is only in this case that the MSPP can be made consistent with the boundary conditions for the power absorption in the peripheral regions of high-temperature plasmas confined in magnetic devices. Since the characteristic pressure gradient corresponding to an MSPP is completely determined by the relative gradient of U (i.e., by the magnetic field line curvature), the alternative method in question is efficient only for highly nonparaxial systems and does not hold promise for many traditional magnetic systems, which are designed for confinement of paraxial plasmas ($|\nabla p/p| \geqslant |\nabla U/U|$). The effects of the nonparaxial nature of a confinement system can be made more pronounced by forming a separatrix surface at the plasma periphery. The separatrix surface should contain lines and points at which the magnetic field vanishes. It can be seen that, as the separatrix surface is approached, $U \longrightarrow \infty$, and the plasma pressure corresponding to an MSPP vanishes. Note that the above considerations are, on the whole, valid under the assumptions used in other hydrodynamic models. In particular, MSPPs that drop off near the external separatrix to zero were obtained when analyzing the divertor stabilization of a plasma in both the Chew–Goldberger–Low anisotropic collisionless hydrodynamic model [7] and in the Kruskal–Oberman semi-kinetic model [14, 15]. Moreover, the MSPPs obtained using these models decrease more rapidly toward the plasma periphery than those obtained using the simplest isotropic MHD model. In some papers, MSPPs were also analyzed with allowance for the plasma pressure anisotropy [11–13, 15] and the restrictions associated with ballooning modes [13, 16–18].

Note that a detailed analysis of MSPPs, being very important in itself, is, at the same time, only the first necessary step in the study of the above alternative method for plasma stabilization. The next fundamental problem to be investigated is that of maintaining a stable plasma state under plasma heating and energy absorption at the plasma periphery and in the presence of the original local transport processes that distort the MSPP. In turn, the distortion of the pressure profile violates the stability condition in certain plasma regions and, thus, may cause a rapid large-scale ejection of a plasma onto the wall. In the approach under discussion, it is, as a rule, intuitively assumed that this undesirable scenario is impossible and that the plasma dynamics is dominated by the tendency to self-consistently restore and maintain the MSPP. An analogous effect is known from the investigations of thermal convection in various natural objects. On the other hand, it is well known that nascent self-consistent convection is a complicated nonlinear phenomenon and is capable of substantially enhancing transport processes. The above considerations show that maintaining the MSPP self-consistently is a fairly nontrivial task, which requires a thorough theoretical analysis. Here, for a relatively simple magnetic configuration (which, nonetheless, reflects the most distinguishing features of nonparaxial magnetic confinement systems), we develop a model of self-consistent MHD plasma convection maintained by the energy input into the plasma and by the original classical transport processes. Numerical simulations based on this model made it possible to reveal the main properties of this convection, to calculate the final (anomalous) heat flux, and to demonstrate that the convection is capable of maintaining the plasma near the state of marginal stability.

The paper is organized as follows. In Section 2, we discuss the plasma configuration under analysis in the context of equilibrium, stability, and the relevant β limit. In Section 3, we employ the one-fluid MHD model with an isotropic plasma pressure in order to derive a self-consistent set of equations for describing plasma convection and plasma transport processes. In Section 4, this set of equations is adapted to a computer code. In Section 5, we discuss the results of numerical calculations. In Section 6, we briefly summarize the results obtained.

2. PLASMA EQUILIBRIUM AND STABILITY IN A MODEL MAGNETIC CONFIGURATION

In this paper, we restrict ourselves to considering MHD convection near the state of marginal stability of

a plasma in a system with an internal levitated ring (such as a dipole reactor, which was discussed in the Introduction [8]) and in a conceptually similar mirror system with a reversed magnetic field—the MIRAGE (Mirror-Internal-Ring Axisymmetric GEometry) system [9]. The theory of plasma confinement in such magnetic systems is now being actively developed, and experiments on the "dipole confinement" of a plasma have already begun in the LDX device [19].

Figure 1 shows a schematic of the magnetic configuration of the MIRAGE device, which is a simple axisymmetric mirror cell with a vertical axis and a levitated ring carrying a current opposite to the current in the external (mirror) coils. The currents in the ring and external coils are chosen in such a way as to form a magnetic configuration of the compact torus type. Specifically, around the ring, there is a toroidal confinement region in which the closed lines of the poloidal magnetic field enclose the ring. The confinement region is bounded from the outside by a separatrix, which exhibits two magnetic null points. On the outside of the separatrix, the magnetic field lines are open: they pass through the magnetic mirrors, forming a natural divertor whose absorbing plates are, in fact, infinite in area. The equilibrium of a finite-β plasma in such a system was investigated by Popovich and Shafranov [10]. The problem reduces to that of solving the Grad–Shafranov equation without the current function; the relevant plasma pressure profile presented as a function of the magnetic flux ψ is shown in Fig. 2, where ψ_c and ψ_s correspond to the surface of the internal levitated ring and to the separatrix, respectively. In the inner region ($\psi_c < \psi < \psi_m$), the plasma is MHD stable, because $p'(\psi) > 0$. In the outer region ($\psi_m < \psi < \psi_s$), the pressure profile is marginally stable: $S(\psi) \equiv pU^\gamma = \text{const}$. A dipole confinement system differs from the system illustrated in Fig. 1 only in that, when the distance between the chamber wall and the levitated ring is sufficiently large, the MSPP is capable of ensuring a sufficiently low pressure at the plasma periphery even in the absence of a separatrix. In Fig. 2, this case corresponds to the limit $\psi_s \longrightarrow \infty$.

Because of the complexity of the Grad–Shafranov equation, it is very difficult to investigate the development of convective modes against the background of a two-dimensional unsteady plasma equilibrium with $\beta \sim 1$. For this reason, it is expedient, at least in the first step, to analyze a simpler, one-dimensional, equilibrium plasma configuration possessing the most basic properties of the above-described two-dimensional equilibrium configurations. For this purpose, instead of the configuration illustrated in Fig. 1, we consider an infinite cylindrical equilibrium plasma column with a cylindrical conductor of radius r_c at its axis. In other words, we consider a Z-pinch configuration in which the plasma is originally in equilibrium with the magnetic field created by both the current flowing in the central conductor and the diamagnetic current flowing

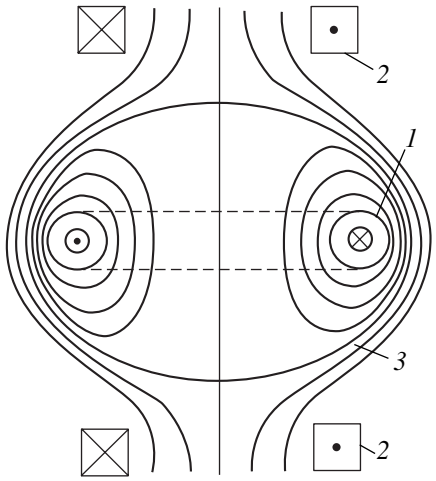

Fig. 1. Schematic of a magnetic confinement system with an internal levitated ring: (*1*) levitated ring, (*2*) external field coils, and (*3*) separatrix.

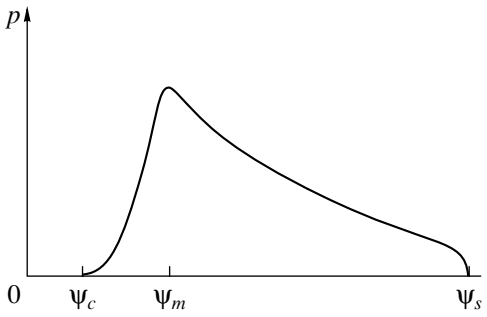

Fig. 2. MSPP in a confinement system with an internal levitated ring and a separatrix.

along the column. In this model configuration, the plasma pressure profile ψ remains the same as that shown in Fig. 2 (for $\psi_s \longrightarrow \infty$), but the magnetic flux ψ depends only on the radius. The separatrix itself and its effect on the development of the convective modes are modeled by appropriately choosing the boundary conditions at the outermost magnetic surface of radius r_s.

The equilibrium and stability conditions for plasmas in such configurations were investigated in [4, 10]. Nevertheless, for our purposes, it is expedient to rewrite these conditions in a different form. To do this, we pass over from the equilibrium magnetic field $B \equiv B_\theta$ and pressure p to two new quantities that are convenient for describing the convection, specifically, $J = \sqrt{\pi}/U = B/2\sqrt{\pi}r$, which is the Jacobian of the transformation to flux coordinates, and the entropy function of a magnetized plasma, $S = p/J^\gamma$, where γ is the adiabatic expo-

nent. In terms of these quantities, the equilibrium equation can be written as

$$J\frac{d}{dr}\left(\frac{\gamma S}{\gamma-1}J^{\gamma-1}+r^2J\right)-\frac{J^\gamma}{\gamma-1}\frac{dS}{dr}=0. \quad (1)$$

In cylindrical coordinates (r, θ, z), the standard variational stability criterion has the form

$$\delta^2W=\int d^3r\left\{r^2(\nabla\cdot(\boldsymbol{\xi}_\perp J))^2+J^2\left[\left(\frac{\partial\xi_r}{\partial\theta}\right)^2+\left(\frac{\partial\xi_z}{\partial\theta}\right)^2\right]\right.$$
$$\left.+\gamma SJ^\gamma(\nabla\cdot\boldsymbol{\xi})^2-(2\xi_r(r^2J)'\nabla\cdot(\boldsymbol{\xi}_\perp J))+\xi_r^2J'(r^2J)'\right\} \quad (2)$$
$$\geq 0,$$

where $\boldsymbol{\xi}$ is an arbitrary plasma displacement from equilibrium conditions, and the prime on the equilibrium parameters indicates the radial derivative d/dr. In criterion (2), the first two positive definite terms reflect the perturbations of the longitudinal and transverse magnetic-field components, respectively, and the third term accounts for adiabatic plasma compression. The last two alternating-sign terms can cause an instability.

Since the z coordinate is an analogue of the toroidal angle φ, we assume that all of the physical quantities are periodic in z: $f(z)=f(z+2\pi R)$. Then, we can expand the displacement $\boldsymbol{\xi}$ in a Fourier series in which all of the harmonics $\sim\exp\{inz/R+im\theta\}$ are independent because the equilibrium plasma state is uniform in z and θ. The perturbations with $m=0$ and $m\neq 0$ correspond to instabilities of different origins. The perturbations with $m=0$ correspond to the convective flute instability, during which the transverse magnetic field remains unperturbed and

$$\nabla\cdot\boldsymbol{\xi}=\nabla\cdot\boldsymbol{\xi}_\perp. \quad (3)$$

In this case, the stability criterion (2) for the equilibrium state (1) can be rewritten as

$$\delta^2W=\int d^3r\left\{(\gamma SJ^{\gamma-2}+r^2)\left[\nabla\cdot(\boldsymbol{\xi}_\perp J)\right.\right.$$
$$\left.\left.+\frac{J^{\gamma-1}\xi_rS'}{\gamma SJ^{\gamma-2}+r^2}\right]^2+\frac{2rJ^\gamma\xi_r^2S'}{\gamma SJ^{\gamma-2}+r^2}\right\}\geq 0. \quad (4)$$

The first term in this criterion can be reduced to zero by appropriately choosing ξ_z, in which case the condition for the equilibrium plasma state to be stable against convective modes simplifies to $S'\geq 0$. Note that, near the marginal stability ($S'=0$), the most dangerous convective modes satisfy the condition $\nabla\cdot(\boldsymbol{\xi}_\perp J)=0$. Consequently, for any values of β, the longitudinal magnetic field also remains unperturbed. At marginal stability, the equilibrium equation (1) is easy to integrate; the resulting equation reduces to the following algebraic equation for J at constant S:

$$\frac{\gamma S}{\gamma-1}J^{\gamma-1}+r^2J=\text{const}. \quad (5)$$

For $m\neq 0$, the compression term in criterion (2) can be reduced to zero by ensuring the equality $\nabla\cdot\boldsymbol{\xi}=0$ through the proper choice of ξ_θ. The transverse magnetic field perturbation, described by the second term in criterion (2), can be minimized by choosing the perturbations for which $\xi_z\longrightarrow 0$ and $n\longrightarrow\infty$, with the product $n\xi_z$ being fixed. As a result, the θ-averaged criterion (2) has the form

$$\langle\delta^2W\rangle_\theta=\frac{1}{2}\int rdrdz\left\{r^2\left[\nabla\cdot(\boldsymbol{\xi}_\perp J)-\frac{\xi_r}{r^2}(r^2J)'\right]^2\right.$$
$$\left.+\xi_r^2J^2\left(m^2+2\frac{p'}{rJ^2}\right)\right\}\geq 0. \quad (6)$$

The positive definite term in criterion (6) can be reduced to zero by appropriately choosing the quantity $n\xi_z$ in the expression for $\nabla\cdot(\boldsymbol{\xi}_\perp J)$. As a result, we arrive at the following stability criterion for the $m=1$ mode:

$$-2p'/rJ^2\leq 1. \quad (7)$$

This criterion guarantees that the modes with $m\geq 2$ are also stable. Note that, for $\gamma>1$, the stability of all modes with $m\geq 2$ is guaranteed by the stability condition $S'\geq 0$ for the convective mode [4]. We can readily see that the stability condition for the $m=1$ mode is governed by the surface current density and that the most dangerous perturbation is the displacement of the flux tube as a whole, accompanied by a slight incompressible deformation. According to Kadomtsev's classification [4], this perturbation should be considered as a sort of current kink mode that is short-wavelength in the z direction. Since the $m=1$ mode perturbs the magnetic field and the current is purely diamagnetic, the corresponding instability occurs only in a finite-β plasma. Taking into account the equilibrium equation (1), we can write condition (7) in the form $rJ'\leq -3J/2$, from which one can readily see that the MSPP for the convective mode fails to satisfy condition (7) at $\beta\equiv 2SJ^{(\gamma-2)}/r^2>2/3\gamma$. On the other hand, as expected, the plasma is stable against all of the modes in the inner region where $p'>0$. Consequently, if $\beta\leq 2/3\gamma$ at the magnetic surface r_m at which the pressure is maximum, then the plasma stability is governed only by the $m=0$ convective flute mode. At higher maximum plasma pressures, condition (7) for the MSPP consistent with Eq. (5) fails to hold at a certain magnetic surface of radius $r_1>r_m$. Therefore, in the region $r_m<r<r_1$, the MSPP should be determined by condition (7). For this MSPP, Eq. (1) implies that β is a linear function of radius, $\beta=1-(3\gamma-2)r/3\gamma r_1$. For a sufficiently large ratio r_1/r_m, we have $\beta_{\max}=\beta(r_m)\longrightarrow 1$. The above anal-

ysis also shows that, because, in the systems under consideration, there is an inner region where $p'(\psi) > 0$ and an outer region with an MSPP, the plasma is *a priori* stable against large-scale kink modes like "tilting" ($m = 1$, $n = 1$) and "twisting" modes ($m = 1$, $n = 2$), which are the most dangerous and destructive in field reversed configurations (FRC) [20, 21].

The above restrictions on β values should be regarded merely as sufficient conditions for plasma stability. In real plasmas, the maximum β values may be significantly higher for the following two reasons. The first reason is associated with the fact that, in the actual toroidal geometry, the magnetic field is nonuniform along magnetic field lines, so that the modes with different m are coupled to each other. In this case, the unstable modes again can be divided into two classes. The first class is represented by the quasipotential flute mode, which is stable when $S'(\psi) \geq 0$ and is a more general case of the $m = 0$ mode. The second class includes the modes that cause alternating radial displacements of the flux tube and whose stability is governed by the magnitude of the current density. Instead of criterion (7), these modes satisfy the following approximate stability criterion:

$$-2p'(\psi)\left(\frac{1}{2\pi}\oint R|\kappa_\psi|^{1/2}dl\right)^2 \leq 1, \qquad (8)$$

where κ_ψ is the covariant component of the magnetic field line curvature in flux coordinates ($\boldsymbol{\kappa} = \kappa_\psi \nabla\psi$). The calculations carried out by Garnier *et al.* [17] showed that, in this case, the maximum β value in a dipole confinement system can be substantially higher than unity. To avoid misunderstandings in terminology, note that the instabilities of the modes of the second class are often referred to as ballooning instabilities [16, 17], because, in the confinement systems under consideration, there exists only the diamagnetic current, which is proportional to $p'(\psi)$.

The second reason for high maximum possible β values is associated with the finite ion Larmor radius effects, which stabilize perturbations with large n. For a finite n and $m \neq 0$, the stability criterion (2) with the minimized magnetic field perturbation contains a term proportional to $(\xi_r')^2$. As a result, the stability condition for the kink (ballooning) modes becomes nonlocal with respect to the radial coordinate and imposes a less stringent restriction on the β value in comparison with stability criterion (7) or (8).

3. ADIABATIC EQUATIONS FOR MHD CONVECTION NEAR THE THRESHOLD FOR FLUTE INSTABILITY

Here, we analyze the self-consistent MHD convection, which occurs as a result of the distortions of the MSPP that are caused by plasma heating and original local transport processes. The fundamental difficulty of this analysis is associated with a significant difference between the time scales of the processes in ideal MHD and the dissipative time scales, which are determined by collisional thermal conductivity, viscosity, and diffusion. For a plasma with parameters at the fusion level, these time scales may differ by eight to nine orders of magnitude. That is why it is desirable to simplify the basic set of equations by eliminating, if possible, unimportant fast processes from consideration. Of course, it is important to realize that the basic set of equations reduced in such a manner remains weakly dissipative and, accordingly, the invariants of the basic ideal MHD equations should be conserved on long time scales. The variational method that was developed in [22–24] for the adiabatic separation of fast and slow motions in continuous Lagrangian systems provides the possibility of removing from consideration fast stable collective degrees of freedom without violating the conservation laws of the basic (unreduced) set of equations. The key element of the method is the determination of the velocity field that does not perturb fast stable degrees of freedom and makes it possible to describe the relatively slow dynamics of the system. This method will be used in our analysis.

We start with the assumption that the stability condition (7) for kink (ballooning) modes is satisfied over the entire plasma volume (this indicates that the maximum β value does not exceed the critical level). As will be seen below, the characteristic frequencies of the self-consistent convection under discussion are much lower than the minimum frequencies of the stable Alfvén waves ($\omega \sim C_A/r_m$). In this case, Alfvén waves are represented by perturbations with $m \neq 0$, so that, in accordance with the principle of the adiabatic separation of motions [23, 24], we can exclude perturbations with $m \neq 0$ from consideration and restrict ourselves to analyzing only the two-dimensional plasma motions ($m = 0$) that do not violate the axial symmetry of the original plasma column. In [23], it was shown that, if the plasma is in a nearly equilibrium state described by Eq. (5), then the dynamic equations can be further simplified by excluding from consideration fast magnetosonic (compressional Alfvén) waves with frequencies $\omega \sim C_A|\nabla_\perp|$.

In the case of two-dimensional plasma motion, the magnetic field has the only nonzero component B_θ. We describe this component in the same way that was used in analyzing plasma equilibrium, specifically, by the Jacobian $J = \mathbf{B} \cdot \nabla\theta/2\sqrt{\pi}$, introduced in Section 2. In this case, the frozen-in equation for the magnetic field becomes equivalent to the equation

$$\partial_t J + \nabla \cdot (\mathbf{v}J) = 0. \qquad (9)$$

It is convenient to write the adiabatic equations for ideal MHD plasma convection in the form

$$\partial_t S + \mathbf{v} \cdot \nabla S = 0, \qquad (10)$$

where S is the entropy function of a magnetized plasma (see Section 2). We represent the plasma density as $\rho = \lambda J$, in which case the continuity equation becomes

$$\partial_t \lambda + \mathbf{v} \cdot \nabla \lambda = 0. \quad (11)$$

Note that, in ideal MHD, the Jacobian J is a Eulerian invariant, while the entropy function S and the quantity λ are Lagrangian invariants.

We assume that, in the convection process in question, the plasma deviates only slightly from a stable equilibrium state. Under this assumption, which will be confirmed in further analysis, we can represent the entropy function as $S(t, r, z) = \bar{S}(t, r) + \tilde{S}(t, r, z)$, where the z-averaged quasi-equilibrium component $\bar{S}$ of S satisfies the condition $\bar{S}' > -\epsilon^2 \bar{S}/r_m$; $\tilde{S} \sim \epsilon^2 \bar{S}$ is the alternating (fluctuating) component of the entropy function; and $\epsilon \ll 1$ is a small parameter, whose value will be determined below. In this case, we can exclude magnetosonic waves from consideration and obtain the following expression for the adiabatic velocity field of the two-dimensional convection [23]:

$$\mathbf{v}_a = \frac{1}{J}[\nabla\theta \times \nabla\Phi] \sim \epsilon c_s, \quad (12)$$

where the quantity $\Phi(t, r, z)$ signifies the electric potential. It is easy to see that, in accordance with Eq. (9), this velocity field does not perturb the magnetic field and corresponds to the most dangerous perturbations in criterion (4).

If weak dissipation is taken into account in the MHD equations, then the equation for the magnetic field should contain a resistive term, the adiabatic equation should be replaced by the energy transport equation with the heat conduction term, and the equations of motion should include the viscosity tensor. This indicates that weak dissipation is taken into account via the three main dissipative processes, which are, respectively, described by the following local coefficients: the magnetic field diffusion coefficient $D = c^2/4\pi\sigma$ (where σ is the plasma conductivity), the thermal diffusivity χ, and the transverse kinematic viscosity η of a magnetized plasma. In essence, the first two coefficients describe a slow restructuring of the equilibrium state and a distortion of the MSPP. One can easily estimate that, on a time scale of $\tau_1 \sim \epsilon^2 a^2/\chi$ (where $a \sim J/J'$ is the characteristic plasma size), heat conduction can distort an MSPP with $\bar{S}' = 0$ by an amount $\delta\bar{S} \sim \epsilon^2 \bar{S}$. The convective processes with the characteristic rate (12) can smooth this distortion and thereby restore the MSPP, provided that $\epsilon c_s \tau_1 \geq a$. We thus arrive at the estimate

$$\chi \leq \epsilon^3 a c_s, \quad (13)$$

which, on the one hand, determines the order of magnitude of the thermal diffusivity χ in reduced, weakly dissipative MHD equations and, on the other hand, provides the physical sense of the small parameter ϵ. The coefficients D and η should also be regarded as being on the order of ϵ^3, because, for a magnetized plasma, all three dissipation coefficients are inversely proportional to the collision time, which thus determines the order of smallness of the dissipation coefficients. In this case, the Reynolds number for the convective flows of interest to us should be on the order of $\mathrm{Re} \sim \epsilon c_s a/\eta \sim \epsilon^{-2}$.

Actually, expression (12) for the adiabatic velocity field contains only the main term, which should be taken into account in the dynamic equations for slow motion. Generally, the principle of the adiabatic separation of motions implies that the expression for $\mathbf{v}_a$ may contain an additive small correction term of the form $\nabla\Phi_v/J$, which is on the order of $\epsilon^3 c_s$. This small correction can be neglected in the inertial terms in reduced dynamic equations and the equations for entropy and density fluctuations. However, it should be retained in the transport equations for the magnetic field and quasisteady plasma parameters. In the case at hand, this small "diffusive" correction to the main velocity depends only on r and can be represented as $u(r)/J$. With the above remarks in mind, we take into account the finite plasma conductivity to pass over from Eq. (9) to the following diffusion equation for the magnetic field:

$$\partial_t J = \frac{1}{r}\frac{d}{dr} r\left(-u + \frac{\bar{D}}{r^2}(r^2 J)'\right), \quad (14)$$

where $\bar{D}$ is the z-averaged diffusion coefficient. The right-hand side of Eq. (14) is on the order of ϵ^3; consequently, when describing the evolution of the Jacobian J, we can assume that $\partial_t \sim \epsilon^3 c_s/a$.

We substitute $\rho = \lambda J$ with $\lambda = \bar{\lambda}(r) + \tilde{\lambda}(r, z)$ into the continuity equation with the density source term Q_ρ, use Eq. (14) to eliminate the term $\partial_t J$ in the resulting equation, and perform averaging over z. As a result, we arrive at the following transport equation for the plasma density:

$$\partial_t \bar{\lambda} + \frac{u}{J}\bar{\lambda}' + \frac{1}{rJ}\frac{d}{dr}\left\langle \tilde{\lambda}\frac{\partial\Phi}{\partial z}\right\rangle = -\frac{\lambda}{rJ}\frac{d}{dr}\left(\frac{\bar{D}}{r}(r^2 J)'\right) + \frac{Q_\rho}{J}, \quad (15)$$

where the angular brackets denote averaging over z. If $\tilde{\lambda}$ is not too small, then Eq. (15) is dominated by the term in the angular brackets, which describes the convective mixing of the passive scalar λ. As a result of this mixing, the function $\bar{\lambda}$ in the convective region should evolve to a nearly constant profile with a low fluctuation level, $\tilde{\lambda} \sim \epsilon^2 \bar{\lambda}$. Consequently, the function $\bar{\lambda}$ should evolve in essentially the same manner as the averaged entropy function $\bar{S}$, the only difference being that, unlike the entropy distribution, the distribution $\bar{\lambda}(r)$ has no impact on plasma stability.

In dissipative hydrodynamics, in place of the adiabatic equation (10), it is necessary to use the complete transport equation for the thermal plasma energy [25], which accounts for heat conduction, external heating, Ohmic heating, and viscous heat release. We express thermal energy in the form $SJ^\gamma/(\gamma-1)$, use Eq. (14) to eliminate the term $\partial_t J$, and perform averaging over z. As a result, we arrive at the following transport equation for the plasma entropy:

$$\partial_t \bar{S} + \frac{u}{J}\frac{d\bar{S}}{dr} + \frac{1}{rJ}\frac{d}{dr}\left\langle \tilde{S}\frac{\partial\Phi}{\partial z}\right\rangle = \frac{\gamma-1}{J^\gamma}\bar{Q}_E(r,t) + \frac{\gamma-1}{2J^\gamma}\frac{1}{r}\frac{d}{dr}r\left\{\bar{\lambda}J\bar{\chi}\frac{d}{dr}\left(\frac{J^{\gamma-1}\bar{S}}{\bar{\lambda}}\right)\right\} - \frac{\gamma\bar{S}}{rJ}\frac{d}{dr}\left\{\frac{\bar{D}}{r}(r^2J)'\right\}, \quad (16)$$

where the function $\bar{Q}_E$ describes the total averaged energy source (including Ohmic heating and viscous heating) and the local heat flux has the form $\mathbf{q} = -\rho\chi\nabla(p/2\rho)$ [25].

In Eqs. (14)–(16), all the terms that are responsible for the transport of the magnetic field, plasma density, and plasma entropy are on the order of ϵ^3. Consequently, the source terms should also be on the order of ϵ^3. Eqs. (14)–(16) constitute a set of equations describing the "slow" ($\partial_t \sim \epsilon^3 c_s/a$) transport of the quasisteady plasma parameters. This set differs from the traditional set of equations with purely local transport fluxes in that it contains convective terms, which cannot, in principle, be described by the local transport coefficients (as will be justified below). As is the case in the traditional transport problem, Eqs. (14)–(16) should be supplemented with Eq. (1), in which the equilibrium quantities S and J should be replaced with $\bar{S}(r,t)$ and $J(r,t)$. In this case, Eq. (1) reflects the quasisteady balance of the main radial forces and makes it possible to determine $J(r,t)$ through the known function $\bar{S}(r,t)$, and Eq. (14) serves to determine $u(r,t)$.

Equation (16) can be somewhat simplified by taking into account the fact that the viscous heat release is proportional to v_a^2 and is on the order of $\epsilon^5 a^2|\nabla_\perp|^2$. The viscous heat release may become important when the dissipation of small-scale vortices with $a|\nabla_\perp| > \epsilon^{-1}$ is taken into account, because the nonlinear processes can act to transfer the energy of large-scale convective flows into the energy of small-scale vortices. Since we expect that the total energy of the convective plasma flows is about ϵ^2 of the thermal plasma energy, viscous heat release should play an insignificant role in the overall energy balance and thus can be neglected in further analysis. Note also that, along with the resistivity, an important role in the magnetic field transport in the systems under consideration is played by the thermal force [26, 27], which contributes additively to the right-hand side of Eq. (14) and, accordingly, to Eqs. (15) and (16). However, the thermal force does not play a decisive role in the development of convection. That is why, in what follows, the thermal force is ignored for simplicity.

Now, we proceed to a derivation of the equations describing "fast" ($\partial_t \sim \epsilon c_s/a$) convective flows and "fast" density and entropy fluctuations. The ideal dynamics of two-dimensional convection is described by a single adiabatic equation for the contravariant vorticity component [23]:

$$w = \nabla\theta\cdot\left[\nabla\times\left(\frac{\rho}{J}\mathbf{v}_a\right)\right] = \nabla\cdot\left(\frac{\rho\nabla\Phi}{r^2J^2}\right) = \nabla\cdot\left(\frac{\nabla\Phi}{C_A^2}\right). \quad (17)$$

According to [23], the reduced dissipative equation of motion can be derived from the basic dissipative equation of motion with the viscosity tensor by making the same transformation that is used to derive the reduced ideal equation of motion. Specifically, we replace $\mathbf{v}$ with $\mathbf{v}_a$ and apply the operation that transforms $\rho\mathbf{v}_a$ into w [see Eq. (17)]. The resulting expression for the viscous term is fairly complicated [25], the lowest nontrivial order being $\epsilon^4 a^2|\nabla_\perp|^2$. In the ideal dynamic equation, all of the terms are on the order of ϵ^2, so that viscous dissipation is important only for plasma motions occurring on sufficiently short spatial scales. Consequently, the viscous term can be simplified to

$$\nabla\cdot\left\{\frac{1}{J}[\nabla\theta\times(\nabla\cdot\hat{\pi})]\right\} \approx \nabla\cdot\left\{\frac{\bar{\lambda}}{r^2J}\nabla\left(\frac{\bar{\eta}r^2J}{\bar{\lambda}}w\right)\right\},$$

in which the leading-order terms and the terms on the order of $\epsilon^4 a|\nabla_\perp|$ are retained. As a result, to within terms of the higher orders in ϵ, the equation of motion has the form

$$\partial_t w + \frac{1}{r}\left[\Phi, \frac{w}{J}\right] + J^{\gamma-2}\frac{dJ}{rdr}\frac{\partial\tilde{S}}{\partial z} = \nabla\cdot\left\{\frac{\bar{\lambda}}{r^2J}\nabla\left(\frac{\bar{\eta}r^2J}{\bar{\lambda}}w\right)\right\}, \quad (18)$$

$$[\Phi, f] = \frac{\partial\Phi}{\partial z}\frac{\partial f}{\partial r} - \frac{\partial\Phi}{\partial r}\frac{\partial f}{\partial z}.$$

The equation for the entropy fluctuations $\tilde{S}$ is obtained by subtracting Eq. (16) from the complete transport equation for the plasma entropy, in which case, among all dissipative terms, it is sufficient to keep the terms that enter the expression for the thermal conductivity and that are linear in $\tilde{S}$ and $\tilde{\lambda}$ (the lowest nontrivial order of these terms is $\epsilon^5 a^2|\nabla_\perp|^2$). In the case of

the classical ion thermal conductivity, we have $\chi \sim \rho/B^2\sqrt{T}$ and the equation for $\tilde{S}$ takes the form

$$\partial_t \tilde{S} + \frac{1}{rJ}[\Phi, \tilde{S}] - \frac{1}{rJ}\frac{d}{dr}\left\langle \tilde{S}\frac{\partial \Phi}{\partial z}\right\rangle + \frac{1}{rJ}\frac{\partial \Phi}{\partial z}\frac{d\bar{S}}{dr}$$
$$= \frac{\gamma - 1}{2J^\gamma}\mathrm{div}\left\{\bar{\rho}\bar{\chi}\left[c_s \nabla\left(c_s\frac{\tilde{S}}{\bar{S}}\right) - c_s^5 \nabla\left(\frac{\tilde{\lambda}}{\lambda c_s^3}\right)\right]\right\}, \quad (19)$$

where $c_s^2 = p/\rho$.

The left-hand sides of Eqs. (18) and (19) describe the ideal plasma dynamics. On each of these left-hand sides, all of the terms are of the same order of magnitude; specifically, the terms on the left-hand side of Eq. (18) are on the order of ϵ^2, and the terms on the left-hand side of Eq. (19) are on the order of ϵ^3 (with allowance for the relationship $\bar{S}' \sim \epsilon^2$ in the convective region). The last terms on the left-hand sides of these equations incorporate the feedback in the plasma and describe the linear instability. The dissipative terms on the right-hand sides are as small as $\epsilon^2 a^2 |\nabla_\perp|^2$ in comparison with the left-hand sides. Consequently, the convective flows and entropy fluctuations are described primarily in terms of the ideal Lagrangian dynamics and the role of dissipation is limited to the suppression of small-scale perturbations driven by nonlinear processes. The classical transverse ion viscosity has the form $\bar{\eta} = 3\rho\chi/20$ [25].

The equation for $\tilde{\lambda}$ is derived in a way similar to the derivation of the equation for $\tilde{S}$—by subtracting Eq. (15) from the complete transport equation for the plasma density. However, we will not use this equation in further analysis for the following reasons. On the one hand, note that, in the above equations for fast motions, $\tilde{\lambda}$ makes only negligible contributions to $\bar{\lambda}$ in Eq. (17), which relates w to Φ, and to the small dissipative term in Eq. (19). Therefore, $\tilde{\lambda}$ does not play a decisive role in describing the development of plasma convection and thus it is merely a passive consequence of the convective process. On the other hand, note that, for the classical local transport [25], we can use the relationship $\chi/D = (\beta/2)\sqrt{m_i/2m_e}$, which, together with Eq. (16), shows that diffusion makes an appreciably smaller contribution to the $\bar{S}$ profile than heat conduction. Consequently, in order to simplify further calculations, we set $D = 0$, in which case the plasma density source term Q_ρ turns out to be unnecessary and can also be set equal to zero. As a result, λ should satisfy Eq. (11). As was noted above, $\bar{\lambda}$ should be nearly constant along the radius in the convective region; therefore, we can impose the initial condition $\lambda|_{t=0} = \bar{\lambda}|_{t=0} =$ const. In this case, Eq. (11) implies that, for any velocity field, λ will remain constant during the further evolution of the convective process.

Hence, the assumption that $D = Q_\rho = 0$, along with the initial condition $\lambda =$ const, makes it possible to exclude from consideration the transport equation (15) for the plasma density and the equation for $\tilde{\lambda}$. The basic set of equations reduced in such a way remains self-consistent and makes it possible to investigate the main parameters of the process in question. We thus succeeded in simplifying further calculations of the convective enhancement of the transport processes, which are now completely described by the subsets of the "slow" equations (1), (14), and (16) and "fast" equations (17)–(19), in which $S = \bar{S}(r, t)$, $D = 0$, $\bar{\lambda} =$ const, $\tilde{\lambda} = 0$, and $\bar{Q}_E = Q_E$ is the external energy source.

4. ADAPTATION OF THE SET OF REDUCED EQUATIONS TO THE COMPUTER CODE

The self-consistent plasma convection and the convective enhancement of transport processes were modeled by solving an evolutionary problem with the given initial and boundary conditions (see Section 3). It was assumed that the plasma occupies the region between the surface of the central conductor of radius r_c and the outermost magnetic surface of radius r_s, which plays the role of a separatrix. All of the plasma parameters were assumed to be periodic in z (the period being $2\pi R$) and were described in terms of the "toroidal" angle $\varphi = z/R$. The Jacobian J at the inner plasma boundary is determined by the current I_c in the central conductor, $J(r_c) = J_c = I_c/\sqrt{\pi c r_c^2}$. The initial profile of the function $\bar{S}$ was defined as follows: on the radial interval $r_c \le r \le r_m$, the function $\bar{S}$ increases monotonically from the value $\bar{S} = S_c \ll S_m$ to the value $\bar{S} = S_m$, and, on the radial interval $r_m \le r < r_s$, this function is constant, $\bar{S} = S_m =$ const. We introduce the dimensionless quasisteady functions and parameters by specifying their initial values at the magnetic surface r_m:

$$x = r/r_m, \quad x_c = r_c/r_m, \quad x_s = r_s/r_m, \quad g = J/J_c x_c^2,$$
$$s_0(x, t) = \bar{S}/S_m, \quad \hat{\beta} = 2S_m(x_c^2 J_c)^{\gamma-2}/r_m^2.$$

The parameter $\hat{\beta}$, which characterizes the maximum initial β value in terms of the vacuum magnetic field, is contained in equation (1) written in a dimensionless form.

The dimensionless parameter ϵ is defined by the expressions

$$\epsilon^3 = \frac{\hat{\chi}}{2r_m\hat{c}_s}, \quad \hat{\chi} = \frac{\hat{c}_s^2}{\hat{\omega}_{ci}^2\hat{\tau}_i},$$

where

$$\hat{c}_s^2 = \frac{2\hat{T}}{m_i} = \frac{S_m}{\bar{\lambda}}(x_c^2 J_c)^{\gamma-1}, \quad \hat{\omega}_{ci} = \frac{2\sqrt{\pi}er_m(x_c^2 J_c)}{m_i c},$$

$$\hat{\tau}_i = \frac{3(m_i\hat{T})^{3/2}}{4\sqrt{\pi}\bar{\lambda}(x_c^2 J_c)\Lambda e^4}.$$

In terms of the parameter ϵ, we also introduce the following dimensionless variables and functions:

$$\tau = \epsilon\frac{\hat{c}_s}{r_m}t, \quad \phi(x, \varphi, \tau) = \frac{\Phi}{\epsilon\hat{c}_s r_m^2(x_c^2 J_c)},$$

$$w(x, \varphi, \tau) = \frac{r_m^2 w(r, z, t)}{\epsilon\bar{\lambda}\hat{c}_s}, \quad \tilde{s}(x, \varphi, \tau) = \frac{\tilde{S}}{\epsilon^2 S_m},$$

$$Q(x) = \frac{r_m Q_E(r)}{\epsilon^3\hat{c}_s S_m(x_c^2 J_c)^\gamma}, \quad u(x, \tau) = \frac{u(r, t)}{\epsilon^3\hat{c}_s(x_c^2 J_c)}.$$

When magnetic field diffusion is neglected, the function $u(x, \tau)$ describes the conservation of the frozen-in magnetic flux and the total number of particles in the plasma region enclosed by the separatrix. Strictly speaking, this indicates that we must solve the problem with a movable outer boundary $x_s(\tau)$, which is determined by Eq. (14) with $\bar{D} = 0$. However, taking into account the fact that the function u does not qualitatively affect the heat transport and the evolution of the convective process, we can set $u = 0$ and solve the problem with a fixed boundary $x_s = \text{const}$. In this case, Eq. (14) is unimportant and can be neglected in numerical calculations.

As a result, we are working only with two slow equations describing the quasisteady plasma equilibrium and heat transport:

$$\frac{d}{dx}\left(\frac{\gamma\hat{\beta}s_0}{\gamma-1}g^{\gamma-1} + 2x^2 g\right) - \hat{\beta}\frac{g^{\gamma-1}}{\gamma-1}\frac{ds_0}{dx} = 0, \tag{20}$$

$$\begin{aligned}\partial_\tau s_0 &= \epsilon^2\frac{\gamma-1}{g^\gamma}Q(x) - \frac{\epsilon^2}{xgA}\frac{d}{dx}\left\langle\tilde{s}\frac{\partial\phi}{\partial\varphi}\right\rangle \\ &+ \epsilon^2\frac{\gamma-1}{g^\gamma}\frac{1}{x}\frac{d}{dx}\left[\frac{1}{x(s_0 g^{\gamma-1})^{1/2}}\frac{d}{dx}(s_0 g^{\gamma-1})\right],\end{aligned} \tag{21}$$

where $A = R/r_m$ is the aspect ratio. In numerical calculations, the source $Q(x)$ was described by a parabolic profile with a variable amplitude and width and centered at the magnetic surface $x = 1$. The boundary conditions were as follows:

$$\begin{aligned}g(x_c, \tau) = x_c^{-2}, \quad s_0(x_c, \tau) = \delta^2 \ll 1, \\ s_0'(x_s, \tau) = \nu s_0(x_s, \tau).\end{aligned} \tag{22}$$

The last of conditions (22) makes it possible to model the enhanced energy loss near the separatrix by choosing sufficiently large negative values of ν.

The functions describing the convective flows and entropy fluctuations were expanded in Fourier series with a finite number of harmonics:

$$\phi(x, \varphi, \tau) = \phi_0(x, \tau) + \sum_{n=1}^{N}(\phi_{sn}\sin n\varphi + \phi_{cn}\cos n\varphi), \tag{23}$$

$$\begin{aligned}w(x, \varphi, \tau) \\ = w_0(x, \tau) + \sum_{n=1}^{N}(w_{sn}\sin n\varphi + w_{cn}\cos n\varphi),\end{aligned} \tag{24}$$

$$\tilde{s}(x, \varphi, \tau) = \sum_{n=1}^{N}(s_{sn}\sin n\varphi + s_{cn}\cos n\varphi). \tag{25}$$

The total number of Fourier harmonics was chosen in accordance with the fact that the dissipative terms are on the order of $(n\epsilon/A)^2$ and that the linear growth rate is maximum at approximately $n \approx A/\sqrt{\epsilon}$. Consequently, reliable results can be obtained only with $N \geq A\epsilon^{-1}$. However, the calculations showed that the macroscopic plasma parameters and the rough characteristics of convective flows can be described correctly with a reduced number of Fourier harmonics, such that it is smaller than the above estimate by about 20–30%, in which case the results obtained with an odd number N of harmonics were found to be more reliable. A numerical analysis of detailed flow characteristics (e.g., the flow spectra) requires that the number N of harmonics be increased by a factor of approximately 1.5.

The equations for the functions w_n and s_n are easy to derive from Eqs. (18) and (19) by using the above dimensionless variables. We will not write out these equations, because they are very lengthy. We only present the relevant boundary and initial conditions. To do this, we should first of all point out the somewhat peculiar nature of the zonal flows that are uniform in φ and are described by the component $\phi_0(x, \tau)$. These flows are linearly stable and are associated exclusively with the coupling between the harmonics with $n \neq 0$. On the other hand, they can exist in a steady plasma state [23, 24]. Since the reduced equations contain the derivative ϕ_0' rather than ϕ_0, we need to impose only one boundary condition on ϕ_0; specifically, we can naturally set $\phi_0'(x_c, \tau) = 0$, which indicates that, at the surface of the central conductor, the zonal flow velocity vanishes. Further, since both the conductor's surface and the separatrix (because of the presence of magnetic null points) should be equipotential surfaces, the boundary conditions for the harmonics ϕ_n with $n \neq 1$ have the form $\phi_n(x_c, \tau) = \phi_n(x_s, \tau) = 0$, which also indicates the vanishing of the normal component of the flow velocity on

both boundaries. Similar boundary conditions can be imposed on the harmonics of the entropy fluctuations: $s_n(x_c, \tau) = s_n(x_s, \tau) = 0$.

The situation with the boundary conditions for the vorticity is somewhat more complicated. The conventional boundary conditions on the tangential component of the vortex velocity lead to integral conditions on w, so that the problem becomes much more difficult to solve. However, at a real separatrix, we have $U \longrightarrow \infty$; consequently, both the vorticity itself and its flux through the separatrix should vanish. The vanishing of the vorticity flux also correlates well with the results of an analysis of the tangential velocity distribution in the boundary layers [28]. That is why it seems reasonable to use the condition that the local vorticity flux vanish at both boundaries. In the case at hand, this condition has the form

$$\frac{\partial}{\partial x}\left(\frac{w(x, \varphi, \tau)}{(s_0 g^{\gamma-1})^{1/2}}\right)_{x_c} = \frac{\partial}{\partial x}\left(\frac{w(x, \varphi, \tau)}{(s_0 g^{\gamma-1})^{1/2}}\right)_{x_s} = 0. \quad (26)$$

Integrating Eq. (18) over the entire confinement region, we can easily convince ourselves that, under condition (26), the zonal flow velocity should also vanish at the separatrix, because the total vorticity in the plasma volume is conserved.

The initial conditions for w and $\tilde{s}$ can be specified in the form of fairly arbitrary small perturbations, because they should not have any impact on the final quasisteady state. It seems to be more convenient to specify initial perturbations of the plasma entropy; in the case at hand, these are a set of harmonics s_n that are localized radially in accordance with the boundary conditions. It is worth noting that the specific character of the nonlinear terms in Eqs. (18) and (19) imposes restrictions on the minimum set of initial harmonics: this set should ensure the generation of the remaining harmonics and their subsequent nonlinear coupling to each other. The minimum possible set consists of the two harmonics, s_{cn} and $s_{s(n+1)}$, where n is an arbitrary odd number smaller than N. In calculations, the amplitude $\tilde{s}$ of the dimensionless perturbations was usually set to be about 0.1, which corresponds to $\delta\tilde{S} \sim 10^{-3} S_m$.

5. RESULTS OF NUMERICAL CALCULATIONS

The reduced set of equations for $\{s_{cn}, s_{sn}\}$, $\{w_{cn}, w_{sn}\}$, $\{\phi_{cn}, \phi_{sn}\}$, s_0, and g with the above boundary and initial conditions was solved by the sweep method using a semi-implicit predictor–corrector scheme on the interval $x_c = 0.5 \le x \le x_s = 2$. As a rule, the spatial step for the scheme was chosen so that the interval contained 200 points. In order to satisfy the Courant condition, the time step was chosen in agreement with the relationship $\Delta\tau = 0.2\Delta x$. All calculations were carried out for the fixed parameter values $\epsilon = 0.1$ and $\delta = 0.1$, while the parameters $\hat{\beta}$, ν, A, and N; the parameters of the source; and the parameters of the initial perturbations were varied. The total computation time was chosen to be longer than the energy lifetime of the plasma.

The results of simulations carried out with the parameter values $\hat{\beta} = 0.5$, $\nu = -4$, $A = 2$, and $N = 33$ are illustrated in Figs. 3–7. The initial perturbations were modeled by the s_{c3} and s_{s4} harmonics. Figure 3 shows the time evolution of the entropy fluctuations $s(\tau)$ and the radial velocity $v_x(\tau)$ of the plasma flow at the point $(x = 1.5, \varphi = \pi)$. A purely linear stage during which the perturbations grow exponentially lasts about $\tau \approx 2$ and is followed by the quasilinear stage, during which the profile of s_0, being distorted in the linear stage, begins to be smoothed by the fairly well developed perturbations, which do not grow monotonically anymore. The quasilinear stage, during which the structure of the initial perturbations is readily seen, lasts up to $\tau \approx 5$. Then, the perturbation harmonics with all possible numbers n start growing rapidly, thereby giving rise to a highly nonlinear rearrangement of the structures of the plasma flows and entropy fluctuations. This stage is highly irregular and, in the main, comes to an end approximately at the time $\tau \approx 15$. Later, the profile of s_0 remains essentially unchanged as time elapses and the convective flows acquire a certain characteristic large-scale structure while remaining at a fairly high level of stochasticity.

Figure 4 illustrates the two-dimensional structure of convective flows and entropy fluctuations late in the quasisteady stage ($\tau = 50$). Figure 4a shows the contours of the constant magnitude of the potential ϕ or, equivalently, the streamlines of the flows. The light and dark regions correspond to the positive and negative values of the potential, respectively. The plasma circulation is clockwise around the lightest regions and counterclockwise around the darkest regions. The overall flow structure is dominated by several large-scale vortices that rotate in opposite directions and are localized almost completely in the region $1 < x < 2$, where $s_0' \approx 0$. The vortices evolve in a fairly complicated and irregular manner, changing their intensity and shape and drifting in the φ direction. Additional information about the structure of the flows can be obtained if we exclude the zonal flows, which, as a rule, have maximum positive or negative velocities near the magnetic surfaces $x \approx 1.3$ and $x \approx 1.7$. In Fig. 4a, we can see that $v_{0\varphi}(1.3) < 0$ and $v_{0\varphi}(1.7) > 0$; moreover, in this case, the zonal flows reverse their direction twice during the time interval $15 < \tau < 50$.

Figure 4b shows the contours of $\tilde{\phi} = \phi - \phi_0$, which indicates the flow structure with no zonal flows present. All simulations carried out for small values of the aspect ratio ($1 < A < 3$) demonstrated the onset of one or two long-lived pairs of coupled vortices with the strictly defined (plus and minus) polarity. In Fig. 4b, such a pair is seen in the region $0.1 < \varphi < 2.2$. In this

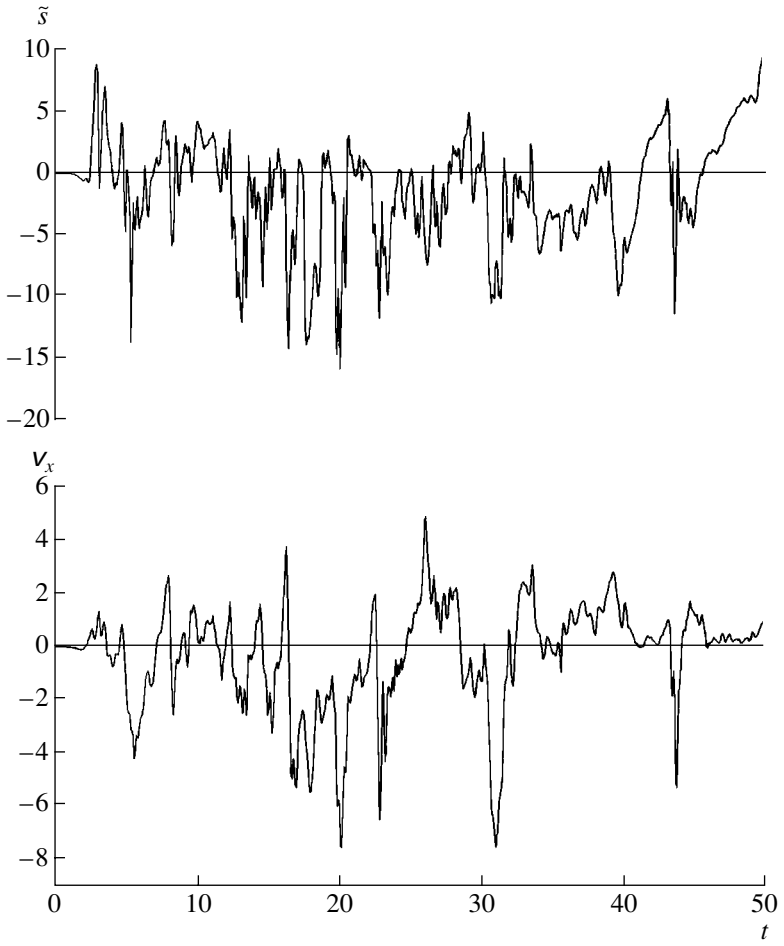

Fig. 3. Fluctuations of the entropy $\tilde{s}$ and radial velocity v_x.

case, the pair of vortices was clearly observed at $\tau > 20$. The characteristic feature of these vortex pairs is the presence of a fairly fast plasma jet localized in the φ coordinate (in Fig. 4b, $\varphi \approx 1.25$) and directed from the separatrix to the plasma center. In Fig. 3, sharp negative peaks in the time evolution of v_x indicate that the observation point occurs inside the jet.

Figure 4c shows the contours of the constant magnitude of the entropy fluctuations $\tilde{s}$. One can see that the structure of the contours is smaller in scale and is less regular in comparison with that of the streamlines of the plasma flows. This result correlates well with the highly irregular behavior of $\tilde{s}(t)$ in Fig. 3. A small-scale sequence of minima and maxima of $\tilde{s}$ in the region $1.8 < x < 2.0$ in Fig. 4c stems from the model boundary condition (22) for s_0 and is very sensitive to the value of ν.

Figures 5 and 6 display the time-averaged spectra of the fluctuations of the potential and entropy computed as functions of n at three radial positions. The spectra were calculated in a standard way by taking the Fourier transformation of the correlation function in the φ coordinate ($F_c = \langle f(\varphi) f(\varphi + \zeta) \rangle$) and then averaging the resulting function over the time interval $20 < \tau < 50$. From Fig. 5, we can see that the spectrum of the fluctuations of the potential I_ϕ is dominated by harmonics with the numbers 1, 2, and 3; for higher harmonics, the spectrum decreases with the harmonic number approximately as n^{-4} and even more sharply for $n > 11$. In Fig. 6, the spectrum of the fluctuations of the entropy I_s at $x = 1.2$ and $x = 1.5$ decreases approximately as $n^{-1.5}$ for harmonic numbers from $n = 1$ to $n = 11$. For higher harmonics, the spectrum decreases more sharply because of the dissipation of small-scale fluctuations. As was mentioned above, an enhanced level of the small-scale fluctuations of $\tilde{s}$ at the magnetic surface $x = 1.8$ in Fig. 6 is associated with the model boundary condition for s_0. Note that, although the spectra decrease fairly sharply as n increases, reducing the total number of harmonics used in simulations below the critical number (in the case at hand, $N < 20$) results in a significant distortion of the spectra. At an arbitrary instant of time, the n-spectra of the fluctuations can differ substantially from the time-averaged spectra shown

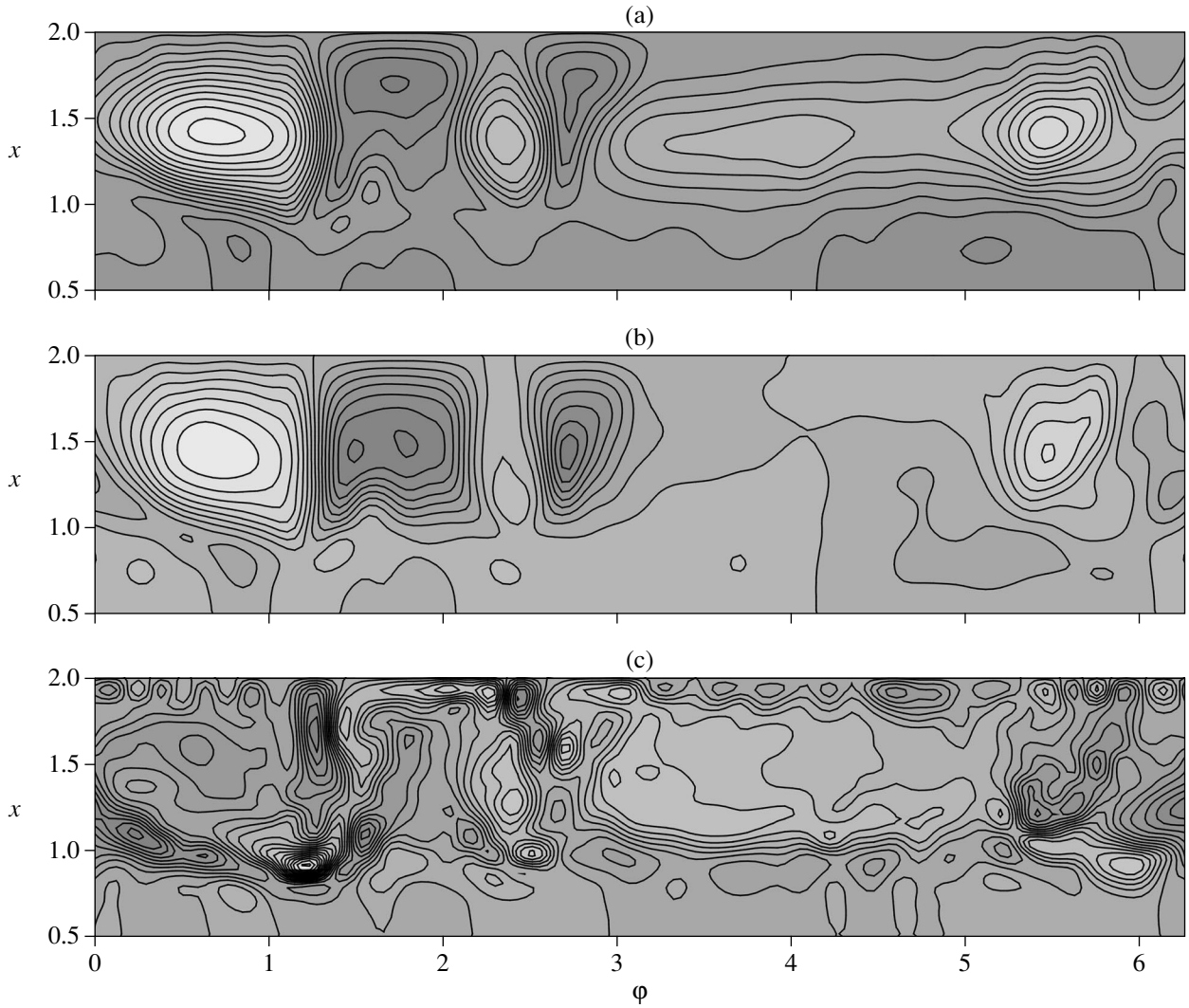

Fig. 4. (a, b) Structures of the plasma flows and (c) structure of the entropy fluctuations.

in Figs. 5 and 6. We can calculate the root-mean-square (rms) deviation for the spectra, $\Delta I = \langle\langle(\delta I)^2\rangle\rangle^{1/2}$ (where the square brackets denote averaging over the above time interval), in order to show that, for both of the spectra $I_s(n, \tau)$ and $I_\phi(n, \tau)$, the relative deviation $\Delta I/I$ is large and changes from about 0.7 for small n to roughly 1.0 for the largest values of n in the spectra.

The solid curve in Fig. 7 shows the profile $s_0(x)$ at the time $\tau = 50$. Over the entire time interval $20 < \tau < 50$, this profile remains essentially unchanged in shape and deviates only slightly (by an amount smaller than 3%) from the MSPP $s_0(x) = \text{const}$ in the plateau region. A decrease in s_0 near the outer boundary stems from the model boundary condition (22) and is very sensitive to the value of ν. In a real plasma bounded by a separatrix, enhanced energy losses are associated with a sharp increase in ∇U as the separatrix is approached, rather than with the fact that the gradient of s_0 is kept artificially large at the plasma boundary. In this case, s_0 may remain constant up to the separatrix. Hence, the calculations confirm the basic assumption that the MSPP is maintained self-consistently.

Now, let us turn to a traditional approach in interpreting the experimental data on anomalous transport and formally introduce the effective dimensionless local thermal diffusivity $\chi_{\text{eff}} = -\bar{q}/g\bar{T}'(x)$, where the dimensionless heat flux density and dimensionless temperature, $\bar{q}(x)$ and $\bar{T}(x)$, can be easily calculated in the model described here. For convenience, we also introduce the "anomaly" factor, which is defined as the ratio of the effective thermal diffusivity to the classical one: $F_a = \chi_{\text{eff}}/\chi_{\text{cl}}$. In Fig. 7, the anomaly factor is shown by the dashed curve. We can see that, in the region $0.5 < x < 0.9$, the anomaly factor is about $F_a \approx 1$, which indicates that the heat transport is classical. In the profile of the anomaly factor, we can see an alternating-sign spike near the magnetic surface $x = 1.1$; this spike is related

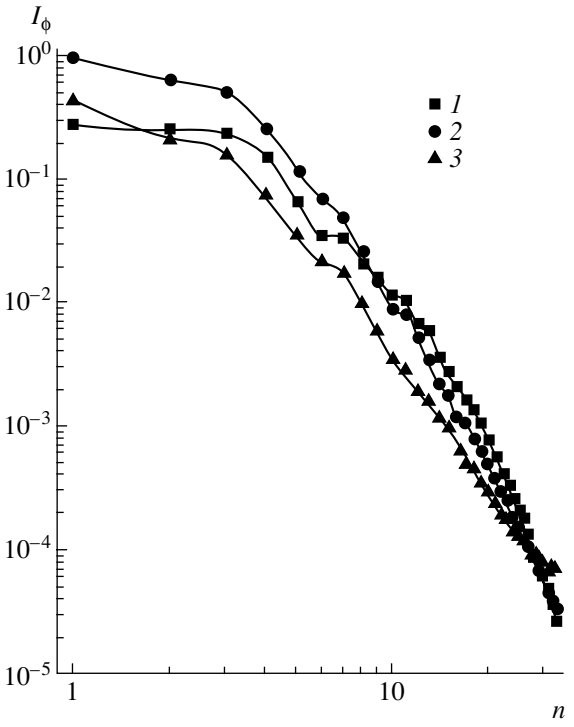

Fig. 5. Spectrum of fluctuations of the potential at x = (*1*) 1.2, (*2*) 1.5, and (*3*) 1.8.

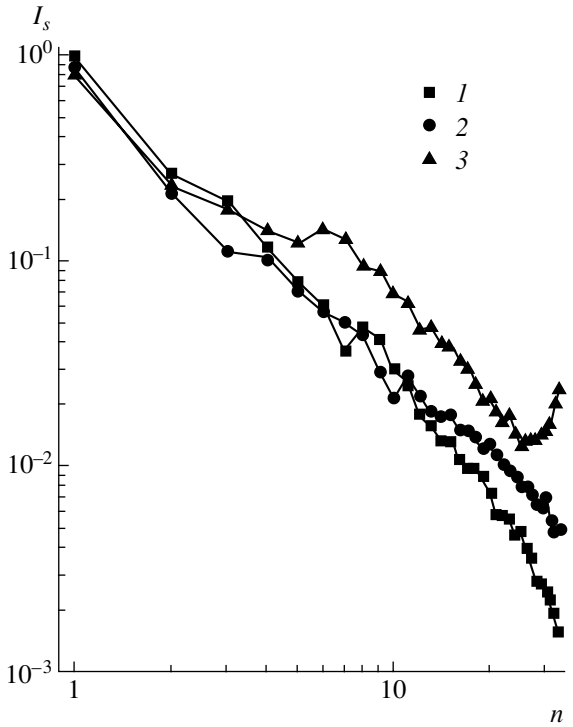

Fig. 6. Spectrum of the entropy fluctuations at x = (*1*) 1.2, (*2*) 1.5, and (*3*) 1.8.

to the fact that $\bar{q}(x)$ and $\bar{T}'(x)$ vanish at different magnetic surfaces. In the convective region at larger radii, the factor F_a first increases to its maximum value and then, near the plasma boundary, decreases sharply up to unity. A decrease in F_a in the edge region can be associated with the notion of an "external transport barrier," which is often used to interpret the experimental data (first of all, from tokamaks). Of course, in the case under discussion, such behavior of the factor F_a stems exclusively from the nonlocal nature of the convective plasma transport, which cannot, in principle, be described by any local transport coefficient. Nevertheless, the above example raises the question of whether the traditional interpretation of transport processes is also correct for tokamaks.

The simulations carried out with different values of the parameter ν (which characterizes the energy losses at the outer plasma boundary) showed that, qualitatively, the plasma convection, as well as the profiles of s_0 and F_a, possess all of the above-described characteristic features. The only quantity that is sensitive to the value of this parameter is the convective transport rate. In order to illustrate the dependence of the convective transport rate on the parameter ν, let us briefly analyze the numerical results calculated for the same source intensity but for ν values other than that in the above example. We characterize the calculated results by the parameters $s_{0\max}$ and $F_{a\max}$, as well as by the rms values of the entropy fluctuations $\Delta\tilde{s}$ and radial velocity Δv_x at the point (x = 1.5, $\varphi = \pi$) (see Fig. 3). The above-described calculations with $\nu = -4$ yielded $\Delta\tilde{s} = 4.2$, $\Delta v_x = 2.0$, $s_{0\max} = 0.81$, and $F_{a\max} = 6.0$. For $\nu = -2$, we

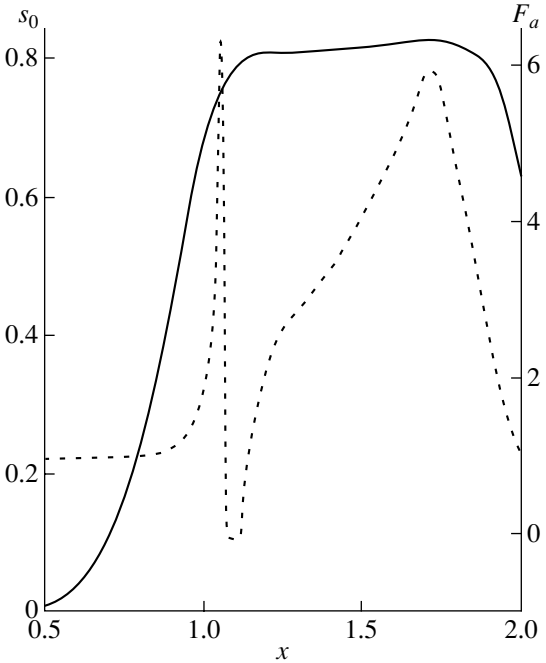

Fig. 7. Radial profiles of the entropy s_0 (solid curve) and anomaly factor F_a (dashed curve).

have $\Delta\tilde{s} = 2.9$, $\Delta v_x = 0.94$, $s_{0\max} = 1.02$, and $F_{a\max} = 3.5$, and, accordingly, for $\nu = -6$, we have $\Delta\tilde{s} = 5.3$, $\Delta v_x = 2.8$, $s_{0\max} = 0.64$, and $F_{a\max} = 8.2$.

Hence, we can conclude that the convective heat transport is governed primarily by the energy loss rate at the plasma edge rather than by the plasma parameters in the main confinement region. Moreover, for the same relative temperature gradients in the central plasma region, the heat fluxes may differ severalfold. Thus, we can draw an analogy between this dependence of transport processes in a plasma on the conditions at the plasma edge and L–H transitions in tokamaks.

6. CONCLUSION

Summing up the results of the above theoretical and numerical analysis, note that, using as an example a simplified magnetic configuration aimed at modeling plasma confinement in a highly nonparaxial system with an internal levitated ring, it has been shown that the plasma heating and local dissipative processes can generate and maintain self-consistent nonlinear MHD convection, which develops near the threshold for the ideal MHD instability and gives rise to essentially nonlocal heat transport. On the basis of the method of the adiabatic separation of fast and slow motions, a closed set of equations has been derived that provides a simultaneous and self-consistent description of relatively fast, nonlinear convective flows and slower transport processes in a weakly dissipative plasma with a large Reynolds number (10^2 and larger) and $\beta \sim 1$. The distinguishing feature of the equations derived is that they possess all the invariant properties of the basic ideal MHD equations and, thus, can be used to describe the plasma evolution on arbitrarily long time scales (longer than the plasma lifetime).

A computer code has been devised and numerical simulations have been carried out, demonstrating that the ideal convective MHD instability self-consistently approaches the regime of the nonlinear quasisteady convection maintained by plasma heating and local classical transport processes. The calculations show that convection, in fact, acts to restore and maintain the MSPP in a plasma. Also, convection gives rise to an essentially nonlocal, enhanced heat transport whose rate is determined by the energy loss rate at the plasma periphery rather than by the plasma parameters in the main confinement region, so that an analogy can be drawn between this effect and L–H transitions in tokamaks.

A large amount of numerical data on the structure of the nascent convective flows has been amassed and analyzed. The velocity of the self-consistent plasma flows is proportional to the cube root of the ratio of the time scales of the processes in ideal MHD to the dissipative time scales and, consequently, can be very low. Nevertheless, the derived equations and numerical simulations show that the structure of convective flows is always formed under the action of highly nonlinear processes that give rise to dominant large-scale vortices with highly irregular temporal and spatial characteristics.

The results obtained are important not only for magnetic confinement systems with internal levitated conductors (like those modeled in this paper) but also for other systems designed to maintain plasma pressure profiles that are marginally stable against ideal MHD modes.

ACKNOWLEDGMENTS

This work was supported in part by the Council of the Federal Program “Government Support of the Leading Scientific Schools,” project no. 00-15-96526.

REFERENCES

1. A. G. Kellman, M. W. Phillips, S. C. Prager, and M. C. Zarnstorff, Nucl. Fusion **23**, 1561 (1983).
2. M. N. Rosenbluth and C. L. Longmire, Ann. Phys. **1**, 120 (1957).
3. I. B. Bernstein, E. Frieman, M. Kruscal, and R. Kulsrud, Proc. R. Soc. London, Ser. A **244**, 17 (1958).
4. B. B. Kadomtsev, in *Reviews of Plasma Physics*, Ed. by M. A. Leontovich (Gosatomizdat, Moscow, 1963; Consultants Bureau, New York, 1966), Vol. 2.
5. P. N. Vabishchevich, L. M. Degtyarev, V. V. Drozdov, *et al.*, Fiz. Plazmy **7**, 981 (1981) [Sov. J. Plasma Phys. **7**, 536 (1981)].
6. B. Lane, R. S. Post, and J. Kesner, Nucl. Fusion **27**, 277 (1987).
7. V. P. Pastukhov and A. Yu. Sokolov, Fiz. Plazmy **17**, 1043 (1991) [Sov. J. Plasma Phys. **17**, 603 (1991)].
8. A. Hasegava, L. Chen, and M. E. Mauel, Nucl. Fusion **30**, 2405 (1990).
9. A. I. Morozov, V. P. Pastukhov, and A. Yu. Sokolov, in *Proceedings of Workshop on D-3He Based Reactor Studies, Moscow, 1991* (Kurchatov Inst. of Atomic Energy, Moscow, 1991), p. 1C1.
10. P. A. Popovich and V. D. Shafranov, Fiz. Plazmy **26**, 519 (2000) [Plasma Phys. Rep. **26**, 484 (2000)].
11. E. Hameiri, P. Laurence, and M. Mond, J. Geophys. Res. **96**, 1513 (1991).
12. C. Z. Cheng and Q. Qian, J. Geophys. Res. **99**, 11193 (1994).
13. A. Chan, M. Xia, and L. Chen, J. Geophys. Res. **99**, 17351 (1994).
14. A. Yu. Sokolov, Fiz. Plazmy **18**, 657 (1992) [Sov. J. Plasma Phys. **18**, 343 (1992)].
15. V. V. Arsenin and A. Yu. Kuyanov, Fiz. Plazmy **27**, 675 (2001) [Plasma Phys. Rep. **27**, 635 (2001)].
16. S. Krasheninnikov, P. Catto, and R. D. Hazeltine, Phys. Rev. Lett. **82**, 2689 (1999).
17. D. T. Garnier, J. Kesner, and M. E. Mauel, Phys. Plasmas **6**, 3431 (1999).
18. A. V. Simakov, P. Catto, S. Krasheninnikov, and J. J. Ramos, Phys. Plasmas **7**, 2526 (2000).

19. J. Kesner, L. Bromberg, D. T. Garnier, and M. E. Mauel, in *Proceedings of the 17th IAEA Fusion Energy Conference, Yokohama, 1998* (IAEA, Vienna, 1999), Vol. 3, p. 1165.
20. A. G. Es'kov, R. Kh. Kurtmullaev, A. P. Kreshchuk, *et al.*, in *Proceedings of the 7th International Conference on Plasma Physics and Controlled Nuclear Fusion Research, Innsbruck, 1978*; Nucl. Fusion Suppl. **2**, 187 (1979).
21. W. T. Armstrong, R. K. Linford, J. Lipson, *et al.*, Phys. Fluids **24**, 2068 (1981).
22. V. P. Pastukhov, Pis'ma Zh. Éksp. Teor. Fiz. **67**, 892 (1998) [JETP Lett. **67**, 940 (1998)].
23. V. P. Pastukhov, Fiz. Plazmy **26**, 566 (2000) [Plasma Phys. Rep. **26**, 529 (2000)].
24. V. I. Ilgisonis and V. P. Pastukhov, Pis'ma Zh. Éksp. Teor. Fiz. **72**, 758 (2000) [JETP Lett. **72**, 530 (2000)].
25. S. I. Braginskii, in *Reviews of Plasma Physics*, Ed. by M. A. Leontovich (Gosatomizdat, Moscow, 1963; Consultants Bureau, New York, 1963), Vol. 1.
26. A. I. Morozov and V. P. Pastukhov, Fiz. Plazmy **18**, 790 (1992) [Sov. J. Plasma Phys. **18**, 410 (1992)].
27. V. P. Pastukhov and A. Yu. Sokolov, Nucl. Fusion **32**, 1725 (1992).
28. L. D. Landau and E. M. Lifshitz, *Fluid Mechanics* (Nauka, Moscow, 1986; Pergamon, New York, 1987).

Translated by G. V. Shepekina

Plasma Physics Reports, Vol. 27, No. 11, 2001, pp. 922–931. Translated from Fizika Plazmy, Vol. 27, No. 11, 2001, pp. 978–987.

PLASMA OSCILLATIONS AND WAVES

Electromagnetic Oscillations near the Critical Surface in a Plasma: Methodological Note

A. V. Timofeev

Russian Research Centre Kurchatov Institute, pl. Kurchatova 1, Moscow, 123182 Russia

Received May 24, 2001

Abstract—Agreement between different approaches to studying the propagation of electromagnetic oscillations near the critical surface is elucidated. The propagation of plane waves, electromagnetic rays, and wave beams are analyzed. The results obtained are valid when the angles between the magnetic field and the plasma density gradient are not too small. © *2001 MAIK "Nauka/Interperiodica".*

1. INTRODUCTION

It is well known that, in a plasma with no magnetic field, electromagnetic oscillations can propagate only at frequencies above the electron plasma frequency ω_{pe}. If the plasma is in a magnetic field, electromagnetic oscillations can also occur in the range $\omega < \omega_{pe}$. In order for the electromagnetic waves launched from free space to reach the dense plasma region ($\omega_{pe} > \omega$), they should pass through the critical surface at which $\omega_{pe} = \omega$. However, the waves are partially reflected from an opaque region in the vicinity of the critical surface. In addition, for small angles χ between ∇n_0 and $\mathbf{B}_0$, oscillations with different polarizations (with different orientations of their electric vectors) can be converted into each other.

The problem of the passage of electromagnetic oscillations through the critical surface was first addressed in the study of the propagation of radio waves in the Earth's magnetosphere [1]. More recently, this problem was investigated in developing the methods of microwave heating of dense plasmas in magnetic confinement systems [2–5]. A dense plasma such that $\omega_{pe} > \omega_e \approx \omega$ (where ω_e is the electron cyclotron frequency) was successfully heated in experiments in the W7-AS stellarator [6]. In existing spherical tokamaks (e.g., the Globus-M device), as well as in planned facilities (e.g., the Drakon-like EPSILON system), the magnetic field is comparatively weak, so that the plasma density also satisfies the condition $\omega_{pe} > \omega_e$.

In [1–5], attention was focused on calculating the transmission, reflection, and conversion coefficients for electromagnetic oscillations in the plane wave approximation. However, other aspects of the propagation of electromagnetic waves in the vicinity of the critical surface are equally important. Thus, it is of interest to investigate some properties of the polarization of oscillations and their ray trajectories as well as the peculiar features of the propagation of spatially bounded wave beams. These aspects of the problem were investigated in my earlier papers [7, 8] for the case of small angles χ. In open systems, plasma configurations with $\chi \ll 1$ are characteristic of the throats of magnetic mirrors, through which the microwave power is conveniently fed in. In closed systems, the angle χ is close to $\pi/2$.

The objective of this paper is to investigate the propagation of electromagnetic oscillations near the critical surface when the angle χ is on the order of unity. A study is made of the ray trajectories of oscillations and their polarization. Special attention is paid to the case $\chi = \pi/2$, which is of the most practical interest for the problem of plasma heating in closed magnetic confinement systems. It is shown that different approaches to the study of the propagation of electromagnetic oscillations in the vicinity of the critical surface (the analysis of the wave equation in the plane plasma slab approximation and the calculation of ray trajectories and the trajectories of the wave beams) are consistent with each other. Rules are derived for conjugating the trajectories of the transmitted and reflected wave beams with the incident beam trajectories.

In what follows, the transverse (with respect to the main magnetic field) component of the electric field of electromagnetic oscillations is represented as a superposition of circularly polarized components. By applying this approach systematically, it is possible to substantially simplify the calculation of both the transmission coefficient for oscillations incident on the critical surface (see below) and the related conversion coefficient (see [7]).

2. PROPAGATION OF OSCILLATIONS NEAR THE CRITICAL SURFACE AND THEIR POLARIZATION

We are interested in oscillations with high frequencies and short wavelengths. Here, we analyze these oscillations under the following standard simplifying assumptions: the ion contribution to the dielectric response function of the plasma is neglected and the

1063-780X/01/2711-0922$21.00

plasma inhomogeneity is described parametrically. If necessary, the range of validity of the analysis will be extended. Under these assumptions, the set of Maxwell's equations reduces to the algebraic equations [9]

$$\begin{pmatrix} N_\parallel^2 + N_+N_- - \varepsilon_+ & -N_-^2 & -N_\parallel N_+ \\ -N_+^2 & N_\parallel^2 + N_+N_- - \varepsilon_- & -N_\parallel N_- \\ -N_\parallel N_- & -N_\parallel N_+ & 2N_+N_- - \varepsilon_\parallel \end{pmatrix} \times \begin{pmatrix} E_+ \\ E_- \\ E_\parallel \end{pmatrix} = 0, \quad (1)$$

where $E_\pm = (E_x \pm iE_y)/\sqrt{2}$, $N_\pm = (N_x \pm iN_y)/\sqrt{2}$, $\varepsilon_\pm = 1 - \omega_{pe}^2/\omega(\omega \pm \omega_e)$, and $\varepsilon_\parallel = 1 - \omega_{pe}^2/\omega^2$. Equations (1) are written in a Cartesian coordinate system with the x-axis directed along the plasma density gradient and the z-axis directed along the main magnetic field. The perturbations are assumed to be plane waves with the electric field in the form $\mathbf{E} \propto \exp(-i\omega t + i\mathbf{kr})$. All of the quantities having the dimensionality of length are normalized to c/ω.

The general picture of the propagation of the oscillations can be constructed by analyzing the dependence of the transverse component of the refractive index on the plasma density. This dependence is described by the following dispersion relation, which is obtained by equating the determinant of Eqs. (1) to zero:

$$D = N_\perp^4\varepsilon_\perp + N_\perp^2(N_\parallel^2(\varepsilon_\perp + \varepsilon_\parallel) - 2\varepsilon_\perp\varepsilon_\parallel - \varepsilon_\perp + \varepsilon_\parallel) + \varepsilon_\parallel(N_\parallel^2 - \varepsilon_+)(N_\parallel^2 - \varepsilon_-) = 0, \quad (2)$$

where $\varepsilon_\perp = (\varepsilon_+ + \varepsilon_-)/2$.

The main objective of this paper is to investigate the penetration of oscillations through an opaque region in the vicinity of the critical surface. In order for the oscillations to be reflected insignificantly, the quantity $|N_\perp|$ should be sufficiently small. For $|\varepsilon_\parallel| \ll 1$, the smallest of the roots of the quartic equation (2) is approximately equal to

$$N_\perp^2 \approx -\varepsilon_\parallel \frac{(N_\parallel^2 - \varepsilon_+)(N_\parallel^2 - \varepsilon_-)}{\varepsilon_\perp(N_\parallel^2 - 1)}. \quad (3)$$

This expression implies that, at the critical surface, the quantity $N_\perp^2$ changes sign at the critical surface where the quantity $\varepsilon_\parallel$ vanishes, so that there should be an opaque region in the vicinity of the critical surface. However, under either of the two conditions $N_\parallel^2 = \varepsilon_{\pm c}$, where $\varepsilon_{\pm c} = \varepsilon_\pm|_{\omega_{pe} = \omega} = \omega_e/(\omega_e \pm \omega)$, the function $N_\perp^2(\omega_{pe}^2)$ has a second-order zero at the critical surface. If, in addition, $N_y = 0$, then, for oscillations with $N_\parallel^2 = \varepsilon_{+c}$, the two transparency regions on both sides of the critical surface merge into one, so that the critical surface is freely penetrated by such oscillations. Note that, for $N_\parallel^2 = \varepsilon_{-c}$, there is no transparency region in the vicinity of the critical surface.

When passing through the critical surface, oscillations change their nature. Thus, ordinary waves that are incident on the critical surface from the side of lower plasma density are converted into extraordinary waves and vice versa. Oscillations are commonly classified by their polarization in the case of purely transverse propagation ($N_\parallel = 0$). In this case, the dispersion relation (2) has two solutions: $N_\perp^2 = \varepsilon_\parallel$ and $N_\perp^2 = \varepsilon_+\varepsilon_-/\varepsilon_\perp$. For $N_\parallel = 0$, ordinary waves (which are described by the solution $N_\perp^2 = \varepsilon_\parallel$) have purely longitudinal polarization, so that they propagate as if there were no magnetic field. It is natural that the critical surface is one of the boundary surfaces of the transparency region for these waves (Fig. 1a). In the same case $N_\parallel = 0$, extraordinary waves (which are described by the solution $N_\perp^2 = \varepsilon_+\varepsilon_-/\varepsilon_\perp$) have purely transverse polarization. For oscillations with $\omega > \omega_e$, there may exist a point at which the condition $\varepsilon_\perp = 0$ holds. At this point, the oscillations are subject to the plasma resonance—they become purely potential and their refractive index increases sharply (Fig. 1a). For $\chi = \pi/2$, extraordinary waves possess this property regardless of the value of $N_\parallel$. At the critical surface, ordinary waves with $N_\parallel^2 = \varepsilon_{+c}$ are converted into extraordinary waves (see below). For this reason, Preinhalter and Kopecky [2] proposed to use ordinary waves to heat dense plasmas.

In a plasma in which $\nabla n_0 \perp \mathbf{B}_0$, the value of $N_\parallel$ remains constant along the paths of waves. Consequently, the only waves that can be launched into the plasma from free space (where $N = 1$) are those with $N_{\parallel c} = \varepsilon_{+c}^{1/2} < 1$. We also assume that the condition $\omega > \omega_e$ is satisfied. The polarization of these waves is described by the expression [9]

$$\mathbf{E} = (E_+, E_-, E_\parallel) = \text{const}\left(\frac{N_+}{\varepsilon_+ - N^2}, \frac{N_-}{\varepsilon_- - N^2}, \frac{N_\parallel}{\varepsilon_\parallel - N^2}\right). \quad (4)$$

For oscillations with $N_\parallel^2 \approx \varepsilon_{+c}$, which we are interested in here, the condition $|N_\perp| \ll 1$ is satisfied in the vicinity of the critical surface. The right-polarized component E_- of the electric field of such oscillations is small, and the expression for the left-polarized component is inde-

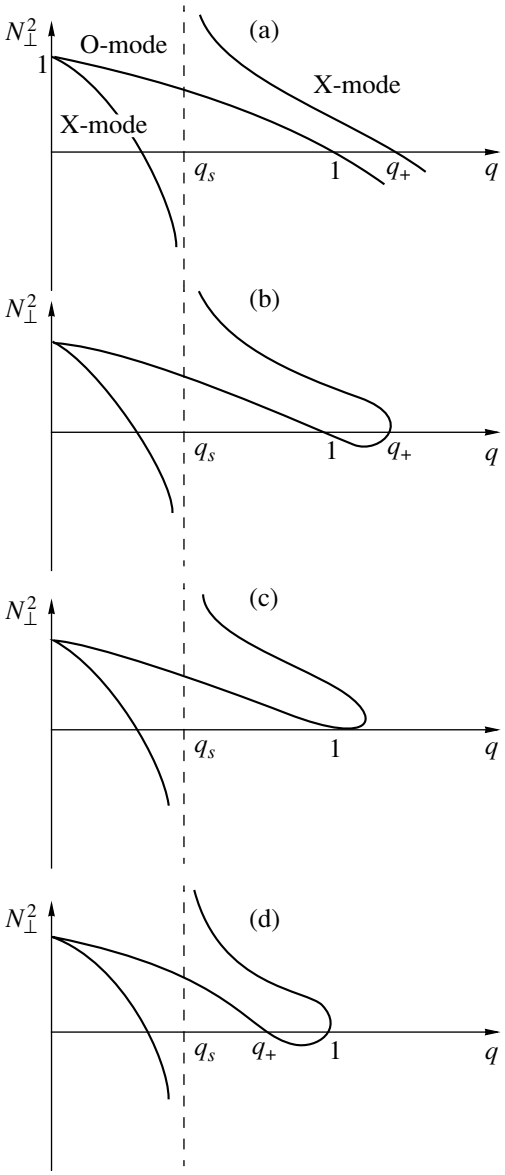

Fig. 1. Dependence of the transverse component of the refractive index on the plasma density for (a) $N_\parallel = 0$, (b) $N_\parallel < N_{\parallel c}$, (c) $N_\parallel = N_{\parallel c}$, and (d) $N_\parallel > N_{\parallel c}$. The abscissa is $q = (\omega_{pe}/\omega)^2$, and the characteristic points on the abscissa are $q_s = 1 - (\omega_e/\omega)^2$ and $q_+ = (1 - N_\parallel^2)(1 + \omega_e/\omega)$.

terminate. In the vicinity of the critical surface, Eqs. (1) simplify to

$$\begin{pmatrix} N_\parallel^2 - \varepsilon_+ & -N_+ N_\parallel \\ N_- N_\parallel & \varepsilon_\parallel \end{pmatrix} \begin{pmatrix} E_+ \\ E_\parallel \end{pmatrix} = 0. \quad (5)$$

Equations (5) yield the dispersion relation

$$N_\perp^2 = -\frac{2\varepsilon_\parallel (N_\parallel^2 - \varepsilon_+)}{N_{\parallel c}^2}, \quad (6)$$

which, of course, can also be derived from relation (3). The dispersion relation (6) implies that, for $N_\parallel > N_{\parallel c}$, the opaque region lies ahead of the critical surface (in the region where $\omega_{pe} < \omega$) and, for $N_\parallel < N_{\parallel c}$, it lies behind the critical surface. For $N_y = 0$, the polarization of oscillations at the boundaries of the opaque region is rather peculiar. The first equation of set (5) [see also expression (4)] shows that, at the boundary at which the condition $N_\parallel^2 = \varepsilon_+$ holds (provided that $\varepsilon_\parallel \neq 0$), the electric field is left-polarized: $E_- = E_\parallel = 0$. At the critical surface, which is another boundary of the opaque region, the oscillations are converted into electron Langmuir waves, whose electric field has only the longitudinal component [see formulas (4)–(6)]. For $N_\parallel = \varepsilon_{+c}^{1/2}$, the opaque region shrinks to a point, so that, in the vicinity of the critical surface, we have

$$E_\parallel \approx \sqrt{\frac{\omega}{\omega + \omega_e}} E_+. \quad (7)$$

At the critical surface itself, this approximate equality becomes exact. Recall that, since the electric-field component E_- is small, we have $E_y \approx -iE_x$.

For waves with a nonzero refractive index, $N_y \neq 0$, the opaque region is larger. The polarization of these waves is mixed ($E_+ \neq 0$, $E_\parallel \neq 0$) everywhere (in particular, at the boundaries of the opaque region).

3. SOLUTION TO THE WAVE EQUATION AND THE TRANSMISSION COEFFICIENT FOR WAVES INCIDENT ON THE CRITICAL SURFACE

For $N_\parallel^2 \neq \varepsilon_{+c}$ or $N_y \neq 0$, the opaque region lies in the vicinity of the critical surface (see above). The waves pass through the opaque region via subbarrier tunneling. In the quasiclassical approximation, the wave-power transmission coefficient has the form

$$T = \exp\left(-2\int_{x_1}^{x_2} dx |N_x|\right), \quad (8)$$

where $x_{1,2}$ are the boundaries of the opaque region.

Assuming that the plasma density is a linear function of the x coordinate $\left(\varepsilon_\parallel = -\frac{x}{L},\ \varepsilon_+ = N_{\parallel c}^2 - \frac{\omega}{\omega + \omega_e}\frac{x}{L}\right)$ and using the dispersion relation (6), we obtain

$$T = \exp\left(-\pi L \sqrt{\frac{\omega_e}{2\omega}}\left(2(N_\parallel - N_{\parallel c})^2 \frac{\omega + \omega_e}{\omega} + N_y^2\right)\right). \quad (9)$$

Based on the solution to the wave equation, Zharov [3] showed that, for oscillations with an arbitrary wavelength along the x-axis, this expression is valid even beyond the applicability range of the quasiclassical approximation.

The approximate wave equation describing the propagation of oscillations in the vicinity of the critical surface can be derived from the set of algebraic equations (5) by making the replacement $N_x \longrightarrow -i\partial/\partial x$. We take into account the linear dependence of the plasma density on the coordinate and introduce the notation $x = L^{1/2}\left(\frac{\omega_e}{2\omega}\right)^{1/4} x_1$ and $F = i\left(\frac{\omega+\omega_e}{\omega}\right)^{1/2} E_+$ to obtain the equations

$$\frac{dE_\parallel}{dx_1} = BE_\parallel - (x_1 + A)F, \qquad \frac{dF}{dx_1} = -BF + x_1 E_\parallel, \tag{10}$$

where $A = 2^{5/4}\left(\frac{\omega_e}{\omega}\right)^{3/4}\frac{\delta N_\parallel}{N_{\parallel c}}L^{1/2}$, $B = L^{1/2}\left(\frac{\omega_e}{2\omega}\right)^{1/4} N_y$, and $\delta N_\parallel = N_\parallel - N_{\parallel c}$.

Following [3], we introduce the new unknown function Y, in terms of which the quantities F and $E_\parallel$ are expressed as $F = (Y' + \alpha Y)\exp(\delta x_1^2)$ and $E_\parallel = (\beta Y' + \nu Y)\exp(\delta x_1^2)$. The constants $\alpha = -B$, $\beta = -\delta = \pm i$, and $\nu = \pm iB - A$ are determined from the condition for the two equations (10) to be identical:

$$Y'' - 2ix_1 Y' + (Ax_1 - B^2)Y = 0.$$

The replacements $Y = e^{ix_1^2} y$ and $x_1 = \frac{1}{\sqrt{2}} s e^{-i\pi/4} - \frac{A}{2}$ reduce this equation to the standard equation for a parabolic cylinder [10]

$$y'' + \left(\gamma + \frac{1}{2} - \frac{s^2}{4}\right)y = 0, \tag{11}$$

where $\gamma = \frac{i}{2}\left(\frac{A^2}{4} + B^2\right)$.

In order to determine which of the solutions to this equation describes the wave incident on the critical surface, we find the x-component of the group velocity using the dispersion relation (6) (recall that the quantities having the dimensionality of length are nondimensionalized by multiplying by the factor ω/c):

$$V_{gx} = \frac{dN_x}{d\omega} \approx \frac{4}{\omega N_\parallel^2 N_x}\left(-N_\parallel^2 + \varepsilon_+ + \varepsilon_\parallel \frac{\omega^2 + \omega_e^2 + 3/2\omega\omega_e}{(\omega+\omega_e)^2}\right). \tag{12}$$

This formula implies that, ahead of the opaque region, the dispersion of the waves under analysis is normal (the components of the group and phase velocities along the x-axis have the same sign) and, behind the opaque region, it is anomalous. Consequently, the solution to Eq. (11) that describes the waves behind the critical surface has the form [10]

$$y = D_\gamma(s) \underset{x\to 0}{\approx} s^\gamma e^{-s^2/4} \tag{13}$$

In the region $x < 0$ ($\arg s = -3\pi/4$), the asymptotic expression for $D_\gamma(s)$ corresponds to the incident and reflected waves:

$$y \approx s^\gamma e^{-s^2/4} - \frac{\sqrt{2\pi}}{\Gamma(-\gamma)} e^{-i\pi\gamma} s^{-1-\gamma} e^{s^2/4}. \tag{14}$$

A comparison of the first term in expression (14) with expression (13) yields the transmission coefficient (9). In terms of A, B, and γ, it is equal to

$$T = \exp(-2\pi|\gamma|) = \exp(-\pi(A^2/4 + B^2)). \tag{15}$$

To determine the reflection coefficient, we should take into account the fact that the incident and reflected waves are characterized by different asymptotics: for the incident wave, we have $F \approx -(B + iA/2)y$ and $E_\parallel \approx i(B + iA/2)y$, whereas, for the reflected wave, we have $F \approx 2ix_1 y$ and $E_\parallel \approx -2x_1 y$. Using the relationship $\frac{1}{|\Gamma(-\gamma)|^2} = \frac{|\gamma|}{\pi}\sinh(\pi|\gamma|)$ [10], we find that, in accordance with the law of energy conservation, the reflection coefficient is equal to

$$R = 1 - T. \tag{16}$$

4. RAY TRAJECTORIES NEAR THE CRITICAL SURFACE

Expression (6) for $N_\perp^2$, which is valid near the critical surface, can be written as the following approximate dispersion relation:

$$D = N_x^2 + N_y^2 - 2\frac{x}{L}\left(2\frac{\delta N_\parallel}{N_{\parallel c}} + \frac{\omega}{\omega_e}\frac{x}{L}\right) = 0, \tag{17}$$

where, as before, we assume that $\omega_{pe}^2 = \omega^2(1 + x/L)$.

In terms of the partial derivatives of the quantity D, the group velocity has the form

$$\mathbf{V}_g = \frac{d\omega}{d\mathbf{N}} = -\frac{\partial D/\partial \mathbf{N}}{\partial D/\partial \omega}. \tag{18}$$

Using expressions (17) and (18), we find the equations for a ray trajectory,

$$\frac{d\mathbf{r}_\perp}{dz} = -\mathbf{N}_\perp \frac{N_{\parallel c} L}{2x}, \tag{19}$$

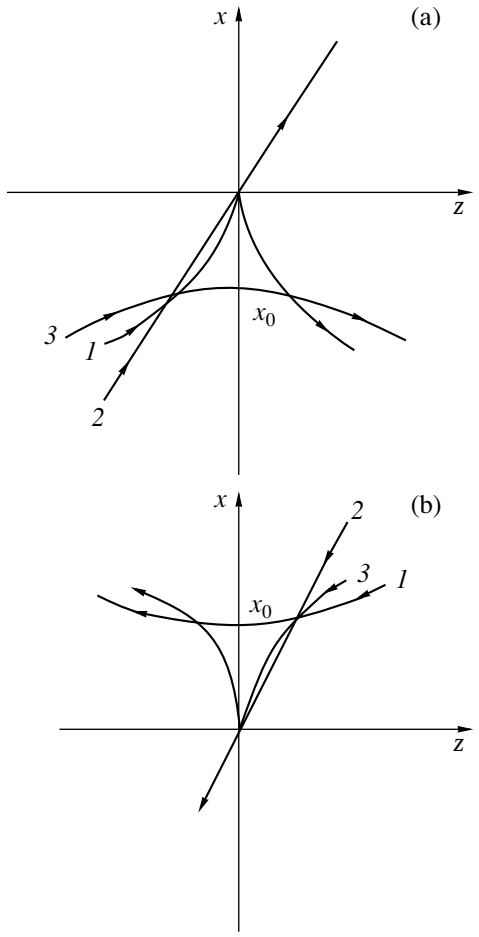

Fig. 2. Ray trajectories of the waves incident on the critical surface from the (a) lower and (b) higher density sides for (*1*) $N_\parallel < N_{\parallel c}$, (*2*) $N_\parallel = N_{\parallel c}$, and (*3*) $N_\parallel > N_{\parallel c}$.

where $\mathbf{N}_\perp = \left(\pm\left(2\frac{x}{L}\left(2\frac{\delta N_\parallel}{N_{\parallel c}} + \frac{\omega}{\omega_e}\frac{x}{L}\right) - N_y^2\right)^{1/2}, N_y\right)$. The x-component of the refractive index is real in the transparency region and is imaginary in the opaque region.

For $N_y = 0$, the ray trajectory lies in the (x, z) plane:

$$z = \pm\left(\frac{2\omega_e}{\omega}\right)^{1/2}\frac{1}{N_{\parallel c}}\left(\sqrt{x(x+x_0)} - \operatorname{sgn}x\frac{x_0}{2}\ln\left(\frac{|x+x_0/2| + \sqrt{x(x+x_0)}}{|x_0/2|}\right)\right), \quad (20)$$

where $x_0 = 2L\frac{\omega_e}{\omega}\frac{\delta N_\parallel}{N_{\parallel c}}$ and different signs of the right-hand side correspond to the reflected and incident rays. The integration constant is chosen in such a way that the reflected and incident rays coincide at the point where they are reflected from the opaque region, i.e., at $x = 0$ or $x = -x_0$.

For $N_y = 0$, one of the boundary surfaces of the opaque region is the critical surface (see above), at which the ray trajectories are intrinsically cusp-shaped (Fig. 2). For ray trajectories in the vicinity of the critical surface, Eq. (20) gives

$$z = \pm\frac{2}{3}\frac{1}{(LN_{\parallel c}|\delta N_\parallel|)^{1/2}}|x|^{3/2}. \quad (21)$$

Recall that, from the side of the negative values of $x \le 0$, the waves can reach the critical surface if $\delta N_\parallel < 0$ and, from the side of the positive values of $x \ge 0$, they can reach the critical surface if $\delta N_\parallel > 0$.

When approaching the critical surface, the oscillations are converted into electron Langmuir waves with longitudinal polarization. In this case, according to Eqs. (19) and (21), the group velocity vector is orthogonal to the magnetic field and, accordingly, to the phase velocity vector. The latter is characteristic of the potential oscillations in a magnetic field. For oscillations propagating at an angle to the magnetic field, this property was established by Piliya and Fedorov [11], who exploited the fact that, as $N \longrightarrow \infty$, such oscillations become potential. For $N \longrightarrow \infty$, Eq. (20) can be approximately represented as a homogeneous equation for the components of the refractive index: $D/N^2 \approx \varepsilon_{ik}N_iN_k = 0$, which gives $V_{g,i}N_i \propto 2\varepsilon_{ik}N_iN_k = 0$. On the other hand, the above analysis shows that, for potential oscillations with a finite refractive index ($\mathbf{N} \parallel \mathbf{B}_0$), the vectors $\mathbf{V}_g$ and $\mathbf{N}$ also remain orthogonal. Note that the ray trajectories calculated in [11] near the boundary of the transparency region are also shaped as semicubical parabolas. In conventional hydrodynamics, semicubical parabolas describe the characteristics of the gas flow in the so-called hodograph plane when the flow velocity passes over from below to above the speed of sound [12].

For $N_y = 0$, oscillations near the other boundary of the opaque region ($x \approx -x_0$) are converted into left-polarized waves ($E_\parallel \approx 0$). The ray trajectories of oscillations are described by the equation

$$z = \pm 4\frac{\omega_e}{\omega}\frac{(L|\delta N_\parallel(x+x_0)|)^{1/2}}{N_{\parallel c}^{3/2}}. \quad (22)$$

The ray trajectories of oscillations reflected from this boundary form a conventional caustic surface.

For $N_y \ne 0$, the ray trajectories near both of the boundaries of the opaque region are described by equations analogous to Eq. (22).

The above features of oscillations in the vicinity of the critical surface are also typical of another branch of oscillations, specifically, those that are extraordinary waves ahead of the critical surface and ordinary waves behind the critical surface. The only difference is that the transverse component of the electric field vector of these oscillations rotates in a different direction. Note that, for $\omega < \omega_e$, $N_\parallel > 1$, and $N_y = 0$, the transparency region for these oscillations is bounded in space and is

adjacent to the critical surface from the side of lower plasma density if $N_\parallel < N_{\parallel c} = \varepsilon_{-c}^{1/2}$ and from the higher density side if $N_\parallel > N_{\parallel c} = \varepsilon_{-c}^{1/2}$. The polarization of oscillations trapped in the transparency region changes from longitudinal at the critical surface to right-hand circular at the other boundary of the transparency region [13].

The component of the group velocity along the y-axis has opposite signs on both sides of the opaque barrier [see Eq. (19)]. Consequently, fairly large y-components of the displacements of the wave packets incident on and transmitted through the critical surface should be expected to cancel each other to a great extent.

For small values of the quantities N_y and $\delta N_\parallel$, the ray trajectories approach straight lines with increasing distance from the critical surface:

$$z = \left(\frac{2\omega_e}{\omega}\right)^{1/2} \frac{x}{N_{\parallel c}}. \tag{23}$$

The polarization of such oscillations is described by formula (7).

For N_y, $\delta N_\parallel \longrightarrow 0$, the ray trajectories are far from being straight and the polarization of oscillations is essentially different from that in formula (7) in a narrower interval along the x direction. In the limit N_y, $\delta N_\parallel = 0$, the opaque region disappears and oscillations pass freely through the critical surface.

According to formula (18), we have $\mathbf{V}_{g\perp} \propto \mathbf{N}_\perp$; consequently, the fact that waves with $\mathbf{N}_\perp = 0$ at the critical surface can pass through it might be viewed as paradoxical. However, the dispersion relation (17) implies that, for $N_y = 0$, the derivative $\partial D/\partial\omega$ at the critical surface also vanishes. As a result, the transverse component of the group velocity remains finite. The vanishing of the derivative $\partial D/\partial\omega$ indicates that, for $N_\parallel^2 = \varepsilon_{+c}$, the dispersion curves $\omega(\mathbf{N})$ for ordinary and extraordinary waves at the critical surface merge (Fig. 1c). In fact, in the vicinity of the critical surface, the dispersion relation (6) gives

$$\omega - \omega_{pe} \approx \pm\frac{|\mathbf{N}_\perp|}{2}\left(\frac{\omega_e\omega_{pe}}{2}\right)^{1/2},$$

where the upper and lower signs (plus and minus) correspond to ordinary and extraordinary waves, respectively. From this relationship, we can see that the transverse component of the group velocity is nonzero even when $\mathbf{N}_\perp = 0$ (see above).

5. WAVE BEAMS NEAR THE CRITICAL SURFACE

The ray approximation fails to hold near the reflection points for oscillations (near the boundaries of the opaque region). The corresponding parts of the ray trajectories shown in Fig. 2 should be discarded, and the ray trajectories of the incident waves should be matched to those of the transmitted and reflected waves in accordance with the solution to the wave equation. In doing so, the ray trajectories should be regarded as the limiting trajectories of the wave packets (wave beams) as the ratio of the beam width to the characteristic scale length of the plasma inhomogeneity tends toward zero. This approach was applied in my recent paper [7], which was aimed at investigating the ray trajectories of the incident and reflected waves for small angles between the plasma density gradient and the magnetic field.

We consider a Gaussian wave beam that is incident on the critical surface from the side of the negative values of x:

$$E(\mathbf{r}) = \int dN_\parallel F(N_\parallel) E(\mathbf{r}, N_\parallel), \tag{24}$$

where $F(N_\parallel) = \exp(-(N_\parallel - N_{\parallel 0})^2 l^2)$, $E(\mathbf{r}, N_\parallel) = \exp(i\Phi(\mathbf{r}, N_\parallel))$, and $\Phi(\mathbf{r}, N_\parallel) = \int^x dx' N_x(x', N_\parallel) + yN_y + zN_\parallel$. In the expression for $E(\mathbf{r}, N_\parallel)$, we omitted an unimportant, slowly varying factor in front of the exponential function.

Far from the critical surface ($|x/x_0| \gg 1$), we have

$$N_x \approx -\frac{x}{\alpha^2} - \frac{A}{2\alpha} + \frac{1}{2x}\left(\frac{A^2}{4} + B^2\right), \tag{25}$$

and, accordingly,

$$\Phi(\mathbf{r}, N_\parallel) \approx -\frac{x^2}{2\alpha^2} - \frac{Ax}{2\alpha} + \frac{1}{2}\left(\frac{A^2}{4} + B^2\right)\ln x + yN_y + zN_\parallel + \text{const}(N_\parallel), \tag{26}$$

where $\alpha = L^{1/2}\left(\frac{\omega_e}{2\omega}\right)^{1/4}$. The sign of N_x in expression (25) was chosen to satisfy the condition $V_{g,x} > 0$, and the constant in expression (26) can be chosen to be $\text{const}(N_\parallel) = -\frac{1}{2}\left(\frac{A^2}{4} + B^2\right)\ln(-4|x_0|)$. With these choices, we can see that, in the region $x/x_0 \gg 1$, the trajectory of the wave beam with phase (26) (see below) is described by the asymptotic equation (20). On the other hand, these choices simplify the analysis of the trajectories of the reflected beam.

The spatial dependence of the electric field of the wave beam can be found by calculating the integral in expression (24) by the stationary-phase method:

$$E(\mathbf{r}) \approx \frac{\sqrt{\pi}}{l_0}\exp\left(i\Phi(\mathbf{r}, N_{\parallel 0}) - \frac{1}{4l_0^2}(\Phi'_{N_{\parallel 0}}(\mathbf{r}, N_{\parallel 0}))^2\right), \tag{27}$$

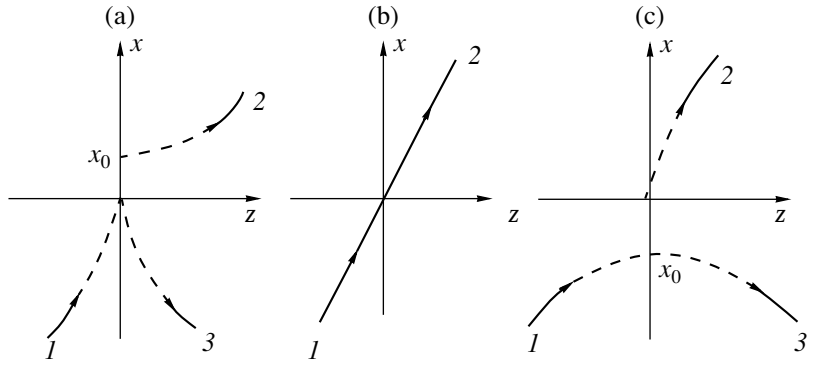

Fig. 3. Trajectories of wide ($l \gg L^{1/2}$) wave packets in the vicinity of the critical surface for (a) $N_{\|0} < N_{\|c}$, (b) $N_{\|0} = N_{\|c}$, and (c) $N_{\|0} < N_{\|c}$. Shown are the trajectories of (*1*) the wave beams incident from the lower density side and (*2*) the transmitted and (*3*) reflected wave beams. The dashed parts of the trajectories lie in the region where the quasiclassical approximation fails to hold.

where $l_0^2 = l^2 - iA_2\ln|4x/x_0|$, $\Phi'_{N_\|}(\mathbf{r}, N_\|) \approx \frac{1}{2}A_1\left(-\frac{x}{\alpha} + \frac{A}{2}\ln|4x/x_0|\right) + z$, $A_1 = \frac{\partial A}{\partial N_\|} = \frac{2^{5/4}}{N_{\|c}}\left(\frac{\omega_e}{\omega}\right)^{3/4}L^{1/2}$, and $A_2 = \frac{1}{8}A_1^2$. Expression (27) is valid far from the critical surface, i.e., when the parameter $|x/x_0| \gg 1$ is much larger than unity. The expression for $\Phi'_{N_\|}(\mathbf{r}, N_\|)$ is valid with logarithmic accuracy in terms of this parameter.

It is natural to associate the ray trajectories that were analyzed in the previous section with the central trajectory of the wave beams. The central trajectory is defined by the condition $\Phi'_{N_\|}(\mathbf{r}) = 0$. One can readily see that, for $|x/x_0| \gg 1$, the central trajectory of the wave beam with the electric field (27) is described by the asymptotic equation (20):

$$z = \frac{A_1}{2}\left(x - \frac{A}{2}\ln|4x/x_0|\right). \tag{28}$$

Simple analytic expressions for the parameters of the transmitted wave beam can be obtained in the limiting cases of wide ($l \gg L^{1/2}$) and narrow ($l \ll L^{1/2}$) beams. Behind the critical surface, a wide beam is described by expression (27) with the additional factor $\exp(-\pi|\gamma(N_{\|0})|)$, which takes into account subbarrier tunneling. Being oriented in the proper manner ($|\gamma(N_{\|0})| \ll 1$), a wide beam can be essentially completely transmitted through the critical surface.

The beam that is narrow in coordinate space is wide in wavenumber space. The critical surface acts on such a beam as a filter that transmits the waves with $N_\| \approx N_{\|c}$. In this case, the factor $\exp(-\pi|\gamma(N_{\|0})|)$, which determines the transmission coefficient for a wide wave beam, should be replaced by $\exp(-(N_{\|0} - N_{\|c})^2 l^2)$. In fact, taking the integral in expression (24) by the saddle point method, we obtain

$$E(\mathbf{r}) \approx \frac{\sqrt{\pi}}{l_1}\exp\left(-(N_{\|0} - N_{\|c})^2 l^2 + i\Phi(\mathbf{r}, N_{\|c}) - \frac{1}{4l_1^2}(\Phi'_{N_{\|c}}(\mathbf{r}, N_{\|c}))^2\right), \tag{29}$$

where $l_1^2 = (\pi/4 - i\ln|4x/x_0|)A_2$ and $\Phi'_{N_{\|c}}(\mathbf{r}, N_{\|c}) \approx -\frac{1}{2\alpha}A_1 x + z$.

One can readily derive an expression that describes the effective transmission coefficient for a wave beam and is valid for arbitrary values of the ratio of l to $L^{1/2}$ [7] [cf. (15)]:

$$T_b = g^{1/2}\exp(-\pi(gA^2(N_{\|0})/4 + B^2)),$$

where $g = \frac{l^2}{l^2 + \pi A_2}$, and the quantity $A_2 = \frac{L}{2^{1/2}N_{\|c}^2}\left(\frac{\omega_e}{\omega}\right)^{3/2}$ characterizes the width of the transmission band of the critical surface in wavenumber space.

The above analysis shows that the ray trajectories of a wide incident beam ($l \gg L^{1/2}$) and those of the transmitted beam are described by the same equation (28).

Figure 3 shows representative ray trajectories calculated for different values of $A \propto \delta N_\|$. The trajectories are terminated at a certain distance from the critical surface, in the vicinity of which the quasiclassical approximation fails to hold and, accordingly, the asymptotic representations (13) and (14), which were taken into account in calculating the spatial dependence of the electric fields of the wave beams, are invalid.

In the case of a narrow beam, the beam component that has passed through the critical surface propagates along a straight trajectory described by Eq. (22) or, equivalently, by Eq. (28) with $A = 0$.

Now, we determine the ray trajectories of the reflected beams. In order to match the ray trajectory of the reflected beam with that of the incident beam, we turn to the asymptotic expression (14), which refers to both incident and reflected plane waves. As was shown above, the trajectory of the incident wave beam is described by Eq. (20), provided that, in the first term in expression (14), the amplitude is chosen in the proper manner. The same factor should also enter into the second term, which describes the reflected wave. To simplify the calculations, we assume that $|\gamma| \gg 1$ and use the asymptotic representation $\Gamma(-\gamma) \underset{|\gamma| \gg 1}{\approx} \exp[-\gamma\ln(-\gamma)]$. From these considerations, we can see that the phase of the reflected wave is again described by expression (26) but with opposite signs of the first three terms:

$$\Phi(\mathbf{r}, N_\parallel) \approx \frac{x^2}{2\alpha^2} + \frac{Ax}{2\alpha}$$

$$-\frac{1}{2}\left(\frac{A^2}{4} + B^2\right)\ln|4x/x_0| + yN_y + zN_\parallel.$$

Applying again the above calculation procedure, we can see that the trajectory of the reflected wave beam is described by the asymptotic equation (20), as is the case with the trajectory of the incident wave beam:

$$z = -\frac{A_1}{2}\left(\frac{x}{\alpha} - \frac{A}{2}\ln|4x/x_0|\right).$$

Knowing the asymptotic trajectories of the beam, we can reconstruct its entire ray trajectory. It turns out that, for $\delta N_\parallel < 0$, the incident ray passes over to the reflected ray at the cusp ($x = 0$, $z = 0$) and, for $\delta N_\parallel > 0$, at the vertex of the parabolic trajectory ($x = -x_0$, $z = 0$). The matching of the trajectories is possible because, in expression (14), the term that describes the reflected wave contains the factor $\Gamma^{-1}(-\gamma)$, which determines the shift of the ray trajectory as a whole from the incident ray trajectory along the z-axis. With this term, the ray trajectory of the transmitted waves is as close as possible to the common ray trajectory of the incident and reflected waves (Fig. 3).

The Fourier spectrum of a narrow wave beam ($l \le L^{1/2}$) changes during the reflection, because the critical surface transmits the waves with $N_\parallel \approx N_{\parallel c}$. As a result, the reflected part of the incident wave beam is no longer Gaussian, so that its spatial structure cannot be described by expressions (27) and (29) and its width increases to about $L^{1/2}$. In fact, the change in the Fourier spectrum during the reflection may be explained as being due to the formation of another reflected beam with a narrower spectrum and, consequently, a larger width in coordinate space. The phase of the new reflected beam is shifted from the phase of the main reflected beam by π.

6. OSCILLATIONS IN A PLASMA WITH A NONORTHOGONAL DENSITY GRADIENT AND MAGNETIC FIELD

The above analysis was based on the simplified set of wave equations (5). These equations can also be used to analyze the propagation of oscillations in a plasma in which the density gradient is not orthogonal to the magnetic field.

We assume that the plasma density gradient lies in the (x, z) plane and introduce the Cartesian coordinate system (ξ, y, ζ) with the ξ-axis parallel to ∇n_0 (Fig. 4). As before, we restrict ourselves to considering the waves with $N_\parallel \approx N_{\parallel c}$, which are the only waves that freely cross the critical surface. The spatial dependence of the field of these waves is described by the expression $f(\xi, y, \zeta)\exp(iN_{\parallel c}(z(\xi, \zeta))$, where f is a gradually varying function. In the quasiclassical approximation, this function has the form $f(\mathbf{r}) = \exp(i(\delta N_\xi \xi + N_y y + \delta N_\zeta \zeta))$, where χ is the angle between the plasma density gradient and the magnetic field, $\delta N_\xi = N_\xi - N_{\parallel c}\cos\chi$ and $\delta N_\zeta = N_\zeta - N_{\parallel c}\sin\chi$, in which case we have $N_x = \delta N_\xi \sin\chi - \delta N_\zeta \cos\chi$ and $N_\parallel = N_{\parallel c} + \delta N_\xi \cos\chi + \delta N_\zeta \sin\chi$. Setting $\delta N_\xi = -i\dfrac{\partial}{\partial\xi}$ and $\varepsilon_\parallel(\xi) = -\dfrac{\xi}{L}$, $\varepsilon_+(\xi) = N_{\parallel c}^2 - \dfrac{\omega}{\omega + \omega_e}\dfrac{\xi}{L}$, we reduce Eqs. (5) to the following set of differential equations, which are a generalization of Eqs. (10):

$$\frac{dE_\parallel}{d\xi_1} = (B + iD)E_\parallel - (\xi_1 + A)F,$$
$$\frac{dF}{d\xi_1} = -B^*F + \xi_1 E_\parallel, \tag{30}$$

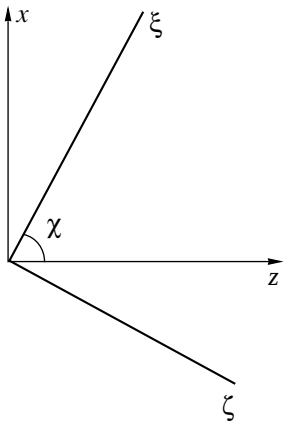

Fig. 4. Coordinate systems used in the analysis.

where $A = \frac{2^{5/4}L^{1/2}}{\sin^{3/2}\chi N_{\|c}}\left(\frac{\omega_e}{\omega}\right)^{3/4}(\delta N_\zeta + iN_y\cos\chi)$,

$$B = \frac{L^{1/2}}{\sin^{1/2}\chi}\left(\frac{\omega_e}{2\omega}\right)^{1/4}(N_y - i\delta N_\zeta\cos\chi),$$

$$D = 2^{3/2}\cot\chi\left(1 + \frac{\omega_e}{\omega}\right)^{1/2},$$

$$\text{and } \xi_1 = \xi\left(\frac{2\omega}{\omega_e}\right)^{1/4}(L\sin\chi)^{-1/2}.$$

Equations (30) correct for the corresponding misprinted equations in [5]. Note that writing the wave equations in terms of the circularly polarized fields made it possible to avoid laborious intermediate manipulations.

Applying the procedure described in Section 3, we reduce Eqs. (30) to a single second-order differential equation:

$$Y'' - i(2\,\mathrm{Im}\,B \pm H\xi_1)Y' + (-|B|^2 + G\xi_1)Y = 0,$$

where $G = A \mp 2H\mathrm{Im}\,B - iD\mathrm{Re}\,B$ and $H = \sqrt{D^2/4 + 1}$.

Then, introducing the new function

$$Y = \exp(i\,\mathrm{Im}\,B\xi_1 \mp 2iH\xi_1^2)y$$

and the new independent variable

$$\xi_2 = H^{1/2}\xi_1 + H^{-1/2}(\mathrm{Im}\,B + G/(2H)),$$

we arrive at the standard parabolic equation (11) with a modified expression for γ [5]:

$$\gamma = \frac{i}{H}\left(\frac{G}{4H^2}(G \pm 4H\,\mathrm{Im}\,B) + |B|^2\right)$$

$$= i\left(\frac{\omega_e}{2\omega}\right)^{1/2}\frac{L}{\left(2\left(1 + \frac{\omega_e}{\omega}\right)\cos^2\chi + \sin^2\chi\right)^{1/2}}$$

$$\times\left\{\frac{2\delta N_\zeta^2\left(1 + \frac{\omega_e}{\omega}\right)}{2\left(1 + \frac{\omega_e}{\omega}\right)\cos^2\chi + \sin^2\chi} + N_y^2\right\}.$$

Of course, since the expression for γ is modified as χ changes, expressions (15) and (16) for the transmission and reflection coefficients are also modified.

For $N_y = 0$, the opaque region is adjacent to the critical surface from the side of the positive values of ξ if $\delta N_\zeta < 0$ and from the side of the negative values if $\delta N_\zeta > 0$ (as in the case $\chi = \pi/2$). For $N_y \neq 0$, the critical surface lies inside the opaque region.

The characteristic shape of the ray trajectories of the waves under consideration remains the same, regardless of the value of the angle χ. In particular, at the critical surface, the ray trajectories have cusps, which are oriented perpendicular to the magnetic field or, equivalently, along the x-axis, as in the case $\chi = \pi/2$. In fact, using the dispersion relation (6) and the above expressions relating N_x to δN_ξ and δN_ζ, we reduce the ray trajectory equation (19) to

$$\frac{dx}{dz} = -N_x\frac{N_{\|c}L}{2\xi}. \tag{31}$$

Close to the cusp, we have $\zeta \approx -\xi\cot\chi$ and $\xi \approx -x\sin\chi$. Consequently, from Eq. (31), we obtain

$$z = \pm\frac{2}{3}\frac{\sin^2\chi}{(LN_{\|c}|\delta N_\zeta|)^{1/2}}|x|^{3/2}.$$

The characteristic properties of the wave polarization are also insensitive to χ, except that, for $\chi \neq \pi/2$ and $N_y = 0$, the wave polarization at the boundary surface of the opaque region other than the critical surface is not purely circular ($E_\| \neq 0$).

7. CONCLUSION

We have thoroughly investigated ordinary waves that are incident on the critical surface from the side of lower plasma density. It is these waves that can serve to heat dense plasmas [2]. The symmetry of the parabolic equation with respect to the sign of the independent variable tells us that the expressions derived for the reflection and transmission coefficients are also valid for ordinary waves that are incident on the critical surface from the higher density side. Extraordinary waves can penetrate through the critical surface at $\chi < \frac{\pi}{2}\left(\frac{\omega_e}{\omega} > 1 + \frac{1}{2}\tan^2\chi\right)$. The transmission and reflection coefficients for extraordinary waves are given by the above expression for γ. In this case, however, it is necessary to change the sign at ω_e and use the absolute value under the square root.

The above analysis is inapplicable for fairly small values of the angle $\chi \leq L^{1/2}$, when coupling between the waves with left-hand and right-hand circular polarizations is important. This coupling is described by a more complicated (fourth-order) wave equation (see [1, 7]).

ACKNOWLEDGMENTS

I am grateful to V.V. Arsenin and A.V. Zvonkov for useful discussions. This work was supported in part by the Russian Foundation for Basic Research, project no. 00-15-96526 (under the program “Leading Scientific Schools”).

REFERENCES

1. V. L. Ginzburg, *The Propagation of Electromagnetic Waves in Plasmas* (Nauka, Moscow, 1967; Pergamon, Oxford, 1970).
2. J. Preinhalter and V. Kopecky, J. Plasma Phys. **10**, 1 (1973).
3. A. A. Zharov, Fiz. Plazmy **10**, 1109 (1984) [Sov. J. Plasma Phys. **10**, 642 (1984)].
4. J. Mjolhus, J. Plasma Phys. **31**, 7 (1984).
5. M. D. Tokman, Fiz. Plazmy **11**, 1205 (1985) [Sov. J. Plasma Phys. **11**, 689 (1985)].
6. H. P. Laqua, W7-AS Team, and ECRH Group, Plasma Phys. Controlled Fusion **41**, A273 (1999).
7. A. V. Timofeev, Fiz. Plazmy **26**, 874 (2000) [Plasma Phys. Rep. **26**, 820 (2000)].
8. A. V. Timofeev, Fiz. Plazmy **27**, 131 (2001) [Plasma Phys. Rep. **27**, 119 (2001)].
9. A. V. Timofeev, *Resonance Phenomena in Plasma Oscillations* (Nauka, Moscow, 2000).
10. *Higher Transcendental Functions (Bateman Manuscript Project)*, Ed. by A. Erdelyi (McGraw-Hill, New York, 1953; Nauka, Moscow, 1966).
11. A. D. Piliya and V. I. Fedorov, in *High-Frequency Plasma Heating*, Ed. by A. G. Litvak (Inst. Prikl. Fiz., Gor'ki, 1983), p. 281.
12. L. D. Landau and E. M. Lifshitz, *Fluid Mechanics* (Nauka, Moscow, 1986; Pergamon, New York, 1987).
13. A. V. Timofeev, Fiz. Plazmy **27**, 282 (2001) [Plasma Phys. Rep. **27**, 265 (2001)].

Translated by O. E. Khadin

Plasma Physics Reports, Vol. 27, No. 11, 2001, pp. 932–937. Translated from Fizika Plazmy, Vol. 27, No. 11, 2001, pp. 988–993.

PLASMA OSCILLATIONS AND WAVES

Distribution of the Absorbed ECRH Power among the Electrons in a Plasma Heated by an Extraordinary Wave

V. L. Erukhimov and V. E. Semenov

Institute of Applied Physics, Russian Academy of Sciences, ul. Ul'yanova 46, Nizhni Novgorod, 603600 Russia

Received December 25, 2000; in final form, April 6, 2001

Abstract—A study is made of the one-dimensional linear problem of the absorption of the energy of an extraordinary wave propagating along a nonuniform magnetic field by a plasma in the ECR region. The plasma electrons are assumed to be nonrelativistic and are described by a collisionless kinetic equation. The distribution of the absorbed power among the electrons and the distribution of the self-consistent field over the confinement system are obtained. The conditions under which the ECRH power is distributed uniformly among the bulk electrons are determined. The limits of applicability of the locally nonuniform magnetic field approximation are established. The solutions derived are compared with the solution to an analogous problem with the collisional absorption mechanism. © *2001 MAIK "Nauka/Interperiodica".*

1. INTRODUCTION

The problem of the interaction of electromagnetic waves with plasmas under electron cyclotron resonance (ECR) conditions has been actively studied over the past several decades in connection with a broad range of applications of ECR plasma heating. Research in this field has concentrated on the following two issues: (i) the propagation and absorption of electromagnetic waves in a plasma and (ii) the formation of the electron velocity distribution function (EDF) during ECR heating. The latter problem seems to be especially important for optimizing the operating modes of ECR sources of multicharged ions [1], because the electron velocity distribution in these sources has a direct effect on plasma confinement in magnetic devices [2]. On the other hand, the problem of determining the EDF in an ion ECR source is fairly complicated, because the formation of the EDF is governed by the combined action of various factors, such as electron production by ionization processes, electron escape from the device through the end plugs, electron scattering in Coulomb collisions, the interaction of electrons with a microwave field, and the perturbation of the field of the heating wave by electron currents induced in the plasma. The solution of such a complicated problem requires a detailed preliminary analysis of each of these processes, most of which were already examined in previous studies. In particular, the ECR interaction between the electrons and the field of an unperturbed wave propagating in a collisionless plasma along the device axis was investigated in [3, 4], where it was shown that, for waves whose amplitudes are not too small, the evolution of the EDF in velocity space is described by a diffusive Fokker–Planck equation with the diffusion coefficient proportional to the wave intensity. The results obtained in [3, 4] were then applied in [5, 6] to calculate the EDF in a magnetic confinement system with allowance for ionization, the Coulomb scattering of electrons, and the escape of electrons through the end plugs. However, in a plasma whose density in the ECR region is not too low, an extraordinary electromagnetic wave propagating along the magnetic field can be perturbed rather strongly. It was found that, in such a plasma, the distribution of the absorbed power among the electrons can be highly nonuniform, thereby significantly affecting the quasilinear electron diffusion coefficient in velocity space and inevitably influencing the structure of the EDF. Hence, in a high-density plasma, which is of primary interest from the standpoint ion ECR sources, the electrodynamic aspects play an important role in the problem under consideration and require a separate analysis, which will be carried out in this paper.

Note that research on the propagation of electromagnetic waves in plasmas is one of the best-developed branches of plasma physics and is elucidated in most of the textbooks and monographs on this topic. Questions related to the propagation of an extraordinary electromagnetic wave through the ECR region have received much attention (see, e.g., [3] and the literature cited therein). However, in most of the published papers, a study was made of the integral parameters of the ECR region, specifically, the coefficients of reflection, transmission, and absorption of the incident wave. To the best of our knowledge, the questions associated with the distribution of the absorbed power among the plasma electrons were considered only in a paper by Kuckes [7], which, unfortunately, contains some errors, so that it is impossible to directly apply the results obtained therein.[1] Here, we present the results of an analysis of the revised linear problem of the propaga-

[1] In particular, the results of [7] conflict with the dependence of the wave absorption coefficient on the parameters of the problem treated by Timofeev [3].

1063-780X/01/2711-0932$21.00

tion of an extraordinary wave through the ECR region. The wave is assumed to propagate from the side of the stronger magnetic field in a warm collisionless plasma. We focus on the questions regarding the distribution of the absorbed power among electrons with different longitudinal velocities and the possibility of describing the electrodynamic aspects of the problem in a simplified (geometrical-optics) approximation. The latter question can also be discussed for the simple case of a cold plasma with a given electron collision frequency. Since the answers to these questions have much in common, we also present the results that were obtained from analysis of the electrodynamics of a cold collision-dominated plasma in the ECR region and that are based on the familiar exact solution to the problem under consideration.

2. SELF-CONSISTENT FIELD AND THE SPATIAL DISTRIBUTION OF THE RELEASED ENERGY IN A COLD PLASMA

Plane extraordinary electromagnetic waves propagating along a uniform magnetic field B_0 in a cold plasma can be described by the equation

$$\frac{d^2E}{dz^2} + \frac{\omega^2}{c^2}\varepsilon_+ E = 0. \quad (1)$$

Here, z is the coordinate along the magnetic field; E is the complex amplitude of the electric field $\mathbf{E} = \mathrm{Re}((\mathbf{x} - i\mathbf{y})E(z)\exp(i\omega t))$ in the wave; ω is the field frequency; c is the speed of light in vacuum; and ε_+ is the square of the complex refractive index,

$$\varepsilon_+ = n^2 = 1 + \frac{\omega_p^2}{\omega(\omega_H - \omega + i\nu)}, \quad (2)$$

where $\omega_p^2 = 4\pi e^2 N/m$ is the square of the electron plasma frequency, N is the plasma density, e and m are the charge and mass of an electron, ω_H is the electron cyclotron frequency, and the electron–ion collision frequency ν is assumed to be constant.

In certain approximations, Eq. (1) can be used to analyze the propagation of an extraordinary wave along a smoothly nonuniform magnetic field under the formal assumption that the electron gyrofrequency is a function of the longitudinal coordinate, $\omega_H(z)$. The main features of the wave propagation through the ECR region can be examined in terms of a simple model with $\omega_p = \text{const}$ and $\omega_H = \omega(1 - z/L)$, where L is the scale on which the magnetic field varies in the resonance zone. In accordance with Eq. (1), written in terms of the dimensionless coordinate $x = \omega z/c$, the solution to our problem in this model is determined by two independent parameters:

$$\frac{d^2E}{dx^2} + \left(1 - \frac{\gamma}{x - id}\right)E = 0, \quad (3)$$

where $\gamma = \omega_p^2 L/\omega c$ and $d = \nu L/c$. In particular, for a wave incident from the side of the stronger magnetic field (i.e., from $x = -\infty$), the solution to Eq. (3) can be represented as

$$E = W_{\frac{i\gamma}{2},\frac{1}{2}}(2i(x - id)), \quad (4)$$

where $W_{k,m}(z)$ is a Whittaker function [8]. This solution implies that the reflection coefficient is identically zero, and the transmission and absorption coefficients are independent of the collision frequency:

$$T = \exp(-\pi\gamma), \quad Q = 1 - T, \quad R = 0, \quad (5)$$

where T and Q are the wave-power transmission and absorption coefficients, respectively. Nevertheless, the spatial field structure and the spatial distribution of the released energy are both very sensitive to the collision frequency (the parameter d). This conclusion can be clearly illustrated by using approximate models that assume certain relationships between the parameters γ and d.

It is convenient to construct such approximate models by analyzing the relative role of collisions in different spatial regions. This approach makes it possible to introduce the concept of the resonance zone, which can be easily generalized to the case of a warm plasma. In the resonance zone, which surrounds the ECR plane ($x = 0$), the electron collisions (or thermal electron motion) markedly perturb electric currents induced by the wave field in the plasma. In contrast, outside the resonance zone, the perturbing effect of collisions (or thermal motion) is relatively insignificant and manifests itself mainly as a weak (over the wavelength) absorption of the wave power.[2] For a cold collision-dominated plasma, the resonance zone is characterized by the inequality $|\omega - \omega_H| \le \nu$; i.e., the dimensionless width Δx_r of the resonance zone is about d. In this case, the wave field structure is very sensitive to the relative width of the resonance zone.

2.1. Broad Resonance Zone, $d \gg (\gamma + 1)^{-1}$

For a broad resonance zone,[3] the solution to Eq. (3) can be described with sufficient accuracy in the Wentzel–Kramers–Brillouin (WKB) approximation,

[2] It can be shown that, despite terminological differences, this concept of the resonance zone is actually equivalent to the notions introduced by Ginzburg [9] when solving hydrodynamic collisional problems and by Kuckes [7] when solving kinetic problems.

[3] Here, the inequality $d \gg (\gamma + 1)^{-1}$ refers simultaneously to the following two limiting cases:

$$d \gg \begin{cases} \gamma^{-1}, & \gamma \gg 1 \\ 1, & \gamma \ll 1. \end{cases}$$

because the inequality $|d\varepsilon_+/dx| \ll |\varepsilon_+^{3/2}|$ holds over the entire plasma volume:

$$E = \frac{E_0}{\sqrt{n}} \exp\left(-i\int_{-\infty}^{x} n(x')dx'\right),$$

where E_0 is the amplitude of the electric field of the incident wave and $n = \sqrt{\varepsilon_+}$. We can see that the local structure of an electromagnetic wave is independent of the magnetic field nonuniformity. The width of the resonance zone is much larger than the local wavelength of the extraordinary wave; i.e., $|nd| \gg 1$. The spatial distribution of the absorbed power depends on the parameter γ. For $\pi\gamma \ll 1$ (i.e., when the total absorption is weak), the plasma perturbs the field of the incident wave only slightly. Accordingly, we have $|E| \approx E_0$, so that the energy is deposited mainly in the resonance zone (where the peak of the function $\mathrm{Im}\varepsilon_+$ is localized). For $\pi\gamma \gg 1$ (i.e., when the total absorption is strong), the field amplitude in the resonance zone is small compared to the amplitude of the incident wave, so that the incident wave loses a major fraction of its energy before reaching the resonance zone, i.e., in the region to which the geometrical-optics approximation can be applied, $-\infty \le x \le -d$, and in which the inequality $\mathrm{Im}(\varepsilon_+) \le \mathrm{Re}(\varepsilon_+)$ holds.

2.2. Narrow Resonance Zone, $d \ll (\gamma + 1)^{-1}$

As in the case of a broad resonance zone, under conditions such that the total absorption is weak ($\pi\gamma \ll 1$), the field of the incident electromagnetic wave is perturbed only slightly by the plasma (the approximate equality $|E| \approx E_0$ holds over the entire plasma volume). Consequently, the wave energy is mainly deposited in the resonance zone. For $\pi\gamma \gg 1$, the field structure and the spatial distribution of the released energy differ radically from those in the case of a broad resonance zone. In particular, in contrast to the conclusion drawn by Ginzburg in his classical monograph [9], the WKB approximation fails to hold in the region $|x| \le 1/\gamma$, which is far wider than the resonance zone ($d \ll 1/\gamma$). By virtue of the condition $\mathrm{Im}(\varepsilon_+) \ll \mathrm{Re}(\varepsilon_+)$, the absorption of the incident wave can be neglected in the region in which the geometrical-optics approximation can be applied and which coincides with the region where the WKB approximation is valid. However, in this region, the refractive index is elevated and, accordingly, the amplitude $|E|$ of the incident wave decreases to about $E_0/\sqrt{\gamma}$. The magnetic field nonuniformity strongly affects the local structure of the wave in the region $|x| \le 1/\gamma$, whose thickness, however, is relatively small, so that the field amplitude $|E|$ across this region does not change significantly. On the other hand, in this region, the function $\mathrm{Im}(\varepsilon_+)$ has a sharp resonance peak, which is localized within the resonance zone. Consequently, the wave energy is mainly deposited in the resonance zone, whose thickness in the case at hand is small in comparison with the local wavelength, $|nd| \ll 1$. This indicates that, in the resonance zone and even in a broader region determined by the condition $|x| \ll \min(1/\gamma, 1)$, the complex field amplitude changes insignificantly: $E \approx$ const.[4] In this region, the amplitude $|E|$ can readily be found from the condition that the Ohmic heating power is equal to the energy flux in the incident wave:

$$P \approx \frac{\omega \mathrm{Im}\,\varepsilon_+(0)|E(0)|^2}{8\pi^2} d\frac{c}{\omega} \approx \frac{c|E_0|^2}{8\pi}.$$

Note that, in the case at hand ($\pi\gamma \gg 1$), this condition gives the amplitude $|E(0)| \approx E_0/\sqrt{\pi\gamma}$, which coincides with the solution to the exact equation (4) in the limit $d \ll \gamma^{-1}$.

3. ABSORPTION IN A WARM COLLISIONLESS PLASMA

As in Section 2, we analyze the propagation of an extraordinary wave through the ECR region using a one-dimensional model. Again, we consider a wave propagating along the magnetic field in a collisionless plasma and assume that the electron gyrofrequency is a linear function of the z coordinate and the plasma density is uniform (i.e., we neglect variations of the longitudinal electron velocity). Under these assumptions, the initial equations for the complex electric-field amplitude E and perturbations of the EDF f_1 have the form

$$\frac{d^2E}{dz^2} + \frac{\omega^2}{c^2}E = \frac{4\pi i\omega}{c^2}j, \tag{6}$$

$$v_\parallel \frac{\partial f_1}{\partial z} + i(\omega - \omega_H) f_1 = \frac{eE}{m}\frac{\partial f_0}{\partial v_\perp}, \tag{7}$$

where the complex amplitude $j(z)$ of the electron current density $\mathbf{j}(z, t) = \mathrm{Re}((\mathbf{x} - i\mathbf{y})j(z)\exp(i\omega t))$ excited by the incident electromagnetic wave is equal to

$$j = -\frac{e}{2}\int v_\perp f_1(v_\perp, v_\parallel) d^2\mathbf{v}_\perp dv_\parallel. \tag{8}$$

The total EDF can be represented as

$$f(z, t, \mathbf{v}_\perp, v_\parallel) = f_0(v_\perp, v_\parallel) + \mathrm{Re}\left(\frac{v_x - iv_y}{v_\perp} f_1(z, v_\perp, v_\parallel)\exp(i\omega t)\right), \tag{9}$$

[4] In the case under analysis (i.e., for $\pi\gamma \gg 1$ and $d(1 + \gamma) \ll 1$), the exact solution shows that, in the resonance zone, in which the incident wave is mainly absorbed, the wave electric field is nearly constant ($E \simeq$ const) and also the amplitude variations in the wave magnetic field are slight. A decrease in the wave energy flux is associated with a change in the phase of the magnetic field by about $\pi/2$.

where $\mathbf{v}_\perp$ and $v_\parallel$ are the velocity components perpendicular and parallel to the magnetic field, $v_\perp = |\mathbf{v}_\perp|$, and the unperturbed EDF f_0 is assumed to be symmetric in transverse velocities.

As in the case of a collision-dominated plasma, we transform Eqs. (6) and (7) with the complex current-density amplitude (8) to the dimensionless coordinate $x = z\omega/c$ and integrate the dimensionless equation (7) multiplied by $v_\perp$ over transverse velocities. As a result, we can see that, for a prescribed structure of the unperturbed EDF, the solution to the problem again depends on two parameters: $\gamma = \omega_p^2 L/\omega c$ and $\delta = \sqrt{\omega L v_T}/c$, where v_T is the longitudinal electron thermal velocity. The resulting equations (6) and (7) with the dimensionless expression (8) can be rewritten in the form

$$\frac{\partial J}{\partial x} + i\frac{x}{\delta^2 U}J = \frac{\gamma}{\delta^2}E\frac{F(U)}{U},$$
$$\frac{\partial^2 E}{\partial x^2} + E = i\int_{-\infty}^{\infty} J(U, x)dU, \tag{10}$$

where $U = v_\parallel/v_T$, $NF(U)/v_T = \int f_0(v_\perp, Uv_T)d^2\mathbf{v}_\perp$, N is the plasma density, and $J(U, x) = 4\pi e v_T \int v_\perp f_1(v_\perp, Uv_T, x)d^2\mathbf{v}_\perp/2\omega$.

In accordance with Eqs. (10), the density of the current induced in the plasma decreases to zero with increasing distance from the resonance point; i.e., $\int J(x, U)dU \longrightarrow 0$ as $|x| \longrightarrow \infty$. Consequently, at infinity, the wave field structure is always the same as in vacuum, so that we can impose the following boundary condition on the complex electric-field amplitude E:

$$E(x) = e^{-ix}, \quad x \longrightarrow -\infty. \tag{11}$$

In this case, the boundary condition on J can be determined from the causality principle, i.e., from the assumption that the electrons that move from infinity toward the resonance zone and that are sufficiently far from the resonance zone do not contribute to the current density:

$$J(U, x) = 0, \quad x \longrightarrow -\mathrm{sgn}(U)\infty. \tag{12}$$

Using the method of phase integrals, we can see that, for the wave incident from the side of the stronger magnetic field, the reflection, transmission, and absorption coefficients are independent of the parameter δ (or, equivalently, the electron thermal velocity). These coefficients turn out to be exactly the same as those in the corresponding problem [see coefficients (5)] of the wave propagation through the ECR region in a cold collision-dominated plasma [3]. Nevertheless, the spread in electron velocities has a substantial impact on the field structure and on the distribution of the absorbed power both in space and among the electrons.

3.1. Resonance Zone

As in the previous problem, it is very convenient to analyze the electromagnetic field structure using an approximate method based on the concept of the resonance zone. However, for a warm collisionless plasma, the width of the resonance zone (i.e., the zone where the effects of spatial dispersion are significant) itself depends on the field structure and can thus be determined only by solving the problem at hand. The width of the resonance zone is generally governed by the following two factors: first, because of the Doppler effect, the displacement of the zone where an electron interacts resonantly with the field depends strongly on the longitudinal electron velocity and, second, because of the finite time taken by an electron to traverse the resonant interaction zone, the width of this zone is finite for each individual electron. Consequently, the resonance zone is characterized by the inequalities

$$|\omega - \omega_H| \le kV_T,$$
$$|\omega - \omega_H| \le \sqrt{\omega V_T/L}. \tag{13}$$

Here, k is the wavenumber of the wave field, provided that the spatial field structure is quasi-monochromatic, $E \propto \exp(-i\int k(z)dz)$. In a more general case, the quantity k can be assigned the characteristic value $\left|\frac{\partial E}{\partial z}/E\right|$. In dimensionless variables, inequalities (13) correspond to the width of the resonance zone,

$$\Delta x_r = \Delta x_1 + \Delta x_2. \tag{14}$$

Here, the quantity Δx_1 is determined by the Doppler effect,

$$\Delta x_1 = n\delta^2, \tag{15}$$

n is the effective refractive index of the plasma for the wave; and the quantity Δx_2 is determined by the finite transit time of an electron through the zone of the resonant interaction with the wave field,

$$\Delta x_2 = \delta. \tag{16}$$

Note that the width of the broad resonance zone ($n\Delta x_r \gg 1$) is governed by the Doppler effect ($\Delta x_1 \gg \Delta x_2$), while the width of the narrow resonance zone ($n\Delta x_r \ll 1$) is governed by the electron transit time ($\Delta x_2 \gg \Delta x_1$). In the latter case, the width of the resonance zone is independent of the electromagnetic field structure.

Outside the resonance zone, the electron thermal motion, by definition, perturbs the conduction current only slightly, so that the refractive index can be described by the approximate formula

$$n^2 \approx 1 - \frac{\gamma}{x}. \tag{17}$$

Following [7], we assume that expression (17) is valid at the boundary of the resonance zone.[5] This assumption makes it possible to estimate the width of the resonance zone in the general case. In particular, the resonance zone is broad when

$$\delta \gg (\gamma + 1)^{-1}, \tag{18}$$

in which case its width is estimated as

$$\Delta x_r \approx \Delta x_1 \approx \delta^2\left(1 + \frac{\gamma}{\delta^2}\right)^{1/3}.$$

In the limit opposite to inequality (18), the resonance zone is narrow and its width is approximately equal to

$$\Delta x_r \approx \Delta x_2 \approx \delta.$$

3.2. Broad Resonance Zone

Using Eqs. (6) and (8), we can show that, when inequality (18) corresponding to a broad resonance zone is satisfied, the local structure of an electromagnetic wave is independent of the magnetic field nonuniformity. In other words, as in the case of a cold collision-dominated plasma, the wave electric field can be described in the WKB approximation over the entire plasma volume:

$$E = \frac{E_0}{\sqrt{n_T}}\exp\left(-i\int_{-\infty}^{x} n_T(x')dx'\right). \tag{19}$$

Here, the refractive index n_T is the root of the following dispersion relation for an extraordinary wave propagating along a uniform magnetic field in a warm plasma [9]:

$$n_T^2 = 1 - \frac{\omega_p^2}{\omega^2}\int_{-\infty}^{\infty}\frac{F(U)dU}{1 - \frac{\omega_H}{\omega} - n_T U\frac{v_T}{c}}. \tag{20}$$

The spatial distribution of the released energy is also analogous to that in the case of a cold collision-dominated plasma. For $\pi\gamma \ll 1$, the electromagnetic wave over the entire plasma volume is perturbed by the plasma only slightly, $|E| \approx E_0$, and the wave energy is deposited mainly in the resonance zone. In this case, the released energy is distributed uniformly among the bulk electrons, because the power absorbed by a monoenergetic electron flow passing through the resonance zone in a spatially monochromatic electromagnetic field is independent of both the flow velocity and the wavenumber [7]. For $\pi\gamma \gg 1$, the wave field in the resonance zone is weak and the incident wave loses a major fraction of its energy before reaching the resonance zone, i.e., in the region in which the geometrical-optics approximation can be applied, $-\infty \le x \le -\Delta x_r$, and in which the inequality $\mathrm{Im}(n_T) \le \mathrm{Re}(n_T)$ holds. The wave energy is mainly absorbed by fast superthermal electrons whose velocities lie in the range $-\infty < v \le v_T U_0$, where U_0 is the root of the equation

$$\gamma\int_{-\infty}^{U_0} F(U)\frac{dU}{\sqrt{1 + (\gamma/U\delta^2)^{2/3}}} = 1. \tag{21}$$

3.3. Narrow Resonance Zone

As in the hydrodynamic model considered above, the cases of a narrow resonance zone and a broad resonance zone differ insignificantly when the total absorption is weak ($\pi\gamma \ll 1$). In both cases, the plasma currents perturb the wave electric field only slightly. Accordingly, a major fraction of the wave energy is deposited in the resonance zone and the released energy is distributed uniformly among all plasma electrons. The two cases differ radically only when the absorption is strong, $\pi\gamma \gg 1$. Under this condition, the electric field distribution is described by the approximate expression (4) in the limit $d \longrightarrow 0$. By analogy with the case of a cold plasma, the WKB approximation fails to hold already in the region $|x| \le 1/\gamma$, which is far from the resonance zone ($|x| < \Delta x_r = \delta \ll 1/\gamma$). In the region where the WKB approximation is valid, the wave absorption is rather weak. In the region where the WKB approximation fails to hold, the electric field amplitude $|E|$ is nearly constant.[6] An analysis of Eqs. (10) makes it possible to show that, in the region $|x| \le 1/\gamma$, which surrounds the resonance zone, the complex electric-field amplitude is also nearly uniform, $E \simeq$ const. Consequently, the incident wave is mainly absorbed in the resonance zone and the released energy is distributed uniformly among the bulk electrons. Equating the power deposited in the uniform electric field region to the energy flux in the incident wave,

$$P = \pi\frac{e^2E(0)^2L}{2m\omega}\int_{-\infty}^{\infty} f_\parallel(v_\parallel)dv_\parallel \sim \frac{c}{8\pi}E_0^2,$$

we find that the electric field amplitude in the resonance zone is approximately equal to $|E(0)| \approx E_0/\sqrt{\pi\gamma}$. This amplitude coincides, within a numerical factor, with the estimate $|E| \sim E_0/\sqrt{\gamma}$ obtained for the field amplitude at the boundary of applicability of the WKB approximation.

4. CONCLUSION

We have analyzed the propagation of an extraordinary wave in a warm collisionless plasma with a non-

[5] Below, we will show that this assumption is confirmed by a more rigorous analysis of Eqs. (10) with boundary conditions (11) and (12).

[6] Note that, as in the hydrodynamic approach, the refractive index is described by expression (17) in a significant part of this region ($\delta \ll |x| \le 1/\gamma$).

uniform longitudinal magnetic field. The results obtained show that, in a high-density ($\omega_p^2 L \gg \omega c$) plasma with hot electrons such that $(\omega L/c)^3 v_T \gg c(\omega/\omega_p)^4$, the wave power is mainly deposited in a small fraction of superthermal electrons, because the zone where they interact efficiently with the wave field is displaced markedly (due to the Doppler effect) from the ECR point toward the incident wave, i.e., toward the regions where the incident-wave amplitude is larger. The ECR heating of the bulk of the electrons, which is required for efficient operation of an ECR source of multicharged ions, can only be achieved in a colder plasma in which the Doppler effect is insignificant. In this case, the deposition of a major fraction of the wave power occurs in a relatively narrow resonance zone and thus cannot be described in the geometrical-optics approximation. As the field frequency increases (at a fixed value of the ratio ω_p/ω), the temperature, at which the bulk of the electrons stop absorbing the wave field energy, decreases. As a result, we can expect that, with increasing field frequency, the plasma density that is optimum for an ECR source will increase far more gradually than according to the law ω^2.

ACKNOWLEDGMENTS

This work was supported in part by the Russian Foundation for Basic Research, project no. 00-02-17200.

REFERENCES

1. W. Halverson, Y. K. Pu, L. Bromberg, *et al.*, J. Phys. (Paris) **50**, C1-751 (1989).
2. A. V. Turlapov and V. E. Semenov, Phys. Rev. E **57**, 5937 (1998).
3. A. V. Timofeev, in *Reviews of Plasma Physics*, Ed. by B. B. Kadomtsev (Énergoizdat, Moscow, 1985; Consultants Bureau, New York, 1987), Vol. 14.
4. A. V. Timofeev, Fiz. Plazmy **1**, 88 (1975) [Sov. J. Plasma Phys. **1**, 47 (1975)].
5. S. V. Golubev, V. E. Semenov, E. V. Suvorov, and M. D. Tokman, in *Proceedings of the International Conference "Strong Microwaves in Plasmas," 1993*, Ed. by A. G. Litvak (Institute of Applied Physics, Russian Academy of Sciences, Nizhni Novgorod, 1993), Vol. 1, p. 347.
6. A. P. Smirnov, N. V. Suetin, and A. B. Shmelev, Plasma Phys. **59**, 243 (1998).
7. A. F. Kuckes, Plasma Phys. **10**, 367 (1968).
8. E. T. Whittaker and G. N. Watson, *A Course of Modern Analysis* (Cambridge Univ. Press, Cambridge, 1952; Fizmatgiz, Moscow, 1963), Vol. 2.
9. V. L. Ginzburg, *The Propagation of Electromagnetic Waves in Plasmas* (Nauka, Moscow, 1967; Pergamon, Oxford, 1970).

Translated by O. E. Khadin

Plasma Physics Reports, Vol. 27, No. 11, 2001, pp. 938–946. Translated from Fizika Plazmy, Vol. 27, No. 11, 2001, pp. 994–1002.

PLASMA KINETICS

Reduced Models of the Dynamics of Light Impurity Stripping

V. I. Gervids[1], V. I. Kogan[2], and D. Kh. Morozov[2, 3]

[1]*Moscow Institute of Engineering Physics, Kashirskoe sh. 31, Moscow, 115409 Russia*
[2]*Institute of Nuclear Fusion, Russian Research Centre Kurchatov Institute, pl. akademika Kurchatova 1, Moscow, 123182 Russia*
[3]*Permanent address: Instituto de Ciencias Nucleares, 70-543, C.U., UNAM, 04510, Mexico, D.F., Mexico*

Received June 13, 2001

Abstract—"Closed" and "open" reduced models of two or three most abundant light impurity ions in an optically thin hydrogen plasma are considered. The models are shown to satisfactorily describe the average ion charge and radiative losses within a wide range of parameters typical of laboratory and astrophysical plasmas, including the case when the relaxation time of the impurity distribution over ionization states is comparable to or longer than the characteristic times of the most important dynamic processes. The potentialities of the models are demonstrated using the carbon impurity as an example. The models proposed make it possible to analytically study the dynamics of a radiating plasma, obtain qualitatively new results, and significantly reduce the computation time when solving complicated self-consistent dynamical problems. © *2001 MAIK "Nauka/Interperiodica".*

1. INTRODUCTION

This study (or, to be more exact, series of studies) originated from discussions with Vitaliĭ Arkad'evich Abramov (now deceased) of the difficulties in describing impurities when optimizing the divertor of the demonstration ITER tokamak reactor. It turned out that the problem is of much greater importance than was first thought. The behavior of impurities plays a significant role in many problems of laboratory and astrophysical plasmas. The energy balance in the divertor plasma; microfaceted asymmetry of radiation from the edge (MARFE); the effects of impurities on the drift waves, wall turbulence, and L–H transitions in tokamaks; the injection of diagnostic carbon pellets into the stellarator plasma; the filamentation of interplanetary and interstellar clouds; solar prominences; and the propagation of shock waves and nonlinear thermal fronts in astrophysics comprise an incomplete list of the problems in which the description of impurities plays a decisive role (see reviews [1–3] and original papers [4, 5]).

A complete description of an impurity is a rather difficult problem that requires solving a cumbersome set of equations accounting for the ionization and recombination kinetics. Thus, hydrodynamic calculations of the plasma flow in the ITER divertor can take many days of supercomputer operation. Therefore, it is desirable to simplify the problem so that it would be possible not only to reduce the computation time but also to carry out qualitative analytical and combined numerical–analytical studies. It is those studies that would allow one to reveal qualitatively new phenomena. In this way, a new type of waves with dispersion properties similar to those of sound but much slower [6]; the shift of the plasma equilibrium during nonthermodynamic temperature oscillations (such a shift should be observed not only in a radiating plasma, but also in any system with properties determined by the balance between threshold and nonthreshold processes) [7]; and rarefaction shock waves with a pressure behind the front lower than that ahead of it (which are forbidden in classical gas dynamics) [8] were predicted to exist in a radiating plasma.

The problem is substantially simplified assuming the coronal equilibrium (see, e.g., review [9]). In this case, the impurity parameters (including such an important characteristic as radiative losses) were calculated by many authors for almost all the elements in the periodic table (see [10, 11]). That is why most of the studies of the radiating plasma stability were carried out in the coronal equilibrium approximation.

At the same time, the distribution of impurities over ionization states is known to be quite inertial (see, e.g., [12]). Therefore, under strong convection typical of the tokamak periphery, impurities are very far from coronal equilibrium and the radiative losses are very different from those at equilibrium. A similar situation also occurs in studying the instabilities in which radiative losses play an important role. With allowance for the dynamics of the impurity distributions, the stability conditions and the instability growth rates turn out to be quite different from those obtained using the simple assumption that the impurity behavior adiabatically follows the change in the electron temperature [12, 13].

The aforesaid has stimulated the development of a simplified impurity theory in recent years.

For heavy impurities (iron, chromium, vanadium, etc.) characterized by the small difference in the properties of the neighboring ionization states, the distribu-

1063-780X/01/2711-0938$21.00

tion over ionization states can be described by a Gaussian function whose parameters are described by simple dynamic equations [14, 15].

However, for light impurities, which play a major role in modern tokamaks, no approximations of this kind are available. Unlike heavy impurities, light impurities differ substantially in the ionization and recombination rates of ions in the neighboring ionization states. Therefore, some authors (including the authors of the present paper) proposed models describing the impurity in terms of the two or three most abundant ions.

Such an approach was first proposed in [16] for calculating the transition time between two neighboring ionization states. The dynamic models for the two or three most abundant ions were discussed and justified in [17–20]. The employment of this simplified approach (unfortunately, without proper justification and estimating the limits of applicability) has already provided a number of qualitatively new results in the theory of the radiating plasma stability [12, 13].

In contrast to [17–20], where only "closed" models, in which the sum of the relative densities of the most abundant ions is exactly equal to unity, were discussed, we consider here both closed and open models. The plasma with a light impurity is described in a form convenient for computer simulations and analytic calculations. Different models for the processes with characteristic times comparable to or shorter than the typical relaxation time of the impurity distribution over ionization states are compared. Calculations are carried out based on modern atomic data [21].

This paper is organized as follows. In Section 2, the two-ion closed model is discussed and the basic dynamic equations are derived. In Section 3, the radiative losses during high-frequency oscillations and sharp jumps in the electron temperature are calculated. The results obtained are compared with those predicted by the exact seven-ion model. Section 4 presents the results obtained with the open three-ion model for the same quantities as in Section 3. In the Conclusion, the potentialities of all the reduced models are discussed and compared to each other. In the Appendix, a summary of the formulas for calculating the rates of all the basic processes for carbon is presented together with the tables of the parameters needed for practical applications. The formulas are given in a form ready for direct employment: searching for literature data on such quantities as oscillator strengths or quantum numbers is necessary.

2. CLOSED TWO-ION MODEL

As was mentioned above, the time during which the impurity relaxes to the equilibrium distribution over ionization states is often greater than the typical hydrodynamic times. Thus, for the temperature $T_e = 8$ eV and the carbon impurity, which are typical of the tokamak divertor plasma, the doubly charged CIII ion is one of the most abundant ions. At the electron density $n_e = 10^{13}$ cm^{-3}, its ionization time is on the order of 10^{-2} s. The velocity of the plasma flow in the divertor can be on the order of the speed of sound, which is $\sim 3 \times 10^6$ cm/s at the given temperature. Hence, over the ionization time, a doubly charged ion can travel a distance on the order of several meters, which exceeds the major radius of a modern tokamak. The typical ionization time is also greater than the typical period of plasma oscillations at the tokamak periphery.

For this reason, attention should be mainly focused on the *dynamics* of the distribution of impurities over ionization states. This dynamics is determined by the structure of the *time-dependent* coronal equations. The dependence on time significantly complicates the mathematical problem to be solved by the reduced models proposed. As in [17], we will not simplify the problem with respect to the spatial properties by, e.g., reducing it to the one-dimensional problem or assuming the diffusion approximation.

First, we consider the approximation of the two most abundant ions. Let the ion charge numbers be z and $z + 1$. A distinctive feature of closed models is the requirement that the normalization condition

$$y_z + y_{z+1} = 1 \tag{1}$$

be satisfied. Here, $y_z = n_z / \sum_k n_k$ is the relative density of the ions with charge number z, n_k is the density of the ions with charge number k, and $\sum_k n_k = n_I$ is the total density of the impurities. In open models, this condition may fail to hold to a small extent. In view of condition (1), the impurity distribution over ionization states is described by a single equation in the Lagrange variables,

$$\frac{dy_z}{dt} = n_e[R_{z+1} - (J_z + R_{z+1})y_z], \tag{2}$$

where n_e is the electron density; J_z and R_z are the ionization and recombination rates, respectively; $dy_z/dt = \partial y_z/\partial t + \mathbf{v}_z \cdot \nabla y_z$; and $\mathbf{v}_z$ is velocity of the ion species. As is shown in [18], the ion velocity is only slightly affected by the ion charge. Therefore, the impurity can be completely described by simply adding the hydrodynamic equations for the total impurity density and the overall ion velocity.

The charge number z of the most abundant ion can be easily determined only for the coronal equilibrium [17]. If the plasma is highly nonequilibrium, then this charge should be determined by solving dynamic equations. For the closed two-ion model, the equation for the average ion charge number,

$$\langle z \rangle = z + 1 - y_z, \tag{3}$$

can be derived by substituting formula (3) into Eq. (2):

$$\frac{d\langle z\rangle}{dt} = -\nu_z(\langle z\rangle - z_*). \quad (4)$$

Here, $\nu_z = n_e(J_z + R_{z+1})$ and $z_* = z + 1 - \dfrac{R_{z+1}}{J_z + R_{z+1}}$ is the approximate value of the equilibrium charge number from the two-ion model. Physically, it is evident that the results would be more precise if the equilibrium average charge number calculated at the given temperature by the exact (seven-ion) model is taken as z_*. The average charge number calculated by the exact model depends exclusively on the electron temperature and is not affected by the history of the process. Hence, it can be calculated analytically, once and for all, for any element from the periodic table. However, because of the awkwardness of the formulas derived, it is reasonable to use an approximated expression presented in the Appendix for carbon.

For the reverse transition from $\langle z\rangle$ to y_z by formula (3), the value of z must be calculated as the integer part of $\langle z\rangle$. In this case, the relative density is given by the expressions

$$y_k = \begin{cases} z + 1 - \langle z\rangle & \text{for} \quad k = z \\ \langle z\rangle - z & \text{for} \quad k = z + 1 \\ 0 & \text{in all the remaining cases.} \end{cases} \quad (5)$$

Obviously, when more than two ion species are present in the plasma, these equations only qualitatively describe the behavior of the relative densities. As will be shown in the next section, these equations are quite sufficient for describing the averaged impurity characteristics, such as the total radiative losses. If a more precise description of the relative densities is required, then the following iterative procedure can be proposed. In the coronal model, the relative density y_z is governed by the "exact" equation of the form

$$\frac{dy_z}{dt} = n_e(J_{z-1}y_{z-1} + R_{z+1}y_{z+1} - (J_z + R_z)y_z), \quad (6)$$

which can be solved with respect to y_z in terms of quadratures:

$$y_z = \exp\left(-\int_0^t (J_z + R_z)dt'\right)\left(y_z(t=0) + \int_0^t (R_{z+1}y_{z+1} + J_{z-1}y_{z-1})\exp\left(\int_0^{t'} (J_z + R_z)dt''\right)dt'\right). \quad (7)$$

At each iteration step, the relative density from the preceding step must be substituted into the integrand.

Being more cumbersome than the two-ion model, the closed three-ion model provides no remarkable increase in accuracy [20, 22] and will not be discussed here.

3. NUMERICAL CALCULATIONS AND THE VALIDITY OF THE MODEL

To test the validity of the reduced models, we performed calculations of the radiative losses at a given temporal behavior of the electron temperature within the temperature ranges that are the least favorable for the model's validity. It was assumed that the impurity density was fairly low and that the degree of its ionization did not affect the electron density. The results obtained were compared with those from the complete seven-ion model. The electron-impact excitation and ionization, spontaneous radiative decay, photorecombination, and dielectronic recombination were taken into account. When calculating dielectronic recombination, five transitions were taken into account, which is more than in the previous studies (see, e.g., [11]). The exact equilibrium value of $\langle z\rangle$ at the initial temperature was taken as the initial condition.

First, we considered the oscillations of the electron temperature in the range $5 \le T_e \le 15$ eV. The electron density was taken to be 10^{13} cm^{-3}. The time dependence of T_e was approximated by the formula $T_e = T_0(1 + a\sin(2\pi\nu t))$. We note that as many as four different ions can be simultaneously present in the plasma in an appreciable amount within the above temperature range. Clearly, in this case, the two-ion model cannot accurately describe the distribution of all the ions over ionization states.

However, the radiative losses calculated as the sum of the contributions from individual ions ($Q = n_e n_I \sum_z y_z L_z(T)$) are described quite satisfactorily. In this case, even qualitative agreement could hardly be expected, because, in addition to the large number of ion species present, the transition in this temperature range occurs from the most abundant ion with $z = 3$ to that with $z = 4$. The radiation intensity of the latter ion is lower by at least one order of magnitude. Nevertheless, as is seen in Fig. 1, which shows the total carbon radiation intensity L, even the simplest two-ion model enables a qualitatively correct description of the radiation behavior. The discrepancy between the two-ion and seven-ion models is no higher than 50%. The two-ion model quite accurately describes the decrease in the time averaged level of radiative losses related to the effect of the equilibrium shift [7]. Note that the seven-ion model can also produce an error of the same order of magnitude because of the insufficient accuracy of the available data on the rates of elementary processes.

The computer time required for numerical calculations by the two-ion model is reduced by at least a factor of 4–5 as compared to the seven-ion model. Thus, the use of the two-ion model provides a significant reduction in the computer-time consumption when solving complex self-consistent problems.

Now, let the temperature rapidly increase over a characteristic time much shorter than the impurity relaxation time. Such a situation is perhaps most inter-

esting for practical applications, because the carbon evaporated from the divertor plate or a diagnostic pellet [23, 24] is usually carried to the high-temperature region. We can expect that the reduced models adequately describe the impurity behavior after an abrupt increase in temperature. In fact, upon a temperature jump, the two or three ion species that are most abundant at the initial time begin to ionize rapidly. As is known, the ionization rate is much higher for ions with a smaller charge. Hence, the initial impurity distribution over ionization states narrows (rather than spreads out) and shifts towards higher z. These considerations are confirmed by the results of calculations shown in Figs. 2 and 3. The time dependence of the temperature was chosen in the form $T_e(t) = (T_{\text{fin}} - T_{\text{in}})(2/\pi)\arctan(t/\tau) + T_{\text{in}}$, where T_{in} and T_{fin} are the initial and final temperatures, respectively. The characteristic rise time of the temperature $\tau = 10^{-6}$ s was chosen to be much less than the characteristic impurity relaxation time. The initial and final temperatures were assumed to be equal to $T_{\text{in}} = 3$ eV and $T_{\text{fin}} = 50$ eV, respectively. The initial distribution over ionization states coincided with the equilibrium one at the initial temperature. It is seen in Fig. 2, which presents the results from the seven-ion model, that no more than two or three ion species with consecutive charges are present simultaneously in the plasma. Therefore, the impurity can actually be described by the two or three most abundant ions.

When calculating radiative losses, difficulties similar to those in the previous case emerge. The model adequately describes ion radiation in the initial and intermediate stages. Later, when the density of the $z = 3$ ions decreases significantly (Fig. 3), the description turns out to be unsatisfactory. Since the $z = 4$ ion radiation is weak, it is the density of the $z = 3$ ions that governs the radiative losses. This is often unimportant because radiative losses themselves become low and, hence, the energy balance is determined by other losses (e.g., heat conduction). If, for some reason, radiative losses are nevertheless important, then the appropriate accuracy can be achieved by slightly correcting the model. Since recombination is of no importance here and the temperature changes only slightly on such long time scales, we can conclude that the density of the $z = 3$ ions decays exponentially to the equilibrium value upon the complete (according to the two-ion model) disappearance of the $z = 2$ ions. In this case, the function y_3 can be represented in the form

$$y_3 = \begin{cases} 0 & \text{for} \quad \langle z\rangle \le 2 \\ \langle z\rangle - 2 & \text{for} \quad 2 \le \langle z\rangle \le 3 \\ \exp\{-n_e J_3 (t - t_0)\} + R_4/J_3 & \text{for} \quad \langle z\rangle \ge 3. \end{cases}$$

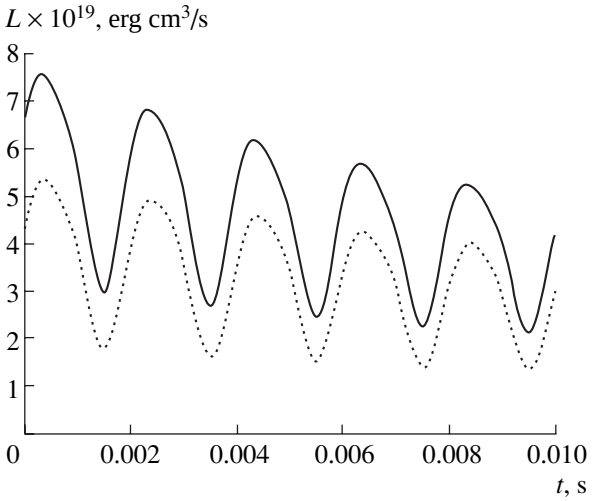

Fig. 1. Time evolution of the specific (divided by both the electron and impurity densities) power $L = Q/n_e n_I$ [erg cm^3/s] of carbon line radiation during temperature oscillations at a frequency of 500 Hz within the range 5–15 eV. The solid and dotted curves show the calculations by the two-ion and seven-ion models, respectively.

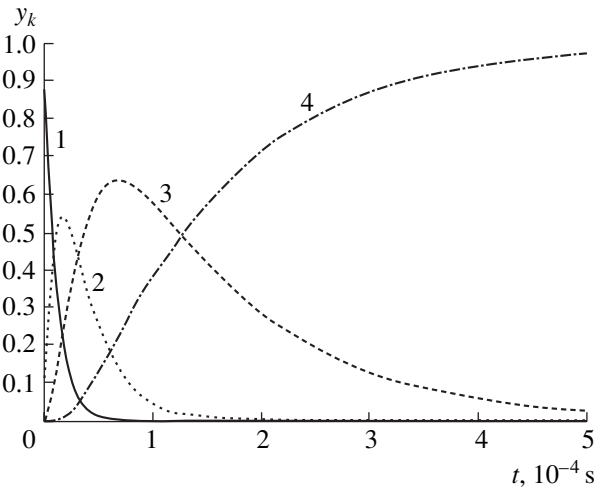

Fig. 2. Time evolution of the relative densities of carbon ions upon the temperature jump from 3 to 50 eV; calculations by the seven-ion model. The numerals by the curves show the ion charge numbers.

Here, t_0 denotes the instant at which y_3 approaches unity in the two-ion model. The results obtained with the corrected model are shown in Fig. 4.

A different situation arises with a jumplike drop in the temperature, which, fortunately, is rare in actual practice. Since the recombination rate varies much more slowly with the temperature than with the ionization rate, the distribution over ionization states spreads out. Figure 5 presents the relative ion densities calculated from the seven-ion model. It can be seen in the figure that, if only the ions with the charge numbers $z = 5$ and 6 and a small admixture of the $z = 4$ ions are present

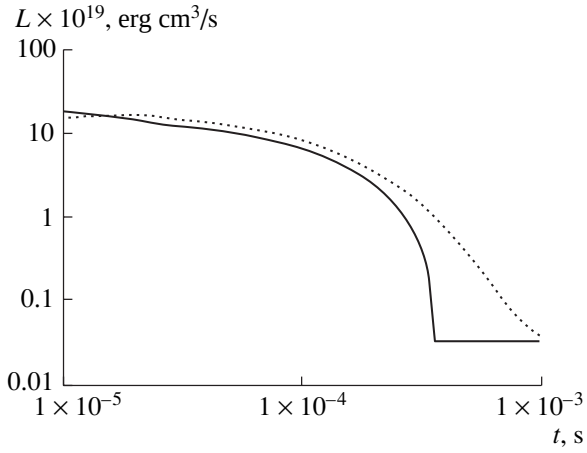

Fig. 3. Time evolution of the specific power of the carbon impurity line radiation upon the temperature jump from 3 to 50 eV; calculations by the two-ion (solid curve) and seven-ion (dotted curve) models.

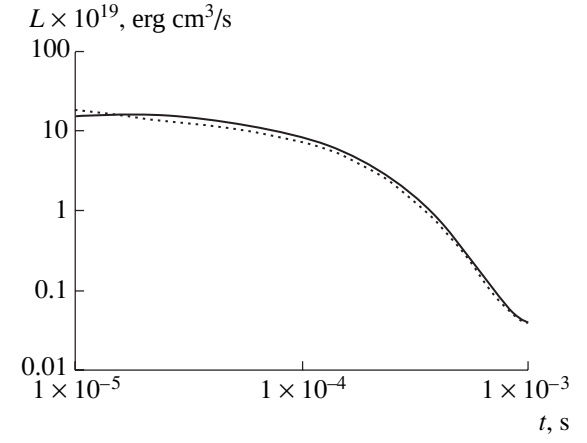

Fig. 4. Same as in Fig. 3, but for the improved two-ion model.

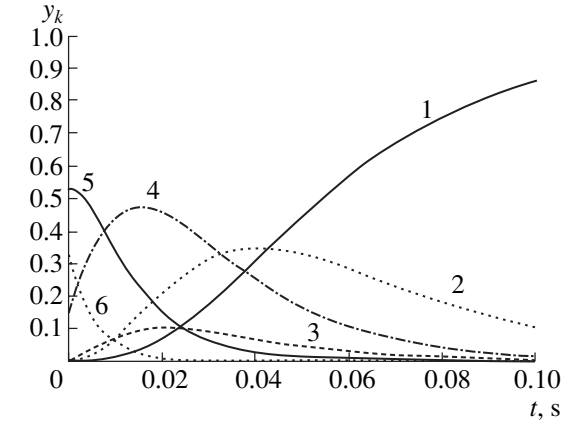

Fig. 5. Time evolution of the relative densities of carbon ions upon the temperature jump from 100 to 2 eV; calculations by the seven-ion model. The numerals by the curves show the ion charge numbers.

in the plasma at the initial time, then four or even five ion species will subsequently be present.

The above difficulties are successfully overcome within the open three-ion model. Although the model is more complicated than the closed two-ion model, it is still substantially simpler than the seven-ion model.

4. OPEN THREE-ION MODEL

An advantage of the open three-ion model over the closed two-ion model is that it almost exactly (rather than qualitatively) describes both the radiation intensity and the relative densities of the impurity ions. The price to be paid for the increase in accuracy is the complication of the model and, hence, an increase in the computation time, which nevertheless remains less than that with the seven-ion model.

Within the exact seven-ion model, the three successive most abundant ions obey the following set of equations:

$$\begin{aligned}
\frac{dy_{z-1}}{dt} &= n_e(R_z y_z + J_{z-2} y_{z-2} - (R_{z-1} + J_{z-1}) y_{z-1}),\\
\frac{dy_z}{dt} &= n_e(J_{z-1} y_{z-1} + R_{z+1} y_{z+1} - (R_z + J_z) y_z), \qquad (8)\\
\frac{dy_{z+1}}{dt} &= n_e(J_z y_z + R_{z+2} y_{z+2} - (R_{z+1} + J_{z+1}) y_{z+1}).
\end{aligned}$$

The relative densities of the $y_{z\pm2}$ satellites entering these equations are low and can be estimated as follows.

As the temperature increases, the ions with charge number $z-2$ burn out most rapidly. The characteristic time during which they disappear is much less than the time during which the densities of the most abundant ions change. Therefore, the ions have time to come into equilibrium with the $z-1$ ions:

$$y_{z-2} = \frac{R_{z-1}}{J_{z-2}} y_{z-1} \quad \text{for} \quad \frac{dT}{dt} > 0. \qquad (9)$$

As the temperature increases, the relative density y_{z+2} is found from the normalization condition.

For a decreasing temperature, such an approximation is incorrect. However, in this case, the density of the $z-2$ ions can be found from the normalization condition. The $z+2$ ions are in approximate equilibrium with the $z+1$ ions in the same manner as the $z-2$ ions were in equilibrium with the $z-1$ ions as the temperature increased. This equilibrium is less exact because the recombination rate depends less strongly on z than the ionization rate.

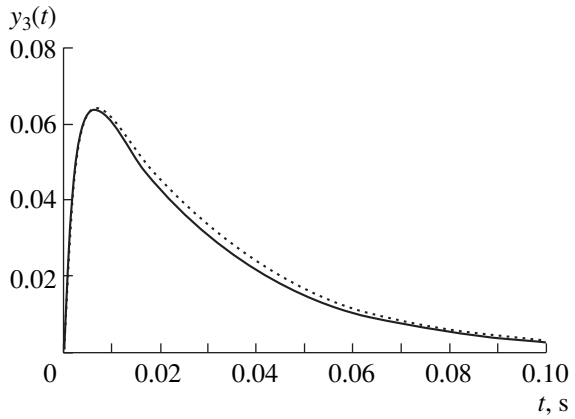

Fig. 6. Time evolution of the relative density of lithium-like carbon ions upon the temperature jump from 50 to 3 eV; calculations by the open three-ion (solid curve) and exact seven-ion (dotted curve) models.

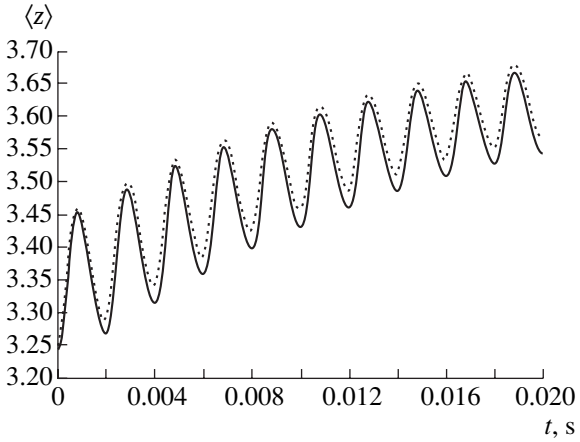

Fig. 7. Time evolution of the average charge number of carbon ions during temperature oscillations at a frequency of 500 Hz within the range 5–15 eV. The solid and dotted curves show the calculations by the open three-ion and exact seven-ion models, respectively.

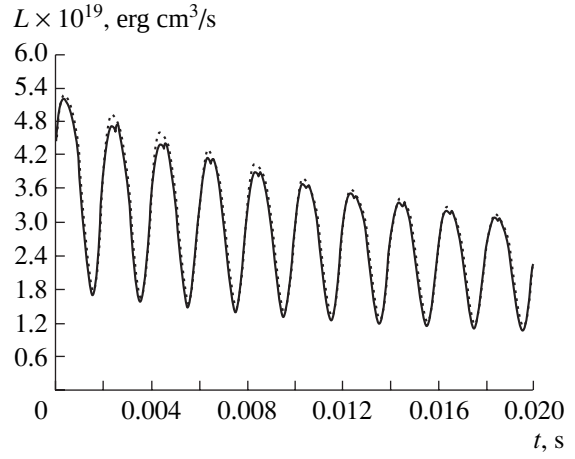

Fig. 8. Time evolution of the specific power of the carbon impurity radiation L during temperature oscillations at a frequency of 500 Hz within the range 5–15 eV. The solid and dotted curves show the calculations by the open three-ion and exact seven-ion models, respectively.

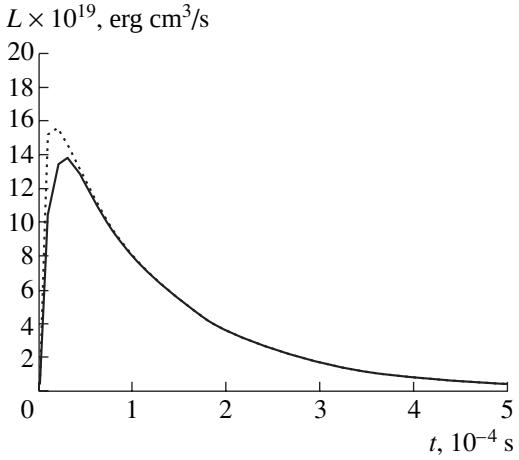

Fig. 9. Same as in Fig. 8, but for the temperature jump from 3 to 50 eV.

Finally, we obtain

$$y_{z-2} = \begin{cases} \dfrac{R_{z-1}}{J_{z-2}} y_{z-1} & \text{for} \quad \dfrac{dT}{dt} > 0 \\ 1 - y_{z-1} - y_z - y_{z+1}\left(1 + \dfrac{J_{z+1}}{R_{z+2}}\right) & \text{for} \quad \dfrac{dT}{dt} < 0, \end{cases} \tag{10}$$

$$y_{z+2} = \begin{cases} \dfrac{J_{z+1}}{R_{z+2}} y_{z+1} & \text{for} \quad \dfrac{dT}{dt} < 0 \\ 1 - y_{z-1} - y_z - y_{z+1}\left(1 + \dfrac{R_{z-1}}{J_{z-2}}\right) & \text{for} \quad \dfrac{dT}{dt} > 0. \end{cases} \tag{11}$$

Expressions (10) and (11) in combination with Eqs. (8) form a closed set of equations for the open three-ion model. The charge number of the most abundant ion z can be found as the integer closest to the quantity $\langle z \rangle = \sum_{z-2}^{z+2} k y_k$. In fact, the set takes into account five rather than three ion species. Therefore, if the temperature range is not too wide, the value of z can be determined, as in the case of the coronal equilibrium (see Introduction). Calculations show that, since five ion species are actually taken into account, we can almost always assume that $z = 3$ for carbon within the temperature range $2 \le T_e \le 50$ eV.

The results of calculations by the open three-ion model are presented in Figs. 6–10. The initial relative

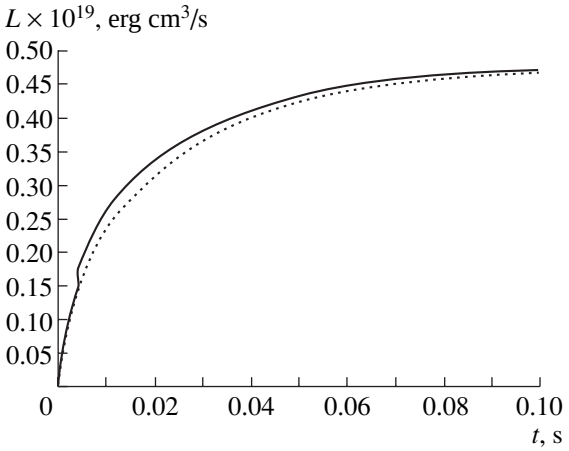

Fig. 10. Same as in Fig. 8, but for the temperature jump from 50 to 3 eV.

densities are equal to those at the coronal equilibrium at the initial temperature. It can be seen in Figs. 6–10 that the open three-ion model and the exact seven-ion model provide almost identical results.

Table 1

z	$K_z \times 10^8$	ΔE_{iz}
0	47.57	11.26
1	10.98	24.384
2	11.18	47.89
3	4.153	64.49
4	1.366	392.09
5	0.5466	489.997

Table 2

z	r_1	r_2	r_3
1	12.67	0.815	0.091
2	11.87	0.725	0.099
3	11.42	0.695	0.081
4	11.11	0.660	0.080
5	10.81	0.615	0.058
6	10.57	0.600	0.041

Table 3

z	R_z^0	R_z^1	R_z^2	R_z^3	R_z^4
1	2.555	2.756	12.08	9.087	3.360
2	52.41	23.88	4.997	3.188	5.183
3	30.21	44.87	14.90	6.826	3.731
4	382.2	81.39	30.65	14.85	8.400
5	378.9	70.13	25.40	12.10	6.767

In a similar way, it is possible to develop the open two-ion model, in which the accuracy and computation time are between those for the closed two-ion and open three-ion models.

5. CONCLUSION

We have proposed various types of the reduced models describing impurities in a hydrogen plasma. The models are tested within the temperature range that is the least favorable for their validity. The calculations performed allow us to draw the following conclusions.

(i) The closed model is attractive because of its exceptional simplicity, which makes it possible to use this model in analytical calculations. The model reduces the computation time by a factor of 4–5 as compared to the complete seven-ion model. For electron temperature oscillations in the range 5–15 eV and for a rapid (in a time on the order of 10^{-6} s) increase in the temperature from 3 to 50 eV, the model provides a qualitatively correct description of the behavior of the relative densities of various ions. For the average charge number and radiative losses, the model even provides a good quantitative description.

When the temperature drops rapidly from 100 to 2 eV, the closed two-ion model turns out to be inapplicable. In this connection, an iterative procedure is proposed that allows one to calculate all the impurity parameters with reasonable accuracy. Within a narrower temperature range, it qualitatively describes the impurity behavior even without iterations.

(ii) The open model is more complicated than the closed two-ion model and, thus, is difficult to apply to analytical calculations. However, the model offers a very high accuracy in all of the cases under consideration. Although the computation time is somewhat longer than for the closed two-ion model, it remains substantially less than for the seven-ion model.

Of course, the models proposed are not universal. The choice of one of them is dictated by the expected temperature ranges and by the requirements for the computation accuracy and computer-time consumption.

ACKNOWLEDGMENTS

This study was supported by the grants CONACyT 29250-E and DGAPA IN105100, Mexico.

APPENDIX

Here, we present the rates of elementary processes taken into account in the coronal model, as well as the radiation intensities of the individual carbon ions in a form convenient for practical applications. The approximate formula for z_*, which is useful for calculations by the closed model, is also presented. The formulas were derived by substituting the principal quantum numbers,

the numbers of the equivalent electrons, the oscillator strengths, etc., into the expressions from review [9]. Recall that the corresponding formulas in [9] were obtained for a Maxwellian electron distribution. The oscillator strengths and the transition energies were taken from the most recent publication on the subject [21]. Below, the temperature and energies are in eV and the ionization and recombination rates are in cm^3/s; z is the charge of the ionized or recombining ion.

The ionization rates are expressed in terms of the integral exponent Ei (or $E_1(x)$ in the notation of [25]):

$$J_z(T_e) = K_z T_e^{-1/2} \mathrm{Ei}\left(\frac{\Delta E_{iz}}{T_e}\right).$$

The coefficients K_z and the ionization energies ΔE_{iz} are listed in Table 1.

The recombination rate R_z is the sum of the conventional photorecombination rate R_z^{ph} and the dielectronic recombination rate R_z^d:

$$R_z = R_z^{ph} + R_z^d.$$

The latter process is only possible for ions that had one or more electrons prior to recombination.

For *photorecombination*, the results of the available numerical calculations within the electron temperature range 1–100 eV are approximated with an accuracy of no less than 2.5% by the formula $R_1^{ph} = 10^{-r_1 - r_2 x - r_3 x^2}$, where $x = \log T_e$ [eV]. The coefficients r_1, r_2, and r_3 are listed in Table 2.

The rate of *dielectronic recombination* R_z^d is calculated by the formula

$$R_z^d = 10^{-10} T_e^{-3/2} \sum_{k=0}^{4} R_z^k \exp\left(-\frac{\Delta E_z^k}{T_e}\right),$$

which accounts for five transitions. The constants R_z^k and ΔE_z^k are listed in Tables 3 and 4.

Overall radiation of the impurity is the sum of the contributions from individual ions, $Q = n_e \sum_z n_z L_z(T_e)$. Within the temperature range $3 \le T_e \le 100$ eV, the results of numerical calculations of the L_z functions are fitted by the formula [26]

$$L_z(T_e) = 10^{-19} L_0 T_e^{a(z)} \exp(-b(z)/T_e), \ \mathrm{erg\ cm^3\ s^{-1}},$$

with an accuracy of no less than 5%. The parameters L_0, a, and b are listed in Table 5.

In order to employ the *closed model*, it is necessary to know the value of z_*. As was mentioned above, this value can be calculated analytically. However, it is sometimes more convenient to employ an approximate formula rather than the cumbersome exact expression. This is justified even more because of the limited accuracy of the available data on the rates of the main processes.

Table 4

z	ΔE_z^0	ΔE_z^1	ΔE_z^2	ΔE_z^3	ΔE_z^4
1	9.281	11.964	13.717	18.049	20.84
2	12.692	32.11	38.43	39.98	42.56
3	8.004	39.68	50.62	55.65	58.37
4	307.901	354.518	370.92	378.53	382.67
5	367.536	435.612	459.420	470.456	476.39

Table 5

z	0	1	2	3	4	5
L_0	21.0	18.6	35.0	31.5	0.22	0.025
a	–0.1	–0.05	–0.1	–0.2	0.66	0.85
b	5.8	11.0	11.5	8.1	242.0	290.0

At temperatures $T_e \ge 2$ eV, the expression

$$z_* \approx 6 - 2.8\exp(-8.0 \times 10^{-4} T_e^{3.25}) - 2.13\exp(-2.5 \times 10^{-8} T_e^{3.8})$$

gives the z_* value with an accuracy of no less than ≈10%.

REFERENCES

1. B. Lipshultz, J. Nucl. Mater. **145–147**, 15 (1987).
2. B. Meerson, Rev. Mod. Phys. **68**, 215 (1996).
3. D. Kh. Morozov and J. J. E. Herrera, Fiz. Plazmy **24**, 379 (1998) [Plasma Phys. Rep. **24**, 347 (1998)].
4. R. R. Domingues and G. M. Stabler, Nucl. Fusion **33**, 51 (1993).
5. M. Tokar, Phys. Rev. Lett. **84**, 895 (2000).
6. D. Kh. Morozov and J. J. E. Herrera, Phys. Rev. Lett. **76**, 760 (1996).
7. V. I. Gervids and D. Kh. Morozov, Pis'ma Zh. Éksp. Teor. Fiz. **67**, 308 (1998) [JETP Lett. **67**, 324 (1998)]; Fiz. Plazmy **25**, 242 (1999) [Plasma Phys. Rep. **25**, 217 (1999)].
8. D. Kh. Morozov and M. Pekker, Phys. Rev. E **64**, 16416 (2001).
9. V. I. Gervids, A. G. Zhidkov, V. S. Marchenko, and S. I. Yakovlenko, in *Reviews of Plasma Physics*, Ed. by M. A. Leontovich and B. B. Kadomtsev (Énergoatomizdat, Moscow, 1982; Consultants Bureau, New York, 1987), Vol. 12.
10. V. I. Gervids and V. I. Kogan, Pis'ma Zh. Éksp. Teor. Fiz. **21**, 329 (1975) [JETP Lett. **21**, 150 (1975)].

11. D. F. Post, R. V. Jensen, C. B. Tarter, *et al.*, At. Data Nucl. Data Tables **20**, 397 (1977).
12. S. I. Krasheninnikov, D. Kh. Morozov, and D. J. Sigmar, Contrib. Plasma Phys. **36**, 271 (1996).
13. D. Kh. Morozov and S. I. Krasheninnikov, in *Proceedings of the International Conference on Plasma Physics, Magoya, Japan, 1996*, Ed. by H. Sugai and T. Hayashi, Vol. 1, p. 626.
14. V. V. Ivanov, A. B. Kukushkin, and V. S. Lisitsa, Fiz. Plazmy **13**, 1341 (1987) [Sov. J. Plasma Phys. **13**, 774 (1987)].
15. A. B. Arutyunov, S. I. Krasheninnikov, and D. Yu. Prokhorov, Fiz. Plazmy **17**, 1150 (1991) [Sov. J. Plasma Phys. **17**, 668 (1991)].
16. Yu. I. Galushkin, V. I. Gervids, and V. I. Kogan, in *Proceedings of the 4th International Conference on Plasma Physics and Controlled Nuclear Fusion Research, Madison, 1971* (IAEA, Vienna, 1971), Vol. 2, p. 271.
17. V. I. Gervids and D. Kh. Morozov, Fiz. Plazmy **26**, 470 (2000) [Plasma Phys. Rep. **26**, 439 (2000)].
18. D. Kh. Morozov, V. A. Rozhansky, J. J. E. Herrera, and T. K. Soboleva, Phys. Plasmas **7**, 1184 (2000).
19. D. Kh. Morozov and V. I. Gervids, in *Proceedings of the International Conference "Astrophysical Plasmas: Codes, Models, and Observations," Mexico-city, Mexico, 1999*; Rev. Mex. Astron. Astrofis., Ser. Conf. **9**, 131 (2000).
20. D. Kh. Morozov, V. I. Gervids, O. Garcia R. O., in *Proceedings of the 27th EPS Conference on Controlled Fusion and Plasma Physics, Budapest, Hungary, 2000*, ECA, Vol. 24B, p. 712.
21. D. A. Verner, E. M. Verner, and G. J. Ferland, At. Data Nucl. Data Tables **64**, 1 (1996).
22. D. Kh. Morozov, J. J. E. Herrera, and V. I. Gervids, Contrib. Plasma Phys. **38**, 278 (1998); V. I. Gervids and D. Kh. Morozov, Fiz. Plazmy **25**, 242 (1999) [Plasma Phys. Rep. **25**, 217 (1999)].
23. D. E. Post, B. Braams, and N. Putvinskaya, Contrib. Plasma Phys. **36**, 240 (1996).
24. G. Pautasso, K. Bücl, J. C. Fuchs, *et al.*, Nucl. Fusion **36**, 1291 (1996).
25. *Handbook of Mathematical Functions*, Ed. by M. Abramowitz and I. A. Stegun (Dover, New York, 1971; Nauka, Moscow, 1979).
26. D. Kh. Morozov, J. J. E. Herrera, and V. I. Gervids, Contrib. Plasma Phys. **38**, 278 (1998).

Translated by N. N. Ustinovskiĭ

Plasma Physics Reports, Vol. 27, No. 11, 2001, pp. 947–952. Translated from Fizika Plazmy, Vol. 27, No. 11, 2001, pp. 1003–1008.

PLASMA DYNAMICS

Generation of *K*-shell Radiation in a Double Shell Plasma Liner with a Microsecond Current Generator

S. A. Chaikovsky and S. A. Sorokin

Institute of High-Current Electronics, Russian Academy of Sciences, Siberian Division, Akademicheskiĭ pr. 4, Tomsk, 634055 Russia

Received May 29, 2001

Abstract—Experiments on the generation of *K*-shell radiation in a double-shell neon liner with a microsecond current generator ($\tau \approx 1$ μs, $I_{max} = 380$ kA) are described. The yield of neon *K*-shell radiation attains 50–80 J per pulse. For the given current amplitude, such a radiation yield could be expected at a rise time as low as $\tau \approx$ 100 ns. Such a high radiation efficiency may be attributed to the sharpening of the front of the inner-shell current pulse because of the detachment of the outer shell from the electrode. © *2001 MAIK "Nauka/Interperiodica".*

1. INTRODUCTION

Plasma liners imploding under the action of the magnetic pressure of a high-current pulse are used as sources of high-power pulsed vacuum ultraviolet and soft X radiation. For a number of applications, radiation in the spectral range ≥1 keV is of great interest [1]. This spectral range is associated with radiative transitions of electrons from the *K* shells of ions with atomic numbers $Z \geq 10$.

Let us consider how the conversion efficiency of the liner kinetic energy into *K*-shell radiation depends on the amplitude and rise time of the generator current. The plasma electron temperature corresponding to the maximum intensity of *K*-shell radiation can be estimated from the expression $T_e \approx 0.3Z^{2.9}$ eV [2]. Such plasma temperatures in the final phase of the liner implosion can be achieved if the kinetic energy per ion is higher than the sum of the thermal energy per ion at the electron temperature T_e and energy E_{ion} needed to ionize an atom down to the *K* shell: $(0.5)MV_f^2 > (1.5)(Z_i + 1)T_e + E_{ion}$. Here, *M* is the ion mass, V_f is the final implosion velocity, and Z_i is the ion charge number. Assuming that $Z_i = Z - 1$, the above condition can be rewritten as $0.5MV_f^2 > 1.49Z^{3.51}$ eV/ion [2]. Using the approximate expressions for the ion mass $M \approx 1.58Z^{1.1}m_p$ (where m_p is the proton mass) and the energy of *K*-shell photons $E \approx 10.2Z^2$ eV, we have for the final velocity

$$V_f\,(\text{cm/s}) > V_{min} = 1.34 \times 10^6 Z^{1.2} \approx 0.33 \times 10^6 E^{0.6}. \quad (1)$$

It follows from here that, for the generation of *K*-shell radiation in the range $E > 1$ keV, the final implosion velocity should be higher than 2×10^7 cm/s. For simplicity, we assume that the generator current pulse has a pronounced maximum. For the generator energy to be efficiently converted into the liner kinetic energy, the liner implosion should occur when the generator current approaches its maximum; i.e., the condition $\tau_{imp} \approx \tau$ must be satisfied, where τ_{imp} is the implosion time (the time interval from the beginning of the generator current to the instant of maximum compression), and τ is the rise time of the generator current. Then, we have $V_f \propto r_0/\tau_{imp} \approx r_0/\tau$.

For an optically transparent plasma under conditions when the radiative cooling time is longer than the plasma inertial confinement time τ_{conf}, the radiation yield per unit length of the liner can be estimated as $Y \propto K(T_e)n_f^2 r_f^2 \tau_{conf}$, where n_f and r_f are the final density and radius of the liner, respectively, and $K(T_e)$ is a function of the electron temperature. The kinetic energy per unit length is equal to $E_k = 0.5\ mV_f^2 \propto I_{max}^2 \ln(r_0/r_f)$, where *m* is the liner mass per unit length, and I_{max} is the maximum generator current. Using the expressions $\tau_{conf} \propto r_f/V_f$ and $V_f \propto r_0/\tau$, we obtain for the efficiency

$$Y/E_k \propto K(T_e) I_{max}^2 (r_0/r_f)\ln(r_0/r_f)/V_f^6\tau\,. \quad (2)$$

This expression is invalid when the *K*-shell radiation yield *Y* is comparable to E_k. In this case, the efficiency is nearly constant and is primarily determined by the radiative losses in the lower photon energy range, and the radiation yield is proportional to the square of the current I_{max} (see, e.g., [3]).

The final velocity is given by condition (1). We neglect the dependence of the yield on the electron temperature T_e, assuming the temperature to be a function of the final velocity. The radial compression ratio (r_0/r_f) is limited by the onset of instabilities in the course of implosion. An analysis of the experimental results shows that, for generators with $\tau \approx 100$ ns at $r_0 \approx$ (1–2.5) cm, the radial compression ratio is 10–20 for final implo-

1063-780X/01/2711-0947$21.00

sion velocities higher than 2×10^7 cm/s. To reach a final velocity higher than 2×10^7 cm/s by using generators with $\tau \approx (0.5–2)$ μs, it is necessary that the initial radius be $r_0 > 3$ cm. In experiments [4–7], in which the initial radius was 5–7 cm and $\tau \approx 0.5–2$ μs, the radial compression ratio also was 10–20. Hence, we can assume that r_0/r_f depends weakly on τ [or on the initial liner radius at the final velocity given by condition (1)] and can be put in (2) r_0/r_f = const. Finally, at I_{max} = const, we have

$$Y/E_k \propto 1/\tau. \quad (3)$$

Hence, it is evident that faster generators are more advantageous from the standpoint of the generation efficiency of *K*-shell radiation.

At present, the fastest generators of megaampere currents have a rise time of $\tau \approx 50–100$ ns. Since the typical time during which energy is output from the primary capacitor storage is ≈1 μs, either water forming lines or intermediate inductive energy storages with plasma opening switches are used to sharpen the current pulse front. Such sharpeners are very expensive and complicated to operate. From the standpoint of decreasing the cost of the *K*-shell radiation source, it is important to develop simpler and less expensive power sharpeners.

One of the possible approaches to creating such sharpeners is to use a double shell liner and switch the current from the outer to the inner shell. The outer shell (outer cascade) is accelerated by the magnetic pressure of the current pulse, whereas the inner shell (inner cascade) remains almost at rest up to the instant of current switching. The switching of the current to the inner shell can be caused by the following processes. (i) A rapid increase in the anomalous resistivity [8] of the outer-shell plasma, which may be related to either the low density of the shell as a whole [9, 10] or a local density decrease in perturbations arising due to instabilities [11]. In this case, the outer liner acts as a plasma erosion switch. (ii) The breaking of the outer shell and the plasmodynamic process of switching the current to the inner shell due to the development of either the Rayleigh–Taylor instability or a perturbation near the electrode because of the initial divergence of the gas jet. The possibility of the plasma liner being destroyed by instabilities and the appearance of a low-density current-carrying plasma inside the shell were demonstrated in two-dimensional simulations (see, e.g., [12]).

When the liner is formed with pulsed gas puffing through a supersonic nozzle without undertaking special measures, the outer surface of the initial gas shell is shaped as a truncated cone with the divergence angle $\alpha \approx 1/M$, where M is the Mach number of the gas jet. First, this can result in the implosion occurring at different times along the liner axis—the so-called "zippering" effect [13]. Second, due to the nonzero axial component of the accelerating force, the liner implosion can be accompanied by a progressive decrease in the density and the formation of a perturbation in the nozzle region because of the detachment of the bulk liner mass from the electrode (nozzle) [13–15]. In [15], this effect was suppressed by using a nozzle with a profiled inner body. From the standpoint of the possible breaking of the outer shell and switching the current to the inner shell, the above effect may play a positive role.

In this paper, we present the results of experiments with double shell liners with the use of a microsecond capacitor bank. The aim of the experiments was to switch the current from the outer to the inner shell and, as a result, to achieve a *K*-shell radiation yield comparable with that obtained by using generators with $\tau \approx$ 100 ns.

It should be noted that direct measurements of the current flowing through the inner shell are complicated because, at the instant of switching, the outer and inner shells are closely spaced. For this reason, the switching efficiency can only be estimated indirectly, e.g., by comparing the radiation power with the ohmic dissipation power in the electric circuit, from the optical photography of the implosion process [9], and from the *K*-shell radiation yield.

2. EXPERIMENT

Experiments were carried out with a low-inductance capacitor bank with a current rise time of 1.2 μs. The amplitude of the liner current was 360–380 kA. Figure 1 shows a schematic of the load unit. A gas liner was formed with the help of two annular supersonic nozzles with a Mach number of 4–5 and was preionized by radiation from a multigap discharger positioned behind the anode grid. The working gas was neon. The cathode was shaped as a truncated cone with an angle of 6° between the generatrix and the plane perpendicular to the liner axis. The liner length was 1.8 cm. The current was measured by a Rogowski coil and magnetic probes positioned near the anode grid at different radii.

The initial radii of the inner and outer shells were $r_{20} = 0.9$ and $r_{10} = 3.8$ cm, respectively. It was reasonable to choose an initial radius of the inner shell of about 1 cm. On one hand, in this case, the integral growth rate of the Rayleigh–Taylor instability for the most rapidly growing perturbations does not exceed $\Gamma \approx 10$ even for rather thin shells (e.g., those made of a foil) [16]. At $\Gamma > 10$, the destructive effect of instabilities becomes more substantial; the shell can break, and the low-density plasma can penetrate into the liner, which hinders the formation of a compact pinch [17]. On the other hand, values of the initial radius much less than 1 cm impose excessively rigid requirements on the current rise time in the inner shell. For example, in order for condition (1) to be fulfilled at $r_{20} < 1$ cm, the current rise time should satisfy the inequality $\tau < (2–3)r_{20}/V_{min} \approx 100–150$ ns.

It is desirable to choose an initial inner-shell radius larger than 2–3 cm. In this case, the Rayleigh–Taylor instability, as well as the perturbation near the nozzle

caused by the divergence of the gas jet, can develop significantly, thereby providing the conditions for current switching to the inner shell.

The mass of the outer shell was chosen such that the maximum liner compression occurred at 0.95–1 μs from the beginning of the generator current. The masses per unit length of the inner and outer shells were estimated in individual shots by comparing the measured implosion time (when only the inner or outer shell imploded) with that calculated by the zero-dimensional model.

The dynamics of the liner implosion was observed with an FER-7 streak camera with a slit oriented perpendicular to the liner axis (radial streak). With the slit oriented parallel to the liner axis (axial streak), we could observe the structure of the plasma shell at different radii (Fig. 1). The *K*-shell radiation yield was measured by X-ray diodes with aluminum cathodes and aluminum filters. Data on the filter transmission and the cathode sensitivities were taken from [18, 19]. To obtain a *K*-shell radiation image of the pinch, we used a pinhole camera with an 8-μm aluminum filter. Note that the line emission from the *K* shell of neon ions lies in the range 0.92–1.2 keV. The spectrum above 1.2 keV is continuous.

At the first stage of experiments, we searched for the optimum inner-shell mass with respect to the *K*-shell radiation yield. The inner-shell mass was varied by varying the critical section of the inner nozzle. In these shots, we determined the power and yield of *K*-shell radiation, recorded the *K*-shell radiation image of the pinch, and measured the implosion velocity. At the second stage of experiments, the radial and axial streak images of the liner implosion were recorded at the optimum mass of the inner shell.

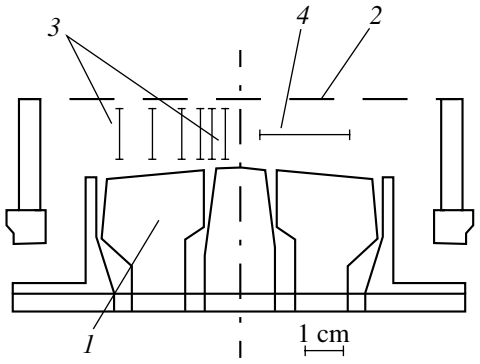

Fig. 1. Schematic of the load unit: (*1*) nozzle and (*2*) anode grid. Orientation of the streak camera slit for (*3*) axial and (*4*) radial streaks.

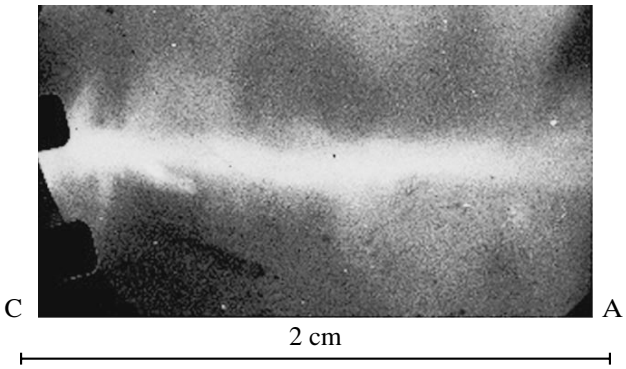

Fig. 2. Integral pinhole image of the implosion of a double shell neon liner recorded behind a 8-μm aluminum filter on UFSh-S film; C is the cathode, and A is the anode.

3. EXPERIMENTAL RESULTS AND DISCUSSION

As the inner-shell mass was varied, the maximum *K*-shell radiation yield, according to estimates, was attained at an inner-shell mass of 10–15 μg/cm and was equal to 50–80 J per pulse. The final implosion velocity was $(1.5–2) \times 10^7$ cm/s. In the integral pinhole camera image, we can see a pinch 0.1–0.15 cm in diameter (Fig. 2). Figure 3 shows the waveforms of the current and the signal from an X-ray diode with an 8-μm aluminum filter. As the inner-shell mass increased, the final implosion velocity and the *K*-shell radiation yield decreased. With the nozzle of the given design, we could not obtain an inner-shell mass less than 10–15 μg/cm.

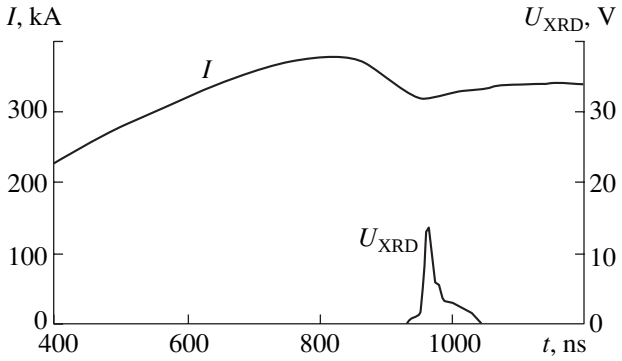

Fig. 3. Waveforms of the current and the signal from an X-ray diode with an 8-μm aluminum filter.

In the absence of an inner shell, no pinch was observed in integral pinhole camera images and the *K*-shell radiation yield did not exceed 5 J. According to estimates by the zero-dimensional model, the outer-shell mass was 15–20 μg/cm and the final velocity at the tenfold radial compression was $\approx 2 \times 10^7$ cm/s. Hence, for a single shell liner, the plasma compression ratio is significantly lower as compared to a double shell liner, which results in a lower *K*-shell radiation yield even though the final implosion velocity is high enough.

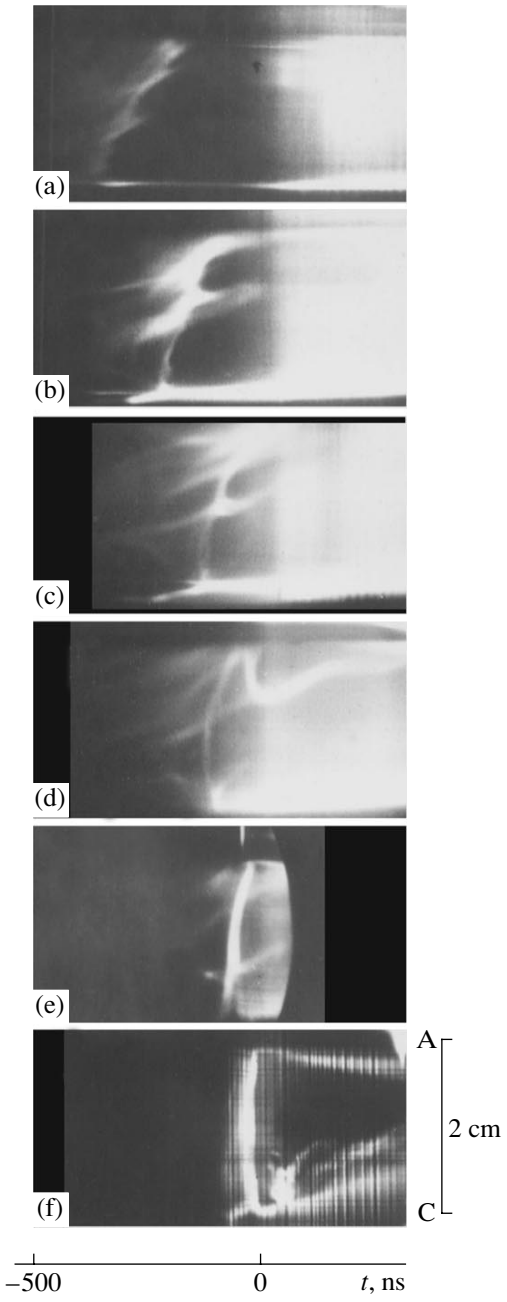

Fig. 4. Streak images of liner implosion recorded with an axially oriented slit sighting at the radii r_{slit} = (a) 3.5, (b) 2.5, (c) 1.7, (d) 1.3, (e) 0.9, and (f) 0.4 cm; C is the cathode, and A is the anode.

Let us estimate the expected neon *K*-shell radiation yield for a generator with τ = 100 ns and a maximum current of 380 kA. Mosher and Krishnan [3] proposed a relatively simple two-level model allowing one to estimate the *K*-shell radiation yield from the plasma liner at a given kinetic energy E_k, final radius r_f, and atomic number Z of the liner material. Comparing the results of calculations with the experiment, they pointed out that the model more adequately describes the optimized liners, whose implosion provides the maximum *K*-shell radiation yield with a given generator. According to [3], the optimum initial liner radius is equal to $r_0 = 1.4 \times 10^6 Z^{0.86}\tau_{imp}$ for the current pulse shape of the Saturn generator. Since r_0 depends weakly on the current pulse shape, we will use this expression setting $\tau_{imp} \approx \tau = 100$ ns. For $Z = 10$, we obtain $r_0 = 1$ cm. For a radial compression ratio of 10, the final radius is equal to $r_f = 0.1$ cm. The liner kinetic energy is approximated by the expression E_k [kJ/cm] $\approx$ (0.7–0.9)$\ln(r_0/r_f) I_{max}^2$ [MA], which gives E_k = 230–300 J/cm for I_{max} = 380 kA and the tenfold compression. Using formulas (34) and (35) from [3], we obtain the expression for the *K*-shell radiation yield

$$Y = \frac{E_b}{8}\left(\frac{4E_k}{E_b} - \sqrt{1 + \frac{8E_k}{E_b}} + 1\right),$$

where $E_b = r_f Z^{6.64}/390$ J/cm. From here, we obtain Y = 30–40 J/cm, which is close to the experimental values.

Figure 4 shows the dynamics of the implosion of a double-shell liner with an inner-shell mass of 10–15 μg/cm. The streak images were recorded in different shots with an axially oriented slit sighting at the radii r_{slit} = 3.5, 2.5, 1.7, 1.3, 0.9, and 0.4 cm. At r_{slit} = 3.5, 2.5, 1.7, and 1.3 cm, the inner shell does not fall into the field of view of the streak camera and only the outer shell is seen. The streak images were recorded at the same initial parameters of the liner; the current amplitudes and the instants of maximum compression were also almost the same.

At r_{slit} = 3.5 cm (Fig. 4a), the plasma glow is relatively uniform along the liner. In the figure, we can see perturbations with a characteristic scalelength of 0.3–0.5 cm and a large-scale perturbation. The latter perturbation manifests itself in the liner parts that are farther from the cathode arrive at the radius r_{slit} with a time delay. This effect may be attributed to the initial divergence of the gas jet. The magnetic probes installed at the anode show that the initial radius of the outer shell near the anode is equal to 4.5 cm. This corresponds to the angular divergence of the initial gas jet $\alpha \approx 17°$, which is somewhat higher than the calculated angular divergence for a nozzle with a Mach number of 4–5.

The large divergence favors the plasma acceleration in the axial direction. As the plasma moves away from the cathode in the course of implosion, the mass per unit length near the cathode should decrease. At r_{slit} = 2.5 cm (Fig. 4b), the glow near the cathode is significantly weaker than near the anode, which can be explained by the fact that the density near the cathode decreases due to the nonzero axial component of the velocity. At a radius of 1.7 cm (Fig. 4c), the bright plasma occupies only half of the interelectrode gap; i.e., the plasma progressively concentrates near the anode during implosion. At a short distance from the cathode, we observe a low-intensity plasma shell, which, at

r_{slit} = 1.3 cm (Fig. 4d), is seen throughout the entire length of the interelectrode gap. At this radius, the bright plasma bunch is located near the anode and lags behind the shell by 50–80 ns.

Starting from the radius r_{slit} = 0.9 cm, the inner shell falls into the field of view of the streak camera. In the streak image (Fig. 4e), we can see that the boundary of the plasma glow is perturbed only slightly and the glow is rather uniform throughout the entire gap, although the outer shell is substantially destroyed by instabilities at the radius close to the initial inner-shell radius. Perturbations are absent down to at least the radius 0.4 cm (Fig. 4f).

According to streak images recorded with a radially oriented slit, the final implosion velocity is (1.5–2) × 10^7 cm/s.

Figure 5 shows the streak image of the liner implosion recorded with a radially oriented slit whose center is adjusted to the radius 1.7 cm. In this case, the slit views the region lying between radii of 0.7 and 2.7 cm at a distance of 1 cm from the cathode (Fig. 1). For about 100–150 ns from the beginning of the glow, only the outer-shell plasma is seen. Then, we can see a flash at a radius nearly equal to the initial radius of the inner shell, which, apparently, indicates that the inner shell starts imploding. The glow of the outer shell continues for 100 ns after the beginning of the inner-shell implosion. Consequently, a fraction of the outer-shell plasma remains at radii larger than the initial inner-shell radius (in the radial region from 1.0 to 1.7 cm) and, apparently, does not take part in the pinch formation.

The development of a large-scale perturbation near the nozzle was observed in the computer simulations of a 3-cm-long gas liner with an initial angular divergence of $\alpha \approx 13°$ and an outer-shell radius of $r_0 \approx 2$ cm at the nozzle exit [14]. When the bulk of the shell mass is still at a radius of ≈ 0.7 cm, the plasma near the cathode has already arrived at the axis. The longitudinal size of the cathode perturbation is about 0.7 cm.

Hence, the structure of the outer shell can be strongly affected by the cathode perturbation, as is evidenced by streak images. The characteristic spatial scale of the cathode perturbation at a radius equal to the initial inner-shell radius can be roughly estimated (Fig. 6) as $\Delta z \approx (r_{10} - r_{20})\tan\alpha$, where r_{10} and r_{20} are the initial radii of the outer and inner shells, respectively. For r_{10} = 3.8, r_{20} = 1.0, and α = 17°, we obtain Δz = 0.86 cm, which is comparable to the liner length. The acceleration of the plasma shell in the cathode perturbation region can occur more rapidly as compared to the bulk of the liner because of the decrease in the mass per unit length in this region. If the total generator current flows through the light shell, then the latter acts as a plasmodynamic current sharpener for the inner shell. In this case, the bulk of the outer shell does not take part in the pinch formation, because the implosion of the inner shell begins before the bulk of the outer shell arrives at the initial inner-shell radius. The high compression ratio and the high *K*-shell radiation yield achieved in the experiments can be explained by the current switching from the outer to the inner shell, which ensures a more rapid rise of the current through the inner shell as compared to the generator current rise time $\tau \approx 1$ μs.

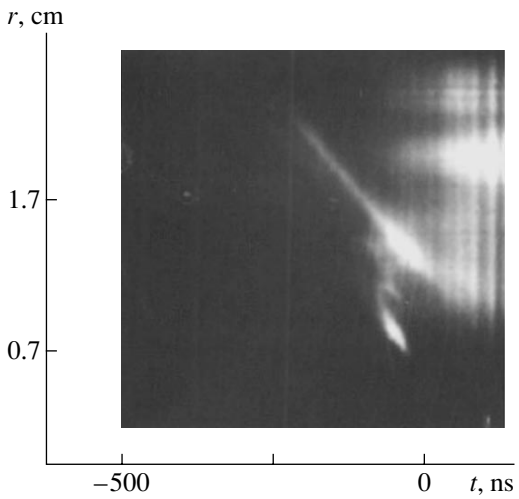

Fig. 5. Streak image of the double shell liner implosion recorded with a radially oriented slit. Time t = 0 corresponds to the maximum compression of the inner shell. At about this time, a glow arises in the radial region from 1 to 2 cm, which may be attributed to the reflection of light from the return-current conductors and the vacuum chamber wall. The vertical strips in the streak image are unrelated to the plasma processes and are probably caused by electromagnetic interference.

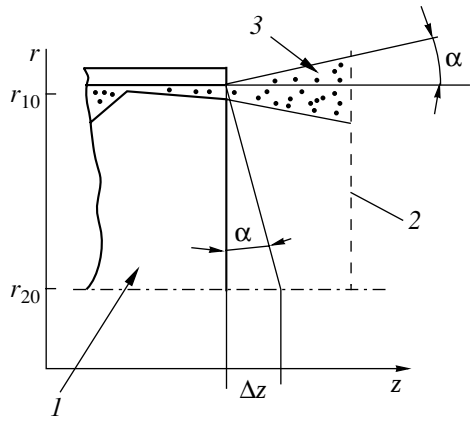

Fig. 6. Schematic diagram of the development of a perturbation near the cathode in the outer shell due to the initial divergence of the gas jet: (*1*) nozzles, (*2*) anode grid, and (*3*) initial outer gas shell; Δz is the spatial scale of the perturbation at a radius equal to the inner-shell radius, and α is the initial divergence angle of the outer shell.

4. CONCLUSION

In a double shell liner with a 360-kA microsecond generator, a neon *K*-shell radiation yield of 50–80 J per pulse is achieved. This yield is close to that calculated by the semiempirical model, which adequately describes the available experimental data on the *K*-shell radiation yield for generators with a current rise time of 100 ns. Streak camera images and the high *K*-shell radiation yield indicate that the outer shell provides faster current switching to the inner shell as compared to the generator current rise time. This effect may be attributed to the development of a large-scale perturbation near the cathode in the outer shell due to the angular divergence of the initial gas shell.

REFERENCES

1. N. R. Pereira and J. Davis, J. Appl. Phys. **64**, R1 (1988).
2. K. G. Whitney, J. W. Thornhill, J. P. Apruzese, and J. Davis, J. Appl. Phys. **67**, 1725 (1990).
3. D. Mosher, N. Qi, and M. Krishnan, IEEE Trans. Plasma Sci. **26**, 1052 (1998).
4. J. H. Degnan, W. L. Baker, and P. J. Turchi, in *Proceedings of the 2nd International Conference on Dense Z-pinches, Laguna Beach, 1989*, p. 34.
5. W. Matuska, H. Lee, R. Hochaday, and D. Peterson, in *Proceedings of the 3rd International Conference on Dense Z-pinches, London, 1993*, p. 525.
6. D. L. Peterson, R. L. Bowers, K. D. McLenithan, *et al.*, Phys. Plasmas **5**, 3302 (1998).
7. W. L. Baker, M. C. Clark, and J. H. Degnan, J. Appl. Phys. **49**, 4694 (1978).
8. P. V. Sasorov, Pis'ma Zh. Éksp. Teor. Fiz. **56**, 614 (1992) [JETP Lett. **56**, 599 (1992)].
9. A. V. Branitskiy, S. A. Dan'ko, A. V. Gerusov, *et al.*, Fiz. Plazmy **22**, 307 (1996) [Plasma Phys. Rep. **22**, 277 (1996)].
10. A. N. Batunin, A. V. Branitsky, I. N. Frolov, *et al.*, in *Proceedings of the 3rd International Conference on Dense Z-pinches, London, 1993*, p. 580.
11. A. Chuvatin, P. Choi, B. Etlicher, *et al.*, in *Proceedings of the 10th IEEE International Pulsed Power Conference, Albuquerque, 1995*, p. 106.
12. N. F. Roderick and T. W. Hussey, J. Appl. Phys. **56**, 1387 (1984).
13. T. W. Hussey, M. K. Matzen, and N. F. Roderick, J. Appl. Phys. **59**, 2677 (1986).
14. C. Deeney, P. D. LePell, F. L. Cochran, *et al.*, Phys. Fluids B **5**, 992 (1993).
15. S. A. Sorokin, A. V. Khachaturyan, and S. A. Chaikovsky, Fiz. Plazmy **17**, 1453 (1991) [Sov. J. Plasma Phys. **17**, 841 (1991)].
16. T. W. Hussey, in *Proceedings of the 3rd International Conference on Megagauss Magnetic Field Generation, Novosibirsk, 1983*, p. 208.
17. T. W. Hussey, N. F. Roderick, and D. A. Kloc, J. Appl. Phys. **51**, 1452 (1980).
18. R. H. Day, P. Lee, E. B. Saloman, and D. J. Nagel, J. Appl. Phys. **52**, 6965 (1981).
19. B. L. Henke and R. L. Elgin, Adv. X-ray Anal. **13**, 639 (1970).

Translated by N. F. Larionova

Plasma Physics Reports, Vol. 27, No. 11, 2001, pp. 953–962. Translated from Fizika Plazmy, Vol. 27, No. 11, 2001, pp. 1009–1018.

PLASMA DYNAMICS

Current Sheets Formed by Alfvén and Magnetosonic Pulses in the Vicinity of the Null Line of the Magnetic Field

G. I. Dudnikova and V. P. Zhukov

Institute of Computational Technologies, Siberian Division, Russian Academy of Sciences, Novosibirsk, 630090 Russia
e-mail: zukov@net.ict.nsc.ru

Received February 16, 2000; in final form, April 19, 2001

Abstract—A study is made of the propagation of an Alfvén pulse and the superposition of an Alfvén and a magnetosonic pulse in the vicinity of the magnetic null line (the X point). It is shown that, on long time scales, the poloidal components of the velocity and magnetic field relax to steady-state distributions similar to those in the case of a magnetosonic pulse. In the essentially nonlinear problem under investigation, the steady-state distributions of the toroidal components of the velocity and magnetic field are found to be close to those in the corresponding linear problem. It is established that two-dimensional effects play an important role in the evolution of the forming current sheets. *© 2001 MAIK "Nauka/Interperiodica".*

1. INTRODUCTION

The investigation of plasma flows near the singularities of the magnetic field has a broad range of applications in laboratory and space plasmas [1, 2]. In laboratory plasmas, which are the most important from the standpoint of applications, the flows are usually initiated by a perturbation of the poloidal magnetic field, as is the case, e.g., with tearing modes in tokamaks [3] and the Current Sheet device [4, 5]. Accordingly, such plasma flows have been investigated thoroughly. Among many theoretical studies that involve numerical modeling, we mention the paper by Brushlinskiĭ *et al.* [6], in which the problem is formulated in essentially the same way as in the present work. The authors of [6] carried out the most comprehensive and systematic analysis of the formation of current sheets and their behavior under the action of the perturbation of the poloidal (i.e., perpendicular to the null line) magnetic field in the vicinity of the X point. The perturbation of the poloidal magnetic field was assumed to be magnetosonic in character. The boundary conditions corresponded to an unbounded plasma; this approach is of interest for studying the processes occurring in space plasmas (such as the solar corona and the Earth's magnetosphere). In astrophysical plasmas, the perturbations of the toroidal (i.e., parallel to the null line) magnetic field also play an important role. These perturbations are of the nature of Alfvén waves and are driven by sheared plasma flows. Here, we investigate the propagation of an Alfvén pulse and the superposition of an Alfvén pulse and a magnetosonic pulse in the vicinity of the X point.

The propagation of an Alfvén pulse in the vicinity of the magnetic null line was studied analytically in [7–10] for a perfectly conducting plasma in the quasistatic approximation. It was shown that, in the vicinity of the null line, an Alfvén pulse gives rise to both poloidal and toroidal current sheets with infinite current density and zero thickness.

Hassam and Lambert [11] studied the propagation of an Alfvén pulse in the vicinity of the X point in the linear approximation under the assumption that the plasma viscosity and plasma conductivity are both finite. They showed that, in a steady state, the current density is proportional to $(\nu\eta)^{-1/4}$, where ν is the magnetic plasma viscosity and η is the conventional plasma viscosity. In [11], the questions associated with nonlinear effects were not discussed, although the magnetic field at the null line vanishes and, therefore, the vicinity of the line cannot be described in the linear approximation. Below, we will show that, for an infinitely long time ($t \longrightarrow \infty$), the solution to the nonlinear problem coincides exactly with the solution to the linear problem even for very small (but finite) values of η and ν and for magnetic field perturbations comparable in strength to the initial magnetic field. According to our numerical results that serve as the basis for the present study, the minimum values of the dimensionless coefficients η and ν may be as low as 5×10^{-5}, and the ratio of the amplitude of the perturbed magnetic field to that of the initial field may be on the order of unity. The relaxation of the system to such a steady state is a nontrivial consequence of the highly nonlinear processes under investigation.

Note that, in the series of papers [12–15], in which the formulation of the problem of the propagation of Alfvén waves was similar to our formulation of the problem, the computations were carried out for time scales as long as $t < 40$ Alfvén times. In those papers, the question of the steady-state character of the calculated configurations, which were found to vary slowly in time, remained open. As a result, the qualitative pat-

tern of plasma flows (in particular, the pattern that served as the basis for the analytic estimates obtained in [12]) was not clarified completely and the steady-state current density was not evaluated quantitatively. In this work, we bridge these gaps. Among other things, we present the results of simulations carried out for time scales as long as thousands (and, in some cases, even tens of thousands) of Alfvén times, so that the calculated final configurations are definitely steady-state.

We start with a mathematical formulation of the problem. Next, we describe the results of mathematical modeling of a purely Alfvén perturbation for nonzero ν and η. The case $\nu = 0$ and/or $\eta = 0$ is discussed in a separate section. Then, we analyze the results of modeling the propagation of the superposition of an Alfvén pulse and a magnetosonic pulse in the vicinity of the X point. Finally, we discuss the results obtained.

2. FORMULATION OF THE PROBLEM

The problem to be considered is formulated as follows. The plasma occupies a square-shaped region and experiences a hyperbolic magnetic field. The waves that come from a remote source are modeled by specifying various magnetic field perturbations at the boundaries of the calculation region. Much larger dimensions of the real plasma are modeled by the boundary conditions that imply plasma flows into and out of the calculation region. The plasma motion is two-dimensional ($\partial/\partial z = 0$) and is described by the following dimensionless equations of one-fluid magnetohydrodynamics [12–15]:

$$\frac{\partial A}{\partial t} + (\mathbf{V}\cdot\nabla)A = \nu\Delta A,$$

$$\frac{\partial H_z}{\partial t} + \nabla\cdot(\mathbf{V}H_z) = (\mathbf{H}\cdot\nabla)V_z + \nu\Delta H_z,$$

$$\rho\left(\frac{\partial \mathbf{V}}{\partial t} + (\mathbf{V}\cdot\nabla)\mathbf{V}\right)$$

$$= -\nabla(p + H_z^2/2) - \Delta A\nabla A + \eta\left(\Delta\mathbf{V} + \frac{1}{3}\nabla\nabla\cdot\mathbf{V}\right),$$

$$\rho\left(\frac{\partial V_z}{\partial t} + (\mathbf{V}\cdot\nabla)V_z\right) = (\mathbf{H}\cdot\nabla)H_z + \eta\Delta V_z,$$

$$\frac{\partial \rho}{\partial t} + \nabla\cdot(\rho\mathbf{V}) = 0,$$

$$\frac{1}{\gamma-1}\left(\frac{\partial p}{\partial t} + \nabla\cdot(\mathbf{V}p)\right) = \nabla\cdot(\chi\nabla T) - p\nabla\cdot\mathbf{V} \quad (1)$$

$$+ \nu((\nabla H_z)^2 + (\Delta A)^2) + \eta Q,$$

$$Q = 2\left(\left(\frac{\partial V_x}{\partial x}\right)^2 + \left(\frac{\partial V_y}{\partial y}\right)^2\right)$$

$$+ \left(\frac{\partial V_x}{\partial y} + \frac{\partial V_y}{\partial x}\right)^2 + \left(\frac{\partial V_z}{\partial x}\right)^2 + \left(\frac{\partial V_z}{\partial y}\right)^2 - \frac{2}{3}(\nabla\cdot\mathbf{V})^2,$$

$$T = p/\rho, \quad \mathbf{H} = (H_x, H_y) = \left(\frac{\partial A}{\partial y}, -\frac{\partial A}{\partial x}\right),$$

$$\mathbf{V} = (V_x, V_y), \quad \gamma = 5/3,$$

where A is the z-component of the vector potential of the magnetic field.

In Eqs. (1), the quantities are normalized as follows: the length is in units of the dimension l of the calculation region, the magnetic field is in units of the magnetic field H_0 at the boundary of the calculation region, the plasma density is in units of the initial density ρ_0, the plasma velocity is in units of the Alfvén velocity $V_A = H_0/(4\pi\rho_0)^{1/2}$, the time is in units of l/V_A, the plasma pressure is in units of $H_0^2/(4\pi)$, and the electric field is in units of H_0V_A/c (where c is the speed of light). For simplicity, the dimensionless plasma viscosity η, plasma resistivity (magnetic viscosity) ν, and plasma thermal conductivity χ are assumed to be constant.

The simulations were carried out in the square calculation region ($-1 < x < 1$, $-1 < y < 1$).

The initial conditions corresponded to the steady solution to Eqs. (1): $A = A_0 = (x^2 - y^2)/2$ (an X-point magnetic configuration), $H_z = 0$, $p = \beta$, $\rho = 1$, $\mathbf{V} = 0$, and $V_z = 0$.

An Alfvén pulse was modeled by specifying the perturbation of the z-component of the magnetic field at the boundaries $y = \pm 1$:

$$H_z(x, y = \pm 1) = \pm H_1\cdot\min(t/t_s, 1), \quad (2)$$

where H_1 is the amplitude and t_s is the rise time of the pulse.

At the boundaries $x = \pm 1$, the derivative along the magnetic field was assumed to be zero,

$$(\mathbf{H}\cdot\nabla)H_z = 0. \quad (3)$$

At the entire boundary of the calculation region, the velocity component satisfied the condition

$$(\mathbf{H}\cdot\nabla)V_z = 0. \quad (4)$$

In Eqs. (3) and (4), the derivatives along the magnetic field reflect the fact that the Alfvén wave propagates in the direction of the magnetic field $\mathbf{H}$. At the points ($x = 0$, $y = \pm 1$) and ($y = 0$, $x = \pm 1$), at which $(\mathbf{H}\cdot\mathbf{n}) = 0$ (where $\mathbf{n}$ is the normal to the boundary), we use $\partial H_z/\partial\mathbf{n} = 0$ and $\partial V_z/\partial\mathbf{n} = 0$ in place of Eqs. (3) and (4). Note that, by virtue of the symmetry properties of the problem, we have $H_z(x, y = 0) = 0$ and $V_z(x = 0, y) = 0$.

A magnetosonic pulse was modeled by specifying the poloidal velocity at the boundary of the calculation region in such a way that the poloidal velocity corresponded to the velocity field in a linearly converging

cylindrical magnetosonic wave with amplitude E_1 [6, 16]:

$$V_x = V_y = 0 \quad \text{for} \quad \xi < \xi_0,$$
$$V_x = E_1 x(\xi^2 - \xi_0^2)/(r\xi)^2, \tag{5}$$
$$V_y = -E_1 y(\xi^2 - \xi_0^2)/(r\xi)^2 \quad \text{for} \quad \xi > \xi_0.$$

Here, $\xi = t + \ln r$, $r = (x^2 + y^2)^{1/2}$, and $\xi_0 = \ln\sqrt{2}$.

At the boundary through which the plasma flows into the computation region, the vector potential A also corresponded to that of a linear cylindrical wave:

$$A = A_0 - E_1 g(\xi), \tag{6}$$

where $g(\xi) = 0$ for $\xi < \xi_0$ and $g(\xi) = (\xi - \xi_0)^2/\xi$ for $\xi > \xi_0$. We can readily see that, as $t \longrightarrow \infty$, the z-component of the electric field at the boundary, $E = -\partial A/\partial t$, approaches E_1.

At the boundary through which the plasma flows out of the calculation region, the vector potential was obtained from the equation

$$\frac{\partial A}{\partial t} + (\mathbf{V}\cdot\nabla)A = 0, \tag{7}$$

where the derivative of A in a direction normal to the boundary was found from the finite difference on the inside of the calculation region.

The formulation of the problem implies that, near the boundary, the perturbations of the magnetic field, which are determined by the parameters H_1 and E_1, should be small compared to the initial magnetic field. In simulations, the typical values of E_1 were no larger than 0.1. However, as was noted in the Introduction, the values of H_1 amounted to unity.

As the boundary conditions for p and ρ, we imposed the following conditions on the plasma flows: $\mathbf{q}_\rho = -\rho\mathbf{V}$ and $\mathbf{q}_p = -p\mathbf{V} + \chi\nabla T$, assuming that $(\mathbf{q}_\rho \cdot \mathbf{n}) = -(\mathbf{V}\cdot\mathbf{n})\rho_*$ and $(\mathbf{q}_p \cdot \mathbf{n}) = -(\mathbf{V}\cdot\mathbf{n})p_*$. For the plasma inflow, the quantities p_* and ρ_* were set at the initial values of the pressure and density, β and 1, respectively. For the plasma outflow, the quantities p_* and ρ_* were set at their values in the calculation cell near the boundary.

Since the coordinate axes are the symmetry axes, it is sufficient to solve the problem as formulated in only one quadrant of the entire calculation region. The numerical solution is based on the explicit first-order finite-difference scheme described in [17], which has been successfully implemented in practice.

The boundary conditions used in [6] differ from conditions (2)–(7) in the following two aspects: first, Brushlinskiĭ *et al.* imposed condition (6) on the vector potential A over the entire boundary and, second, instead of conditions (3)–(5), they used the conditions

$$\partial H_z/\partial\mathbf{n} = \partial V_z/\partial\mathbf{n} = \partial V/\partial\mathbf{n} = 0.$$

Additionally, for the plasma inflow into the calculation region, they set p and ρ at their initial values, and, for the plasma outflow, they set $\partial p/\partial n = \partial\rho/\partial n = 0$.

We also carried out computations with other versions of the boundary conditions, with the common features being that the perturbations of H_z and A were specified by conditions (2) and (6) and that the plasma flows into and out of the calculation region were assumed to be present. For various reasons, the most illustrative results were obtained in simulations with conditions (2)–(7) (below, we will present precisely these results). Other versions of the boundary conditions had a number of drawbacks. Thus, for a purely Alfvén perturbation, the boundary conditions used in [6] lead to the following situation. On long time scales, the plasma temperature and density become much higher than their initial values and the velocity $\mathbf{V}$ approaches zero. The boundary conditions used in [6] imply that, as the velocity V changes its sign at the boundary (while at the same time remaining close to zero), the plasma pressure experiences either a jumplike increase from a small initial value to a certain very large value or an analogous jumplike decrease. Of course, such jumps in pressure are physically meaningless.

We emphasize that calculations with all versions of the boundary conditions yielded the same qualitative pattern of the plasma flow, while the revealed quantitative differences were found to play an insignificant role. This circumstance is very important, because the boundary conditions in our simulations correspond only approximately to the physics of the processes under consideration. We can thus conclude that, qualitatively, slight differences between the boundary conditions should not change the overall pattern of plasma motion.

3. PROPAGATION OF A PURELY ALFVÉN PERTURBATION WITH $E_1 = 0$ ($\eta \neq 0$, $\nu \neq 0$)

Our simulations for nonzero η and ν revealed that, in the presence of a purely Alfvén pulse ($E_1 = 0$), the plasma flow evolves through the following three successive stages.

(i) An Alfvén wave perturbation of the field component H_z propagates along the magnetic field $\mathbf{H}$ from the boundaries $y = \pm 1$ toward the null line (the origin of the coordinates). At distances from the origin of the coordinates at which the background poloidal field becomes comparable in strength to the field H_z of the wave perturbation, i.e., at $r \sim H_1$, the plasma flow becomes highly nonlinear. The magnetic pressure $H_z^2/2$ pushes the plasma toward the x-axis, thereby perturbing the poloidal magnetic field. As a result, a current sheet stretched out in the x direction and formed by the z-component of the current $j_z = -\Delta A$ appears at the magnetic null line. At the same time, a sheet of the poloidal

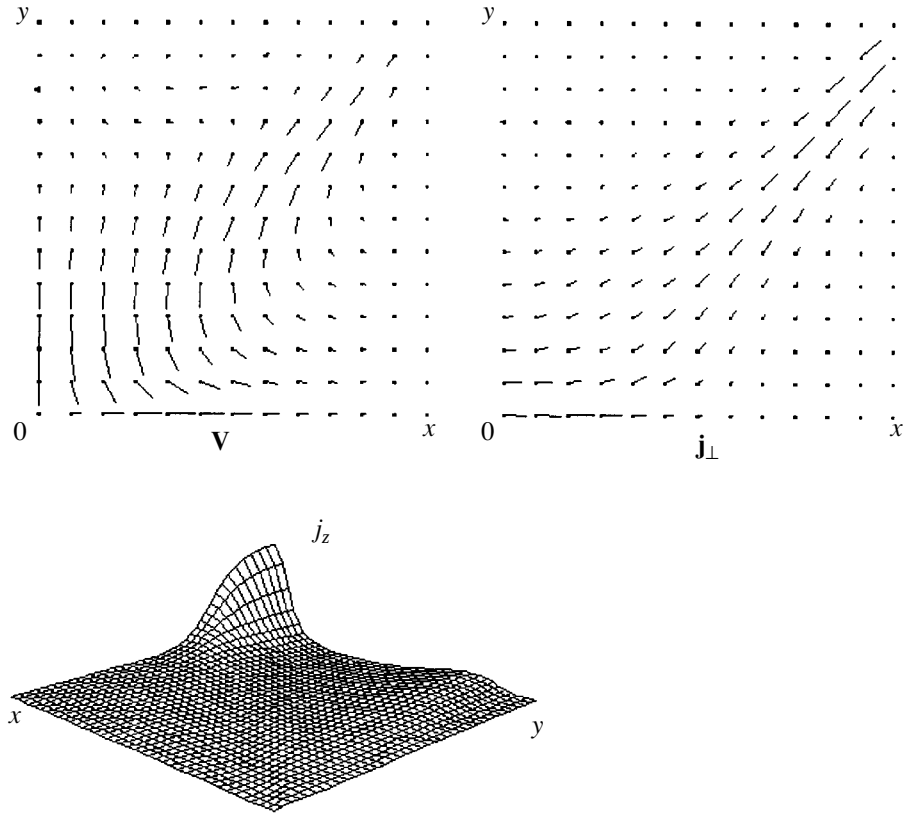

Fig. 1. Fields of the poloidal velocity and poloidal current density and the distribution of the toroidal current density on short time scales ($t \sim 4$) for a purely Alfvén perturbation. Shown is one quadrant of the computation region.

current $\mathbf{j}_\perp = (-\partial H_z/\partial y, \partial H_z/\partial x)$ is formed. The current components j_z and $j_\perp$ can be much greater in magnitude than the component $j_\perp$ in the quasisteady stage; moreover, a situation is possible in which $j_z \gg |\mathbf{j}_\perp|$. In these two current sheets, the plasma density and plasma pressure increase. For this stage, the fields of the poloidal velocity and poloidal current density and the distribution of j_z are shown in Fig. 1.

(ii) The current sheets that form in the initial stage are not steady: they exist on time scales of about several Alfvén times. Because of the Ohmic heating, the plasma density in the sheet increases, giving rise to a gas-kinetic pressure wave that propagates along the magnetic field from the sheet toward the boundaries $x = \pm 1$. The propagation of this wave toward the boundaries $y = \pm 1$ is hindered by the field H_z in the region $|y| > |x|$. As a result, on time scales of about ten Alfvén times, the system relaxes toward a configuration in which

$$p + H_z^2/2 \approx C(t). \tag{8}$$

We stress that the total duration of the first and second stages depends weakly on the values of transport coefficients and amounts to 10–20 Alfvén times.

(iii) The characteristic feature of the third stage is that, as $t \longrightarrow \infty$, the approximate equality (8) is increasingly well satisfied. Since, in this stage, the excess pressure of the field H_z is counterbalanced by the gas-kinetic plasma pressure, rather than by the pressure of the perturbed poloidal field, the poloidal magnetic field relaxes toward its initial distribution. Accordingly, the current j_z and velocity V both approach zero. Consequently, on infinitely long time scales ($t \longrightarrow \infty$), the distributions of H_z and V_z satisfy the time-independent equations

$$\begin{aligned}(\mathbf{H}\cdot\nabla)V_z + \nu\Delta H_z &= 0,\\ (\mathbf{H}\cdot\nabla)H_z + \eta\Delta V_z &= 0,\end{aligned} \tag{9}$$

in which the distribution of the magnetic field $\mathbf{H}$ coincides with its initial (at $t = 0$) distribution. Hence, Eqs. (9) coincide with the linearized time-independent equations for H_z and V_z.

We can easily see that the solution to Eqs. (9) depends on the single parameter $\nu\eta$, in which case the distribution of H_z can be approximately represented as

$$\begin{aligned}H_z &= H_1 \text{ for } y > |x|,\\ H_z &= -H_1 \text{ for } y < -|x|,\\ H_z &= 0 \text{ for } |x| > |y|.\end{aligned} \tag{10}$$

In the vicinity of the separatrices $|x| = |y|$, the distribution of H_z is smoothed by the effect of the magnetic

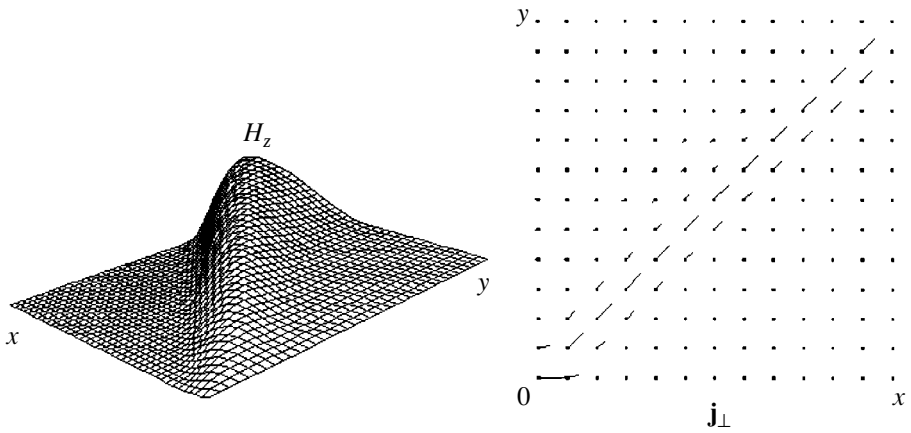

Fig. 2. Distribution of H_z and the field of the poloidal current density on infinitely long time scales ($t \longrightarrow \infty$) for a purely Alfvén perturbation. Shown is one quadrant of the computation region.

(η) and plasma (ν) viscosities. Assuming that the gradients along the field **H** are on the order of unity and the gradients across the field **H** (in the vicinity of the separatrices $|x| = |y|$) are large, we can readily estimate the poloidal current density as

$$|\mathbf{j}_\perp| \approx \text{const} \cdot H_1/(\nu\eta)^{1/4}. \quad (11)$$

Our simulations show that, for small values of $\nu\eta < 10^{-3}$, this dependence is valid with a high accuracy. If the poloidal current density $j_\perp$ in dependence (11) is understood as the maximum current density, which is reached at the origin of the coordinates, then we have const ≈ 100.

The distributions of H_z and $j_\perp$ on infinitely long time scales are shown in Fig. 2. The sheet of $j_\perp$ is seen to be stretched out along the separatrices $|y| = |x|$.

In the linear case, dependence (11) is obvious. A nontrivial point is that, for $t \longrightarrow \infty$, the magnetic field distribution described by the nonlinear equations (1) exactly corresponds to the distribution obtained in the linear problem. The distributions coincide not only over the entire calculation region (including the vicinity of the X point, where $H = 0$) but also when the amplitude of the Alfvén pulse is about unity ($H_1 \sim 1$). We emphasize that the steady-state distribution of the magnetic field is independent of the other parameters of the problem.

The time scale on which the system relaxes to a steady state may be as long as hundreds and even thousands of Alfvén times; the lower the transport coefficients, the longer this time.

Now, we analyze how the plasma density evolves with time. Although the evolution is governed by the boundary conditions and the parameters of the problem, all of the cases under consideration have one feature in common. At the end of the second stage and at the beginning of the third stage, the plasma density in the vicinity of the separatrices $|x| = |y|$ becomes lower (sometimes, by more than an order of magnitude) than the initial density. As a rule, the plasma density is lowest at the origin of the coordinates. The width of the regions of low plasma density in the vicinity of the separatrices is not associated with the width of the current sheet and is comparable to the dimension of the calculation region. This distribution of the plasma density may remain unchanged for an infinitely long time ($t \longrightarrow \infty$). The boundary conditions (2)–(7) imply that, as $t \longrightarrow \infty$, the gradients of ρ decrease slowly, which can be explained as follows. We substitute p extracted from the approximate equality (8) into Eq. (1) for the plasma pressure and take into account the fact that, as $t \longrightarrow \infty$, the functions $\mathbf{V}$, $\partial H_z/\partial t$, and j_z all approach zero. As a result, we arrive at the equation

$$\frac{dC}{dt} = (\gamma - 1)\nabla \cdot \left(\chi \nabla \frac{C - H_z^2/2}{\rho}\right) + q,$$
$$q = (\gamma - 1)(\nu(\nabla H_z)^2 + \eta(\nabla V_z)^2). \quad (12)$$

Integration of this equation over the entire calculation region yields

$$dC/dt = \langle q \rangle,$$

where the angular brackets $\langle\ \rangle$ denote averaging over the calculation region. Consequently, as time elapses, the quantity C increases linearly without bound, so that Eq. (12) can be reduced to the approximate form

$$\Delta\frac{1}{\rho} = \frac{\langle q \rangle - q}{(\gamma - 1)\chi\langle q \rangle t}.$$

Since the gradients of H_z and V_z are largest in regions of width $(\eta\nu)^{1/4}$ about the separatrices, we have $q/\langle q \rangle \sim (\eta\nu)^{-1/4}$ and, accordingly, obtain

$$\Delta\frac{1}{\rho} \sim \frac{1}{\chi t(\eta\nu)^{1/4}}.$$

Hence, the gradients of ρ should decrease with time. The asymptotic behavior $(\chi t)^{-1}(\eta\nu)^{-1/4}$ is confirmed by the computations. Calculational results show that, as $t \longrightarrow \infty$, the velocity V decreases according to the power law, but the power index characterizing the behavior of V is smaller than minus unity.

Let us consider the steady-state ($t \longrightarrow \infty$) distribution of the electric charge. Taking into account the properties of the distributions of the velocity and magnetic field on long time scales, we can write the divergence of the electric field $\mathbf{E} = -\mathbf{V} \times \mathbf{H} + \nu\mathbf{j}$ as $\nabla \cdot \mathbf{E} = -(\nabla A \cdot \nabla V_z)$. Since the gradients of V_z are largest in the vicinity of the separatrix planes $|x| = |y|$ and are directed across the magnetic field, the divergence of the electric field is also maximum ($\nabla \cdot \mathbf{E} = \max$) at the separatrix planes, which, thus, are the planes where the electric charge concentrates.

4. PROPAGATION OF A PURELY ALFVÉN PERTURBATION WITH $E_1 = 0$ ($\eta = 0$ AND/OR $\nu = 0$)

For $\nu = 0$, the problem under investigation has a singular solution, regardless of the value of η: the current density in the sheets that form in the first stage (Fig. 1) becomes infinitely high on a finite time scale, on which the sheets themselves become infinitely thin. These results agree with the conclusions obtained analytically in [7–10]. The case at hand was analyzed in more detail in [18]. Note that, even for a low magnetic viscosity, the solution becomes nonsingular and the plasma flow evolves in precisely the same way as described in the preceding section.

For $\eta = 0$ and $\nu \neq 0$, the pattern of the plasma flow is analogous to that in the case $\eta \neq 0$. The only exception is that, for $\eta = 0$, the poloidal current density $j_\perp$ does not reach a steady level in the third stage but instead continues to increase. The reason for this increase is clear from Eqs. (9), which imply that, for $\eta = 0$, the field component H_z should be constant along the lines of the magnetic field **H**. In principle, be true this may of the magnetic field lines that do not intersect the x-axis. However, the lines that cross this axis pass through the regions in which the component H_z has different signs. Consequently, along these lines, the component H_z cannot be constant.

The numerical solution of Eqs. (1) with the boundary conditions (2)–(7) and with $\eta = 0$ shows that, as $t \longrightarrow \infty$, the distribution of H_z approaches the discontinuous distribution (10). Accordingly, as time elapses, the current increases without bound. The current sheet along the separatrix planes $|x| = |y|$ corresponds to a tangential discontinuity. According to [19], tangential discontinuities are stable against small perturbations, in which case, however, the width of the discontinuities increases with time in proportion to $(\nu t)^{1/2}$. In contrast, in our problem, the width of the discontinuity decreases as time progresses. This contradiction stems from the fact that the relevant problem treated in [19] is one-dimensional, while the problem under analysis is one-dimensional only in a small vicinity of the separatrices $|x| = |y|$ and is two-dimensional over the entire computation region. In our problem, an important role is played by the regions $y > 0$ and $y < 0$, which are related to each other by the magnetic field **H** and in which the magnetic field component H_z has different signs. Hence, the evolution of the tangential discontinuity is governed not only by the local plasma parameters but also by the global parameters of the entire plasma configuration.

The above analysis implies that, in the hydrodynamic approximation, there is no mechanism capable of stopping the increase in $j_\perp$ in the case $\eta = 0$. However, the poloidal current density $j_\perp$ increases sufficiently slowly. Depending on the value of ν, the poloidal current density increases by a factor of two over thousands of Alfvén times. In real plasmas, the driving force for this plasma flow may disappear on such long time scales; i.e., the field component H_z at the boundary may change. Importantly, even a low viscosity should cause the current to relax toward a quasisteady distribution with a finite current density.

Note that, for certain boundary conditions and for $\eta = 0$ and $\chi = 0$, the plasma density at the origin of the coordinates rapidly decreases to zero at the beginning of the third stage ($t < 30$), in which case the poloidal current density $j_\perp$ constantly increases. Accordingly, the computation procedure was stopped at these times. For $\chi \neq 0$, the pattern of the plasma flow was described above.

5. PROPAGATION OF THE COMBINED ALFVÉN–MAGNETOSONIC PERTURBATION WITH $E_1 \neq 0$

The case of simultaneous propagation of an Alfvén and a magnetosonic perturbation implies that, at the very beginning of the process, the wave perturbation of A and H_z starts propagating from the periphery toward the center [13–15]. As the wave perturbation approaches the magnetic null line, it becomes highly nonlinear. At later times, for $\nu = 0$, the wave perturbation gives rise to singular current sheets. For $\nu \neq 0$, the wave perturbation is reflected from the center and the system evolves to a steady-state configuration. Let us consider the properties of this configuration.

The distributions of the poloidal velocity and poloidal magnetic field coincide qualitatively (and even quantitatively for a small amplitude H_1) with their steady-state distributions in the case of a purely magnetosonic perturbation ($H_1 = 0$). Our simulations show that the steady-state current density j_z at the origin of the coordinates is equal to E_1/ν for any value of H_1. On infinitely long time scales ($t \longrightarrow \infty$), the distributions of

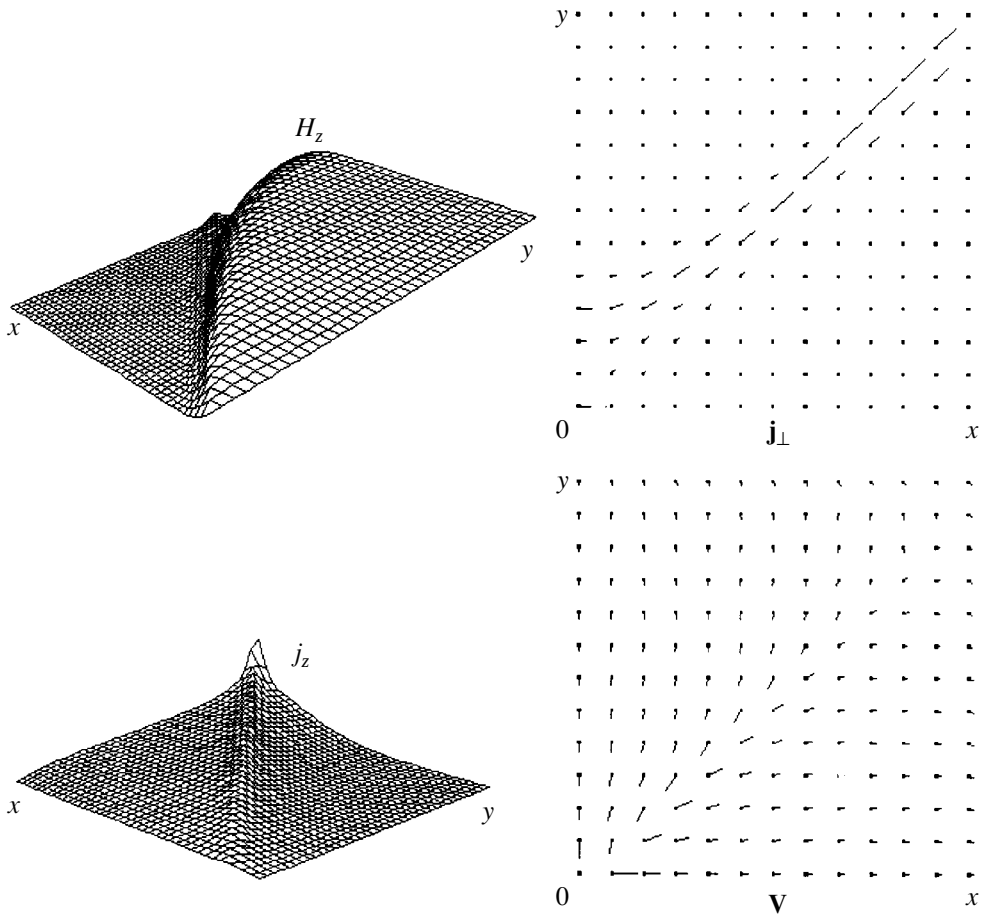

Fig. 3. Distributions of H_z and j_z and the fields of the poloidal velocity and poloidal current at $E_1 < \nu$ and at small η values on infinitely long time scales ($t \longrightarrow \infty$) for a combined Alfvén–magnetosonic perturbation. Shown is one quadrant of the computation region.

H_z and V_z are described by the equations

$$\begin{aligned} \nabla \cdot (\mathbf{V} H_z) &= (\mathbf{H} \cdot \nabla) V_z + \nu \Delta H_z, \\ (\mathbf{V} \cdot \nabla) V_z &= (\mathbf{H} \cdot \nabla) H_z + \eta \Delta V_z. \end{aligned} \tag{13}$$

In order to obtain qualitative distributions of H_z and V_z for $H_1 \sim 1$, it is sufficient to consider Eqs. (13), in which **V** and **H** correspond to the steady solution to Eqs. (1) for a purely magnetoacoustic perturbation. For $H_1 \ll 1$, this approximate approach yields correct quantitative results. It should be noted that, in the case of a purely Alfvén perturbation ($E_1 = 0$), the results obtained for $H_1 \sim 1$ are also qualitatively correct.

Let us analyze the steady-state distributions of the parameters of the problem in more detail. For $E_1/\nu > 1$, the quantities **H**, *V*, and j_z obey conventional distributions [6, 13–16]. At the *x*-axis, there is a j_z sheet with four characteristic satellites. For $E_1/\nu < 1$, the length of the sheet becomes comparable to its width and the sheet itself degenerates into a configuration in which the satellites are stretched out just from the origin of the coordinates along the separatrices, which lie near the planes $|x| = |y|$ (Fig. 3).

The distributions of **H** and *V* have the following two characteristic features, which make it possible to better understand how the distributions of H_z and $j_\perp$ depend on the parameters E_1, η, and ν.

(i) For a purely magnetosonic perturbation, the magnetic field lines that pass through the points ($x = 1$, $y = \pm 1$) are described by the expressions $y = \pm Y_c(x)$ and cross the *y*-axis at the points $y = \pm Y_c(0) \neq 0$, rather than at the origin of the coordinates. Consequently, if the velocity *V* in Eqs. (13) is equal to zero, then the field component H_z obeys the distribution

$$\begin{aligned} H_z &= H_1 \text{ for } y > Y_c(x), \\ H_z &= -H_1 \text{ for } y < -Y_c(x), \\ H_z &= 0 \text{ for } |y| < Y_c(x). \end{aligned} \tag{14}$$

In this case, in the vicinity of the line $|y| = Y_c(x)$, the distribution of H_z is smoothed by the effect of η and ν. For $E_1 < \nu$, the quantity $Y_c(0)$ increases with E_1; consequently, in the vicinity of the origin of the coordinates,

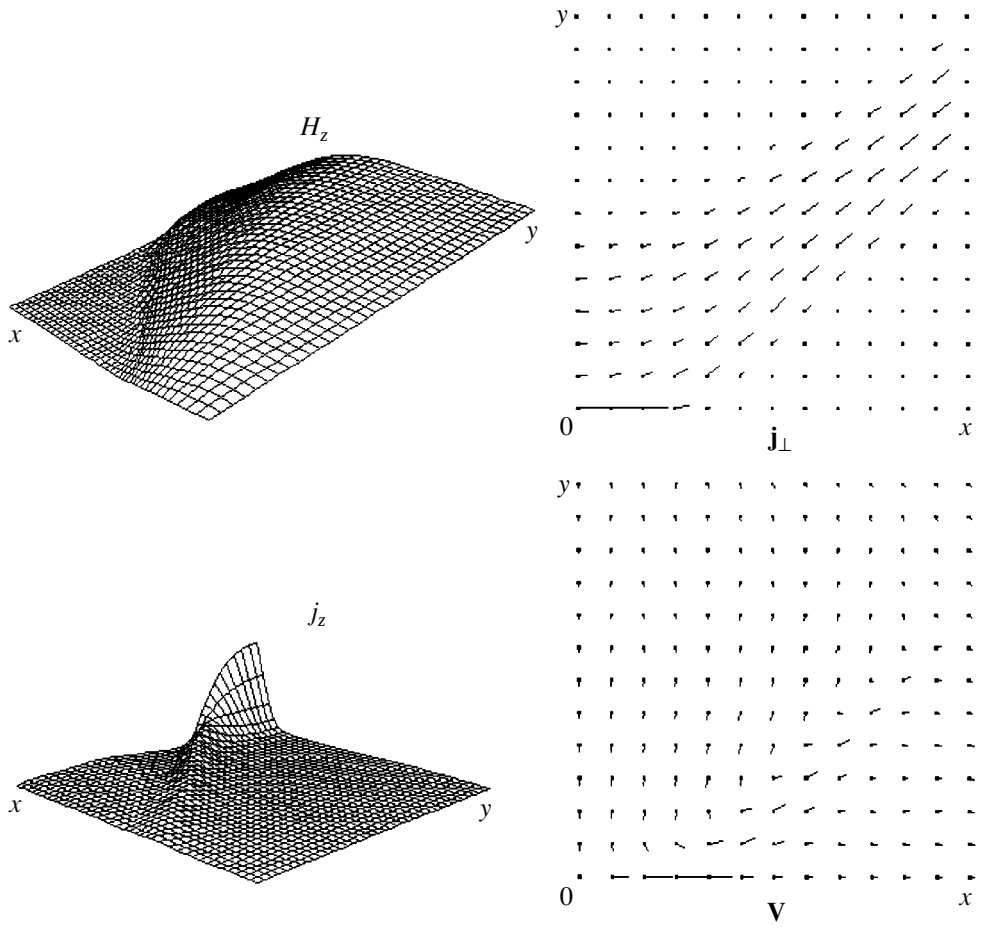

Fig. 4. Distributions of H_z and j_z and the fields of the poloidal velocity and poloidal current at $E_1 > \nu$ and at large η values on infinitely long time scales ($t \longrightarrow \infty$) for a combined Alfvén–magnetosonic perturbation. Shown is one quadrant of the computation region.

the component H_z decreases with increasing E_1 and, accordingly, the central poloidal current density j_c decreases. For $E_1 > \nu$, the quantity $Y_c(0)$ changes only slightly; accordingly, the current density j_c also remains essentially unchanged.

(ii) The velocity field **V** is such that all of the current lines originate from the boundaries $|y| = 1$ and terminate at the boundaries $|x| = 1$. Specifically, the current lines pass from the boundaries $y = \pm 1$ toward the x-axis and, then, turn toward the boundaries $|x| = 1$. The turn is sharpest inside the current sheet (see [6] and Fig. 3). Consequently, the field **V** tends to displace the region where the field component H_z is nonzero toward the x-axis and, accordingly, to increase the central current density j_c. The larger the parameter E_1, the more pronounced is this tendency. Note that, for $E_1 \neq 0$, such a velocity field ensures that a continuous solution to Eqs. (13) also exists at $\eta = 0$.

Properties (i) and (ii) govern the evolution of the field component H_z. Let us consider how the distribution of H_z and, accordingly, the profile of j_x along the y-axis depend on the values of the parameters of the problem.

For $E_1 = 0$ (Fig. 2), the quantity $H_z(x = 0, y)$ is close to H_1 over almost the entire y-axis. The component H_z falls to zero over distances of about $(\nu\eta)^{1/4}$ from the origin of the coordinates. Accordingly, the current density component $j_x(x = 0, y)$ has a maximum at the origin. In the region $|x| \geq (\nu\eta)^{1/4}$, the poloidal current density is low.

For $0 < E_1 < \nu$ and for low viscosity (the results shown in Fig. 3 were obtained for $\nu = 0.00167$, $E_1 = 0.001$, $\eta = 0$, $H_1 = 0.05$, $\chi = 0.001$, and $\beta = 0.05$), the quantity $H_z(x = 0, y)$ is close to H_1 in the region where the values of the y-coordinate are larger than a certain value y_* lying between 0 and $Y_c(0)$. In the vicinity of y_*, the field component H_z decreases abruptly and, accordingly, the current density component j_x has a local maximum, which we denote by $j_{\max}$. In the region of smaller values of $|y|$, the quantity j_x ($x = 0$, y) decreases to a minimum value $j_{\min}$. In the vicinity of the

origin of the coordinates, where the field component H_z changes sign, the component j_x has another maximum. Thus, for the parameter values of Fig. 3, we have $j_c \approx j_{max} \approx 0.28$, $j_{min} = 0.028$, $y_* = 0.24$, and $Y_c(0) = 0.34$. Note that, first, in some cases, the value j_{max} can be significantly larger than j_c and, second, for $E_1 < \nu$, the value j_c decreases as E_1 increases.

For $E_1 > \nu$ (the results shown in Fig. 4 were obtained for $\nu = 0.005$, $\eta = 0.0005$, $E_1 = 0.05$, $H_1 = 0.5$, $\chi = 0.001$, and $\beta = 0.05$), the effect of the velocity field and/or the smoothing effect of the viscosity (at sufficiently high values of η) causes the quantity $H_z(x = 0, y)$ to vary relatively uniformly over the region $y < y_*$. Accordingly, over the region $y < y_*$, the quantity j_x ($x = 0$, y) changes comparatively slightly and thus is plateau-shaped (the values j_{max} and j_{min} are close to one another). However, the maximum in j_x at $y = 0$ is, as before, pronounced. Thus, for the parameter values of Fig. 4, we have $j_{min} = 0.72$, $j_{max} = 0.91$, $y_* = 0.28$, $Y_c(0) = 0.5$, and $j_c = 3.35$. For $E_1 > \nu$, the quantity j_c does not change significantly and can increase with E_1 only slightly.

Notably, for $E_1 \neq 0$, the ratio j_c/H_1, as a rule, somewhat decreases as H_1 increases. Thus, for the above parameter values and for $E_1 = 0.03$ and $H_1 = 0.1$, we have $j_c/H_1 = 7.81$. For $H_1 = 0.5$, this ratio is equal to 6.6.

As $E_1 \longrightarrow 0$, the quantity j_c approaches its final value corresponding to the case of a purely Alfvén perturbation. In particular, for $\eta = 0$, we have $j_c \longrightarrow \infty$ as $E_1 \longrightarrow 0$.

Note that the time scale on which the system relaxes to a steady-state configuration varies from several tens of Alfvén times (for $E_1 > \nu$) to several tens of thousands of Alfvén times (for $E_1 < 10^{-3}\nu$). However, such long computation times are needed to obtain quantitative results. The qualitative pattern of the plasma flow (specifically, the shape of the current sheets and the characteristic velocity distribution) becomes quite clear as early as $t > 100$.

The results discussed above refer to the case $E_1 > 0$. For $E_1 < 0$, the distribution of H_z is governed by the following factors: (i) The relative positions of the magnetic field lines that pass through the points ($x = \pm 1$, $y = \pm 1$) (in the case at hand, the field lines cross the x-axis and end up at the boundaries $y = 1$ and $y = -1$, at which the field component H_z has different signs). (ii) The relative positions of the separatrices, which originate from the boundaries $y \pm 1$, cross the y-axis, and terminate at the same boundaries without intersecting the x-axis. (iii) The velocity field, which corresponds to the plasma inflow through the boundaries $x = \pm 1$ and the plasma outflow through the boundaries $y \pm 1$. However, in this situation, the distributions of the velocity V and poloidal magnetic field H are close to those in the case of purely magnetosonic perturbation only on time scales of several tens of Alfvén times or shorter and, on longer time scales, they are radically different.

The case $E_1 < 0$ requires further investigation and is not treated here.

6. CONCLUSION

We have investigated the formation of steady-state current sheets in the vicinity of the X point by an Alfvén perturbation of the magnetic field or a combination of an Alfvén perturbation and a magnetosonic perturbation. We have also analyzed the properties of the steady-state current sheets.

In the case of a purely Alfvén perturbation, the most interesting result is that the final steady-state distributions of the poloidal magnetic field and poloidal plasma velocity coincide exactly with their initial distributions. Accordingly, even in *a priori* nonlinear regimes, the toroidal magnetic field and toroidal plasma velocity relax toward the same distributions as those obtained in the linear approximation. The properties of the steady-state configuration of the magnetic field are governed only by the value of the parameter $\nu\eta$. In particular, we have shown that the poloidal current density obeys the dependence $H_1/(\nu\eta)^{1/4}$. Such parameters as the plasma thermal conductivity and initial plasma pressure affect the plasma density distribution on long time scales ($t \longrightarrow \infty$), but they have no impact on the distributions of the plasma velocity and magnetic field.

According to the analysis carried out in [7–10], it might be expected that, in a perfectly conducting plasma ($\nu = 0$), the magnetic field should have singularities. However, we have demonstrated for the first time that, in a plasma with a zero viscosity and finite conductivity, a tangential discontinuity may form whose thickness approaches zero as $t \longrightarrow \infty$. This result provides evidence that the evolution of tangential discontinuities is governed not only by the local but also by the global properties of the magnetic plasma configuration, because, in a plasma with a finite conductivity, the width of the one-dimensional tangential discontinuity increases as time elapses [19].

In the case of the combination of an Alfvén perturbation and a magnetosonic perturbation, the steady-state distributions of the poloidal magnetic field (equivalently, the toroidal current) and poloidal plasma velocity in the vicinity of the X point agree qualitatively with those in the case of a purely magnetosonic perturbation. In particular, the combined perturbation gives rise to a toroidal current sheet. The Alfvén component of the perturbation leads to the formation of a poloidal current sheet. In contrast to the case of a purely Alfvén perturbation, the density of the poloidal current driven by the magnetosonic component of the combined perturbation in a plasma with a zero viscosity but finite conductivity remains bounded as $t \longrightarrow \infty$. In a perfectly conducting

plasma, singular current sheets form even in the early stages of the evolution of the plasma flow.

ACKNOWLEDGMENTS

We are grateful to S.V. Bulanov for his interest in this work and fruitful discussions.

REFERENCES

1. B. B. Kadomtsev, Usp. Fiz. Nauk **151**, 3 (1987).
2. A. B. Severnyĭ, Izv. Krym. Astrofiz. Obs. **20**, 22 (1958).
3. B. B. Kadomtsev, Fiz. Plazmy **1**, 710 (1975) [Sov. J. Plasma Phys, **1**, 389 (1975)].
4. S. Yu. Bogdanov, N. P. Kiriĭ, and A. G. Frank, in *Magnetic Reconnection in Two- and Three-Dimensional Configurations* (Nauka, Moscow, 1996); Tr. Inst. Obshch. Fiz. Akad. Nauk **51**, 5 (1996).
5. S. Yu. Bogdanov, V. B. Burilina, N. P. Kiriĭ, *et al.*, in *Magnetic Reconnection in Two- and Three-Dimensional Configurations* (Nauka, Moscow, 1996); Tr. Inst. Obshch. Fiz. Akad. Nauk **51**, 76 (1996).
6. K. V. Brushlinskiĭ, A. M. Zaborov, and S. I. Syrovatskiĭ, Fiz. Plazmy **6**, 297 (1980) [Sov. J. Plasma Phys. **6**, 165 (1980)].
7. W. Zwingmann and K. Schindler, Sol. Phys. **99**, 133 (1985).
8. G. Vekstein, E. R. Priest, and T. Amari, Astron. Astrophys. **243**, 492 (1991).
9. G. Vekstein, Astron. Astrophys. **182**, 324 (1987).
10. G. Vekstein and E. R. Priest, Astrophys. J. **384**, 333 (1992).
11. A. B. Hassam and R. P. Lambert, Preprint no. UMIPR 94-011 (Department of Physics and Institute for Plasma Research, University of Maryland, 1995).
12. S. V. Bulanov, I. Ya. Butov, Yu. S. Gvaladze, *et al.*, Fiz. Plazmy **12**, 309 (1986) [Sov. J. Plasma Phys. **12**, 180 (1986)].
13. S. V. Bulanov, G. I. Dudnikova, V. P. Zhukov, *et al.*, in *Magnetic Reconnection in Two- and Three-Dimensional Configurations* (Nauka, Moscow, 1996); Tr. Inst. Obshch. Fiz. Akad. Nauk **51**, 101 (1996).
14. S. V. Bulanov, G. I. Dudnikova, V. P. Zhukov, *et al.*, Kratk. Soobshch. Fiz., Nos. 5–6, 28 (1994).
15. S. V. Bulanov, G. I. Dudnikova, V. P. Zhukov, *et al.*, Fiz. Plazmy **22**, 867 (1996) [Plasma Phys. Rep. **22**, 783 (1996)].
16. A. I. Podgornyĭ and S. I. Syrovatskiĭ, in *Burst Processes in Plasma* (Nauka, Moscow, 1979); Tr. Fiz. Inst. Akad. Nauk SSSR **110** (1979).
17. Yu. A. Berezin and G. I. Dudnikova, *Numerical Models of Plasma and Processes of Reconnection* (Nauka, Moscow, 1985).
18. G. I. Dudnikova and V. P. Zhukov, Vychisl. Tekhnol. **4** (11), 108 (1995).
19. L. D. Landau and E. M. Lifshitz, *Electrodynamics of Continuous Media* (Nauka, Moscow, 1982; Pergamon, New York, 1984).

Translated by O. E. Khadin

Plasma Physics Reports, Vol. 27, No. 11, 2001, pp. 963–966. Translated from Fizika Plazmy, Vol. 27, No. 11, 2001, pp. 1019–1022.

PLASMA DYNAMICS

K-shell Radiation from Double-Shell Argon Plasma Liners

S. A. Sorokin

Institute of High-Current Electronics, Siberian Division, Russian Academy of Sciences, Akademicheskiĭ pr. 4, Tomsk, 634055 Russia

Received April 19, 2001

Abstract—Experiments on the generation of argon *K*-shell radiation during the implosion of double-shell plasma liners are described. The optimum liner length with respect to the maximum *K*-shell radiation yield is determined. At a liner current of ~1.4 MA, the conversion efficiency of the generator electric energy into the *K*-shell radiation energy attains 8–9%. The spectrum of the argon *K*-shell radiation is measured by a set of photoemission X-ray diodes with different filters (including an argon gas filter). Based on the measurements of the emission power in different spectral intervals and calculations by the collision-radiative model, the ion density and electron temperature of the pinch plasma are estimated. © *2001 MAIK "Nauka/Interperiodica".*

1. INTRODUCTION

The electric energy of a high-current generator can be efficiently transferred to a plasma liner and then converted into soft X radiation [1]. The conversion efficiency decreases with decreasing radiation wavelength because of both the increase in the energy spent on heating electrons to a higher temperature and the higher degree of gas ionization. Furthermore, the necessity of increasing the energy imparted to each imploding atom dictates the necessity of decreasing the liner mass per unit length and, consequently, the density and emissivity of the plasma. This circumstance can decrease the efficiency if the characteristic time of plasma radiative cooling τ_r is longer than the time $\tau_i \sim r_f/v_f$, during which the pinch is in the compressed state. As a result, for a generator with a given energetic resource (maximum current), the requirement that the conversion efficiency of the generator electric energy into radiation be high limits the attainable minimum radiation wavelength. At the same time, at a given mass per unit length, the radiation power of an optically transparent plasma depends on the compression ratio as $P \propto n_i^2 r_f^2 \propto m^2/r_f^2 \propto I_m^4/r_f^2$. Here, n_i is the ion density, r_f is the final pinch radius, m is the liner mass per unit length, and I_m is the amplitude of the current through the liner. Consequently, the ratio of the radiative cooling time ($\tau_r \propto P^{-1}$) to the inertial confinement time ($\tau_i \propto r_f$) is proportional to r_f and can be maintained at a level of $\tau_r/\tau_i < 1$ by decreasing r_f. In other words, the generator current I_m providing a given radiation power can be reduced by increasing the radial compression ratio $I_m \propto r_f^{0.5}$ [2].

To estimate the generator current I_m above which the energy can be efficiently (>25%) converted into *K*-shell radiation, we can use one of the phenomenological models [3, 4]. For estimates, the simplest and most convenient model is the two-level model (TLM) [4]. In this model, the efficiency is defined as the ratio of the total *K*-shell radiation yield per pulse to the energy transferred from the generator to the liner. Figure 1 shows the efficiency predicted by this model for two values of the final argon pinch radius, 0.1 and 0.02 cm. It can be seen that the efficiency $\varepsilon \sim 25\%$ is attained at $I_m \sim 5$ MA for $r_f = 0.1$ cm and at $I_m \sim 2$ MA for $r_f = 0.02$ cm.

In [2], it was demonstrated that, at a liner current of ~0.9 MA, the more stable and, consequently, more compact implosion of a double-shell liner ($r_f \sim 0.02$ cm) makes it possible to increase the conversion efficiency of the generator energy into the energy of argon *K*-shell radiation. It is of interest to carry out experiments with a double-shell liner at a current close to 2 MA, at which, according to the TLM, the ~25% efficiency can be

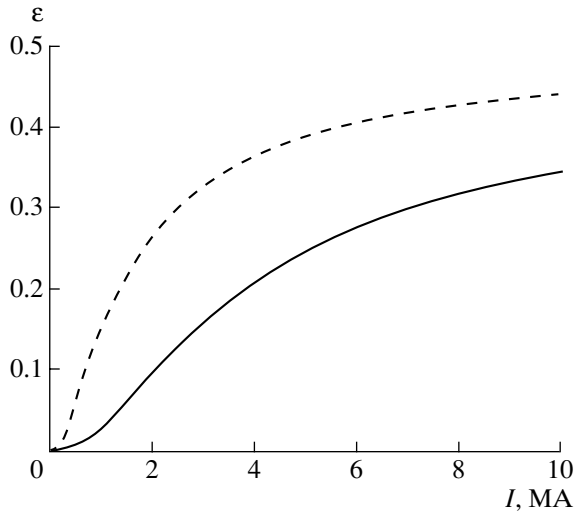

Fig. 1. Generation efficiency of argon *K*-shell radiation for pinch radii of 0.1 cm (solid line) and 0.02 cm (dashed line).

1063-780X/01/2711-0963$21.00 © 2001 MAIK "Nauka/Interperiodica"

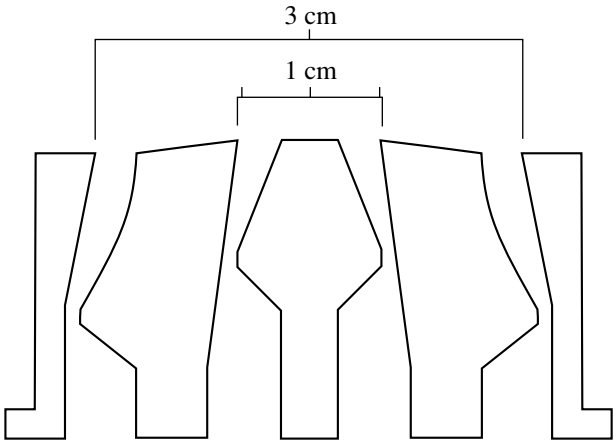

Fig. 2. Design of nozzles for producing a double-shell liner.

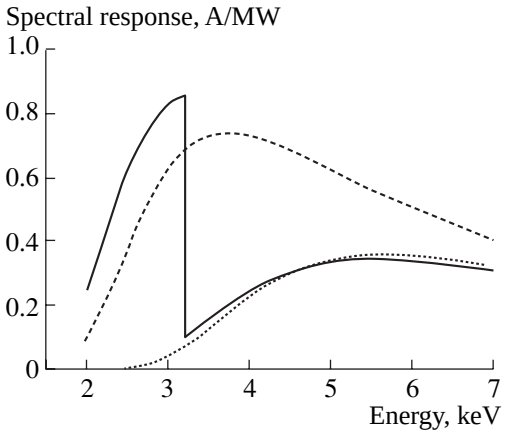

Fig. 3. Spectral response of XRDs with different filters: 11-μm teflon filter + 1.7 mg/cm^2 argon filter (solid curve), 22-μm teflon filter (dashed line), and 75-μm teflon filter (dotted line).

attained with a single-shell liner. Experiments described in this paper were carried out in the MIG generator at a liner current of ~1.4 MA and were, in part, a continuation of the experiments performed in [2]. The initial parameters of the liner were close (according to [2]) to the optimum parameters with respect to the maximum *K*-shell radiation yield. The measured dependence of the radiation yield on the liner length is also discussed.

2. EXPERIMENTAL SETUP AND DIAGNOSTIC TECHNIQUES

The MIG generator is the upgraded SNOP-3 facility [5, 6], in which the stored energy of the capacitor bank of the pulse transformer is increased from 140 to 300 kJ by increasing the number of capacitors from 48 to 108. The generator transmission line with a wave impedance of 0.65 Ω provides the maximum current up to 2 MA with a rise time of ~80 ns through a diode with an inductance of 25 nH. A nozzle design for producing a double-shell liner is shown in Fig. 2. The outer nozzle radii are 1.5 and 0.5 cm. The widths of the annular exits are 2 mm. The shape of the nozzles was selected so as to ensure the spatial separation of shell jets over at least a distance from the nozzle z = 1.5 cm. The area ratio between the outer and inner annular gaps in the nozzle throats is equal to 3/2. The liner length was specified by the position of the anode grid and was varied from 1.5 to 4.5 cm. The diode current was measured with Rogowski coils situated on the anode disk at radii of 35 and 5 cm. The pinch image in argon *K*- and *L*-shell radiation was recorded with pinhole cameras. The power and the spectrum of *K*-shell radiation was measured with three X-ray diodes (XRD) with an aluminum cathode and different filters: (i) 11-μm teflon filter + 1.0- to 1.8-mg/cm^2 argon filter; (ii) 22-μm teflon filter; and (iii) 75-μm teflon filter (Fig. 3). To calculate the XRD spectral response, we used the available data on the quantum efficiency of aluminum cathodes [7] and the filter transmission [8]. The argon filter was formed by means of pulsed gas puffing into the diagnostic line-of-sight region [9]. The argon *K* edge (3.2 keV) is located between the He_α and H_α lines of the helium- and hydrogen-like argon, respectively, which makes it possible to separate out the He_α line emission with the help of the argon filter. As is seen in Fig. 3, the difference between the signals from the detectors with the argon filter and the 75-μm teflon filter determines the intensity of the He_α line. The recombination radiation power (>4.1 keV) was measured by a detector with a 75-μm teflon filter and then was corrected by subtracting the contribution from the measured He_α radiation. The detector with a 22-μm teflon filter measured the total power in *K*-shell radiation. Absolute spectral measurements of *K*-shell radiation performed with the XRD allowed us to simplify the procedure of determining the ion density n_i and the electron temperature T_e of the pinch plasma. The procedure is based on the comparison of the measured values of the pinch diameter, the power (energy) of *K*-shell radiation, and the ratio between the intensities of He_α and H_α lines with the calculations by the collisional–radiative equilibrium (CRE) model [10]. In this case, it is not necessary to use a spectrograph to measure the relative line intensities. The time-resolved measurements are significantly simplified, because the time dependence of the line intensity ratio is directly deduced from the XRD signals. In this case, the intensity ratio between the He_α and H_α lines can be replaced with the intensity ratio between other spectral intervals that are more convenient for measurements and have a pronounced dependence on the electron temperature. In this paper, we estimated the plasma parameters from the ratio of the radiation yield

in the He_α line to the total radiation yield in other *K* lines.

3. EXPERIMENTAL RESULTS

Figure 4 shows the waveforms of the current measured with the Rogowski coil placed at a radius of 5 cm and the total power of *K*-shell radiation from a 2.8-cm-long liner. The full width at half maximum of the radiation pulse is ~5 ns, and the peak power is about 10^{11} W. As follows from an analysis of a series of shots, the radiation pulse duration depends on the liner length, which may be attributed to the fact that pinching occurs at different times for different points along the *z*-axis. This circumstance, in particular, makes it difficult to measure the radiation power per unit length of the liner (this quantity is used to determine the parameters of the pinch plasma). The measurements showed that the radiation pulse duration from the liner segment $\Delta z = 1$ mm is no longer than 2 ns [11]. In some shots of this series, individual peaks with a duration of ~1.2 ns were observed in the radiation signals. It is reasonable to assume that these peaks arise from pinching of individual short segments of the liner. The measured durations of the radiation pulses from the entire liner of length *l* are well approximated by the expression $\tau[\text{ns}] = \tau_0 + 1.5\, l[\text{cm}]$, where $\tau_0 = 1.2$ ns. Note that τ_0 is close to the estimate for the inertial confinement time of the pinch, $2r_f/v_f \sim 0.8$ ns. This means that, when estimating the plasma parameters, it is reasonable to use the ratio E_r/τ_0 (where E_r is the total *K*-shell radiation yield per pulse) for the comparison with the power of *K*-shell radiation calculated by the CRE model. The scatter in the values of the radiation yield for liners of lengths 2.5–3 cm was in the range 600–850 J. The radiation yield decreased as *l* was decreased to 1.8 cm or increased to 4 cm. An analysis of the pinhole photographs shows that a compact pinch of radius $r_f \le 0.2$ mm is only formed in the anode region of the liner over a length of 15–20 mm. At $z > 20$ mm, the pinch radius measured in *L*-shell radiation was ~0.3–0.4 mm and the intensity of *K*-shell radiation was relatively low. The 15-mm distance from the nozzle corresponds to the estimate (at the Mach number $M = 4$) for the distance over which the jets of the shells are spatially separated. This means that the compact pinch intensively emitting *K*-shell radiation is formed only in the region where the double-shell structure of the liner is well pronounced. In a shot with a total radiation yield of 850 J (shot no. 27), the He_α radiation yield was 430 J and the recombination radiation yield was 160 J. Consequently, the radiation yield in all the other lines (except for the He_α line) was 240 J. According to calculations by the CRE model, such radiation yields within the given spectral intervals from the pinch of radius 0.2 mm can be obtained at the density $n_i \sim 10^{20}$ cm^{-3} and the temperature $T_e \sim 1.3$ keV. The efficiency, with which the energy transferred to the liner in shot no. 27 was converted into *K*-shell radiation, was ~8.4%.

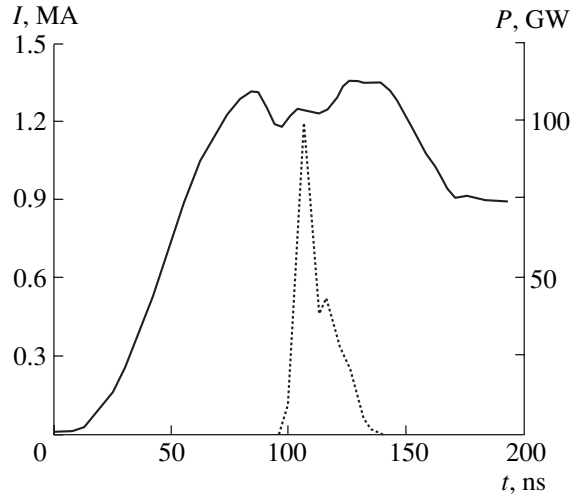

Fig. 4. Current through the load *I* (solid line) and the argon *K*-shell radiation power *P* (dashed line) for a 2.5-cm-long liner.

The conversion efficiency observed in our experiments and the results obtained in other devices in experiments with single-shell liners can be compared using the TLM, which predicts a universal dependence of the conversion efficiency on the energy transferred to the liner [4]. As was pointed out in [4], the radiation yield predicted by the TLM agrees satisfactorily with the experiments in the Saturn and Hawk devices assuming the radial compression ratio to be $r_0/r_f \sim 7$–8. The calculated *K*-shell radiation yield for the MIG device at a radial compression ratio of 8 is 90 J/cm at an efficiency of ~2.8%. For a compression ratio of 10, the calculated yield is 130 J/cm at an efficiency of ~3.6%. This means that, using a double-shell liner, it is possible to increase the conversion efficiency by a factor of ~3.

4. DISCUSSION AND CONCLUSIONS

It follows from zero-dimensional simulations (see also [13]) that, for the load of the MIG generator, the optimum liner length with respect to the energy deposition is 6–8 cm. At $\tau_r \ll \tau_i$, when the conversion efficiency ε is constant, the optimum length *l* with respect to the energy deposition coincides with the optimum length with respect to the radiation yield. At $\tau_r \ge \tau_i$, the efficiency ε depends on the current I_m ($\varepsilon \propto I_m^2$ at $\tau_r \gg \tau_i$) and the optimum liner length with respect to the radiation yield is shorter than the optimum liner length with respect to the energy deposition, because the current decreases with increasing *l* and, consequently, diode inductance. We calculated the *K*-shell radiation yield as a function of the liner length. The deposited energy was calculated by the zero-dimensional model, whereas for the radiation yield E_r, we used a TLM analytic dependence on the energy deposited in the liner. Figure 5 shows the dependences $E_r(l)$ for pinch radii of 1 and

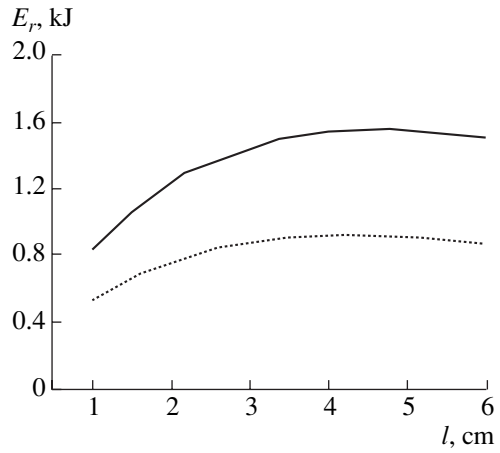

Fig. 5. Dependence of the argon *K*-shell radiation yield E_r on the liner length l for pinch radii of 0.05 cm (solid line) and 0.1 cm (dashed line).

0.5 mm. It can be seen in the figure that, first, the optimum length depends weakly on the pinch radius and, second, it makes no sense to increase l above 2.5–3 cm. This circumstance, along with the experimental fact that compact pinches cannot be formed for $z > 2$ cm, explains why the radiation yield decreases as the liner length increases to 4 cm. A decrease in the yield for $l < 2$ cm is obviously explained by the shape of the dependence $E_r(l)$.

In summary, it has been demonstrated that, at a liner current of ~1.4 MA, the double-shell liner structure promotes the formation of a compact pinch; as a result, the conversion efficiency of the electric energy into the energy of argon *K*-shell radiation increases. The optimum liner length with respect to the maximum *K*-shell radiation yield has been determined. The spectrum of argon *K*-shell radiation has been measured with a set of XRDs with different filters (including an argon gas filter). Using the measurements of the X-ray emission power (yield) in certain spectral intervals and calculations by the CRE model, the ion density and electron temperature of the pinch plasma have been estimated.

ACKNOWLEDGMENTS

I am grateful to V.I. Oreshkin for providing me with a computer code for calculating X-ray emission from the plasma column and to N.G. Motov and S.A. Chaikovsky for assistance in the experiments.

REFERENCES

1. N. R. Pereira and J. Davis, J. Appl. Phys. **64**, R1 (1988).
2. S. A. Sorokin and S. A. Chaikovsky, Fiz. Plazmy **22**, 992 (1996) [Plasma Phys. Reports **22**, 897 (1996)].
3. K. G. Whitney, J. W. Thornhill, J. P. Apruzese, and J. Davis, J. Appl. Phys. **67**, 1725 (1990).
4. D. Mosher, N. Qi, and M. Krishnan, IEEE Trans. Plasma Sci. **26**, 1052 (1998).
5. N. F. Kovsharov, A. V. Luchinsky, G. A. Mesyats, *et al.*, Prib. Tekh. Éksp., No. 6, 84 (1987).
6. A. V. Luchinsky, N. A. Ratakhin, V. F. Fedushchak, *et al.*, Izv. Vyssh. Uchebn. Zaved., Fiz. **38**, 58 (1995).
7. R. H. Day, P. Lee, E. B. Salomen, and D. J. Nagel, J. Appl. Phys. **52**, 639 (1981).
8. B. L. Henke, E. M. Gullikson, and J. C. Davis, At. Data Nucl. Tables **54**, 181 (1993).
9. S. A. Sorokin, Prib. Tekh. Éksp., No. 3, 136 (1999).
10. M. C. Coulter, K. G. Whitney, and J. W. Thornhill, J. Quant. Spectrosc. Radiat. Trasf. **44**, 443 (1990).
11. S. A. Sorokin and S. A. Chaikovsky, in *Proceedings of the 3rd International Conference on Dense Z-pinches, London, 1993*, p. 83.
12. V. I. Oreshkin and V. V. Loskutov, Preprint No. 5 (Institute of High-Current Electronics, Siberian Division, Russian Academy of Sciences, Tomsk, 1991).
13. J. Katzenstein, J. Appl. Phys. **52**, 676 (1981).

Translated by N. F. Larionova

Plasma Physics Reports, Vol. 27, No. 11, 2001, pp. 967–970. From Fizika Plazmy, Vol. 27, No. 11, 2001, pp. 1023–1026.

BEAMS IN PLASMA

Laser Radiation Guiding in a Plasma Channel Created by a Relativistic Electron Beam[1]

A. G. Khachatryan

Yerevan Physics Institute, Alikhanian Brothers Str. 2, Yerevan, 375036 Armenia

Received November 20, 2000; in final form, December 6, 2000

Abstract—The diffraction broadening of laser radiation restricts its efficient utilization in many applications. In this work, a method for laser radiation guiding in a density channel formed in a plasma by a relativistic electron beam is considered. The conditions and parameters of the relativistic beam ensuring the guiding are examined. © *2001 MAIK "Nauka/Interperiodica".*

Progress in the technology of high-intensity lasers opens new opportunities for the use of lasers in various branches of science and industry. In the last few years, the development of the chirped-pulse amplification technique [1] has permitted the production of subpicosecond laser pulses of multiterrawatt power with a peak intensity up to 10^{19} W/cm^2 and higher [2]. With such intensities, we are dealing with a new interaction range of laser radiation with matter, where the nonlinear effects are of crucial importance. At present, the interactions of high-power laser radiation with plasma have been actively investigated in connection with different applications: the excitation of strong plasma wake waves for the acceleration of charged particles with acceleration rates up to tens of GeV/m [3], the generation (due to nonlinear interaction with plasma) of radiation at harmonics of the laser carrier frequency [4], "photon acceleration" [5], X-ray sources [6], and others. We also note such application ranges of high-power laser radiation as Compton scattering, laser cooling of charged particle beams, and inertial confinement fusion.

The diffraction broadening of laser radiation is one of the main phenomena (frequently, the principal phenomenon) inhibiting the effective use of laser energy in many applications. In vacuum, the laser spot size r_s grows with the longitudinal coordinate according to the formula $r_s = r_0(1 + z^2/Z_R^2)^{1/2}$, where $Z_R = \pi r_0^2/\lambda$ is the Rayleigh length, r_0 is the minimum spot size at the focus ($z = 0$), and λ is the laser wavelength. For this reason, the intensity of radiation quickly decreases as the laser beam propagates. For high-intensity laser pulses, the value of Z_R is usually on the order of several millimeters. For instance, in the laser wakefield accelerator (LWFA) scheme, the energy gain of the electrons that are accelerated by the longitudinal field of the wake wave excited by a short laser pulse in a plasma is limited by the value $e\pi Z_R E_z$ [3], where E_z is the amplitude of the accelerating electric field of the plasma wave and e is the electron charge. Thus, without optical guiding, the diffraction limits the laser–matter interaction distance to one or two Rayleigh lengths.

If the refractive index of a medium (in particular, plasma) is maximum at the axis of the laser beam and decreases in the radial direction, one can eliminate or slow down the process of diffraction broadening of laser radiation (see review [7] and the literature cited therein). For the laser power $P > P_c = 2c(e/r_e)^2[\omega/\omega_{pe}(r=0)]^2 \approx 17[\omega/\omega_{pe}(r=0)]^2$ GW, where $r_e = e^2/m_e c^2$ is the classical electron radius, ω is the laser frequency, and ω_{pe} is the plasma frequency, relativistic self-focusing takes place. However, for short pulses with the length $l \lesssim \pi c/\omega_{pe}$, relativistic self-focusing is inefficient for preventing diffraction broadening [7]. In experiments, the plasma channel is usually created in a gas or plasma by a laser pulse, which, in turn, is also subject to diffraction. For example, the parabolic plasma density profile $n_p = n_0 + \Delta n r^2/r_0^2$ may provide the guiding of a low-intensity ($a_0^2 = (eE_0/m_e c\omega)^2 \ll 1$, where E_0 is the amplitude of laser radiation) Gaussian laser beam if $\Delta n \geq \Delta n_c = 1/\pi r_e r_0^2 = 1.13 \times 10^{20}/((r_0[\mu\text{m}])^2\ \text{cm}^{-3})$ [7]. The guiding of high-intensity laser radiation in a preformed plasma density channel at distances from several millimeters to 1–3 cm was demonstrated by different research groups. In this paper, we considered the creation of a plasma channel by a long relativistic electron beam (REB). The REB can traverse (without any significant change in the parameters), in the plasma, a distance much longer than the Rayleigh length for high-intensity laser pulses. The main advantage of the guiding method consists in the fact that the REB can form a plasma channel with a length greatly exceeding that obtained in experiments. Thus, the method in question could provide longer-term interaction of high-intensity

[1] This article was submitted by the author in English.

laser radiation with plasma, as well as with relativistic electrons.

Let us consider the propagation of a cylindrical electron beam with velocity $\mathbf{v}_0 = \mathbf{e}_z v_0$ in a cold homogeneous plasma. From Poisson's equation, the equation of motion, and the continuity equation for the plasma electrons (the plasma ions are assumed to be immobile due to their large mass), we have

$$\frac{\partial^2 \delta n_e}{\partial t^2} + \omega_{pe}^2(\delta n_e + n_b) = 0, \tag{1}$$

where $\delta n_e = n_e - n_0$, n_e is the density of the plasma electrons, n_0 is their equilibrium density, n_b is the density of beam electrons, and $\omega_{pe} = (4\pi n_0 e^2/m_e)^{1/2}$ is the plasma frequency. For a long beam with the density $n_b = n_b(r)$ and a length greatly exceeding the plasma wavelength $\lambda_p = 2\pi v_0/\omega_{pe}$, one can omit the first term in Eq. (1). Then, we have (see, e.g., [8])

$$n_e(r) = n_0 - n_b(r). \tag{2}$$

The plasma electrons are blown out of the beam, and density profile (2) is established. Although Eq. (1) was obtained for the linear case in which $n_b \ll n_0$, expression (2) also holds true for $n_b \leqslant n_0$ [8]. Hence, for a function $n_b(r)$ with a maximum at the axis, we have a plasma electron density channel. At the same time, the total electron density is constant ($n_e + n_b = n_0 = \text{const}$) and is equal to the density of the ions. Therefore, the force acting on the plasma ions is zero. In this paper, we will show that, in this case, the guiding of laser radiation is possible in spite of the fact that the total electron density is constant during the propagation of a long electron beam through the plasma. The problem of the formation of a plasma channel and the stability of the electron beam will be discussed below.

In order to consider the problem of laser radiation guiding in a plasma density channel with density profile (2), we first examine the dispersion properties of electromagnetic (EM) waves in the channel. For the electric field of the EM wave, from Maxwell's equations we have

$$\begin{aligned} \nabla \times \nabla \times \mathbf{E} &= \nabla(\nabla \mathbf{E}) - \Delta \mathbf{E} \\ &= -c^{-2}(\partial^2 \mathbf{E}/\partial t^2 + 4\pi \partial \mathbf{j}/\partial t), \end{aligned} \tag{3}$$

where $\mathbf{j} = -e(n_e \mathbf{v}_e + n_b \mathbf{v}_b)$ is the current density and $\mathbf{v}_e$ and $\mathbf{v}_b$ are the velocities of the plasma and beam electrons, respectively. For a linearly polarized wave, we have $\mathbf{E} = \mathbf{e}_x E_x = \mathbf{e}_x E_0 \exp[i(\omega t - kz)]$ and $\mathbf{B} = \mathbf{e}_y (ck/\omega) E_x$, where $\mathbf{B}$ is the magnetic induction. Then, from Eq. (3), we obtain

$$\begin{aligned} &(k^2 c^2 - \omega^2) E_x \\ &= 4\pi e[n_e(r) \partial v_{ex}/\partial t + n_b(r) \partial v_{bx}/\partial t]. \end{aligned} \tag{4}$$

When deriving expression (4), we assumed that the plasma channel response to the propagation of laser radiation is linear; hence, the change in n_e and n_b under the action of the EM wave is negligible (i.e., the nonlinear terms $v_{ex}\partial n_e/\partial t$ and $v_{bx}\partial n_b/\partial t$ are ignored). This takes place when $a_0^2 = (eE_0/m_e c\omega)^2 \ll 1$ [3]. To be exact, in our case, Eq. (4) is valid if the change in the plasma electron density under the action of the EM wave (which is proportional to a_0^2) is much less than the change in the density under the action of the electron beam; i.e., $a_0^2 \ll n_b/n_0$. The derivatives of the velocities v_{ex} and v_{bx} on the right-hand side of Eq. (4) can be obtained from the equations of motion

$$\frac{\partial v_{ex}}{\partial t} = -\frac{e}{m_e} E_x, \tag{5.1}$$

$$\left(\frac{\partial}{\partial t} + v_{bz}\frac{\partial}{\partial z}\right)(v_{bx}\gamma_b) = -\frac{e}{m_e}\left(E_x - \frac{v_{bz}}{c} B_y\right), \tag{5.2}$$

where $\gamma_b = (1 - \mathbf{v}_b^2/c^2)^{-1/2}$ is the relativistic factor. For an REB (i.e., for $\gamma_0 = (1 - v_0^2/c^2)^{-1/2} \gg 1$), we can set $v_{bx} \ll v_{bz} \approx v_0 \approx c$. Taking into account that $\gamma_0^2 v_{bx}^2/c^2 = (eE_x/m_e c\omega)^2 = a^2 \ll 1$, we obtain from Eq. (5.2) that $\partial v_{bx}/\partial t = -(e/m_e\gamma_0)E_x$. Substituting this expression and Eq. (5.1) into Eq. (4) and taking into account expression (2), we obtain the dispersion relation

$$\begin{aligned} \omega^2 &= k^2 c^2 + \omega_{pe}^2[1 - \alpha(1 - \gamma_0^{-1})] \\ &\approx k^2 c^2 + \omega_{pe}^2(1 - \alpha), \end{aligned} \tag{6}$$

where $\alpha = n_b(r)/n_0$. In the absence of a beam ($\alpha = 0$), we obtain from expression (6) an ordinary dispersion relation for transverse waves in a cold homogeneous plasma. Expression (6) is also valid for a circularly polarized wave, because it can be represented as a superposition of two linearly polarized waves. The EM wave does not "feel" the REB because the relativistic mass of the beam electrons is much larger than that of the plasma electrons (analogously, the plasma ions make a negligible contribution to the dispersion relation due to their large mass). For this reason, instead of an REB, one can use a beam of relativistic or nonrelativistic negatively charged ions. It is noteworthy that, instead of a continuous beam, one can use a long train of bunches separated by a distance less than the plasma wavelength. The EM wave can propagate both along and opposite to the REB. The latter is important for such applications as Compton scattering or a plasma-based free electron laser (FEL) [9].

For the refractive index $N = ck/\omega$ of the EM wave (laser radiation), we have from Eq. (6)

$$N^2 = 1 - [1 - \alpha(r)]\omega_{pe}^2/\omega^2. \tag{7}$$

The guiding of laser radiation is possible when $dN/dr = (\omega_{pe}^2/2N\omega^2)d\alpha/dr < 0$. Let the REB have a parabolic density profile ($\alpha = \alpha_0(1 - r^2/r_b^2)$ at $r < r_b$) and the laser radiation have a Gaussian profile ($a = (a_0 r_0/r_s)\exp(-r^2/r_s^2)$). Then, we have $n_e(r) = n_e(0) + n_b(0)r^2/r_b^2$, where $n_e(0) = n_0 - n_b(0)$. In this case, the plasma electron density channel produced by the REB provides the matched laser pulse guiding if $\Delta n_{ch} > 1/\pi r_e r_{ch}^2$ (see [7], Section VI). In our case, $\Delta n_{ch} = n_b(0)$ and $r_{ch} = r_b$. Then, we have the following guiding condition:

$$n_b(0) > 1.13 \times 10^{20}/((r_b\ \mu\text{m})^2\ \text{cm}^{-3}). \quad (8)$$

The use of a CO_2 laser pulse ($\lambda = 10$ μm) as a driver in the resonant LWFA has certain advantages [10]. For a CO_2 laser, the longitudinal and transverse pulse sizes are about several hundreds of a micrometer; the peak intensity is $I_{\max} \sim 10^{16}$ W/cm^2; the power is $P \sim 50$ TW; and the plasma density is relatively low, $n_0 \approx 3 \times 10^{15}$ cm^{-3} [10]. The latter implies $n_b(0) \sim 10^{14}$–10^{15} cm^{-3} for laser guiding. For example, for $r_b = r_s = 2r_0 = 600$ μm, from condition (8) we have $n_b(0) > 3.14 \times 10^{14}$ cm^{-3}. The Rayleigh length for the laser wavelength $\lambda = 10$ μm is $Z_R \approx 2.8$ cm.

The linear approximation ($\delta n_e \ll n_0$) considered above is valid for $a_0^2 \ll \alpha_0 \ll 1$. As this condition fails to hold, the mathematical description of the problem becomes rather complicated, but the guiding again is possible. Moreover, for $a_0^2 \gtrsim \alpha_0$, the guiding condition (8) can weaken, first, because the plasma electrons are blown out of the channel by the ponderomotive force (as a result, the guiding effect is amplified) and, second, due to relativistic self-focusing [7].

The large plasma density gradient in the channel may be formed by a dense REB with $n_b \gtrsim n_0$. In this case, a region is formed near the beam axis from which all the plasma electrons are expelled. For a thin beam (with the radius $r_b \ll \lambda_p$), such a region is formed when $n_b > n_0$; for a broad beam ($r_b \gg \lambda_p$), it is formed when $n_b > n_0/2$. The diameter of the region increases with increasing beam density [11]. The possibility of plasma channel creation by the leading portion of a narrow dense electron beam ($n_b \sim 10^{17}$ cm^{-3}, $r_b = 17$ μm) was discussed in [12]; however, the problem of laser guiding was not considered.

Now, we consider the problems of the plasma channel formation and the plasma stability. To avoid the excitation of the plasma wave by the leading edge of the electron beam, the REB density at the entrance to plasma should grow slowly; the rise time of the beam density being $t_b \gg \omega_{pe}^{-1}$. However, for applications related to charged particle acceleration, the excitation of the plasma wave by the electron beam may be desirable. During the propagation of the REB through the plasma, it is subject to various instabilities. The condition under which the instabilities can be neglected can be written as $\delta\Delta t \lesssim 3$, where δ is the instability growth rate and Δt is the time during which the electron beam propagates through the plasma. For an REB, we have $\Delta t \approx l/c$, where l is the length of the plasma column. The fastest instability is the beam–plasma instability, which results in the excitation of a plasma wave with wave number $k \approx \omega_{pe}/v_0$. Eventually, the onset of the beam–plasma instability leads to the breaking of the beam into bunches separated by a distance equal to the period of the plasma wave. The growth rate of the beam–plasma instability for waves propagating along the electron beam axis is (see, e.g., [13])

$$\delta = (3^{1/2}/2^{4/3})\omega_{pe}(n_b/n_0)^{1/3}/\gamma_0. \quad (9)$$

It follows from formula (9) that the growth rate of the beam–plasma instability decreases with increasing energy of the beam electrons; i.e., for sufficiently large γ_0, the instability can be neglected. According to formula (9), the instability does not develop when

$$\gamma_0 \gtrsim \gamma_* \sim 4.3 \times 10^{-7} n_0^{1/2}\ \text{cm}^{-3}\ (n_b/n_0)^{1/3} l\ \text{cm}. \quad (10)$$

For $n_0 = 3 \times 10^{15}$ cm^{-3}, $n_b(0)/n_0 = 0.1$, and $l = 30$ cm, we have $\gamma_* \sim 300$. The onset of the beam–plasma instability may be desirable for a number of applications. For a long laser pulse (with a duration of $\tau_L \gg \omega_{pe}^{-1}$), the beam–plasma instability can provide the effective modulation of the laser pulse, which will result in the generation of a strong plasma wave, as in the self-modulated LWFA [3] but with the laser power below the critical power P_c.

Let us consider the problem of guiding from the energetic standpoint. The maximum energy densities of the REB and laser beam are $W_{\text{REB}} = m_e c^2 \gamma_0 n_b(0)$ and $W_{\text{Las}} = E_0^2/8\pi = (m_e c\omega/e)^2 a_0^2/8\pi$, respectively. For their ratio, we have

$$\kappa \equiv \frac{W_{\text{REB}}}{W_{\text{Las}}} = \frac{2\gamma_0[n_b(0)/n_0]}{a_0^2}\left(\frac{\lambda}{\lambda_p}\right)^2. \quad (11)$$

For $n_0 = 3 \times 10^{15}$ cm^{-3} ($\lambda_p = 600$ μm), $n_b/n_0 = 0.1$, $\gamma_0 = 300$, $\lambda = 10$ μm, and $a_0^2 = 0.468$ (which corresponds to the peak intensity of a circularly polarized laser beam $I_{\max} \approx 1.3 \times 10^{16}$ W/cm^2 [10]), it follows from expression (11) that $\kappa \approx 3.6 \times 10^{-2}$. For $n_0 = 10^{14}$ cm^{-3}, $n_b/n_0 = 0.1$, $\gamma_0 = 300$, $\lambda = 1$ μm, and $a_0^2 = 0.05$ (which corresponds to the laser beam intensity $I_{\max} \approx 1.4 \times 10^{17}$ W/cm^2), we have $\kappa \approx 1.08 \times 10^{-4}$. Thus, the REB allows one to guide laser radiation with an energy density much higher than that of the REB. For the parame-

ters of the problem of practical interest, the total REB energy $\varepsilon_{REB} \sim \pi r_b^2 l_{REB} W_{REB}$ is less than the total energy of laser beam $\varepsilon_{Las} \sim \pi r_0^2 l_{Las} W_{Las}$; here, l_{REB} and l_{Las} are the lengths of the REB and laser beam, respectively.

Thus, we have shown that an REB can form a plasma channel in which laser radiation guiding is possible. The considered guiding method is based on the capacity of an REB to traverse (without a significant change in the parameters), in the plasma, a distance much longer than the diffraction length of high-intensity laser radiation. The plasma electrons are blown out of the region occupied by the REB; as a result, a plasma channel is formed. It has been shown that, due to the large relativistic factor of the REB, its contribution to the dispersion properties of the channel is negligible. The method under consideration permits a significant increase in the time during which the laser pulse interacts with the plasma and REB and, hence, in the efficiency of utilizing the radiation energy. This method is interesting for such applications as LWFA, X-ray generation, and plasma-based FEL.

ACKNOWLEDGMENTS

I am grateful to B. Hafizi, R. Hubbard, and P. Sprangle (Naval Research Laboratory, Washington, DC) for helpful discussions. This work was supported by the International Science and Technology Center, project no. A-405.

REFERENCES

1. D. Strickland and G. Mourou, Opt. Commun. **56**, 219 (1985).
2. G. A. Mourou, C. P. J. Barty, and M. D. Perry, Phys. Today **51**, 22 (1998).
3. E. Esarey, P. Sprangle, J. Krall, and A. Ting, IEEE Trans. Plasma Sci. **24**, 252 (1996).
4. P. Sprangle, E. Esarey, and A. Ting, Phys. Rev. A **41**, 4463 (1990).
5. S. C. Wilks, J. M. Dawson, W. B. Mori, *et al.*, Phys. Rev. Lett. **62**, 2600 (1989).
6. N. H. Burnett and P. B. Corkum, J. Opt. Soc. Am. B **6**, 1195 (1989).
7. E. Esarey, P. Sprangle, J. Krall, and A. Ting, IEEE J. Quantum Electron. **33**, 1879 (1997).
8. D. Hammer and N. Rostoker, Phys. Fluids **13**, 1831 (1970); A. A. Rukhadze and V. G. Rukhlin, Zh. Éksp. Teor. Fiz. **61**, 177 (1971) [Sov. Phys. JETP **34**, 93 (1972)].
9. K. Nakajima, M. Kando, T. Kawakubo, *et al.*, Nucl. Instrum. Methods Phys. Res. A **375**, 575 (1996).
10. I. V. Pogorelsky, Nucl. Instrum. Methods Phys. Res. A **410**, 524 (1998).
11. I. A. Kotel'nikov and V. N. Khudik, Fiz. Plazmy **23**, 146 (1997) [Plasma Phys. Rep. **23**, 130 (1997)].
12. G. Shvets and N. J. Fisch, Phys. Rev. E **55**, 6297 (1997).
13. A. B. Mikhailovskii, *Theory of Plasma Instabilities* (Nauka, Moscow, 1971; Consultants Bureau, New York, 1974), Vol. 1.

Plasma Physics Reports, Vol. 27, No. 11, 2001, pp. 971–978. Translated from Fizika Plazmy, Vol. 27, No. 11, 2001, pp. 1027–1034.

PLASMA DIAGNOSTICS

Small-Angle Scattering of an Extraordinary Wave near the Upper Hybrid Resonance

E. Z. Gusakov* and A. V. Surkov**

Ioffe Physicotechnical Institute, Russian Academy of Sciences, Politekhnicheskaya ul. 26, St. Petersburg, 194021 Russia

**e-mail: Evgeniy.Gusakov@pop.ioffe.rssi.ru*

***e-mail: a_surkov@aport2000.ru*

Received May 22, 2001

Abstract—The small-angle scattering of an extraordinary wave by plasma density fluctuations near the upper hybrid resonance is analyzed. It is shown that the efficiency of the small-angle scattering increases markedly as the upper hybrid resonance is approached. The power lost by the probing wave is calculated as a function of distance from the upper hybrid resonance, the parameters of the wavenumber spectrum of density fluctuations, and plasma parameters. The estimates obtained indicate that small-angle scattering, first, may have a strong impact on the experimental results obtained from the enhanced-scattering diagnostic and, second, may be the main cause of the broadening of the frequency spectrum of a signal recorded by this diagnostic technique.

1. INTRODUCTION

According to current opinions, ion-temperature-gradient (ITG) driven ion drift waves play a leading role in the anomalous ion energy transport in tokamaks. The same is true of the role played by the electron-temperature-gradient (ETG) driven electron drift waves in the anomalous electron energy transport. This circumstance has stimulated interest in investigating the behavior of the spectra of small-scale low-frequency plasma turbulence during Ohmic and auxiliary heated discharges, as well as during transitions to improved energy and particle confinement modes.

A diagnostic technique based on the effect of enhanced scattering of microwaves [1] is an efficient tool for studying small-scale plasma density fluctuations. This effect, which is observed when an extraordinary electromagnetic wave is scattered by plasma density fluctuations near the upper hybrid resonance (UHR), is associated with an increase in the potential component of the wave electric field as the UHR is approached.

The enhanced-scattering diagnostic implies that an extraordinary wave is launched into the plasma from the side of the stronger magnetic field along the plasma density gradient. The signals recorded are waves that are scattered backward and have the same polarization as the launched waves.

The effect of the increase in the wave vector of the probing wave in the vicinity of the UHR makes it possible to investigate small-scale plasma density fluctuations. The decrease in the group velocity in this region, accompanied by an increase in the field amplitudes of the probing and scattered waves, leads to the amplification of the scattered signal. That the probing wave is scattered mainly in the UHR region provides high spatial resolution for measurements. The frequency spectrum of the recorded signals contains information about the frequency spectrum of fluctuations, and the wavenumber spectra of fluctuations can be obtained from the time-of-flight and correlation modifications of the enhanced-scattering diagnostic technique [2, 3].

Note that the frequency shift of the backscattered signal corresponds to the frequency of fluctuations that scatter the probing wave in the backward direction only if the probing wave is not acted upon by large-scale plasma turbulence (which dominates the fluctuation spectrum and results in the small-angle scattering) before being scattered. When the probing wave experiences numerous small-angle scatterings, the backscattered signal contains information about the frequency spectra of both small-scale fluctuations and large-scale turbulence. Consequently, in order to correctly interpret the experimental results, it is necessary to know how important is the role played by the small-angle scattering during the propagation of the probing wave with a given directional pattern in the presence of plasma density fluctuations. In this paper, the effect of the small-angle scattering on the propagation of an extraordinary wave in the vicinity of the UHR is investigated using the first Born approximation, i.e., to the first order in the fluctuation amplitude. We calculate the Poynting vector of an extraordinary wave scattered by an ensemble of plasma density fluctuations and estimate the fluctuation level above which the probing wave is strongly scattered in the near-forward directions.

1063-780X/01/2711-0971$21.00

2. EMISSION OF WAVES IN AN INHOMOGENEOUS PLASMA

We consider a cold collisionless plasma in a magnetic field. We direct the z-axis along the magnetic field and assume that the field and the plasma are both inhomogeneous in the x direction. The electric field $\mathbf{E}$ of the wave emitted by an external current harmonic with density $\mathbf{j}$ is described by the equation

$$-ik_y E_y' - ik_z E_z' + \left(\frac{\omega^2}{c^2}\varepsilon - k_y^2 - k_z^2\right)E_x + ig\frac{\omega^2}{c^2}E_y = \frac{4\pi\omega}{c^2}j_x,$$

$$E_y'' - ik_y E_x' - ig\frac{\omega^2}{c^2}E_x + \left(\frac{\omega^2}{c^2}\varepsilon - k_z^2\right)E_y + k_y k_z E_z = \frac{4\pi\omega}{c^2}j_y, \quad (1)$$

$$E_z'' - ik_z E_x' + k_y k_z E_y + \left(\frac{\omega^2}{c^2}\eta - k_y^2\right)E_z = \frac{4\pi\omega}{c^2}j_z,$$

where ε, η, and g are the elements of the plasma dielectric tensor. We assume that, in the UHR region, the plasma density profile is linear, $\varepsilon = (x - x_{UH})/l$, where l is the scale on which the plasma density varies.

When solving the problem of small-angle scattering, we assume that the external nonlinear current density is related to the plasma density fluctuations by

$$\mathbf{j} = e\delta n_e \mathbf{v}_E, \quad (2)$$

where $\mathbf{v}_E = \hat{\sigma}\mathbf{E}_i/(en_0)$ and $\hat{\sigma} = i\omega(\hat{\varepsilon} - \hat{I})/(4\pi)$ is the conductivity tensor of the plasma.

The emission of waves in an inhomogeneous plasma was previously studied in [4, 5] by using the Wentzel–Kramers–Brillouin (WKB) approximation, which we will use below. However, in those papers, the Green's function was calculated for a locally homogeneous plasma, whose inhomogeneity was taken into account only in matching the solution obtained with the WKB solution far from the localized current source. Note that, on the one hand, the applicability of this approach [4] to microwave scattering in an inhomogeneous plasma is questionable and, on the other hand, this approach is *a priori* inapplicable to the region where refraction is strong and, therefore, the amplitude of the emitted wave is governed exclusively by the detuning of the Bragg resonance. Unfortunately, the method based on the reciprocity theorem [1], being very efficient for calculating the backward scattering of signals in the UHR region, is, at the same time, very difficult to generalize to the case of small-angle scattering. That is why we will consider the problem of wave scattering in an inhomogeneous plasma in more detail.

The field of the emitted wave can be obtained from Eqs. (1) by varying the arbitrary constants. To do this, we solve the corresponding homogeneous equation (with $j_x = j_y = j_z = 0$) in the geometrical-optics approximation. We represent the sought-for electric field of the wave as

$$\mathbf{E} = \mathbf{E}^{(0)}(x)\exp\left\{i\int^x k_x(x')dx' + ik_y y + ik_z z\right\}.$$

Taking into account the paraxial character of the probing wave propagating along the plasma density gradient,

$$N_y = \frac{k_y}{\omega/c} \ll 1, \quad N_z = \frac{k_z}{\omega/c} \ll 1,$$

we obtain the following expressions for the refractive index of the extraordinary wave and for the polarization of the wave electric field:

$$\left(\frac{k_x c}{\omega}\right)^2 = N_x^2 = \varepsilon - \frac{g^2}{\varepsilon} - N_y^2 - A(x)N_z^2,$$
$$\text{where} \quad A(x) = 1 + \frac{g^2\eta}{\varepsilon^2(\varepsilon - \eta - g^2/\varepsilon)}, \quad (3)$$

$$E_x^{(0)} = \frac{N_x \mp iN_y\varepsilon/g}{N_y \pm iN_x\varepsilon/g}E_y^{(0)},$$
$$E_z^{(0)} = \frac{N_z}{N_x}\frac{N_x \mp iN_y\varepsilon/g}{N_y \pm iN_x\varepsilon/g}E_y^{(0)}, \quad (4)$$

where the upper and lower signs refer to the waves propagating toward ($N_x > 0$) and away from ($N_x < 0$) the UHR, respectively.

Since the probing wave is scattered primarily in the vicinity of the UHR, we neglect, for simplicity, the second terms in the numerators of expressions (4) for E_x and E_y (these terms are important only at the plasma boundary). As a result, we obtain

$$E_x^{(0)} \simeq \frac{N_x}{N_y \pm iN_x\varepsilon/g}E_y^{(0)}, \quad E_z^{(0)} \simeq \frac{N_z}{N_y \pm iN_x\varepsilon/g}E_y^{(0)}. \quad (5)$$

The amplitude $E_y^{(0)}$ can be found from the condition that the projection of the Poynting vector onto the x-axis be conserved:

$$S_x = \frac{c^2}{8\pi\omega}\left|E_y^{(0)}\right|^2 \frac{k_x^3\varepsilon^2/g^2}{k_y^2 + k_x^2\varepsilon^2/g^2} = S_x^{(i)} = \frac{c}{8\pi}|E_0|^2, \quad (6)$$

where E_0 is the amplitude of the wave field in vacuum. As a result, relationships (5) and (6) give the following

expressions for the field amplitudes $E_x^{(0)}$, $E_y^{(0)}$, and $E_z^{(0)}$:

$$E_y^{(0)} = E_0\frac{gN_y \pm i\varepsilon N_x}{\varepsilon N_x^{3/2}}, \quad E_x^{(0)} = E_0\frac{g}{\varepsilon N_x^{1/2}}, \qquad E_z^{(0)} = E_0\frac{gN_z}{\varepsilon N_x^{3/2}}. \tag{7}$$

Taking into account the corrections associated with the propagation of waves at small angles with respect to the plasma density gradient, we can write the refractive index for an ordinary wave in the form

$$N_{0x}^2 = \eta - N_y^2 - \frac{\eta(\eta-\varepsilon)}{g^2+\varepsilon(\eta-\varepsilon)}N_z^2. \tag{8}$$

In the WKB approximation, the corresponding expressions for the polarization of the wave electric field are

$$E_{0x}^{(0)} = \frac{(N_{0x}^2-\varepsilon)N_{0x}N_z}{\varepsilon^2-g^2-\varepsilon N_{0x}^2}E_{0z}^{(0)}, \qquad E_{0y} = \frac{\mp igN_{0x}N_z + (N_{0x}^2-\varepsilon)N_yN_z}{\varepsilon^2-g^2-\varepsilon N_{0x}^2}E_{0z}^{(0)}. \tag{9}$$

The amplitude $E_{0z}^{(0)}$ in plasma and vacuum can be related through the condition for the Poynting vector to be conserved:

$$E_{0z}^{(0)} = \frac{E_0}{\sqrt{N_{0x}}}. \tag{10}$$

Having derived solutions to the set of homogeneous equations, we can find the field of the wave emitted by the current harmonic with density **j**. To do this, we substitute the component E_x found from the first equation into the second and third equations. We thus arrive at the following set of two second-order inhomogeneous differential equations with variable coefficients:

$$E_y''\left(1+\frac{N_y^2}{\varepsilon_1}\right) + E_z''\frac{N_yN_z}{\varepsilon_1} - E_y'\frac{N_y^2}{l\varepsilon_1^2} + E_z'\left(g\frac{\omega}{c}\frac{N_z}{\varepsilon_1} - \frac{N_yN_z}{l\varepsilon_1^2}\right)$$
$$+ E_y\left[\frac{\omega^2}{c^2}\left(\varepsilon - N_z^2 - \frac{g^2}{\varepsilon_1}\right) + g\frac{\omega}{c}\frac{N_y}{l\varepsilon_1^2}\right] + \frac{\omega^2}{c^2}E_zN_yN_z = F_y,$$

$$E_y''\frac{N_yN_z}{\varepsilon_1} + E_z''\left(1+\frac{N_z^2}{\varepsilon_1}\right) + E_y'\left(-g\frac{\omega}{c}\frac{N_z}{\varepsilon_1} - \frac{N_yN_z}{l\varepsilon_1^2}\right)$$
$$- E_z'\frac{N_z^2}{l\varepsilon_1^2} + E_y\left(\frac{\omega^2}{c^2}N_yN_z + g\frac{\omega}{c}\frac{N_z}{l\varepsilon_1^2}\right) + E_z\frac{\omega^2}{c^2}(\eta - N_y^2) = F_z,$$

where we introduced the notation $\varepsilon_1 = \varepsilon - N_\perp^2$. The right-hand sides of these equations can be written in vector form:

$$\mathbf{F} = \frac{4\pi}{c}\begin{pmatrix} \frac{\omega}{c}j_y + i\frac{N_y}{\varepsilon_1}j_x' + \frac{i}{\varepsilon_1}\left(g\frac{\omega}{c} - \frac{N_y}{l\varepsilon_1}\right)j_x \\ \frac{\omega}{c}j_z + i\frac{N_z}{\varepsilon_1}j_x' - \frac{iN_z}{l\varepsilon_1^2}j_x \end{pmatrix}.$$

We represent the solution to this set of equations as

$$\mathbf{E} = C_1\mathbf{E}_1 + C_2\mathbf{E}_2 + C_3\mathbf{E}_3 + C_4\mathbf{E}_4.$$

Here, subscripts 1 and 2 refer, respectively, to an extraordinary wave propagating toward the UHR and a wave propagating in the opposite direction; subscripts 3 and 4 stand for the corresponding ordinary modes; and **E** and $\mathbf{E}_i$ are two-dimensional vectors, the latter, E_i, being determined by relationships (7), (9), and (10). Varying the arbitrary constants yields the following set of four linear algebraic equations for the derivatives of the coefficients C_i:

$$C_1'\mathbf{E}_1 + C_2'\mathbf{E}_2 + C_3'\mathbf{E}_3 + C_4'\mathbf{E}_4 = 0,$$
$$P(C_1'\mathbf{E}_1' + C_2'\mathbf{E}_2' + C_3'\mathbf{E}_3' + C_4'\mathbf{E}_4') = \mathbf{F},$$

$$P = \begin{pmatrix} 1+\frac{N_y^2}{\varepsilon_1} & \frac{N_yN_z}{\varepsilon_1} \\ \frac{N_yN_z}{\varepsilon_1} & 1+\frac{N_z^2}{\varepsilon_1} \end{pmatrix}.$$

We omit the constant amplitude E_0 and take into account the relationship $\varepsilon \ll 1$, which is valid in the vicinity of the UHR. Then, we represent this set of equations in the form

$$A_{11}\mathbf{X}_1 + A_{12}\mathbf{X}_2 = 0, \qquad A_{21}\mathbf{X}_1 + A_{22}\mathbf{X}_2 = P^{-1}\mathbf{F}, \tag{11}$$

where

$$A_{11} = \begin{pmatrix} E_{1y} & E_{2y} \\ E_{1z} & E_{2z} \end{pmatrix} = \begin{pmatrix} N_y\sqrt{N_x} - \frac{ig}{\sqrt{N_x}} & N_y\sqrt{N_x} + \frac{ig}{\sqrt{N_x}} \\ N_z\sqrt{N_x} & N_z\sqrt{N_x} \end{pmatrix}$$
$$\times \begin{pmatrix} \exp\left\{i\int^x k_x dx\right\} & 0 \\ 0 & \exp\left\{-i\int^x k_x dx\right\} \end{pmatrix},$$

$$A_{12} = \begin{pmatrix} E_{3y} & E_{4y} \\ E_{3z} & E_{4z} \end{pmatrix}$$

$$= \begin{pmatrix} \frac{iN_z}{g}\sqrt{\eta} - \eta\frac{N_yN_z}{g^2} & -\frac{iN_z}{g}\sqrt{\eta} - \eta\frac{N_yN_z}{g^2} \\ \eta^{-1/4} & \eta^{-1/4} \end{pmatrix}$$

$$\times \begin{pmatrix} \exp\left\{i\frac{\omega}{c}\int^x \sqrt{\eta}\,dx\right\} & 0 \\ 0 & \exp\left\{-i\frac{\omega}{c}\int^x \sqrt{\eta}\,dx\right\} \end{pmatrix},$$

$$A_{21} = A_{11}\begin{pmatrix} 1 & 0 \\ 0 & -1 \end{pmatrix} ik_x, \quad A_{22} = A_{12}\begin{pmatrix} 1 & 0 \\ 0 & -1 \end{pmatrix} i\frac{\omega}{c}\sqrt{\eta},$$

$$\mathbf{X}_1 = \begin{pmatrix} C_1' \\ C_2' \end{pmatrix}, \quad \mathbf{X}_2 = \begin{pmatrix} C_3' \\ C_4' \end{pmatrix}.$$

We solve Eqs. (11) by the substitution method and, taking into account the paraxial character of the probing wave, neglect the terms in the elements of the matrix $A_{22}A_{12}^{-1}A_{11}$ that are small in comparison with the corresponding elements of the matrix A_{21}. As a result, we obtain

$$\mathbf{X}_1 = (A_{21} - A_{22}A_{12}^{-1}A_{11})^{-1}P^{-1}\mathbf{F} = -i\frac{c}{\omega}\begin{pmatrix} \exp\left\{-i\frac{\omega}{c}\int^x \sqrt{\eta}\,dx\right\} & 0 \\ 0 & \exp\left\{i\frac{\omega}{c}\int^x \sqrt{\eta}\,dx\right\} \end{pmatrix}$$

$$\times \begin{pmatrix} \frac{gN_xN_y + i(g^2 + \eta^{1/4}N_x^2N_z^2)}{2g\sqrt{N_x}(g^2 + N_x^2N_y^2 + \eta^{1/4}N_x^2N_z^2)} & \frac{\eta^{1/4}\sqrt{N_x}(g - iN_xN_y)N_z}{2g(g^2 + N_x^2N_y^2 + \eta^{1/4}N_x^2N_z^2)} \\ -\frac{gN_xN_y - i(g^2 + \eta^{1/4}N_x^2N_z^2)}{2g\sqrt{N_x}(g^2 + N_x^2N_y^2 + \eta^{1/4}N_x^2N_z^2)} & -\frac{\eta^{1/4}\sqrt{N_x}(g + iN_xN_y)N_z}{2g(g^2 + N_x^2N_y^2 + \eta^{1/4}N_x^2N_z^2)} \end{pmatrix} P^{-1}\mathbf{F}, \tag{12}$$

where we can set

$$P^{-1}\mathbf{F} \simeq \frac{4\pi}{c}\begin{pmatrix} i\frac{N_y}{\varepsilon}j_x' - \frac{\omega}{c}\frac{i}{\varepsilon_1}\left(1 - \frac{N_y^2}{\varepsilon}\right)j_x \\ i\frac{N_z}{\varepsilon}j_x' + \frac{\omega}{c}\frac{i}{\varepsilon_1}\frac{N_yN_z}{\varepsilon} \end{pmatrix}.$$

The two-dimensional vector $\mathbf{X}_2$, which contains the unknown coefficients C_3 and C_4, can be found from expression (12) with the help of the relationship

$$\mathbf{X}_2 = -A_{12}^{-1}A_{11}\mathbf{X}_1. \tag{13}$$

Expressions (12) and (13) constitute the desired solution to the problem of the field of the wave emitted by the external current in the vicinity of the UHR.

3. CALCULATION OF THE SIGNAL SCATTERED IN THE NEAR-FORWARD DIRECTION

In the case of scattering by a fluctuation harmonic with the wave vector $\mathbf{q}$ and frequency Ω,

$$\delta n_e(\mathbf{r}, t) = \delta n_{\mathbf{q}}\exp\{i\mathbf{qr} - i\Omega t\},$$

the main component of the nonlinear current with density (2) has the form

$$j_x = \frac{\delta n_{\mathbf{q}}}{n}\sigma_\perp E_{ix}\exp\{i\mathbf{qr} - \Omega t\}, \tag{14}$$

where

$$\sigma_\perp = \frac{ne^2\omega}{im_e(\omega^2 - \omega_{ce}^2)} \simeq \frac{\omega}{4\pi i}.$$

In what follows, we can neglect the dependence on time by virtue of the relationship $\omega_i + \Omega = \omega$.

Since the main contribution to the amplitude of the scattered wave comes from the point at which the Bragg condition is satisfied, $\mathbf{k}_i + \mathbf{q} = \mathbf{k}$ (where $\mathbf{k}_i$ is the wave vector of the probing wave), the derivative of the nonlinear current density,

$$j_x \sim \exp\left\{iq_xx + i\int^x k_{xi}dx' + i(k_{yi} + q_y)y + i(k_{zi} + q_z)z\right\}$$

can be represented as

$$j_x' = ik_x j_x.$$

Taking into account the paraxial character of the probing wave, we can use expressions (12) and (13), together with the relationship $\varepsilon \ll 1$, to obtain

$$C_1' = -\frac{2\pi i}{c} N_x^{3/2} j_x \exp\left\{-i\int^x k_x(x')dx'\right\},$$
$$C_2' = \frac{2\pi i}{c} N_x^{3/2} j_x \exp\left\{i\int^x k_x(x')dx'\right\}, \quad (15)$$

where the wavenumber k_x of the scattered wave is determined by formula (3). The equations for the amplitudes of extraordinary waves propagating toward and away from the UHR have the form

$$C_3' = -\frac{2\pi i}{c} N_x^3 \eta^{1/4} N_z j_x \exp\left\{-i\int^x k_{0x}(x')dx'\right\},$$
$$C_4' = \frac{2\pi i}{c} N_x^3 \eta^{1/4} N_z j_x \exp\left\{i\int^x k_{0x}(x')dx'\right\},$$

where k_{0x} is determined by formula (8).

In the case of the scattering of a probing extraordinary wave by large-scale fluctuations ($q_x \ll k_{xi}$) in the UHR region, the amplitudes of the backscattered waves and the ordinary mode are exponentially small, because the wavenumber k_{xi} increases sharply as the UHR is approached, so that the Bragg condition for the corresponding processes is impossible to satisfy. Because of this, we restrict ourselves to calculating the amplitude C_1, which describes the small-angle scattering process.

We substitute expression (14) for the nonlinear current density into relationships (15) in order to reduce the equation for the amplitude of the forward-scattered wave to a form suitable for further analysis:

$$C_1' = \frac{2\pi}{c} E_0^i \frac{\delta n_q}{n} \sigma_\perp N_x^3 \exp\{if(x)\}, \quad (16)$$

where the phase is described by the expression

$$f(x) = q_x x + \int^x [k_{xi}(x') - k_x(x')]dx'. \quad (17)$$

The point where phase (17) is stationary gives the following Bragg condition, which determines the scattering point in an inhomogeneous plasma:

$$f'(x_s) = q_x + k_{xi}(x_s) - k_x(x_s) = 0.$$

With expression (3) for the refractive index of an extraordinary wave, this condition becomes

$$k_{xi} - k_x = \frac{1}{2k_x(x)}[q_y(2k_{yi} + q_y) + A(x)q_z(2k_{zi} + q_z)], \quad (18)$$

where

$$A(x) = 1 + \frac{g^2\eta}{\varepsilon^2(\varepsilon - \eta - g^2/\varepsilon)}.$$

In the vicinity of the UHR, the expression for $A(x)$ simplifies to $A \simeq -1/\varepsilon$, so that Eq. (18) becomes

$$q_y(2k_{yi} + q_y) - \frac{c^2}{\omega^2}k_x^2(x_s)q_z(2k_{zi} + q_z) = -2q_x k_x(x_s).$$

Using the stationary-phase method, we obtain from Eq. (16) the desired amplitude C_1:

$$C_1 = \frac{2\pi}{c} E_0 \frac{\delta n_q}{n} \sigma_\perp N_x^3(x_s) \times \exp\{i(f(x_s) + \pi/4)\}\sqrt{\frac{2\pi}{f''(x_s)}}, \quad (19)$$

where the second derivative of the phase under the square root in the denominator,

$$f''(x) = k_{xi}' - k_x' = \frac{c}{\omega}\frac{N_x(x)}{4l}[-q_y(2k_{yi} + q_y) + N_x^2(x)q_z(2k_{zi} + q_z)]$$

determines the length of the wave interaction region (the coherent-scattering length)

$$\delta x = \frac{1}{\sqrt{f''(x_s)}}. \quad (20)$$

In the resonance case in which the Bragg condition is satisfied over the entire plasma volume, the wave interaction region becomes infinitely long:

$$\delta x \longrightarrow \infty, \quad \begin{cases} q_x \longrightarrow 0 \\ q_y \longrightarrow -2k_{yi} \\ q_z \longrightarrow -2k_{zi}. \end{cases} \quad (21)$$

Note that, strictly speaking, this case cannot be described by the stationary-phase method. Moreover, the necessary condition for the validity of expression (19), which was obtained using this method, is the inequality

$$\delta x \ll |x_s - x_{UH}|,$$

where x_{UH} is the UHR point. The case in which this condition fails to hold will be analyzed below.

With the help of expression (19) for the amplitude C_1 and expressions (5) for the polarization of the wave electric field, the projection of the Poynting vector of

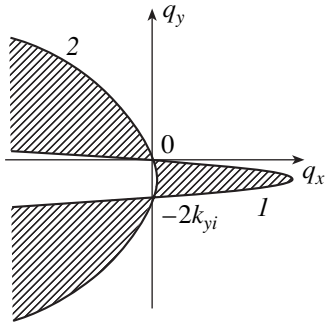

Region of integration over q_x and q_y: curves *1* and *2* correspond to the Bragg conditions at the plasma boundary and at the current point, respectively.

the scattered wave onto the direction in which the plasma is inhomogeneous can be represented as

$$S_x = \frac{c}{8\pi}|C_1|^2 = \frac{4\pi^2}{c^2}S_x^{(i)}\left|\frac{\delta n_{\mathbf{q}}}{n}\right|^2|\sigma_\perp|^2 N_x^6(x_s)\frac{2\pi}{|f''(x_s)|}. \quad (22)$$

It should be noted that, as the point x_s approaches the UHR, the energy flux density of the scattered wave increases very sharply: $S_x \sim N_x^5 \sim |x - x_{UH}|^{-5/2}$. This dependence allows us to conclude that, in the vicinity of the UHR, both backward and small-angle scattering processes are enhanced.

Expression (22) describes the scattering by one fluctuation harmonic. However, in a real plasma, there is an ensemble of fluctuations, each of which scatters the probing wave. Let us generalize expression (22) to this case by calculating the total Poynting vector of a probing wave with the wave vector $\mathbf{k}_i$, which is assumed to be scattered by an ensemble of fluctuations. We consider fluctuations with the spectral density

$$|\delta n_{\mathbf{q}}|^2 = \frac{\langle\delta n^2\rangle q_0\delta(q_z)}{2\pi(q_x^2 + q_y^2 + q_0^2)^{3/2}},$$

which is a good approximation for the large-scale component of the fluctuation spectra observed in experiments on CO_2 laser scattering in a tokamak [6]. Here, q_0 is the characteristic transverse (with respect to the magnetic field) wavenumber of the fluctuations and $\langle\delta n^2\rangle$ is the average of the squared fluctuation amplitude.

The total Poynting vector of the probing wave that is scattered before reaching the point x can be represented in integral form:

$$\frac{S(x)}{S^{(i)}} = \frac{4\pi^2}{c^2}\frac{\langle\delta n^2\rangle}{n^2}q_0|\sigma_\perp|^2 4l\frac{c^4}{\omega^4} \times\iint\limits_\Theta \frac{k_x^5(x_s)}{|q_y(2k_{yi}+q_y)|}\frac{dq_x dq_y}{(q_x^2+q_y^2+q_0^2)^{3/2}}, \quad (23)$$

where $k_x(x_s)$ is determined by the Bragg condition,

$$2q_x k_x(x_s) = -q_y(2k_{yi} + q_y), \quad (24)$$

and the contribution of all the scattering points $x_s < x$ is incorporated. The region of integration Θ is shown in the figure. At each point x_s, a probing wave propagating toward the UHR is scattered by fluctuations that satisfy the Bragg condition (24). In the space of wavenumbers of such fluctuations, the integration region Θ is bounded by curves corresponding to the Bragg condition at the plasma boundary and at the current point x.

In order to carry out integration over this region, we transform from the variables q_x and q_y to the variables $k_x(x_s)$ and q_y. Integration over q_y actually corresponds to integration along a curve determined by the Bragg condition at the scattering point x_s, while integration over $k_x(x_s)$ corresponds to integration over all of the scattering points between the plasma boundary ($k_x = \omega/c$) and the current point ($k_x(x)$). The Jacobian of the transformation is

$$dq_x dq_y = \left|\frac{q_y(2k_{yi}+q_y)}{2k_x^2}\right| dk_x dq_y.$$

In this case, the singularity in the denominator of the integrand in expression (23) (which corresponds to an increase in the length of the region of interaction between the modes) is removed; this indicates that fluctuations satisfying condition (21) do not dominate the scattering spectrum. In the new variables, expression (23) takes the form

$$\frac{S(x)}{S^{(i)}} = \frac{8\pi^2}{c^2}\frac{\langle\delta n^2\rangle}{n^2}|\sigma_\perp|^2 l q_0\frac{c^4}{\omega^4} \times\int\limits_{k_0}^{k_x(x)} k_x^3 dk_x\int\limits_{-\infty}^{+\infty}\frac{dq_y}{[q_y^2(2k_{yi}+q_y)^2/(4k_x^2) + q_y^2 + q_0^2]^{3/2}}. \quad (25)$$

Taking into account that the probing wave is paraxial ($k_{yi} \ll \omega_i/c \ll k_x$) and fluctuations are large-scale ($q_0 \ll k_x$), we can neglect the term $q_y^2(2k_{yi}+q_y)^2/(4k_x^2)$ in comparison with $q_y^2 + q_0^2$ and estimate the integral in expression (25) as

$$\int\limits_{-\infty}^{+\infty}\frac{dq_y}{[q_y^2(2k_{yi}+q_y)^2/(4k_x^2) + q_y^2 + q_0^2]^{3/2}} \simeq \frac{2}{q_0^2}.$$

Since the terms with k_{yi} only introduce small corrections, different components of the directional pattern of the antenna make equal contributions to the scattered radiation.

Substituting the above approximate expression for the integral into formula (25), we can readily take the resulting integral over k_x and thus obtain the following expression for the Poynting vector of the scattered

wave, divided by the absolute value of the Poynting vector of the probing wave:

$$\frac{S_x}{S^{(i)}} = \frac{\omega^2}{4c^2}\frac{\langle \delta n^2 \rangle}{n^2}\frac{l}{q_0}N_x^4(x). \quad (26)$$

The necessary condition for the validity of expression (26) is the inequality $S(x)/S^{(i)} < 1$, which determines the boundaries of the region where the Born approximation is applicable and describes the region of transition to multiple small-angle scattering.

On the other hand, the applicability region of expression (26) is restricted by the stationary-phase method, which was used to derive this expression. Thus, the requirement that the coherent-scattering length δx defined by relationship (20) be shorter than the distance from the scattering point to the UHR point yields the criterion

$$N_x^3 < \frac{clq_0^2}{\omega}. \quad (27)$$

At large values of the refractive index N_x, the contribution of the end part of the interval of integration over x to the integral becomes significant. At even larger values of the refractive index, the phase $f(x)$ is essentially unchanged. In this case, Eq. (16) for the amplitude C_1 is easy to integrate:

$$C_1 = \frac{4\pi}{c}E_0\frac{\delta n_{\mathbf{q}}}{n}\sigma_\perp l N_x(x)\exp\{if(x)\}.$$

We can see that the Poynting vector of the wave that is scattered by one fluctuation harmonic is independent of the wave vector. This circumstance allows us to obtain the following expression for the projection of the Poynting vector of the wave that is scattered by the full ensemble of fluctuations:

$$\frac{S}{S^{(i)}} = \frac{\omega^2}{c^2}\frac{\langle \delta n^2 \rangle}{n^2}l^2 N_x^2(x). \quad (28)$$

The criterion for the validity of this expression has the form

$$N_x^2 > q_0 l. \quad (29)$$

In order to match expressions (26) and (28), we consider Eq. (16) in the intermediate region where criterion (27) and inequality (29) both fail to hold. It turns out that, in this region, a significant contribution to the integral comes from the end part of the interval of integration. We can show that, for the values of q_x and q_y that typically make the main contribution to the integral over the spectrum, the second term in expression (17) for the phase can also be neglected, in which case the coefficient C_1 becomes

$$C_1 = \frac{2\pi}{c}E_0\frac{\delta n_{\mathbf{q}}}{n}\sigma_\perp l\int_1^{-\varepsilon(x)}\epsilon'^{-3/2}\exp\{-iq_x l\epsilon'\}d\epsilon' \simeq -\frac{2\pi}{c}E_0\frac{\delta n_{\mathbf{q}}}{n}\frac{\sigma_\perp l}{\sqrt{-\varepsilon}}\frac{\exp\{iq_x l\varepsilon\}}{3/2 - iq_x l\varepsilon}, \quad (30)$$

where $\varepsilon(x) = (x - x_{UH})/l$.

The expression for the energy flux density of the scattered waves can be obtained by integrating expression (30) over the fluctuation spectrum:

$$\frac{S}{S^{(i)}} \simeq \frac{\langle \delta n^2 \rangle}{n^2}\frac{\omega^2}{c^2}l^2\frac{N_x^4(x)}{q_0 l + 3/2N_x^2}. \quad (31)$$

This expression for the power lost by the probing wave during small-angle scattering is valid over the entire applicability region of the WKB approximation. When criterion (29) is satisfied, expression (31) coincides with expression (28) to within a constant coefficient on the order of unity. If the inequality opposite to (29) is satisfied, expression (31) passes over to expression (26).

Under conditions typical of the tokamak experiments of interest to us ($l = 10$ cm, $\omega_i/2\pi = 60$ GHz), the criterion for the applicability of the WKB approximation, which was used to derive the above formulas, is not too stringent:

$$\frac{1}{k_x^2}\frac{dk_x}{dx} = \frac{1}{2l}\frac{c^2}{\omega^2}k_x \ll 1.$$

The conditions under which the cold plasma approximation, used to derive the basic equations, fails to hold are far more restrictive. Thus, the cold plasma approximation is violated for

$$k_x \sim \frac{\omega}{c}\sqrt{\frac{c}{v_{Te}}},$$

in which case the conversion of an electromagnetic wave into a Bernstein mode becomes important [7].

Expression (31) implies that, because of the above-described effect of enhanced scattering, the small-angle scattering is sharply enhanced as the UHR is approached and the rate at which the probing wave loses its energy due to the small-angle scattering is highest precisely in the vicinity of the UHR. Let us estimate the corresponding refractive index of the probing wave for the parameters of experiments on backscattering in the UHR region in the FT-1 tokamak [8]. We set $\omega_i/c \sim 6$ cm^{-1}, $q_0 \sim 2$ cm^{-1}, $l \sim 2.5$ cm, and $\delta n/n_{UH} = 10^{-2}$. Then, in accordance with formula (28), the condition $S(x) = S^{(i)}$ gives $N_x(x) = 6.7$, so that we have $k_x = 40$ cm^{-1}. This value is smaller than the wavenumber corresponding to the maximum backscattering efficiency, $k_x =$

$q_x/2 = 50\ \text{cm}^{-1}$. On the other hand, at the plasma periphery, the value of the ratio $\delta n/n_{UH}$ may be larger than that used in our estimates by a factor of ten or more. This circumstance allows us to conclude that multiple small-angle scattering by large-scale plasma density fluctuations may play an important role in the formation of backscattering spectra in the UHR region. This nonlinear (in the fluctuation amplitude) regime will be treated in a separate paper.

4. CONCLUSION

Our calculations have shown that both the small-angle scattering and the backscattering of an extraordinary wave are enhanced as the wave approaches the UHR. Even when the scattering is relatively weak, large-scale plasma density fluctuations can completely scatter the probing wave. As a result, the spectrum of the probing wave can become broader at the expense of multiple scattering. Of course, this effect should be taken into account in interpreting the spectrum of backscattered radiation from the UHR region. Note that, since the small-angle scattering process is highly localized in the UHR region, the backscattering spectra may provide information about the level and spectra of large-scale plasma density fluctuations in the UHR region.

ACKNOWLEDGMENTS

We are grateful to Prof. A.D. Piliya for his interest in this work and critical comments. This study was supported in part by the Russian Foundation for Basic Research (project nos. 99-02-17975, 01-02-17926, and 00-15-96762) and INTAS (grant no. 97-11018) and the Ministry of Science and Technology of the Russian Federation.

REFERENCES

1. K. M. Novik and A. D. Pilia, Plasma Phys. Controlled Fusion **35**, 357 (1993).
2. E. Z. Gusakov and A. D. Piliya, Pis'ma Zh. Tekh. Fiz. **18** (10), 63 (1992) [Sov. Tech. Phys. Lett. **18**, 325 (1992)].
3. V. I. Arkhipenko, V. N. Budnikov, E. Z. Gusakov, *et al.*, Pis'ma Zh. Tekh. Fiz. **19** (11), 20 (1993).
4. L. Vahala, G. Vahala, and N. Bretz, Phys. Fluids B **4**, 619 (1992).
5. I. B. Bernstein and L. Fridland, in *Handbook of Plasma Physics*, Vol. 1: *Basic Plasma Physics*, Ed. by A. A. Galeev and R. N. Sudan (Énergoatomizdat, Moscow, 1983; North-Holland, Amsterdam, 1983).
6. P. Devynck, X. Garbet, C. Laviron, *et al.*, Plasma Phys. Controlled Fusion **35**, 63 (1993).
7. B. Brüsehaber, E. Z. Gusakov, M. Krämer, and A. D. Pilia, Plasma Phys. Controlled Fusion **36**, 997 (1994).
8. A. D. Gurchenko, E. Z. Gusakov, M. M. Larionov, *et al.*, in *Proceedings of the 26th EPS Conference on Controlled Fusion and Plasma Physics, Maastricht, 1999*, ECA, Vol. 23J, p. 37.

Translated by I. A. Kalabalyk

Plasma Physics Reports, Vol. 27, No. 11, 2001, pp. 979–989. Translated from Fizika Plazmy, Vol. 27, No. 11, 2001, pp. 1035–1045.

LOW-TEMPERATURE PLASMA

Current Dynamics and Mechanisms for the Instability of a Non-Self-Sustained Glow Discharge in Nitrogen

Yu. A. Mankelevich*, A. F. Pal', N. A. Popov*, T. V. Rakhimova*, and A. V. Filippov****

**Skobeltsyn Institute of Nuclear Physics, Moscow State University, Vorob'evy gory, Moscow, 119899 Russia*

***Troitsk Institute for Innovation and Fusion Research, Troitsk, Moscow oblast, 142092 Russia*

Received June 13, 2001

Abstract—The current dynamics in a non-self-sustained glow discharge in atmospheric-pressure nitrogen (with a small admixture of oxygen) at cryogenic and room temperatures is studied experimentally and theoretically. For the first time, the theoretical model incorporates the processes of the decomposition of $O_2^+ \cdot N_2$ and $NO^+ \cdot N_2$ complex ions in collisions with vibrationally excited nitrogen molecules and the associative ionization reactions with the participation of excited nitrogen and oxygen atoms. The computation results agree quite satisfactorily with the experimental data on the current dynamics and the duration of the stable phase of a non-self-sustained discharge for various applied voltages. Even a small (0.01%) oxygen admixture is found to greatly affect the dynamics of the ion composition and the characteristic duration of the stable phase of a non-self-sustained discharge in atmospheric-pressure nitrogen. © *2001 MAIK "Nauka/Interperiodica".*

1. INTRODUCTION

High-pressure non-self-sustained glow discharges (NGDs) in molecular gases are widely used in laser technologies, plasmochemical reactors, and other applications [1–3]. One of the main characteristics of the NGD is the duration of the stable phase, which is restricted by the onset of NGD instabilities. The restriction is associated with either the appearance of one or several high-conductivity channels emerging from the cathode or the onset of one of the bulk instabilities [3, 4]. In nitrogen and air, high-conductivity channels emerge at relatively high electric fields, $E/N \geq 25$–30 Td (1 Td = 10^{-17} V cm^2), whereas at $E/N < 25$–30 Td, the discharge contraction is usually of volume nature [5]. In the latter case, the instability is related to the volume processes that sharply increase the plasma conductivity throughout the entire discharge gap.

The processes determining the duration of the stable phase of a non-self-sustained discharge substantially depend on the gas mixture composition. Discharges in nitrogen and nitrogen-containing mixtures have been studied most thoroughly [5–10]. In nitrogen, within a wide range of the reduced field (E/N = 5–75 Td), the main fraction of the discharge energy is spent on the excitation of the vibrational degrees of freedom of N_2 molecules. Hence, a complete modeling of the nitrogen vibrational kinetics is required to adequately describe the discharge characteristics. Since the rates of VT relaxation and VV exchange depend strongly on the gas temperature [1], the study of the non-self-sustained discharge parameters at various initial temperatures is very important.

Baiadze *et al.* [6, 7] numerically investigated high-pressure NGDs in nitrogen using a uniform model adequately describing vibrational kinetics. The calculated durations of the stable phase of the discharge turned out to be 1.5–2 times longer than the corresponding experimental values, which indicates that additional reactions of associative ionization must be taken into account in order to describe sharp current growth in the final stage of the discharge. The instabilities of a non-self-sustained microwave discharge in nitrogen with a small (up to 0.1%) oxygen admixture were investigated numerically in [8]. The main reactions were the reactions of associative ionization with the participation of $O(^1S)$ excited oxygen atoms created in the quenching of the nitrogen electronic states by $O(^3P)$ atoms. Allowing for those reactions enabled an adequate description of the experimental data [9] on the dependences of the duration of the discharge stable phase on E/N, the oxygen concentration, and other parameters. Thus, even a small admixture of oxygen can significantly affect the characteristics of high-pressure non-self-sustained discharges in nitrogen.

Deryugin *et al.* [10] studied the emission dynamics of the 1^+ nitrogen system N_2 ($N_2(B^3\Pi_g, v) \longrightarrow N_2(A^3\Sigma_u^+, v')$ transitions) in an NGD in nitrogen. In the initial stage of the discharge, the emission intensity was shown to be relatively low. However, in the final stage, when the discharge current sharply increased, the emission intensity of the 1^+ nitrogen system also sharply increased (somewhat leaving behind the current growth).

1063-780X/01/2711-0979$21.00

If the duration of a non-self-sustained discharge is long enough so that the density of the $N_2(X^1\Sigma_g^+, v \geq 5)$ vibrationally excited molecules is fairly high, then the emitting $N_2(B^3\Pi_g)$ state is populated mainly via the reaction [10, 11]

$$N_2(A^3\Sigma_u^+) + N_2(X^1\Sigma_g^+, v \geq 5) \longrightarrow N_2(B^3\Pi_g, v') + N_2(X^1\Sigma_g^+, v''). \quad (1)$$

Since the density of the $N_2(X^1\Sigma_g^+, v = 5\text{–}7)$ molecules changes insignificantly during the emission intensity growth, then, according to (1), the density of $N_2(A^3\Sigma_u^+)$ molecules over this time interval can be regarded as being almost proportional to the emission intensity of the 1^+ nitrogen system. Hence, the fairly rapid increase in the current in the final stage of the discharge should be preceded by an equally rapid increase in the density of $N_2(A^3\Sigma_u^+)$ molecules. This circumstance should be taken into account when analyzing the processes determining the ionization balance and the duration of the stable phase of a non-self-sustained discharge.

In spite of a great number of theoretical studies concerning non-self-sustained discharges in nitrogen, the reasons for the experimentally observed significant increase in the current in the stable phase of the discharge are still unknown. Moreover, the calculated durations of this phase are substantially longer than the experimental ones. The aim of our study is to investigate (both experimentally and theoretically) the current dynamics, the emission intensity of the 1^+ nitrogen system, and the mechanisms for the instability of an NGD in nitrogen with a small oxygen admixture at both cryogenic and room temperatures.

2. EXPERIMENTAL SETUP

The experiments were carried out using a facility [12] consisting of a discharge chamber and an electron gun with a beam current density of $j_b \leq 300\ \mu A/cm^2$ and an electron energy of 120 keV. The discharge was ignited between a grid cathode and sectioned copper anode (the electrode surface area is 1 cm^2, and the interelectrode distance is 1 cm). A rectangular voltage pulse with an amplitude of up to 5 kV and a duration of 25–1000 μs was applied to the discharge gap. In order to take into account the nonuniformity of the energy deposition, we used a sectioned anode consisting of a central and two side sections. Below, the current flowing through the central section is referred to as the discharge current. High-purity nitrogen (with an impurity content of about 0.01%) was used in the experiments.

To study discharges at cryogenic temperatures, the experimental facility was supplemented with a liquid nitrogen jacket, which enclosed the discharge chamber from all sides except the output flange of the electron gun; a gas pipeline ~2 m long (also surrounded by a liquid nitrogen jacket); and a thermostat, in which a specially designed copper tube coil was placed. After passing through the coil and pipeline, the working gas acquired a temperature of 90–100 K and then entered the discharge chamber. The initial cryogenic temperature and its uniformity throughout the discharge volume were monitored with two calibrated chromel–copel thermocouples; one of them was set in the middle of the discharge gap and the other at the electron gun output flange, which was not cooled with liquid nitrogen. At the initial temperature in the middle of the discharge gap $T \sim 100$ K, the temperature in the gap varied by no more than 4 K. To measure the gas temperature in the discharge, we used a Mach–Zehnder interferometer [13].

The homogeneity of the discharge was monitored by an image converter tube, which operated in the multiframe mode. An analysis of the experimental data showed that the electrode conditions and design substantially affected the duration of the stable phase of the discharge. In some experiments, plasma pinches were observed in the discharge gap, which resulted in a significant decrease in the duration of the stable phase. The pretreatment of the electrodes with a glow discharge or UV radiation from an auxiliary source, as well as the optimization of the electrode design, enabled a nearly homogeneous discharge to be obtained. Figure 1 presents typical images of the discharge with pretreated electrodes. It is seen that, in most of the interelectrode gap, the discharge is homogeneous and pinching occurs only in its final stage (Fig. 1c). Below, we only consider the results of the experiments with pretreated electrodes, which allows us to describe the discharge within the spatially uniform model.

We also performed spectral measurements of the discharge using a photomultiplier with the maximum sensitivity at a wavelength of ~800 nm [10]. The spectral measurements in the wavelength range 600–1000 nm revealed that, in the final stage of the discharge and in the afterglow, the 1^+ nitrogen system $[N_2(B^3\Pi_g, v) \longrightarrow N_2(A^3\Sigma_u^+, v')]$ emission dominates in the spectrum, the main transitions being those between the low-lying vibrational levels $N_2(B^3\Pi_g, v = 1, 2)$ and $N_2(A^3\Sigma_u^+, v' = 0, 1)$. To calibrate the measured emission intensity, we used the calculated density of $N_2(C^3\Pi_u)$ molecules produced by the electron beam and the measured ratio of the emission intensities of the 1^+ and 2^+ nitrogen systems.

3. DESCRIPTION OF THE MODEL

The numerical model for simulating the NGD incorporates three groups of equations:

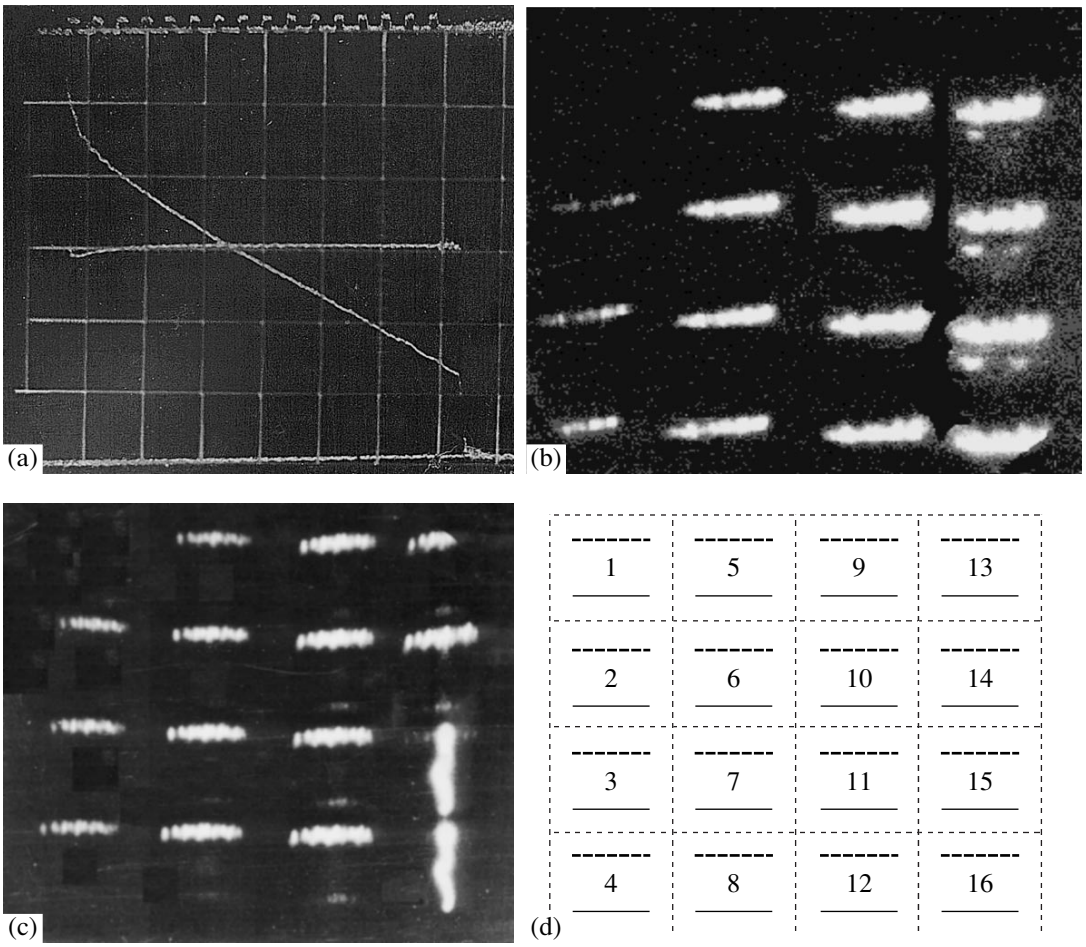

Fig. 1. (a) Oscillograms and (b, c) images of an NGD in atmospheric-pressure nitrogen obtained with an image converter tube and (d) the sequence order of the frames in panels (b) and (c). The upper and lower traces in oscillograms (a) show the discharge current (0.2 A/div) and the discharge voltage (1 kV/div), respectively; the time scale is 100 μs/div. Steps on the upper trace correspond to the instants of the opening of the image converter shutter. In the discharge images, the time interval between the frames is 26 μs and the frame exposure is 16 μs. Images (b) correspond to oscillograms (a) and images (c) are obtained at a slightly higher voltage. The upper electrode is the anode in images (b) and the cathode in images (c).

(i) the Boltzmann equation for the spherically symmetric part of the electron energy distribution function (EEDF),

(ii) a set of balance equations for the main charged and neutral particle species, and

(iii) the enthalpy conservation equation for determining the gas temperature.

The model takes into account the influence of superelastic collisions on the EEDF. The cross sections for the scattering of electrons by N_2 molecules were taken from [14]. The model incorporates about 400 reactions involving the following neutral particles: $N_2(X^1\Sigma_g^+, v = 0–45)$, $N_2(A^3\Sigma_u^+)$, $N_2(B^3\Pi_g)$, $N_2(C^3\Pi_u)$, $N_2(a'^1\Sigma_u^-)$, $N(^4S)$, $N(^2D)$, $N(^2P)$, O_2, $O(^3P)$, $O(^1D)$, and $O(^1S)$. The basic reactions were taken from [11, 15].

The electric field in the discharge was determined by the formula $E = (U - U_c)/d$, where U is the applied voltage, U_c is the cathode potential drop, and d is the interelectrode distance. The dependences of U_c on the gas pressure and the beam current density were taken from [16].

The electron density was determined from the equation

$$dN_e/dt = N_e\nu_{ion} + Q_{beam} + Q_{as} - Q_{rec}; \qquad (2)$$

where ν_{ion} is the rate of electron-impact ionization of molecules, Q_{beam} is the rate of electron–ion pair production by the electron beam, Q_{as} accounts for associative ionization reactions, and Q_{rec} is the rate of electron–ion recombination. Similar balance equations were used for all of the charged particles.

Main ion–molecular reactions incorporated in the model

No.	Reaction	Rate constant
R1	$N_2^+ + N_2 + N_2 \longrightarrow N_4^+ + N_2$	8×10^{-29} cm^6/s
R2	$N_4^+ + O_2 \longrightarrow O_2^+ + N_2 + N_2$	4×10^{-10} cm^3/s
R3	$O_2^+ + N_2 + N_2 \longrightarrow O_2^+ \cdot N_2 + N_2$	9×10^{-31} cm^6/s
R4	$O_2^+ \cdot N_2 + N_2(v) \longrightarrow O_2^+ + N_2 + N_2$	$k_4(v)$ (see text)
R5	$N_4^+ + NO \longrightarrow NO^+ + N_2 + N_2$	4×10^{-10} cm^3/s
R6	$O_2^+ + NO \longrightarrow NO^+ + O_2$	4×10^{-10} cm^3/s
R7	$O_2^+ \cdot N_2 + NO \longrightarrow NO^+ + O_2 + N_2$	4×10^{-10} cm^3/s
R8	$NO^+ + N_2 + N_2 \longrightarrow NO^+ \cdot N_2 + N_2$	9×10^{-31} cm^6/s
R9	$NO^+ \cdot N_2 + N_2(v) \longrightarrow NO^+ + N_2 + N_2$	$k_9(v)$ (see text)
R10	$N_4^+ + e \longrightarrow N_2(C) + N_2$	$2 \times 10^{-6}\,(300/T_e)^{0.5}$ cm^3/s
R11	$O_2^+ \cdot N_2 + e \longrightarrow O_2 + N_2$	$1.4 \times 10^{-6}\,(300/T_e)^{0.5}$ cm^3/s
R12	$NO^+ \cdot N_2 + e \longrightarrow O_2 + N_2$	$1.4 \times 10^{-6}\,(300/T_e)^{0.5}$ cm^3/s
R13	$O_2^+ + e \longrightarrow O(^3P) + O(^3P, {}^1D)$	$2 \times 10^{-7}\,(300/T_e)^{0.7}$ cm^3/s
R14	$NO^+ + e \longrightarrow N(^4S, {}^2D) + O(^3P)$	$4 \times 10^{-7}\,(300/T_e)^{0.9}$ cm^3/s

To describe the action of the electron beam on the gas, we used the results from [14, 17]. The rates of ionization, dissociation, and excitation of various electronic states of nitrogen molecules by the beam electrons can be written in the form [17]

$$Q_k = \frac{dE}{dx}\frac{j_b}{e}\frac{N}{\varepsilon_k}, \tag{3}$$

where dE/dx is the electron energy loss per unit path length (this quantity depends on the electron energy), j_b is the beam current density, N is the density of molecules in the mixture, and ε_k are the energy costs of the corresponding process.

Since the density of oxygen molecules in the experiments under consideration was fairly high ($[O_2^0] \leq 2.5 \times 10^{15}$ cm^{-3}), the reactions involving the N_2^+, N_4^+, NO^+, $NO^+ \cdot N_2$, O_2^+, and $O_2^+ \cdot N_2$ ions (see table) were incorporated into the model. The basic ion–molecular reactions were taken from [11, 15].

The rates of the ion–molecular reactions involving $N_2(X^1\Sigma_g^+, v)$ vibrationally excited nitrogen molecules (see table, reactions R4 and R9) were expressed in the form [2]

$$k_v(T) = k_0 \exp\left(-\frac{E_a - \alpha E_v}{T}\right), \tag{4}$$

where E_a is the activation energy for the corresponding reaction, α is the utilization coefficient of the vibrational energy in the reactions, E_v is the vibrational energy of the $N_2(X^1\Sigma_g^+, v)$ state, and T is the translational temperature.

The decomposition rate of the N_4^+ ions in the reaction

$$N_4^+ + N_2 \longrightarrow N_2^+ + N_2 + N_2 \tag{5}$$

was studied in [18] as a function of the vibrational and translational temperatures of nitrogen molecules. We used the corresponding dependences to estimate the coefficient α using formula (4). Under the conditions of [18], we have $\alpha = 0.2$–0.35. According to this estimate, for the similar decomposition reactions of $O_2^+ \cdot N_2$ (R4) and $NO^+ \cdot N_2$ (R9) ions, the coefficient α was assumed to be $\alpha = 0.3 \pm 0.05$. Such an analogy seems to be justified because, according to [19, 20], the rates of vibrational energy transfer between the $N_2(X^1\Sigma_g^+, v)$ molecules and the N_2^+, O_2^+, and NO^+ ions are comparable in magnitude.

As many as 45 vibrational levels of the $N_2(X^1\Sigma_g^+, v = 0$–$45)$ nitrogen molecule (up to the dissociation limit) were taken into account. For the rate constants of VT relaxation and VV exchange, we used expressions derived based on the Schwartz–Slavsky–Hertzfeld the-

ory. The rate constants of the reverse processes were determined from the detailed balance principle. The dimensionless inverse radius of VV exchange $\delta_{vv} = 6.8/\sqrt{T}$ (here, T is in K) and the VV transfer rate constant $Q_{10} = 2.5 \times 10^{-14}(T/300)^{3/2}$ cm^3/s were taken from [21, 22].

When calculating the rate of $N_2(A^3\Sigma_u^+)$ molecule production due to electron-impact excitation,

$$e + N_2(X^1\Sigma_g^+, v) \longrightarrow e + N_2(A^3\Sigma_u^+, v'), \qquad (6)$$

we took into account the dependence of the cross section for reaction (6) on the level number v in the form [23]

$$\sigma_{vv'}(\varepsilon) = q_{vv'}\Psi(\varepsilon/U_{vv'}). \qquad (7)$$

Here, ε is the electron energy; $q_{vv'}$ and $U_{vv'}$ are the Franck–Condon factor and the excitation energy for the corresponding transition, respectively; and Ψ is a function describing the energy dependence of the cross section. The latter function was chosen to best fit the experimental data from [24]. The experimental data (circles), the $\Psi(\varepsilon)$ function, and the calculated cross sections

$$\sigma_v(\varepsilon) = \sum_{v'}\sigma_{vv'}(\varepsilon)$$

for the vibrational levels with $v = 0$, 10, and 20 are presented in Fig. 2. It can be seen that, as v increases, the threshold for reaction (6) substantially decreases; for $v \geq 15$, we have $U_v \leq 2.5$–3 eV.

In the case at hand, the populations of the N(^4S) ground state and the N(^2P) excited state of nitrogen atoms are governed by the electron beam and the reaction [11]

$$N_2(A^3\Sigma_u^+) + N(^4S) \longrightarrow N_2(v) + N(^2P),$$
$$k = 5 \times 10^{-11}\ \text{cm}^3/\text{s}.$$

In the presence of oxygen in the mixture, O_2 molecules are intensively dissociated in the quenching reactions of electronically excited nitrogen molecules

$$N_2(A^3\Sigma_u^+) + O_2 \longrightarrow N_2(v) + 2O(^3P),$$
$$N_2(B^3\Pi_g) + O_2 \longrightarrow N_2(v) + 2O(^3P).$$

Among the processes of charged particle production, our model incorporates the associative ionization reactions with the participation of excited atoms,

$$N(^2P) + O(^3P) \longrightarrow NO^+ + e,$$
$$N(^4S) + O(^1S) \longrightarrow NO^+ + e, \qquad (8)$$

which were taken into account in [25] when modeling plasmochemical processes in air. These reactions have no activation barriers, and their rate can be estimated as [26]

$$k_8 = 3\pi\left(\frac{C_6^*}{4kT}\right)^{1/3}\sqrt{\frac{8kT}{\pi\mu}}\Gamma\left(\frac{5}{3}\right)$$
$$\simeq (1\text{–}3) \times 10^{-11}\left(\frac{T}{300}\right)^{1/6}\ \text{cm}^3/\text{s}, \qquad (9)$$

where C_6^* is the van der Waals coefficient in the expression for the attraction force potential of the colliding atoms, μ is the reduced mass of the atoms, and $\Gamma(x)$ is the gamma function.

It should be noted that the creation of charged particles in the reaction between the N(^2P) and O(^3P) atoms was observed in experiments [27]; the rate constant of the decay of the N(^2P) atoms in the reaction with O(^3P) was found to be $(1.7 \pm 0.4) \times 10^{-11}$ cm^3/s. This value agrees with estimate (9).

Under our experimental conditions, the time of gas heating is much longer than the characteristic time of gasdynamic processes. For this reason, we used the isobaric approximation when calculating the gas temperature.

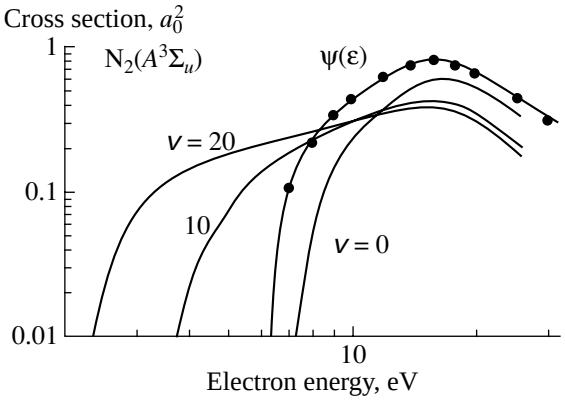

Fig. 2. Cross sections (in atomic units) for electron-impact excitation from different vibrational levels of the $N_2(A^3\Sigma_u^+)$ state to the $N_2(X^1\Sigma_g^+, v)$ molecular state. Circles present the data from [24], and the $\Psi(\varepsilon)$ curve shows the energy dependence of the cross section used in computations.

4. COMPUTATION RESULTS

In our experiments, the gas pressure and the initial temperature were varied in such a way that the initial density of nitrogen molecules remained equal to $[N_2^0] = 2.5 \times 10^{19}$ cm^{-3}. This was taken as the initial value in all of the computations.

Figure 3 presents the experimental data and the computation results on the current dynamics in an NGD at $U = 3$ kV for $T_0 = 300$ K and $j_b = 225$ μA/cm^2 (curve *1*)

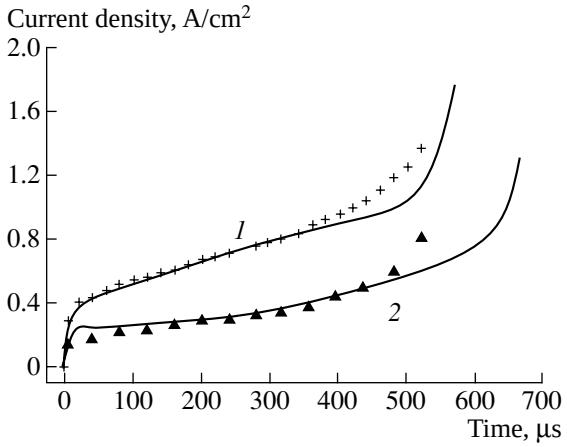

Fig. 3. Waveforms of the current in a non-self-sustained discharge in the N_2 + 0.01% O_2 mixture at U = 3 kV for (*1*) T_0 = 300 K and j_b = 225 μA/cm^2 and (*2*) T_0 = 100 K and j_b = 140 μA/cm^2. The symbols show the experimental data, and the curves show the computation results.

and for T_0 = 100 K and j_b = 140 μA/cm^2 (curve *2*), the reduce field $(E/N)_0$ being ≈10 Td. The increase in the current density in the initial stage of the discharge is related to the decrease in the effective coefficient of dissociative electron–ion recombination β_{eff} due to the change in the ion composition:

$$\beta_{eff} = \frac{\sum \beta_{ion} N^+_{ion}}{\sum N^+_{ion}}.$$

The computed time evolution of the coefficient β_{eff} is shown in Fig. 4. It can be seen that, at T_0 = 100 K, the effective recombination coefficient is substantially larger than at room temperature at each phase of the discharge. The decrease in β_{eff} with time is mainly related to the increase in the degree of vibrational excitation of N_2 because the gas temperature increases insignificantly over 200–300 μs (see the experimental data and computation results in Fig. 9). As was mentioned above, this decrease is a consequence of the change in the ion composition. The computed time evolution of the density of the main positive ions is shown in Figs. 5 and 6. As the degree of vibrational excitation of N_2 increases, the rates of decomposition of the $O_2^+ \cdot N_2$ and $NO^+ \cdot N_2$ ions in reactions R4 and R9 also increase; the produced O_2^+ and NO^+ ions recombine much more slowly (see table). The dominating role of NO^+ ions in the final stage of the discharge is explained by the fact that, in this stage, most of the charged particles are produced in the reactions of associative ionization (8).

Figure 7 presents the experimental and simulated dependences of the NGD current density on $(E/N)_0$ 100 μs after the discharge ignition; the beam current density is j_b = 130 μA/cm^2. It can be seen that the computation results are in good agreement with the experimental data. At T_0 = 100 K, the increase in the discharge current with $(E/N)_0$ is related mainly to the increase in the electron drift velocity. At T_0 = 300 K, the decrease in the effective rate of dissociative electron–ion recombination due to the change in the ion composition also comes into play. As a result, the slope of the curve in Fig. 7 is higher at T_0 = 300 K.

It should be noted that, the applied voltage U being kept constant, the reduced electric field E/N in the discharge positive column changes substantially with time. Over the first 50–70 μs, the cathode potential drop U_c decreases (due to the heating and expansion of the

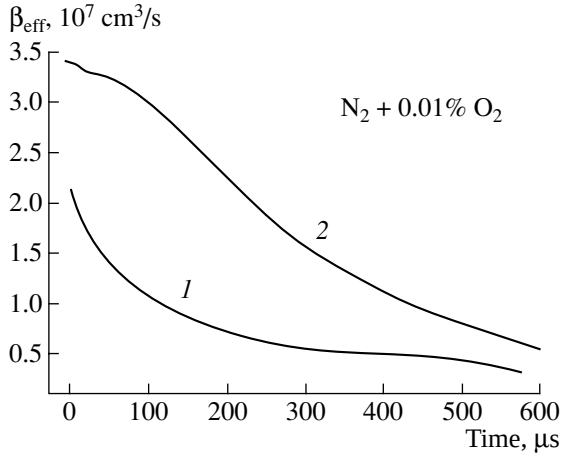

Fig. 4. Time evolution of the effective rate constant of electron–ion recombination at U = 3 kV for (*1*) T_0 = 300 K and j_b = 225 μA/cm^2 and (*2*) T_0 = 100 K and j_b = 140 μA/cm^2.

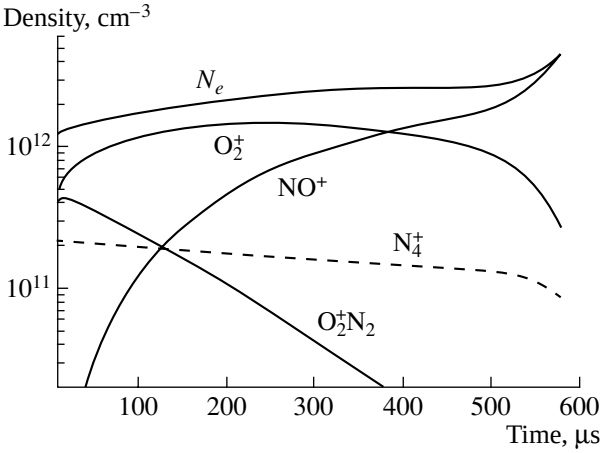

Fig. 5. Time evolution of the charged particle densities in the N_2 + 0.01% O_2 mixture for U = 3 kV, T_0 = 300 K, and j_b = 225 μA/cm^2.

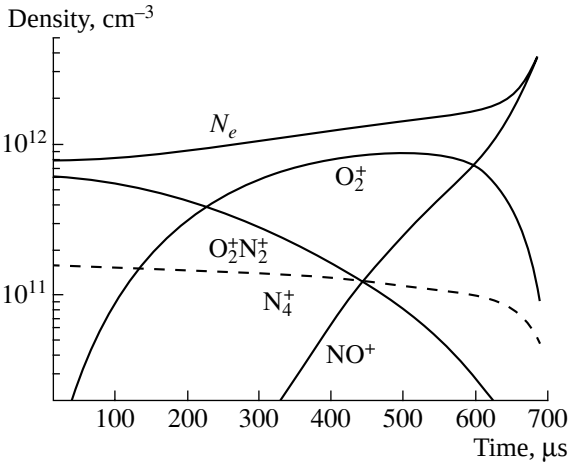

Fig. 6. Same as in Fig. 5, but for T_0 = 100 K and j_b = 140 μA/cm^2.

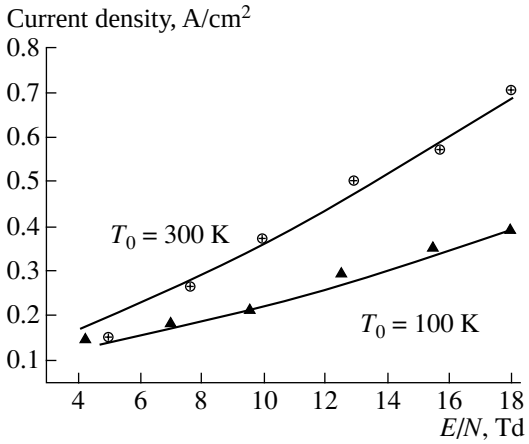

Fig.7. NGD current vs. $(E/N)_0$ for t = 100 μs and j_b = 130 μA/cm^2. The symbols show the experimental data, and the curves show the computation results.

gas in the cathode sheath [16]); as a result, the electric field in the discharge increases. The further slower increase in E/N is related to both the decrease in the gas density in the positive column due to the increase in the temperature and the decrease in the cathode potential drop U_c due to the growth of the discharge current ($U_c \sim 1/\sqrt{j}$) [16]. Recall that the $(E/N)_0$ values in Fig. 7 correspond to the time t = 100 μs after the discharge ignition.

Figure 8 shows the time evolution of the densities of some components (very important for the processes of associative ionization discussed below) of the N_2 + 0.01% O_2 mixture excited by an NGD for j_b = 225 μA/cm^2, U = 3 kV, and T_0 = 300 K. We note the intense dissociation of nitrogen and oxygen molecules in the discharge. The former are decomposed by the electron beam, whereas the latter are decomposed via the quenching of electronically excited nitrogen molecules [15, 25]. In the final stage ($t \geq 500$ μs), reactions [11]

$$N_2(A^3\Sigma_u^+) + N_2(X^1\Sigma_g^+, v' \geq 5) \longrightarrow N_2(B^3\Pi_g, v) + N_2(X^1\Sigma_g^+, v''),$$

$$N_2(B^3\Pi_g, v \geq 13) \longrightarrow N(^4S) + N(^4S)$$

make a significant contribution to nitrogen atom production.

In the initial stage of the discharge, the electronically excited $N_2(A^3\Sigma_u^+)$ molecules are produced by the electron beam. The decrease in the population of the $N_2(A^3\Sigma_u^+)$ state at t = 200–450 μs is related to the quenching by nitrogen and oxygen atoms, whose overall density is higher than 10^{14} cm^{-3}. As the population of the high-lying vibrational levels $N_2(X^1\Sigma_g^+, v \geq 10\text{–}15)$ of the ground state increases, processes (6),

$$e + N_2(X^1\Sigma_g^+, v \geq 10\text{–}15) \longrightarrow e + N_2(A^3\Sigma_u^+),$$

begin to play a more important role.

The major contribution to the production of the $N_2(A^3\Sigma_u^+)$ molecules comes from the vibrational levels $N_2(X^1\Sigma_g^+, v \geq 15)$, for which the threshold for reaction (6) decreases to $\varepsilon_0 \leq 2.5$ eV. Under the conditions corresponding to Fig. 8, the contribution from reaction (6) and the production by the electron beam becomes comparable at $[N_2(X^1\Sigma_g^+, v \geq 15)] \geq (1\text{–}2) \times 10^{16}$ cm^{-3}.

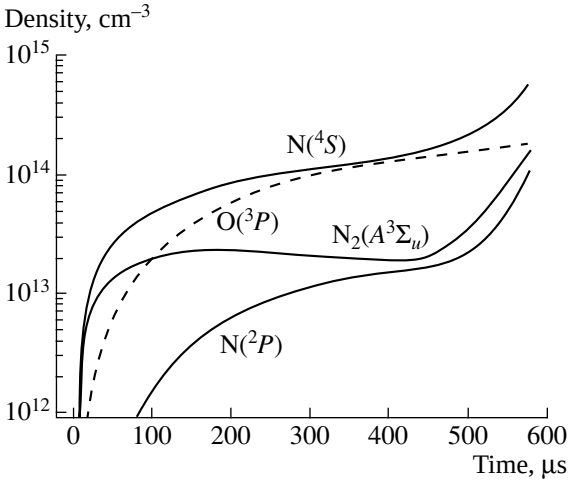

Fig. 8. Time evolution of the particle densities in the N_2 + 0.01% O_2 mixture for U = 3 kV, T_0 = 300 K, and j_b = 225 μA/cm^2.

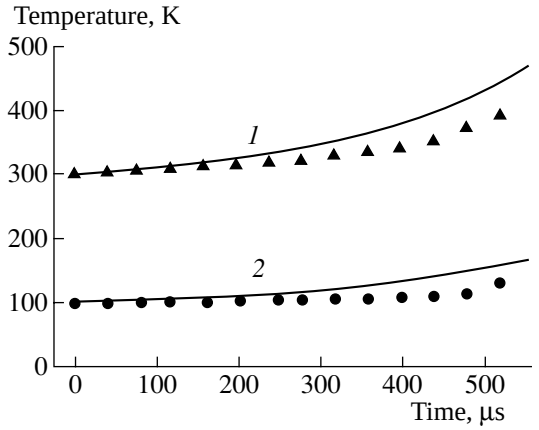

Fig. 9. Dynamics of gas heating in the discharge at $U = 3$ kV for (*1*) $T_0 = 300$ K and $j_b = 225$ μA/cm^2 and (*2*) $T_0 = 100$ K and $j_b = 140$ μA/cm^2. The symbols show the experimental data, and the curves show the computation results.

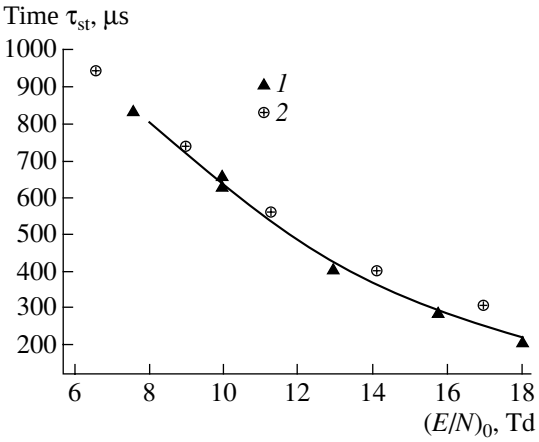

Fig.10. Duration of the stable phase of a non-self-sustained discharge vs. $(E/N)_0$ for $j_b = 130$ μA/cm^2. The symbols show the experimental data for $T_0 =$ (*1*) 300 and (*2*) 100 K, and the curve shows the computation results for $T_0 = 300$ K.

Figure 9 presents the experimental data and the computation results on the dynamics of gas heating for different initial temperatures $T_0 = 300$ K ($j_b = 225$ μA/cm^2, curve *1*) and $T_0 = 100$ K ($j_b = 140$ μA/cm^2, curve *2*). We note that, at $t > 250$ μs, the calculated gas temperature is higher than the experimental one. This is related to the nonuniform energy deposition because of the nonuniform ionization of nitrogen by the electron beam. As a result, the gas in the axial region is heated more efficiently than at the periphery and the measured radius-averaged temperature is lower than in the central NGD region, for which computations were carried out. However, even in the axial region, the gas heating rate is relatively low and the sharp increase in the discharge current at $t \geq 600$ μs (Fig. 3) cannot be attributed to the onset of the thermal instability. The same is true for all other discharge modes under study.

To account for the experimentally observed sharp increase in the current in the final stage of the discharge, the model incorporates the reactions of associative ionization (8) involving excited atoms. In the final stage of the discharge, charged particles are produced via the following reactions [25]:

$$N_2(A^3\Sigma_u^+) + N(^4S) \longrightarrow N_2(v) + N(^2P),$$

$$N_2(A^3\Sigma_u^+) + O(^3P) \longrightarrow N_2(v) + O(^1S),$$

$$O(^1S) + N(^4S) \longrightarrow O(^3P) + N(^2P),$$

$$N(^2P) + O(^3P) \longrightarrow NO^+ + e.$$

Taking into account reactions (8) allowed us to adequately describe the experimental data on the dynamics of the NGD current at different applied voltages and electron beam currents. Figure 10 shows the experimental and calculated dependences of the duration of the stable phase of a non-self-sustained discharge on $(E/N)_0$ for $j_b = 130$ μA/cm^2. The value of τ_{st} was derived from the time dependence of the rate at which the discharge current density changed. For all of the discharge modes under study, the time evolution of dj/dt drawn on the logarithmic scale showed a pronounced bend. The instant of the bend was taken as τ_{st}. It can be seen in Fig. 10 that the calculated values of τ_{st} agree well with the experiment for all applied voltages under study. Therefore, we can conclude that reactions (8) with the participation of excited atoms must be included in the discharge ionization balance equations and that even a small (0.01%) oxygen admixture substantially affects both the dynamics of the ion composition and the characteristic duration of the stable phase of an NGD in atmospheric-pressure nitrogen. We note that models incorporating the associative ionization reactions involving only electronically excited molecules [28],

$$N_2(A^3\Sigma_u^+) + N_2(a'^1\Sigma_u^-) \longrightarrow e + N_4^+,\ 5 \times 10^{-11}\ \text{cm}^3/\text{s},$$

$$N_2(a'^1\Sigma_u^-) + N_2(a'^1\Sigma_u^-) \longrightarrow e + N_4^+,\ 2 \times 10^{-10}\ \text{cm}^3/\text{s}$$

without taking into account reactions (8) do not provide an adequate description of the experimental data on the NGD current dynamics and strongly overestimate the τ_{st} values.

In studies of the quasi-steady glow discharge in nitrogen [28], it was found that the time evolution of the density of the $N_2(X^1\Sigma_g^+,\ v = 15–25)$ vibrationally excited molecules correlated with the time variations in the secondary ionization rate. Based on this observation, the $N_2(X^1\Sigma_g^+,\ v \geq 15)$ molecules were assumed to participate in the processes of associative ionization. The possible ionization processes with the participation

of $N_2(X^1\Sigma_g^+,\ v \geq 25)$ vibrationally excited molecules were also analyzed in [29].

Within our model, the $N_2(X^1\Sigma_g^+,\ v \geq 15)$ vibrationally excited molecules are not directly involved in the reactions of associative ionization, but they significantly accelerate the production of $N_2(A^3\Sigma_u^+)$ molecules in reaction (6), which, in turn, increases the densities of excited nitrogen and oxygen atoms participating in the associative ionization reactions (8).

Figure 11 shows the measured time evolution of the discharge current and the emission intensity of the 1^+ system of nitrogen for $U = 2.5$ kV, $j_b = 250$ μA/cm^2, and $T_0 = 300$ K. The current pulse duration is ~580 μs. Both the current and the emission intensity are seen to increase sharply in the final stage of the discharge. As was mentioned in the Introduction, the increase in the emission intensity indicates a substantial increase in the density of the $N_2(A^3\Sigma_u^+)$ molecules in the final stage of the discharge.

The absolute value of the emission intensity of the 1^+ nitrogen system was estimated using the expression

$$I_{1^+} = \left(\frac{I_{1^+}}{I_{2^+}}\right)\frac{[N_2(C^3\Pi_u)]}{\tau_C},$$

where I_{1^+} and I_{2^+} are the emission intensities of the 1^+ and 2^+ nitrogen systems and τ_C is the radiative lifetime of the $N_2(C^3\Pi_u)$ state. In [30], it was shown that, under the given conditions, the $N_2(C^3\Pi_u)$ molecules are produced mainly by the electron beam. Hence, taking into account formula (3), the density of the $N_2(C^3\Pi_u)$ molecules can be expressed as

$$[N_2(C^3\Pi_u)] = \frac{dE}{dx}\frac{1}{e\varepsilon_C}\frac{j_b}{k_C},$$

where ε_C is the energy cost of the $N_2(C^3\Pi_u)$ production with allowance for reaction R10 (see table) and $k_C = 1.5 \times 10^{-11}$ cm^3/s is the rate constant for the reaction

$$N_2(C^3\Pi_u,\ v = 0, 1) + N_2(X^1\Sigma_g^+,\ v') \longrightarrow \text{products},$$

which, at $P = 760$ torr, is the main channel for quenching the $N_2(C^3\Pi_u)$ state.

In computations, the emission intensity of the 1^+ nitrogen system was determined as

$$I_{1^+} = \frac{[N_2(B^3\Pi_g)]}{\tau_B},$$

where τ_B is the radiative lifetime of the $N_2(B^3\Pi_g)$ state.

In the final stage of the discharge, the emitting $N_2(B^3\Pi_g)$ state is populated mainly via reaction (1).

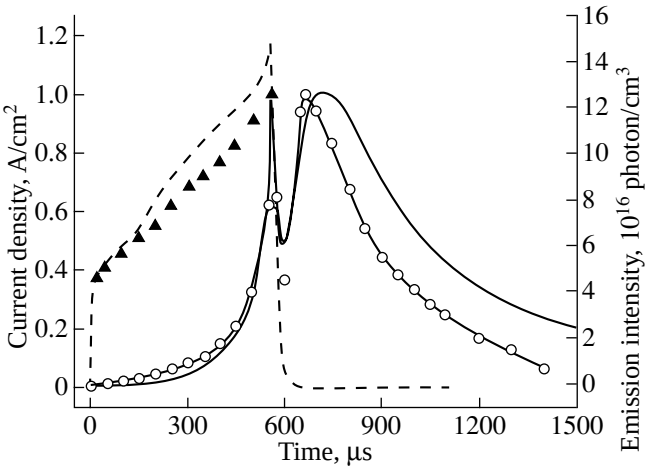

Fig. 11. Dynamics of the current density (dashed line) and emission intensity of the 1^+ nitrogen system (solid line) in an NGD for $j_b = 250$ μA/cm^2, $U = 2.5$ kV, and $T_0 = 300$ K. The symbols show the experimental data, and the curves show the computation results.

To take into account the production of $N_2(B^3\Pi_g)$ molecules in the afterglow phase, we included the reaction

$$N_2(X^1\Sigma_g^+,\ v \geq 31) + N_2(X^1\Sigma_g^+)$$
$$\longrightarrow N_2(B^3\Pi_g,\ v') + N_2(X^1\Sigma_g^+), \qquad (10)$$
$$k = 5 \times 10^{-17}\ \text{cm}^3/\text{s},$$

which was suggested in [10].

The computation results on the dynamics of the discharge current and the emission intensity of the 1^+ nitrogen system are presented in Fig. 11. In computations, the emission intensity begins to appreciably increase at $t = 350$–400 μs, whereas in the experiment, it starts to increase immediately after the discharge ignition, which is related to the appearance of cathode spots [10]. The measurements with slit diaphragms that cut off the emission from the electrode regions showed that the emission from the discharge positive column becomes significant starting approximately from the middle of the current pulse, which agrees with the computation results.

Taking reaction (10) into account allowed us to match the calculated emission intensity of the 1^+ nitrogen system in the discharge afterglow with the experimental data (Fig. 11). However, computations also showed an increase in the emission intensity of the 2^+ nitrogen system (due to the reaction $2N_2(A^3\Sigma_u^+) \longrightarrow N_2(C^3\Pi_u) + N_2(X^1\Sigma_g^+)$), which was not observed in the experiments. Thus, the reasons for the nonmonotonic behavior of the emission intensity of the 1^+ nitrogen system in the NGD afterglow still remain unclear.

5. CONCLUSION

The current dynamics in NGDs in atmospheric-pressure nitrogen at cryogenic and room temperatures and the emission intensity of the 1^+ nitrogen system in the main phase of the discharge and in the discharge afterglow have been studied both experimentally and theoretically. The effect of gas heating on the discharge parameters has also been investigated.

In order to describe the kinetic processes in nitrogen (with a small admixture of oxygen) excited by an NGD, we have developed a numerical code incorporating the balance equations for the densities of the main neutral and charged particles. For the first time, the model incorporates the decomposition reactions of $O_2^+ \cdot N_2$ and $NO^+ \cdot N_2$ complex ions in collisions with vibrationally excited nitrogen molecules and the associative ionization reactions with the participation of excited nitrogen and oxygen atoms. The increase in the gas temperature and the degree of vibrational excitation leads to a change of the ion composition, a decrease in the electron–ion recombination coefficient, and an increase in the discharge current.

In the model developed, the mechanism for the increase in the current in the final phase of the discharge can be described as follows. The increase in density of the $N_2(X^1\Sigma_g^+,\ v \geq 15)$ vibrationally excited molecules significantly speeds up the production of $N_2(A^3\Sigma_u^+)$ molecules by electron-impact excitation, which, in turn, increases the densities of the excited nitrogen and oxygen atoms participating in associative ionization.

The computation results adequately describe the experimental data on the current dynamics and the duration of the stable phase of a non-self-sustained discharge for various applied voltages and electron beam currents. Based on the results obtained, we can conclude that reactions (8), involving excited atoms, must be included in the discharge ionization balance equations and that even a small (0.01%) oxygen admixture substantially affects both the dynamics of the ion composition and the characteristic duration of the stable phase of an NGD in atmospheric-pressure nitrogen.

In [31], under similar experimental conditions, the influence of the condensed disperse phase (grains 24 μm in diameter) on the NGD parameters in atmospheric-pressure nitrogen was studied. Grains with the number density $N_d \geq 10^4$ cm^{-3} were shown to substantially affect the current dynamics, the duration of the stable phase, and other discharge characteristics. The proposed model of kinetic processes in the plasma of an NGD in nitrogen will enable a more complete and detailed analysis of the grain influence on the discharge parameters.

ACKNOWLEDGMENTS

This study was supported by the Russian Foundation for Basic Research, project nos. 00-02-16508, 00-15-96554, and 01-02-17726.

REFERENCES

1. B. F. Gordiets, A. I. Osipov, and L. A. Shelepin, *Kinetic Processes in Gases and Molecular Lasers* (Nauka, Moscow, 1980).
2. V. D. Rusanov and A. A. Fridman, *Physics of Chemically Active Plasma* (Nauka, Moscow, 1984).
3. E. P. Velikhov, A. S. Kovalev, and A. T. Rakhimov, *Physical Phenomena in Gas Discharge Plasma* (Nauka, Moscow, 1987).
4. A. P. Napartovich and A. N. Starostin, in *Plasma Chemistry* (Atomizdat, Moscow, 1979), Vol. 6.
5. I. G. Persiantsev, A. T. Rakhimov, N. V. Suetin, and M. A. Timofeev, Fiz. Plazmy **9**, 637 (1983) [Sov. J. Plasma Phys. **9**, 371 (1983)].
6. K. V. Baiadze, V. M. Vetsko, S. A. Zhdanok, *et al.*, Dokl. Akad. Nauk SSSR **249**, 832 (1979) [Sov. Phys. Dokl. **24**, 979 (1979)].
7. K. V. Baiadze, V. M. Vetsko, A. P. Napartovich, and A. N. Starostin, Teplofiz. Vys. Temp. **19**, 361 (1981).
8. N. A. Popov, Teplofiz. Vys. Temp. **32**, 177 (1994).
9. N. A. Bogatov, M. S. Gitlin, S. V. Golubev, and S. V. Razin, Teplofiz. Vys. Temp. **30**, 1041 (1992).
10. A. A. Deryugin, I. V. Kochetov, A. F. Pal', *et al.*, Fiz. Plazmy **17**, 1138 (1991) [Sov. J. Plasma Phys. **17**, 661 (1991)].
11. D. I. Slovetskiĭ, *Mechanisms of Chemical Reactions in Nonequilibrium Plasma* (Nauka, Moscow, 1980).
12. G. B. Lopantseva, A. F. Pal', A. F. Perevoznov, *et al.*, Fiz. Plazmy **5**, 1117 (1979) [Sov. J. Plasma Phys. **5**, 626 (1979)].
13. A. A. Deryugin, I. V. Kochetov, A. I. Loboĭko, *et al.*, Fiz. Plazmy **14**, 340 (1988) [Sov. J. Plasma Phys. **14**, 200 (1988)].
14. K. S. Klopovskiĭ, A. V. Mukhovatova, A. M. Popov, *et al.*, Fiz. Plazmy **19**, 1162 (1993) [Plasma Phys. Rep. **19**, 607 (1993)].
15. I. A. Kossyi, A. Y. Kostinsky, A. A. Matveev, and V. P. Silakov, Plasma Sources Sci. Technol. **1**, 207 (1992).
16. A. N. Lobanov, Ya. N. Menakhin, and K. N. Ul'yanov, Zh. Tekh. Fiz. **52**, 1959 (1982) [Sov. Phys. Tech. Phys. **27**, 1204 (1982)].
17. V. P. Konovalov and É. E. Son, in *Plasma Chemistry* (Énergoatomizdat, Moscow, 1988), Vol. 14, p. 194.
18. L. S. Polak, P. A. Sergeev, and D. I. Slovetskiĭ, in *Chemical Reactions in Low-Temperature Plasma* (Inst. Neftekhimicheskogo Sinteza Akad. Nauk SSSR, Moscow, 1977), p. 122.
19. E. E. Ferguson, N. G. Adams, D. Smith, and E. Alge, J. Chem. Phys. **80**, 6095 (1984).
20. A. A. Viggiano, R. A. Morris, F. Paulson, *et al.*, J. Chem. Phys. **99**, 6579 (1993).
21. Yu. S. Akishev, A. V. Dem'yanov, I. V. Kochetov, *et al.*, Teplofiz. Vys. Temp. **20**, 818 (1982).

22. A. Kh. Mnatsakanyan and G. V. Naĭdis, Teplofiz. Vys. Temp. **23**, 640 (1985).
23. M. Cacciatore, M. Capitelli, and C. Gorse, Chem. Phys. **66**, 141 (1982).
24. D. C. Cartwright, A. Chutjian, S. Trajmar, and W. Williams, Phys. Rev. A **16**, 1013 (1977).
25. N. A. Popov, Fiz. Plazmy **20**, 335 (1994) [Plasma Phys. Rep. **20**, 303 (1994)].
26. S. A. Losev, S. Ya. Umanskiĭ, and I. T. Yakubov, in *Handbook of Physicochemical Processes in Gas Dynamics* (Mosk. Gos. Univ., Moscow, 1995), Vol. 1, p. 293.
27. L. G. Piper, J. Chem. Phys. **98**, 8560 (1993).
28. Yu. S. Akishev, K. V. Baiadze, V. M. Vetsko, *et al.*, Fiz. Plazmy **8**, 999 (1982) [Sov. J. Plasma Phys. **8**, 563 (1982)].
29. A. V. Filippov, I. V. Kochetov, and A. F. Pal', in *Proceedings of the Conference on Physics of Low-Temperature Plasma, Petrozavodsk, 1998*, Vol. 1, p. 26.
30. A. A. Deryugin, I. V. Kochetov, A. F. Pal', *et al.*, in *Proceedings of the XIX International Conference on Phenomena in Ionized Gases, Belgrad, 1989*, Vol. 4, p. 1016.
31. A. F. Pal', A. O. Serov, A. N. Starostin, *et al.*, Zh. Éksp. Teor. Fiz. **119**, 272 (2001) [JETP **92**, 235 (2001)].

Translated by N. N. Ustinovskiĭ

Plasma Physics Reports, Vol. 27, No. 11, 2001, pp. 990–993. Translated from Fizika Plazmy, Vol. 27, No. 11, 2001, pp. 1046–1049.

BRIEF COMMUNICATIONS

Escape of Electron Langmuir Waves from a Magnetized Plasma

A. V. Timofeev

Russian Research Centre Kurchatov Institute, pl. Kurchatova 1, Moscow, 123182 Russia

Received May 24, 2001

Abstract—A study is made of electromagnetic oscillations of a plasma in open field line geometry (open magnetic devices). The oscillations that propagate from the critical surface and are originally of the nature of the electron Langmuir waves are shown to continuously change their nature and to escape from the plasma into vacuum in the form of electromagnetic waves. This phenomenon may give rise to wave energy losses from a thermodynamically nonequilibrium (unstable) plasma, e.g., a plasma penetrated by charged particle beams. *© 2001 MAIK "Nauka/Interperiodica".*

1. In [1], it was shown that, in an inhomogeneous plasma whose density varies across the magnetic field, there exist eigenmodes localized near the critical surface (by the critical surface we mean the surface defined by the condition $\omega_{pe} = \omega$, where ω_{pe} is the electron Langmuir frequency and ω is the frequency of electromagnetic oscillations). The longitudinal refractive index for such eigenmodes is close to $N_{\|c} = \sqrt{\frac{\omega_e}{\omega_e - \omega}}$ (where ω_e is the electron cyclotron frequency), and the transparency region for the eigenmodes is adjacent to the critical surface from the side of higher plasma density if $N_\| > N_{\|c}$ and from the lower density side if $N_\| < N_{\|c}$.

The characteristic feature of the oscillations under consideration is that their polarization is different in different zones of the transparency region. At the critical surface, the electric field of the oscillations is parallel to the main magnetic field and the oscillations themselves are electron Langmuir waves propagating along the magnetic field ($\mathbf{N} \| \mathbf{B}_0$). At the other boundary surface of the transparency region, the electric field is perpendicular to the main magnetic field and rotates in the same direction as the electrons; in other words, the oscillations are so-called whistlers, whose wave vector is also aligned with the main magnetic field.

Plasma configurations typical of closed devices in which $\nabla n_0 \perp \mathbf{B}_0$ were considered in my earlier paper [1], where the calculations were carried out for tokamak plasmas. However, the study of plasmas in open magnetic configurations has also been the subject of extensive laboratory investigation. Plasma configurations of open geometry are characteristic of, e.g., gas-discharge plasmas in a magnetic field and plasmas in open magnetic confinement systems. The goal of the present paper is to analyze oscillations that propagate along the critical surface in a plasma in open field line geometry. To be specific, the case of a plasma confined in an open device is considered. In open configurations, the plasma density gradient is orthogonal to the magnetic field only in the median plane. However, if the configuration is highly stretched out along the magnetic field, then the angle χ between ∇n_0 and $\mathbf{B}_0$ is close to $\pi/2$ over most of the plasma volume, so that the spatial structure of the oscillations and the shape of their ray trajectories will be approximately the same as those for the mutually orthogonal vectors ∇n_0 and $\mathbf{B}_0$. On the other hand, in magnetic mirrors of any open device, the angle χ is small, indicating that the situation in mirror regions should differ significantly from that in the case $\chi = \pi/2$.

2. We are interested in the ray trajectories of electromagnetic oscillations with $N_\| \approx N_{\|c}$ in a plasma of open magnetic devices. The magnetic field is defined in terms of the potential

$$\Phi(\mathbf{r}) = \Phi_0(z) - \frac{r^2}{4}\Phi_0''(z),$$

where $\Phi_0(z) = \frac{1}{2}\left((R+1)z - (R-1)\frac{L_B}{\pi}\sin\left(\pi\frac{z}{L_B}\right)\right)$.

Here and below, all of the quantities having the dimensionality of length are normalized to c/ω. We use a cylindrical coordinate system in which the z-axis is the symmetry axis of the device.

We assume that the plasma is ellipsoidal in shape and is stretched out along the device axis:

$$n_0(\mathbf{r}) = n_0(0)\exp\left(-\left(\frac{r}{L_{nr}}\right)^2 - \left(\frac{z}{L_{nz}}\right)^2\right).$$

1063-780X/01/2711-0990$21.00 © 2001 MAIK "Nauka/Interperiodica"

In the approximation of a cold plasma and immobile ions, the oscillations are characterized by the dispersion relation

$$D = N_\perp^4\varepsilon_\perp + N_\perp^2(N_\parallel^2(\varepsilon_\perp + \varepsilon_\parallel) - 2\varepsilon_\perp\varepsilon_\parallel - \varepsilon_\perp + \varepsilon_\parallel) + \varepsilon_\parallel(N_\parallel^2 - \varepsilon_+)(N_\parallel^2 - \varepsilon_-) = 0,$$

where $\varepsilon_\pm = 1 - \dfrac{\omega_{pe}^2}{\omega(\omega \pm \omega_e)}$, $\varepsilon_\perp = (\varepsilon_+ + \varepsilon_-)/2$, and $\varepsilon_\parallel = 1 - \dfrac{\omega_{pe}^2}{\omega^2}$.

The ray trajectories of the oscillations can be described by the equations of the geometrical-optics approximation:

$$\frac{d\mathbf{r}}{dt} = -\frac{\partial D/\partial \mathbf{N}}{\partial D/\partial \omega}, \qquad \frac{d\mathbf{N}}{dt} = \frac{\partial D/\partial \mathbf{r}}{\partial D/\partial \omega}. \tag{1}$$

Since we are interested only in the shape of the ray trajectories, we simplify the calculations by changing from the ordinary time variable to the dimensionless parameter τ, which is defined as $d\tau = dt\left(\dfrac{\partial D(\mathbf{r}(t), \mathbf{N}(t))}{\partial \omega}\right)^{-1}$. As a result, Eqs. (1) reduce to

$$\dot{\mathbf{r}} = -\frac{dD}{d\mathbf{N}}, \qquad \dot{\mathbf{N}} = \frac{dD}{d\mathbf{r}}. \tag{2}$$

The ray trajectories discussed below were calculated for the mirror ratio $R = 2$, the remaining parameter values characterizing the problem being $L_B = 200$, $\omega_{pe}(0)/\omega = 2$, $\omega_e(0)/\omega = 2$, $L_{nr} = 10$, and $L_{nz} = 100$.

Representative ray trajectories behind the critical surface are shown in Figs. 1 and 2. Both of the trajectories originate from the same point ($r = 10$, $z = 0.1$) and are characterized by the same value $N_\perp(0) = 0.2$. However, in Fig. 2, the angle that the wave vector makes with the (z, r) plane is equal to 0.75 ($N_\varphi \neq 0$). In [1], it was shown that, for $N_\varphi \neq 0$, the ray trajectory does not come into contact with the critical surface. For $N_\varphi \neq 0$, the "centrifugal force" in the region of low plasma density outside the device acts to turn the ray away from the device axis. Along both trajectories, the value of $N_\parallel$ changes insignificantly: from about 1.25 inside the plasma to about 1 outside the plasma. Since, in the plasma, the projection of the wave phase velocity onto the magnetic field direction is smaller than the speed of light, the waves under investigation can undergo a Cherenkov interaction with charged particle beams moving along the magnetic field.

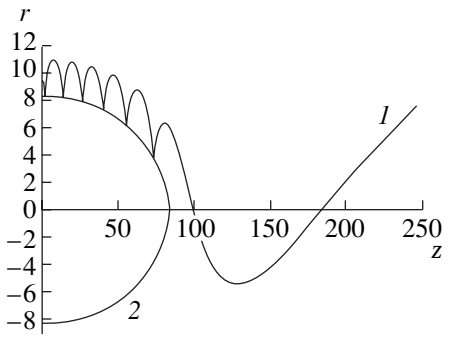

Fig. 1. Ray trajectory behind the critical surface for $N_\varphi = 0$: (*1*) the ray trajectory and (*2*) the intersection of the critical surface with the (z, r) plane.

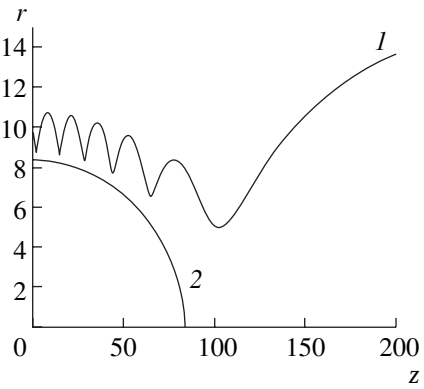

Fig. 2. Same as in Fig. 1, but for $N_\varphi \neq 0$: (*1*) the projection of the ray trajectory onto the (z, r) plane and (*2*) the critical surface.

The fact that, at the critical surface, the ray trajectories have cusps, which are oriented perpendicular to the magnetic field, indicates the potential nature of the oscillations. Actually, at the critical surface, we have $N_\perp = 0$; in addition, according to [1, 2], the phase and group velocities of the potential oscillations in a magnetic field are mutually orthogonal.

In a cold plasma, the polarization of oscillations is described by the relationship (see [3])

$$\mathbf{E} = (E_+, E_-, E_\parallel) = \text{const}\left(\frac{N_+}{\varepsilon_+ - N^2}, \frac{N_-}{\varepsilon_- - N^2}, \frac{N_\parallel}{\varepsilon_\parallel - N^2}\right). \tag{3}$$

Here, $E_\pm = (E_x \pm iE_y)/\sqrt{2}$ and $N_\pm = (N_x \pm iN_y)/\sqrt{2}$, where the subscripts x and y refer to the vector components in a local right-handed coordinate system with the z-axis directed along the main magnetic field.

Figures 3 and 4 illustrate how the polarization of oscillations changes along the ray trajectory. According to [1], the oscillations continuously change their nature with increasing distance from the critical surface: the

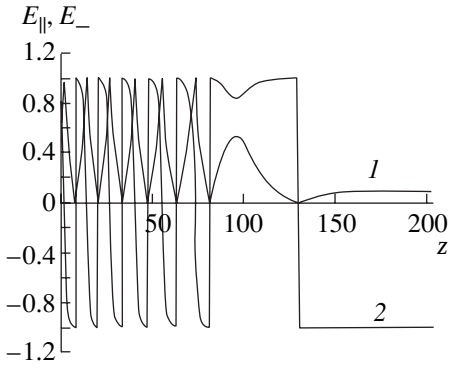

Fig. 3. Polarization of oscillations for the ray trajectory shown in Fig. 1: the z-dependences of (*1*) $E_\parallel$ and (*2*) E_-. In order not to complicate the figure, the small component E_+ is not plotted.

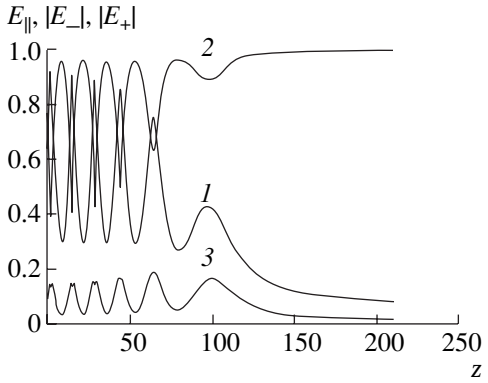

Fig. 4. Same as in Fig. 3, but for the ray trajectory shown in Fig. 2: the z-dependences of (*1*) $E_\parallel$, (*2*) $|E_-|$, and (*3*) $|E_+|$.

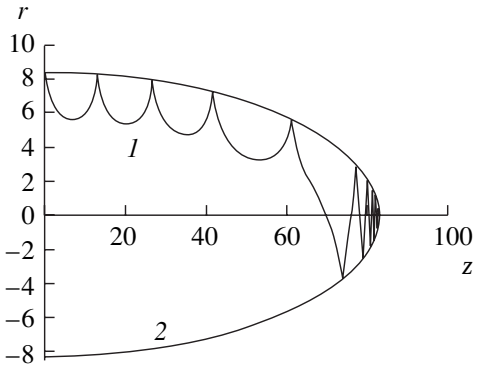

Fig. 5. Ray trajectory on the inside of the critical surface for $N_\varphi = 0$: (*1*) the ray trajectory and (*2*) the critical surface.

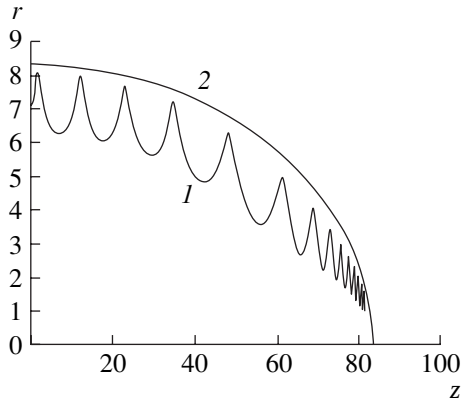

Fig. 6. Same as in Fig. 5, but for $N_\varphi \neq 0$: (*1*) the projection of the ray trajectory onto the (z, r) plane and (*2*) the critical surface.

potential electron Langmuir waves are eventually converted into right-polarized electron whistlers. Along both of the ray trajectories, the left-polarized component of the electric field of the waves is insignificant. Note that, in Fig. 3, the dependence $E_-(z)$ is discontinuous. The discontinuities are peculiar to ray trajectories lying in the (r, z) plane ($N_\varphi = 0$, $\mathrm{Im}E_- = 0$) and occur at the "reflection" points, at which the transverse (with respect to the main magnetic field) component N_x of the refractive index changes sign and the group and phase velocity vectors are aligned with the magnetic field. At the reflection points, the oscillations are of the nature of whistlers, whose electric field is right-polarized [see relationship (3)]. It is well known that whistlers tend to propagate along the magnetic field. As the ray trajectory deviates from the median plane of the device, this tendency becomes dominant; as a result, the trajectory eventually escapes from the plasma.

Figures 5 and 6 show the representative ray trajectories of oscillations on the inside of the critical surface. The initial conditions for these trajectories are $r(0) = 7$, $z(0) = 0.1$, and $N_\perp(0) = 0.2$. Along the first trajectory, we have $N_\varphi = 0$, while, at the initial point of the second trajectory, the angle between the wave vector and the (z, r) plane is equal to 0.75. These figures clearly demonstrate that the rays are focused toward the vertex of the ellipsoidal critical surface: $\omega_{pe}(\mathbf{r}) = \omega$ (see [2]). For $N_\varphi \neq 0$, the centrifugal force in the vicinity of the focal point acts to displace the ray toward the critical surface. The unbounded increase in the refractive index during the focusing of the rays should result in the absorption of oscillations. We note that Langmuir oscillations with $N_\parallel < 1$ can escape from the plasma at a large angle to the magnetic field as electromagnetic oscillations of the other type (ordinary waves). Unlike whistlers trajectories, their trajectories are not tied to the critical surface.

3. Plasma confined in an open confinement system is a useful object for studying the beam–plasma interaction. Theoretically, the injection of an electron beam through the throats of the magnetic mirrors should give rise to electron Langmuir waves. Although electron

Langmuir waves, like all other potential oscillations, cannot escape from the plasma into vacuum, in many experiments (see, e.g., [4]), electromagnetic fields with frequencies of the characteristic plasma frequency were recorded outside the device. This was the case, in particular, in experiments with beam–plasma discharges in magnetic fields [5, 6]. This phenomenon was explained in terms of nonlinear effects, such as the scattering of electron Langmuir waves by plasma particles and decay interactions (see, e.g., [4, 7]), and the linear conversion of waves in the vicinity of the critical surface in an inhomogeneous plasma [8, 9]. The theory of linear conversion was developed in connection with the problem of radio emissions from celestial objects. As a result of linear conversion, potential oscillations escape from the plasma resonance region, in which case the wave energy is transferred through the opaque region from one oscillation branch to another. The phenomenon under discussion differs from the process of linear conversion in that the oscillations continuously change their nature: with increasing distance from the critical surface, potential electron Langmuir waves are converted into electromagnetic waves.

Hence, in a spatially bounded plasma, there exists a natural mechanism by which the energy of electron Langmuir waves escapes into vacuum. It cannot be excluded that this mechanism is also operative in space plasmas.

The general pattern of ray trajectories in open magnetic devices should also persist in other types of plasma configurations with open magnetic field lines. This conclusion is supported by the results of the above calculations for an ellipsoidal plasma in a uniform magnetic field.

In conclusion, note that, in the case of electron beam injection into a plasma, the phenomenon in question should increase in importance with decreasing beam intensity and increasing beam velocity. On the one hand, the lower the beam intensity, the lesser is the importance of the nonlinear processes. On the other hand, the higher the beam velocity, the lower is the refractive index. In the opposite case of a slow (nonrelativistic) beam, the refractive index for the excited oscillations is much larger than unity. Such oscillations can escape from the plasma due to the linear conversion mechanism (see [8, 9]).

ACKNOWLEDGMENTS

This study was supported in part by the Russian Foundation for Basic Research, project no. 00-15-96526 (under the program “Leading Scientific Schools”).

REFERENCES

1. A. V. Timofeev, Fiz. Plazmy **27**, 282 (2001) [Plasma Phys. Rep. **27**, 265 (2001)].
2. A. D. Piliya and V. I. Fedorov, in *High-Frequency Plasma Heating*, Ed. by A. G. Litvak (Inst. Prikl. Fiz., Gorki, 1983), p. 281.
3. A. V. Timofeev, *Resonance Phenomena in Plasma Oscillations* (Nauka, Moscow, 2000).
4. B. A. Demidov, N. I. Elagin, D. D. Ryutov, and S. D. Fanchenko, Zh. Éksp. Teor. Fiz. **48**, 454 (1965) [Sov. Phys. JETP **21**, 302 (1965)].
5. A. K. Berezin, G. P. Berezin, L. I. Bolotin, and Ya. B. Faĭnberg, At. Énerg. **14**, 249 (1963).
6. V. E. Golant, A. P. Zhilinskiĭ, I. F. Liventsova, and I. E. Sakharov, Zh. Tekh. Fiz. **35**, 2034 (1965) [Sov. Phys. Tech. Phys. **10**, 1559 (1965)].
7. V. N. Tsytovich, *Nonlinear Effects in Plasmas* (Nauka, Moscow, 1967; Plenum, New York, 1970).
8. V. L. Ginzburg, *The Propagation of Electromagnetic Waves in Plasmas* (Nauka, Moscow, 1967; Pergamon, Oxford, 1970).
9. V. V. Zheleznyakov, *Electromagnetic Waves in Space Plasmas* (Nauka, Moscow, 1977).

Translated by O. E. Khadin

Plasma Physics Reports, Vol. 27, No. 11, 2001, pp. 994–996. Translated from Fizika Plazmy, Vol. 27, No. 11, 2001, pp. 1050–1052.

BRIEF COMMUNICATIONS

Effect of the Radial Electric Field on the Results of Measurements of the Poloidal Rotation of a Tokamak Plasma by Charge Exchange Recombination Spectroscopy

A. N. Romannikov and A. P. Chernobai

Troitsk Institute for Innovation and Fusion Research, Troitsk, Moscow oblast, 142092 Russia

Received April 9, 2001; in final form, May 23, 2001

Abstract—The effect of the radial electric field E_r on the results of measurements of the poloidal rotation of a tokamak plasma by charge exchange recombination spectroscopy is considered. It is shown that the emission line shift arising from the finite lifetime of the excited state of the ions is proportional to E_r. For helium ions, the maximum shift corresponds to the poloidal rotation velocity, which is about one-third of the drift velocity in the crossed radial electric (E_r) and toroidal magnetic (B_t) fields. *© 2001 MAIK "Nauka/Interperiodica".*

The onset of improved confinement modes in tokamaks (such as H-modes and modes with internal transport barriers) is attributed to the change in the radial electric field in a plasma. The main experimental results on the radial electric field E_r in tokamaks were obtained from laboratory investigations of the poloidal and toroidal rotation velocities of light impurity ions (He^{+2}, C^{+6}, etc.) by spectroscopic measurements of charge exchange ions [1]. This spectroscopic method, which will be referred to as CXRS (charge exchange recombination spectroscopy), is based on measurements of the Doppler shift of the spectral lines emitted in charge exchange reactions such as

$$C^{+6} + H^0 \longrightarrow C^{+5*} + H^{+1} \longrightarrow C^{+5} + H^{+1} + h\nu. \quad (1)$$

Hydrogen atoms participating in charge exchange reactions are usually injected into the plasma in the form of heating or diagnostic beams. The rotation velocity of the tokamak plasma can be calculated from the measured Doppler shift of a particular spectral line (for C^{+5} ions, it is usually the 529.07-nm line and, for He^{+1} ions, it is the 4685.2-nm line).

Tokamak experiments with strong radial fields E_r and large gradients of E_r (see, e.g., [2, 3]) showed that the poloidal plasma rotation velocity measured by the CXRS method is significantly higher than that predicted by the neoclassical theory. According to neoclassical theory, the poloidal plasma rotation velocity in a tokamak with circular magnetic surfaces is closely related to both the ion temperature gradient and the collisionality parameter but it does not depend explicitly on E_r (see, e.g., formula (33) in [4]). In some cases, agreement between theory and experiment can be improved by taking into account such factors as the friction of ions on neutral atoms in charge exchange processes, anomalous viscosity, the actual plasma geometry, and the effect of the possible large gradients of E_r on ion trajectories.

Recently, it has been suggested that one of the possible ways of explaining the discrepancy between theory and experiment is to take into account the finite lifetime τ of the excited state of an ion in experiments aimed at spectroscopic measurements of the parameters of charge exchange ions [3, 5]. In this way, however, the measured Doppler shift of the chosen spectral line depends on τ in a complicated manner and is highly sensitive to the actual experimental arrangement. It was shown that, under certain conditions, the real plasma rotation and the measured Doppler shift have opposite signs.

The way in which the effect of the finite lifetime of the excited state of an ion on the measured poloidal plasma rotation is explained in the present paper differs from that given in [3, 5]. From reaction (1), we can see that the CXRS method actually yields the parameters of the excited C^{+5*} (rather than the original C^{+6}) ions. Consequently, in the presence of the radial electric field E_r, the velocities of C^{+6} and C^{+5*} ions, being essentially the same at the instant of the charge exchange event, become different at the instant of the emission event (after the time interval τ). As a result, the actually measured distribution function of the C^{+5} ions differs from the original distribution function of the C^{+6} ions [6].

This difference can be estimated from the following analysis. We consider the charge exchange of X^Z ions (where Z is the ion charge number) with the hydrogen atoms of an injected neutral beam. Let the spectral line (at frequency ν) of an ion whose excited state exists for a finite lifetime τ be measured by the CXRS method. We assume that the drift velocity in crossed toroidal magnetic and radial electric fields is small in comparison with the velocities of the ions in question. For each of the X^Z and X^{Z-1} ions whose initial velocity compo-

1063-780X/01/2711-0994$21.00

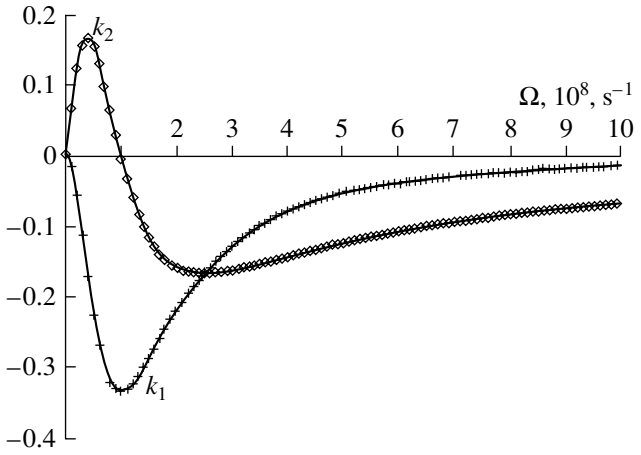

Dependence of the coefficients k_1 and k_2 in formula (2) on the Larmor frequency Ω of helium ions. For the chosen spectral line, the transition probability is $A = 1.44 \times 10^8$ s^{-1}.

nents are V_{r0} and V_{p0} (where r and p stand for the radial and poloidal directions, respectively; the third coordinate axis is oriented so that it is parallel to the toroidal magnetic field B_t, and the coordinate system is right-handed), we can exactly calculate their velocities at any subsequent instant. We also assume that the X^Z ions obey a Maxwellian distribution function f_1 shifted by the magnitude of the drift velocity, in which case, just after the charge exchange event, the distribution functions of the X^Z and X^{Z-1} ions essentially coincide. Under all of the above assumptions, we take into account the probability $A = 1/\tau$ of the decay of the excited state in order to show that

$$f_2 \simeq f_1 \exp\left(Mc\frac{E_r}{B_t}\frac{k_1 V_{p0} + k_2 V_{r0}}{T_i}\right), \qquad (2)$$

where M is the mass of an ion, T_i is the ion temperature, c is the speed of light,

$$k_1 = A^2\Omega^2\frac{1-2Z}{(A^2+(Z-1)^2\Omega^2)(A^2+Z^2\Omega^2)},$$

$$k_2 = A\Omega\frac{A^2 - Z(Z-1)\Omega^2}{(A^2+(Z-1)^2\Omega^2)(A^2+Z^2\Omega^2)},$$

and Ω is the Larmor frequency of a singly charged X^1 ion.

We propose to interpret the difference between f_1 and f_2 in the CXRS measurements as a direct measure of the poloidal rotation velocity, which is proportional to E_r. Note that the radial motion of X^{Z-1} ions differs from that of X^Z ions. It is this difference that causes the observed spectral line to shift by an amount proportional to E_r. The shift is maximum when the reciprocal of the lifetime, $1/\tau$, is equal to the Larmor frequency of the ions under investigation. The transition probability for light impurity ions is on the order of 10^8 s^{-1}, which corresponds to the Larmor frequency of these ions in a toroidal magnetic field of about 2–4 T. The figure shows the dependence of the coefficients k_1 and k_2 on Ω (which is assumed to be a variable quantity) for helium ions. One can see that the absolute value of the coefficient k_1 is maximum ($k_1 = -0.33$) at the Larmor frequency $\Omega \simeq 10^8$ s^{-1} (for the $N = 4 \longrightarrow 3$ spectral line of He^{+1} ions, the transition probability is $A = 1.44 \times 10^8$ s^{-1}). For carbon ions, the maximum absolute values of k_1 and k_2 are smaller than those for helium ions by a factor of about three.

CONCLUSION

In the presence of the radial electric field E_r, the finite lifetime of the excited state of the ions in question leads to additional poloidal and radial shifts of the ion distribution function in comparison with the shifts of the distribution function of the same ions before the charge exchange. The poloidal velocities corresponding to these additional shifts are proportional to E_r. The largest shifts can be observed when the CXRS method is used to measure the parameters of helium ions, whose poloidal rotation velocity in a toroidal magnetic field of about 3–4 T may amount to approximately $\sim 0.3cE_r/B_t$. Unfortunately, cascade transitions alter the effective transition probability in real plasmas. Consequently, the effect under investigation, first of all, worsens the accuracy in the measurement of the poloidal rotation velocity of a tokamak plasma by the CXRS method.

Nevertheless, the magnitudes of the poloidal rotation velocity V_p measured in experiments with strong radial electric fields E_r can be partially explained in terms of this effect. This conclusion refers primarily to the comparative measurements of the poloidal velocity V_p of He^{+2} and C^{+6} ions in the DIII-D tokamak [2]. In those experiments, it was found that the poloidal velocity of C^{+6} ions is close to the neoclassical velocity in the observed region near the plasma boundary, whereas the poloidal velocity of He^{+2} ions is higher than the predicted neoclassical velocity by a factor of 3 to 10. The effect under consideration barely manifests itself in the measured poloidal velocity of C^{+6} ions; however, when it is taken into account, the measured velocity of He^{+2} ions turns out to be lower by a factor of 1.2–1.3.

Note that a similar effect may also manifest itself in investigations of the ion spectral lines in recombination reactions in the radial electric field, in which case the ions can be excited and exist for a finite time before they emit light.

ACKNOWLEDGMENTS

We are grateful to S. Tugarinov and V. Agapov for discussing the physical interpretation of the phenomenon under investigation.

REFERENCES

1. R. J. Fonck, R. J. Goldston, R. Kaita, and D. Post, Appl. Phys. Lett. **42**, 239 (1983).
2. J. Kim, K. H. Burrell, P. Gohil, *et al.*, Phys. Rev. Lett. **72**, 2199 (1994).
3. D. R. Ernst, R. E. Bell, M. G. Bell, *et al.*, Phys. Plasmas **7**, 615 (2000).
4. Y. B. Kim, P. H. Diamond, and R. J. Groebner, Phys. Fluids B **3**, 2050 (1991).
5. M. C. Zarnstorff, Private communication (Princeton Plasma Physics Laboratory, 1998).
6. A. N. Romannikov and A. P. Chernobai, in *Proceedings of the 27th EPS Conference on Controlled Fusion and Plasma Physics, Budapest, Hungary, 2000*, Vol. P3.110, p. 409.

Translated by I. A. Kalabalyk

Plasma Physics Reports, Vol. 27, No. 11, 2001, pp. 997–999. Translated from Fizika Plazmy, Vol. 27, No. 11, 2001, pp. 1053–1055.

BRIEF COMMUNICATIONS

Dielectric Permittivity of a Plasma in an External Electric Field

V. A. Schweigert†

Institute of Theoretical and Applied Mechanics, Siberian Division, Russian Academy of Sciences, Tomsk, Russia

Received February 7, 2000; in final form, June 25, 2001

Abstract—The ion contribution to the dielectric function of a plasma in an external electric field is determined by applying a kinetic approach to the ions in a parent gas in which the main mechanism for ion scattering is resonant charge exchange. The ion scattering frequency is assumed to be constant. © *2001 MAIK "Nauka/Interperiodica".*

Dielectric permittivity is a fundamental characteristic of plasmas; in particular, it governs the screening of the electric charge in plasmas. In an equilibrium plasma in which the electrons and ions obey Maxwellian velocity distributions, the potential of a test particle is described by the well-known Debye–Hückel law. The electric field–driven electron and ion flows cause the potential of a test particle in the plasma to become asymmetric. The asymmetry is most pronounced in experiments with plasmas containing crystals of charged dust grains [1]. In RF discharges, micron-size charged particles usually occur in the electrode sheaths, where the gravity force is counterbalanced by the electric force. In the electrode sheath, the hydrodynamic velocity V of the ions is, as a rule, higher than their thermal velocity v_t. As a result, the distribution of screening ions around a grain is highly asymmetric and most of them (which form a so-called ion cloud [2]) occur downstream from the grain. It is the asymmetry of the grain potential that governs both the structural type of dust crystals [2–5] and the mechanism for their melting [2, 6, 7].

To the best of my knowledge, the dielectric permittivity of a plasma with charged particle flows was investigated only in the limiting cases of a collisionless plasma ($k\lambda \gg 1$, see, e.g., [3]) and a strongly collisional plasma ($k\lambda \ll 1$) in a weak field such that $V \ll v_t$, when the plasma can be described in the drift–diffusion approximation [8]. Here, k is the wavenumber and λ is the mean free path of the charged particles. The objective of the present paper is to calculate the contribution of the ion component to the plasma dielectric function for an arbitrary value of $k\lambda$.

We consider the linear response of the ion distribution function (IDF) $f_i(t, \mathbf{v}, \mathbf{r})$ to a perturbation of the potential ϕ of the electric field in the presence of an external electric field E in a noble gas in which the main mechanism for ion scattering is resonant charge exchange. The cross section for this process is almost independent of the ion velocity [8]. Nevertheless, in order to simplify the analytic treatment, we describe resonant charge exchange by the so-called Maxwell model, in which the scattering frequency ν of the ions is assumed to be constant (this model was used, e.g., in [9]). Then, the IDF is described by the kinetic equation

$$\frac{\partial f_i}{\partial t} + \mathbf{v}\frac{\partial f_i}{\partial \mathbf{r}} - \frac{e\nabla\phi}{M}\frac{\partial f_i}{\partial \mathbf{v}} = \nu[n_i f_g(\mathbf{v}) - f_i(\mathbf{v})], \quad (1)$$

where $f_g = (M/2\pi T)^{3/2}\exp(-Mv^2/2T)$ is the Maxwellian velocity distribution function of the gas atoms, T is the gas temperature, M is the mass of a gas atom, and

$$n_i(\mathbf{r}) = \int f_i(t, \mathbf{v}, \mathbf{r})d\mathbf{v} \quad (2)$$

is the spatial ion density distribution. We represent the electric potential, ion density distribution, and IDF as $\phi = \phi_0 + \phi'$, $n_i = n_0 + n$, and $f_i = f_0 + f$, respectively. Then, we linearize Eq. (1) and normalization condition (2) with respect to the small perturbations ϕ', n, and f. Taking the Fourier transformation of Eq. (1) in the coordinates and time, ϕ', n, $f \sim \exp(i\mathbf{kr} + i\omega t)$, we arrive at the following equation for the perturbed IDF:

$$\frac{eE}{M}\frac{\partial f}{\partial v_z} + i\omega f + i\mathbf{kv}f + \nu f = \nu f_g n + \frac{e\phi'}{M}i\mathbf{k}\frac{\partial f_0}{\partial \mathbf{v}}, \quad (3)$$

where the z-axis is oriented along the external field ($\phi_0 = -zE$) and the unperturbed IDF satisfies the equation

$$\frac{eE}{M}\frac{\partial f_0}{\partial v_z} + \nu f_0 = \nu n_0 f_g. \quad (4)$$

The solution to Eqs. (3) and (4) can be written as

$$f = \int_{-\infty}^{v_z} dv_z' \exp\left\{-\frac{v_z - v_z'}{\nu V}[\nu + i\omega + i\mathbf{kv} + ik_z(v_z' - v_z)/2]\right\}\left(n\frac{f_g}{V} + \frac{\phi'}{E}i\mathbf{k}\frac{\partial f_0}{\partial \mathbf{v}}\right), \quad (5)$$

† Deceased.

1063-780X/01/2711-0997$21.00 © 2001 MAIK "Nauka/Interperiodica"

$$f_0 = n_0 \int_{-\infty}^{v_z} \frac{f_g}{V} \exp\left(-\frac{v_z - v_z'}{V}\right) dv_z', \quad (6)$$

where $\mathbf{k} = (k_\perp, k_z)$ and $V = eE/\nu M$ is the ion drift velocity. The perturbed ion density can be found by substituting expression (5) into normalization condition (2). After a fairly lengthy integration over the ion velocities, we can write the perturbed ion density as

$$n = -\frac{en_0 k^2}{M\nu^2} \frac{\phi'}{G}, \quad (7)$$

where

$$G = \frac{1 - \int_0^\infty \exp[-x - ix\omega/\nu - x^2(D_\perp k^2 + iVk_z)/2\nu]dx}{\int_0^\infty x(1 + iVxk_z/\nu)^{-1} \exp[-x - ix\omega/\nu - x^2(D_\perp k^2 + iVk_z)/2\nu]dx}, \quad (8)$$

with $D_\perp = T/\nu M$ being the transverse ion diffusion coefficient. In this case, the ion contribution to the longitudinal dielectric function of the plasma is determined from the formula

$$\epsilon_l - 1 = \frac{\omega_i^2}{\nu^2} G^{-1},$$

where $\omega_i = \sqrt{4\pi e^2 n_0/M}$ is the ion plasma frequency.

Since the thermal velocity of the electrons is usually much higher than their hydrodynamic velocity, the electron contribution to the plasma dielectric function can be calculated from the familiar expressions [10] that were obtained for a Maxwellian electron distribution function. In this case, the potential of a negatively charged test particle (with charge $-eZ$) in a plasma has the form

$$\phi = -\frac{4\pi eZ}{k^2 + \kappa_e^2 + \kappa^2 k^2 G^{-1}}, \quad (9)$$

where $\kappa_e = \sqrt{4\pi e^2 n_0/T_e}$ is the reciprocal of the electron Debye length, $\kappa = \omega_i/\nu$, and T_e is the electron temperature. In some cases, the screening effect of the plasma electrons can be neglected, so that the ion density distribution within the ion cloud can be written as

$$n = Z\frac{\kappa^2}{G + \kappa^2}. \quad (10)$$

Recall that we will not examine expressions (9) and (10) in detail. Our aim here is merely to analyze the function G, which determines the linear response of the ion density to the electric field perturbation in a steady state ($\omega = 0$). In the long-wavelength limit ($D_\perp k^2$, $V|k_z| \ll \nu$), we have

$$G = \frac{D_\perp}{\nu} k^2 + i\frac{V}{\nu} k_z - 2\frac{V^2}{\nu^2} k_z^2. \quad (11)$$

Note that, since the electric field nonuniformity leads to the renormalization of the kinetic coefficients, the first two terms in expression (11) can only be correctly obtained in the drift–diffusion approximation. The hydrodynamic approximation for cold ions [4] yields $G = iVk_z/\nu - V^2 k_z^2/\nu^2$ and, therefore, fails to produce a correct coefficient in front of the last term in expression (11). The reason for this is that the unperturbed IDF under consideration differs from the ion distribution function in the hydrodynamic model, in which the ions are assumed to form a monoenergetic beam. Note also that, in the collisionless limit ($V|k_z| \gg \nu$), the hydrodynamic approximation gives $G = -V^2 k_z^2/\nu^2$. This expression, which describes undamped oscillations of the ion density downstream from the test particle, was used in [3] in order to analyze the distribution of the potential of a charged particle in the presence of an ion flow. The deviation of the unperturbed IDF from a monoenergetic distribution function leads to another asymptotic expression in the collisionless (or, in other words, short-wavelength) limit:

$$G = -2\frac{V^2 k_z^2}{\nu^2}\{e^\gamma \mathrm{Ei}(-\gamma) + i[\sqrt{\pi/\gamma} - \pi e^\gamma(1 - \Phi(\sqrt{\gamma}))]\}^{-1}, \quad (12)$$

where Ei is the integral exponent, Φ is the probability integral, and $\gamma = \nu(D_\perp k^2 + iVk_z)/V^2 k_z^2$. For cold ($T = 0$) ions, expression (12) reduces to $G = -(1 - i)(Vk_z/\nu)^{3/2}/\sqrt{\pi}$. Consequently, because of the spread in ion velocities,

the oscillations of the ion density downstream from the test particle are always damped.

ACKNOWLEDGMENTS

This work was supported in part by INTAS–RFBR, project no. IR-97-775.

REFERENCES

1. J. H. Chu and I. Lin, Phys. Rev. Lett. **72**, 4009 (1994); H. Thomas, G. E. Morfill, V. Demmel, *et al.*, Phys. Rev. Lett. **73**, 652 (1994); Y. Hayashi and K. Tachibana, Jpn. J. Appl. Phys. **33**, L804 (1994); A. Melzer, T. Trottenberg, and A. Piel, Phys. Lett. A **191**, 301 (1994).
2. A. Melzer, V. A. Schweigert, I. V. Schweigert, *et al.*, Phys. Rev. E **54**, R46 (1996); V. A. Schweigert, I. V. Schweigert, A. Melzer, *et al.*, Phys. Rev. E **54**, 4155 (1996).
3. S. V. Vladimirov and M. Nambu, Phys. Rev. E **52**, 2172 (1995); S. V. Vladimirov and O. Ishihara, Phys. Plasmas **3**, 444 (1996); O. Ishihara and S. V. Vladimirov, Phys. Plasmas **4**, 69 (1997).
4. F. Melandso and J. Goree, Phys. Rev. E **52**, 5312 (1995).
5. V. A. Schweigert, I. V. Schweigert, V. M. Bedanov, *et al.*, Zh. Éksp. Teor. Fiz. **115**, 877 (1999) [JETP **88**, 482 (1999)].
6. F. Melandso, Phys. Rev. E **55**, 7495 (1997).
7. V. A. Schweigert, I. V. Schweigert, A. Melzer, *et al.*, Phys. Rev. Lett. **80**, 5345 (1998); Zh. Éksp. Teor. Fiz. **114**, 1672 (1998) [JETP **87**, 905 (1998)].
8. E. W. McDaniel and E. A. Mason, *The Mobility and Diffusion of Ions in Gases* (Wiley, New York, 1973; Mir, Moscow, 1976).
9. K. Kumar, Aust. J. Phys. **48**, 365 (1995); H. Sugawara, H. Tagashira, and Y. Sakai, J. Phys. D **29**, 1168 (1996).
10. E. M. Lifshitz and L. P. Pitaevskii, *Physical Kinetics* (Nauka, Moscow, 1979; Pergamon, Oxford, 1981).

Translated by O. E. Khadin